CRANFIELD UNIVERSITY

GAMAL MOHAMED ASHAWESH

FLUTTER BEHAVIOUR OF COMPOSITE AIRCRAFT WINGS

COLLEGE OF AERONAUTICS

Ph.D. THESIS

CRANFIELD UNIVERSITY

COLLEGE OF AERONAUTICS

Ph.D. THESIS

ACADEMIC YEAR 1998/99

GAMAL MOHAMED ASHAWESH

FLUTTER BEHAVIOUR OF COMPOSITE AIRCRAFT WINGS

Supervisor: Dr. R. S. Battoo

1999

This thesis is submitted in partial fulfillment of the requirements for the degree of Doctor of Philosophy

Proclaim ! (or Read!) In the name of thy Lord and Cherisher. Created man, out of a (mere) clot of congealed blood. Proclaim ! And thy Lord is Most bountiful. He who taught (the use of) the Pen. Taught man that which he knew not.

Al-Qur'an 96:1-5

ACKNOWLEDGMENTS

First of all, I thank Allah (God) Almighty, for giving me the ability, health and knowledge, which enabled me to complete the requirements of my academic career.

I would especially like to thank my supervisor Dr. R. S. Battoo for his invaluable help and encouragement throughout the course of this research.

I would also like to thank Mr. J. Brown for his suggestions regarding the modelling techniques of aircraft wing structure using finite element method through the use of MSC/NASTRAN.

I would also like to thank the computer manager Dr. R. L. Oswald for providing enough quota to finish all the required analysis in the sun system of the college of aeronautics.

I would also like to thank the Flight System and Measurements Laboratory group at Cranfield Aerospace for the loan of equipment and their device for the vibration experimental test.

I would also like to thank Mr. Brookman from the Flight System and Measurements Laboratory group for his help and support during the vibration test.

Most importantly, I wish to take this opportunity to thank all of my family for their support throughout my time at Cranfield and before, especially my wife for her patience and generosity and our children (Mohamed, Ahmed and Sara), who always cheer me up.

I would like to dedicate this manuscript to my mother and the soul of my father, who were interested in my education and inspired me with their enthusiasm and love.

ABSTRACT

This research work presents series of investigations into the structural dynamics and dynamic aeroelastic (flutter) behaviour of composite and metal wings. The study begins with a literature review where the development and an over view of the previous investigations in this field are presented. Static stiffness is very important to any type of analysis, especially in both dynamic and flutter analysis as in this case. Therefore, different methods are presented and used for the determination of cross-sectional rigidities such as bending, torsional and bending-torsional coupling rigidities properties for beams constructed of laminated and thin-walled structures materials.

A free vibration experimental analysis was conducted on the physical Cranfield A1 aerobatic composite wing box structure. The composite wing box was exited in the frequency range of 0 to 300 Hz, with both sinusoidal and random excitations, which yields to six resonant frequencies.

The theoretical free vibration and flutter analysis was then carried out firstly on the physical Cranfield A1 aerobatic metal wing box. The metal wing was modeled using two techniques; the first model was a simplified wing structure (beam with lumped mass). This analysis of the simplified model was done using CALFUN program for the free vibration analysis and using MSC/NASTRAN for both free vibration and flutter analysis. The second model was a detailed model created by MSC/PATRAN and analyzed by MSC/NASTRAN for the free vibration and flutter analysis. The obtained results (natural frequencies and mode shapes) showed a good agreement between the simplified, detailed model and the experimental test. It was found that even with using the simplified model, but having the physical characteristics of the wing leads to a good agreement with the detailed model and experimental work. This also showed the importance of simplified model at early stage of the design to the structural designer in terms of the accuracy, time, and size of the model.

Free vibration and flutter analysis was carried out on the Cranfield A1 aerobatic composite wing box with the original laminate lay ups using Lanczos method for extracting the eigenvalues and eigenvectors and using PK method for finding the flutter speed and frequency provided by MSC/NASTRAN. The results

were compared with the experimental vibration analysis and were found a large difference in the first frequency mode. To investigate the cause of the variation, a series of static loading tests were performed on the composite wing box. Also a comparison of the results between the metal and composite aerobatic wing box is presented. It was found that the large difference could be due to the combination of different parameters such as stiffness (age of the wing, delamination and boundary condition), and increase of mass of the physical wing box (due to environmental effect such as moisture) and modelling differences.

The free vibration characteristics of ten wing models constructed from balanced and unbalanced laminate configurations were carried out using Lanczos method provided by MSC/NASTRAN. The analysis was done on ten wing models modeled to simulate Circumferentially Asymmetric Stiffness (CAS) and Circumferentially Uniform Stiffness (CUS). The static equivalent stiffness was calculated using two different modeling methods for a wide range of fibre angles θ (-90° to 90°) of the skins. The variations and the importance of the stiffness ratio (EI/GJ), parameter (K/GJ), and the frequency ratio (ω_b/ω_t) are illustrated against the fibre angle θ. It was found that the fundamental bending frequency is slightly lower in the case of CUS ($K = 0$) as compared to the CAS ($K \neq 0$), which was not the case in the plate model. Also, the first torsion frequency mode in the case of CUS was much lower than the first torsion frequency of the CAS, which was not the case of the plate model. However, the effect of bend-twist coupling stiffness on the mode shapes was pronounced in both structures especially at the area of higher coupling stiffness.

The flutter analysis was done using the PK method for all the wing models of both (CAS) and (CUS) configurations. The results showed the optimum value of flutter speed and the importance of the stiffness ratio (EI/GJ), parameter (K/GJ), the frequency ratio (ω_b/ω_t), which will lead to the maximum flutter speed. The effects of the above parameters, geometrical coupling and the wash-in and washout on the non-dimensional flutter speed are presented. It was concluded that, negative bend-twist coupling stiffness is beneficial for flutter speed compared to the positive bend-twist coupling stiffness at $0° < \theta \leq 30°$. It was also found that the flutter speed for the CUS was higher at $0° < \theta \leq 30°$ compared to the CAS. Also creating an offsite between the

elastic axis and center of gravity (behind) decreases the flutter speed whereas having more ribs increases the flutter speed compared with adding stringers.

The analysis was carried out on a more practical composite wing box, which was the physical Cranfield A1 aerobatic composite wing box. There are some simplifications on the physical structure, which are the cancellation of the woven materials and keeping the same laminate lay ups for the upper and lower skin. The natural frequency and mode shapes was obtained and plotted against the fibre angle θ of the upper and lower skin for the (CAS) and (CUS) configurations using both symmetric and asymmetric laminate for the upper and lower skin. The flutter analysis was done for the composite wing box for the same configurations as in the free vibration analysis. The effects of the fibre angle θ of the upper and lower skin, material coupling stiffness, wash-in and wash-out, and structural damping on the non-dimensional flutter speed and flutter frequencies are illustrated. It was found that in this configurations both structural and bend-twist coupling are exist, negative bend-twist coupling (wash-in) increases the flutter speed compared with the positive bend-twist coupling, and the possibility of increasing the flutter speed at higher frequency ratio, structural coupling and positive bend-twist coupling (wash-out).

LIST OF CONTENTS

LIST OF FIGURES

LIST OF TABLES

CHAPTER 1

GENERAL INTRODUCTION

1. GENERAL INTRODUCTION:

1.1 Background:

The optimal use of structural materials in aircraft design has always been an objective of the designers. The minimum weight aspect of aircraft design is well known. Reference [1.1] writes,

> "Primary function of the aircraft structure is to transfer forces through space…. The objective is to do this with minimum possible weight and minimum cost…the optimum structure is the one that does the best overall job of minimizing the undesirable quantities (weight, air resistance, cost, service troubles, production time, etc.)."

Flexibility is generally associated with light weight so that aeroelastic problems were discovered and known from the earliest days of flight. We may recall that the Wright Brothers in 1903 made favourable use of flexibility in the lateral control of their aircraft by wing warping and that they were aware of the adverse effect of torsional deformations on the thrust of a propeller. Wing divergence, static aeroelastic problem, has been surmised as the probable cause of S.P. Langley's failure to control his machine in its first flight over Potomac in the same year. During World War I, in 1916, elevator flutter of a British bomber was investigated by the pioneer F. W. Lanchester and was solved by increasing the torsional rigidity of the elevators.

Although numerous other aeroelastic incidents followed in the pre-World War II period, problems in aeroelasticity did not attain the prominent role that they now play until the early stages of the war. This is partly because by that time the problem had been understood and the foundation of the basic theory had been laid with sources of contributions in many countries, such as, UK, USA and the Netherlands. This is because aircraft speeds were relatively low and their thickness to chord ratio was relatively high, thus giving the structural engineer the required design flexibility to obtain the required bending and torsional rigidities and thus producing structures sufficiently rigid to prevent most aeroelastic phenomena.

Although many isolated aeroelastic incidences still occurred in that period (1916), they could generally be explained away and gave an ad-hoc solution. In particular, problems relating to flutter were prevented by isolating the motions in several freedoms, such as mass balancing of the lifting surfaces at the expense of an additional weight, and/or by raising the lowest critical flutter speed safely beyond possible speeds of flight by increase of the relevant natural frequencies. The latter was usually effected by designing for increased stiffness with a less than proportional increase of weight or, preferably, without any increase of weight.

Thus the two basic solutions for aeroelastic problems, increased stiffness and mass balance, were already well established, and together with damping mechanisms, are still the basic elements that must be used in the vehicle structure to prevent aeroelastic instabilities.

For most designs developed between the two World Wars, flutter, which usually involved coupling between an almost pure bending and a pure torsional mode due to the unswept and more or less constant chord wing planform, would most often occur at a lower airspeed than divergence and as result it was given more attention. This situation changed in the late 40's with the first approaches towards transonic flight as a result of the advent of jet engine and the introduction of improved light alloy structures. It was found that the best way to reduce the high transonic drag build-up was to sweep the wing relative to the airflow forward or backward. However, the divergence speed drops dramatically for even slight forward sweep angles due to the wash-in effect. The spanwise bending of a swept-forward wing induces an increase in the local streamwise angle of attack, resulting in an increase in aerodynamic loads. A swept back wing experiences an opposite, or wash-out effect.

The objective of ever improved performance has led to thinner, lighter and more flexible wings which, coupled with moderately high aspect ratio and sweep, induced unintentional coupling between the various modes of structural deformation. Therefore, the classical flutter problem, where almost pure bending mode couples with almost pure torsional one, has been transformed into a more complex one. These unintentional couplings, which proved to have adverse effects in design, have overlapped stability, response, and flutter. Correspondingly this has narrowed the aeroelastic margins of required stiffness, so that aeroelastic problem have become more complex.

In the ten years period from 1947-1957 a survey by [1.4] indicated that more than 100 different aeroelastic incidents occurred in the United State alone, for civil and military aircraft. These occurred mostly for control surfaces and tabs, but also induced all-movable surface, wings carrying external stores, and one case of a T-tail airplane.

As a result, structural engineers were conformed with requirements for stiffness, which were now very severe (especially for the transonic speed range) so that their ability to meet such stiffness levels become increasingly marginal. This necessitated thinner and lighter wings, so designers turned to more complicated designs in order to control aeroelastic problems. Hill's isoclinic wing is an example of such practice. Hills idea to improve the aeroelastic performance of the wing, being primarily concerned with aircraft longitudinal and lateral stability as well as aileron reversal. This wing was designed so that its incidence to the airflow remained constant along the span when the wing flexed. This was achieved, in part, by placing the torsion box well back in the wing. This showed that with careful design, bending-torsion coupling on a scale, which had not previously been experienced, could be successfully accommodated.

Almost 20 years elapsed before the idea to control passively the wing incidence due to flexural distortion was again proposed as a result of the more or less simultaneous invention, around 1960, of graphite fibres in the UK and boron fibres in the USA. The introduction of composite material into the area of the aircraft design in the early 70s, has led to new airframe design concepts as well as the re-evaluation of older concepts. The main attraction in using composite material is the substantial weight saving that could be achieved because of their superior strength-to-weight and stiffness-to-weight ratios, compared with conventional materials of aircraft construction such as aluminum alloy. Weight savings of the order of 25% can generally be achieved using current composite instead of isotropic materials. The drawback of the composite structure as it is effected by the environment such as moisture and delamination in the laminate of the structure, which leads to a change in the static elastic and inertia stiffness of the structure especially the dynamic behaviour of the structure.

Today almost every aerospace company is developing products made with fibre reinforced composite materials. The most common application of composites in fixed

wing aircraft structures is the skin of wings, tail, and control surfaces as shown in table (1.1).

Table (1.1) Composite materials used in aircraft structures

Aircraft	Applications
F-14	Boron/epoxy horizontal stabilizer
F-15	Boron/epoxy horizontal and vertical tail skins, cabin Floor, and stabilator
F-16	Graphite/epoxy horizontal and vertical tail skins and Control surfaces
F/A-18	Graphite/epoxy wing skins, horizontal and vertical Tail skins, speed brake, and control surfaces
AV-8B	Graphite/epoxy wing (skin and substructure), horizontal Tail skin, forward fuselage, and control surfaces
X-29	Graphite/epoxy wing skins
Boeing 757 and 767	Graphite/epoxy control surfaces, graphite-aramid/epoxy Fairings, cowlings, etc.
Lear Fan 2100	Almost all graphite/epoxy structure
DC-10	Graphite/epoxy rudder and vertical fin structural boxes
Lockheed L-1011	Graphite/epoxy inboard aileron and vertical fin box
Boeing 727	Graphite/epoxy elevators
Boeing 737	Graphite/epoxy horizontal stabilizer box
A300/A310	Carbon/epoxy vertical fin
A320	Composite horizontal tail and vertical fin
P-180 Avanti	Composite on the nose cone, canard, nacelles, wing Trailing edge, empennage, and control surfaces

Due to their outstanding properties, fibre reinforced laminated composite thin-walled structures are likely to play a very important role in the construction of aeronautical and aerospace vehicles. While the main driving force behind their

increasing use has been their high specific stiffness and strength, fibre-reinforced materials have another property, anisotropic. This anisotropic property can be used to induce elastic coupling between various modes of structural deformation of fibre composite structures to a far greater degree than is possible, if at all, in their metallic counterparts. However, these elastic couplings are typically not exploited in composite designs. In particular, this inherent tailorability of composite structures has not taken advantage of in aeroelasticity, partly because the mechanisms of inducing favourable effects by control deformation are insufficiently understood. As with the introduction of any new technology, a large amount of basic research is needed in order to obtain a better understanding of new problems created by the use of composite structure materials.

As a consequence, the successful application of laminated composite materials in aircraft structures, coupled with their anistropic property has generated a renewed interest in the field of aeroelasticity. Exploiting the directional properties of composite materials, and thereby creating aerodynamic loads through controlled deformation could control aeroelastic problems such as flutter and divergence, without excessive weight (i.e., mass balance, increase in bending and torsional rigidities by adding material, etc). The technology to design for a predetermined aeroelastic response of a lifting surface using composite materials has been named aeroelastic tailoring. Aeroelastic tailoring was defined by [1.2] as,

> "the embodiment of directional stiffness into an aircraft structural design to control aeroelastic deformation, static or dynamic, in such a fashion as to affect the aerodynamic and structural performance of that aircraft in a beneficial way."

As a result, a great deal of research activity has been devoted to the improvement of aeroelastic stability of wings by use of composites. The application of this new technology has resulted in the possibility of practically eliminating (without any extra weight) the occurrence of aeroelastic divergence of a swept forward wing aircraft. The successful construction of the Grumman X-29 swept forward wing experimental aircraft (here the anisotropic nature of the fibre composite is utilized to

minimize the torsional divergence problem) reveal the exceptional interest expended to this problem. Along with many, known advantages conferred or contributed by the use of structural composites, a series of challenges arises in consequence.

Some of these challenges derived from the complexities arising from anisotropic nature of composite materials themselves, and the multiplicity of structural couplings, which do not exist in the case of isotropic material structures such as light alloy materials. If one looks closer at the problem of flutter, only an increase in a wash-in deformation is required to increase the flutter speed, and vise versa is required for the divergence problem. Thus, the directional properties of laminated composite materials can be oriented to alter the static and dynamic characteristics of composite aircraft wings, leading to aeroelastic tailoring and thus to possible optimum design.

The introduction of composite materials can be regarded as a landmark in the history of aircraft design and the unusual static and dynamic characteristics of these materials are expected to have a beneficial application in the field of aeroelasticity.

1.2 Flutter Phenomena:

Aeroelasticity is the study of the effect of aerodynamic forces on elastic bodies, such as aircraft wings or compressor blades. The generated aerodynamic forces depend fully on the deformed shape of the structure in the flow. One of the aeroelastic problems is the stability, or rather the instability, of a structure in a flow. For a given initial shape of an elastic structure, the aerodynamic force increases rapidly with the flow speed, and there may exist a critical flow speed at which the structure becomes unstable. Such instability may cause excessive deformation, and may lead to the destruction of the structure.

The interplay of aerodynamic, elastic, and inertia forces is usually called flutter or dynamic aeroelastic instability. If a structure is excited with external forces in the presence of no flow the structure will oscillate and the oscillation will damp gradually. With the presence of a flow, the rate of damping of the oscillation may increase at low flow speeds, and on increasing the flow speed, a point will be reached at which the damping rapidly decreases, and the oscillation can just maintain itself with a steady amplitude. This speed is known as the critical flutter speed, and at speed of flow just

above that critical speed, a great violent oscillation will be triggered, at any small disturbance to the structure, and the structure is said to flutter.

1.2.1 Definitions of Flutter:

There are many references (texts and papers), which deal with the subject of aeroelasticity, presented in [1.3] and [1.4], and not to be repeated here. Unfortunately, there are many definitions of flutter within the literature on aeroelasticity, and some of these definitions are given:

- Aeroelastic and self-excited vibration, in which the external source of energy is the air stream;
- Aerodynamic self-exited oscillations;
- Self-sustained oscillatory instability;
- Cyclic and high frequency oscillation of the airfoil caused by a struggle between the aerodynamic forces and the stiffness of the surfaces;
- Dynamic instability of an elastic body in an airstream produced by aerodynamic forces which result from the deflection of the elastic body from its undeformed state;
- Dynamic aeroelastic instability;
- Dynamic instability occurring in an aircraft in flight at a certain speed where the elasticity of the structure plays an essential part in the instability;
- Self-excited or unstable oscillation arising out of the simultaneous action of elastic, inertia and aerodynamic lift forces upon a mass or a system of masses;
- Oscillatory instability arising from the condition where one degree of freedom is driven at resonance by a second degree of freedom, both oscillating at the same frequency;
- Unstable divergent motion or vibration caused by the aerodynamic forces;
- A condition at which the total damping of a system under the action of airforces (and the inertia, elastic, and friction forces) changes from positive to negative, at flutter speed the damping is zero so that sustained oscillations would occur.

There are different types of flutter, which can be encountered by the aircraft structures in different flight regions as presented in [1.5 and 1.6], such as classic flutter or coupled-mode flutter, stall flutter, and shock wave oscillation.

1.3 Objectives of the research:

As mentioned later in chapter 2, the analysis, or the study is carried out mainly for three different aircraft wings, which are as follows:

1.3.1 Thin-walled aircraft wing structures:

Four thin-walled structural geometry configurations are considered in the investigations, these are given below

1. The first thin-walled structure constructed from the upper and lower skins, front and rear spars as shown in figure (1.1);
2. The second thin-walled structure constructed from upper and lower skins, front and rear spars and three ribs located at equal spacing as shown in figure (1.2);
3. The third thin-walled structure constructed from upper and lower skins, front and rear spars and one stringer attached to the middle of the upper and lower skins as shown in figure (1.3);
4. The fourth thin-walled structure constructed from upper and lower skins, front and rear spars and one stringer attached to the upper skins and very close to the rear spar to provide structural coupling as shown in figure (1.4).

The summaries of wing models created from the above thin-walled structures, which used in the analysis were presented in table (8.6).

The main aim of the present work in the first section is to study the potential of composite materials to improve the dynamic aeroelastic stability (flutter) for aircraft clean wings listed above. This study will discuss the effects of aeroelastic tailoring (fibre angle orientations as a design variable from –90 to 90 degrees) for two

configurations, namely, the Circumferentially Asymmetric Stiffness (CAS) and the Circumferentially Uniform Stiffness (CUS) using symmetric and asymmetric laminates in each of the above models. The study will also illustrate the effects of material bending-torsional coupling stiffness, stiffness ratio (EI/GJ), frequency ratio of the first bending frequency to the first torsional frequency (ω_b/ω_t), and the effect of wash-in and wash-out of unswept uniform constant chord cantilever composite wing in the subsonic region on the flutter speed.

Firstly, in order to understand the mechanics of the composite structure, analytical stiffness modeling of the laminated first composite box beam model (wing 1 and wing 6) is examined using two different methods as explained in chapter 3. The effect or the variation of the fibre angle of the upper and lower skin on the on the following parameters of the composite model (wing 1 and wing 6) were investigated.

- Effective bending stiffness (EI),
- Effective torsion stiffness (GJ),
- Bending-torsion coupling stiffness (K),
- Stiffness ratio (EI/GJ), and (K/GJ).

These investigations were carried out with the help of the Microsoft EXECL program for these particular laminate lay-ups.

To achieve the main objective of the first section of the present research, the following steps are taken:

- Free vibration analysis of the first thin-walled structure modeled to simulate both (CAS) and (CUS) (see section 8.4.4 of chapter 8) using symmetric and asymmetric laminate in each configuration (wing 1, wing 2, wing 6 and wing 7) with orienting the fibre angle θ of the upper and lower skin only from –90 to 90 degree using MSC/NASTRAN as shown in figure (8.15) of chapter 8.
- Aerodynamic modeling of the wing models using the Doublet Lattice Method (DLM), with a spline method for the interconnection of the structural and aerodynamic grids provided by MSC/NASTRAN.
- Flutter analysis of the wing models (no ribs and stringers) for both (CAS) and (CUS) using symmetric and asymmetric laminate in each configuration with

orienting the fibre angle from –90 to 90 degree using the PK method provided in MSC/NASTRAN.

- Free vibration analysis of the remaining composite wing models (see table 8.6) for both (CAS) and (CUS) using symmetric laminate in each configuration with orienting the fibre angle from –90 to 90 degree using the finite element code MSC/NASTRAN.
- Aerodynamic modeling and interpolations of the remaining wing models were done using the same method applied wing 1 model.
- Flutter analysis of the remaining composite wing models for both (CAS) and (CUS) using symmetric laminate in each configuration with orienting the fibre angle from –90 to 90 degree using the PK method provided in MSC/NASTRAN.

1.3.2 Cranfield A1 Aerobatic metal wing structures:

The main aim in this section is to model the Cranfield A1 aerobatic metal wing box using two different modeling techniques for performing normal mode analysis and flutter analysis. The metal wing plane form and the root and tip airfoil sections are the same as in the composite wing as shown in figure (6.1) of chapter 6. The physical metal wing box modeling techniques are as follows:

- Simplified metal wing model
- Detailed metal wing model

Firstly, the analysis of the simplified wing model was done using two programs, namely MSC/NASTRAN and CALFUN programs. The wing model was modeled as beam with lumped masses in MSC/NASTRAN for the free vibration and flutter analysis, while as beam with distributed masses in CALFUN program for the free vibration analysis. Secondly, the detailed physical metal wing box model, which was created and analyzed using MSC/PATRAN 6.0 and MSC/NASTRAN 69 programs respectively. This methodical approach of starting the analysis with the simplified and then with detailed metal wing models before modeling the more complex composite wing box of the same aircraft will provide the following:

- Eliminate any inconsistency in model development and means of verifications.

- Provide experience in modeling of physical aircraft structures before dealing with the more complex aircraft wing constructed from carbon fibre reinforced plastic (CFRP) for the same aircraft.
- Provide a good way of comparison between the use of isotropic and composite material (see chapter 7) in the same physical wing box such as weight saving, even though there is a small difference in the length of the wing box.

1.3.3 Cranfield A1 Aerobatic composite wing structures:

The main aim of the present work in this section is to study the potential of composite materials to improve the dynamic aeroelastic stability (flutter) for aircraft composite wing box representing the real Cranfield A1 aerobatic aircraft as shown in chapter 7 and 9. This study will show the effects of aeroelastic tailoring (fibre angle changes as design variable from –90 to 90 degrees) for two configurations, namely, the Circumferentially Asymmetric Stiffness (CAS) and the Circumferentially Uniform Stiffness (CUS) using symmetric and asymmetric laminates in each of the above aircraft wings. This will also show the effects of material bending-torsional coupling stiffness, the ratio of the first bending frequency to the first torsional frequency (ω_b/ω_t) and the effect of wash-in and wash-out of the Cranfield A1 aerobatic composite wing structure in the subsonic region.

The other aim is to investigate the effect of the structural damping, modeled as complex stiffness matrix, on the flutter speed.

The following steps are carried out in order to achieve the objectives of this section of the present research:

- Normal mode analysis, flutter analysis and experimental vibration analysis is carried out on the original laminate and material properties (see table 7.1 and 7.2 of chapter 7) of the A1 composite wing box. The experimental work is basically done to study and illustrate the dynamic characteristics of the physical composite box, and to compare the results with the analytical free vibration results.
- Free vibration analysis of the physical Cranfield A1 aerobatic composite wing box modeled to simulate both (CAS) and (CUS) using symmetric and asymmetric

laminate in each configurations with orienting the fibre angle from –90 to 90 degrees using the simplified material properties presented in table (9.1) of chapter 9.

- The same aerodynamic modeling method, interpolation techniques, and flutter solutions were used for both configurations as presented previously in section 1.3.1.

1.4 Structure of the thesis:

In this chapter the main objectives of the study are defined and the important of the work is emphasised. The procedure and the layout of the research that is necessary to achieve the main aim behind the research is presented. The results and the research effort are organized as follows:

Literature review, which covers all the existing work in the area of dynamic aeroelasticity (flutter) for the cantilevered aircraft wings modeled as plate or box beams structures are presented in chapter 2. This is necessary in order to establish the development in this field and to identify the key areas of the research.

Chapter 3 deals with stiffness modeling of composite box beams. Firstly, the basic laminate constitutive equations are presented and a summary of relevant literature in the stiffness modeling of thin-walled structure is outlined. Then the most popular stiffness models are discussed. These cover both beams, and thin-walled box beams. Explicit expressions for the bending, torsional and bending-torsion rigidities are provided for all the models and with using three different methods for the thin-walled box beams presented.

Chapter 4 gives a brief summary about the solutions and the capability provided in the finite element package MSC/NASTRAN. These are listed as follows:

- Normal mode analysis (solution 103)
- Aerodynamic modeling methods
- Interpolation techniques
- Flutter solution techniques (solution 145)

Chapter 5 describes the setup and discusses results of the experimental vibration analysis of the physical Cranfield A1 aerobatic composite wing box. The test is carried out simulating a cantilevered boundary condition within the frequency range of (0-300 Hz). The test is done for five test locations in order to cover the entire wing box, which is done using sinosoidal for the first location and random excitations for all the test locations.

Chapter 6 presents the way the Cranfield A1 metal wing box was modeled using two techniques. The first model of the wing box is the simplified wing model, which was modeled as beam with a lumped mass using MSC/NASTRAN, and as beam with distributed mass in the case of CALFUN program, but having the same physical properties of the physical structure. The second wing model was the detailed model with the physical properties of the structure as if it is attached to the aircraft. In the second model, the rib caps were included in the modeling of the wing structure, while the third wing detailed model was the same as the second wing model, but without including the rib caps. The detailed wing models were created using MSC/PATRAN and analyzed using MSC/NASTRAN. The normal mode analysis was obtained using the Lanczos method for getting the natural frequency and mode shapes in the case of using MSC/NASTRAN, while using the dynamic stiffness matrix method in the case of CALFUN program. The flutter analysis was then done using the PK method provided by the finite element MSC/NASTRAN for different aerodynamic models and values of induced frequency parameter.

Chapter 7 presents the way the Cranfield A1 composite wing box was modeled using two different meshes (coarse and fine meshes) for the same composite wing box to examine the effect of increasing the mesh density on the natural frequencies. Both wing models were modeled with the original material properties provided by [7.2] and in table (7.1) and analyzed using the finite element code MSC/NASTRAN for the free vibration and flutter analysis in the subsonic region. The free vibration analysis was done using the Lanczos method for the frequency range from 0 to 300 Hz, while the flutter analysis was done using PK method for obtaining the flutter speed and flutter

frequency for different aerodynamic modeling, induced frequency parameter values and different number of vibration modes.

In chapter 8, the variation of the bending, torsional, bending-torsion coupling stiffness, stiffness ratio (EI/GJ), and (K/GJ) against the fibre angle for the wing1 and wing 6 models are presented using the procedure shown in chapter 3. Three published examples are considered and compared with results obtained using MSC/NASTRAN in this research, one for the free vibration analysis and the second and the third examples for the flutter analysis. A total of ten structural configurations given in table (8.6) were created and analyzed using MSC/NASTRAN for normal mode analysis. The variation of the frequency ratio (ω_b/ω_t) is then plotted against the fibre angle of the upper and lower skin for wing 1 and wing 6 models. The flutter analysis was then carried out for all the ten wing model configurations using the PK method. The effects of fibre orientations, stiffness ratios, frequency ratio, material and structural coupling, structural geometry and wash-in and wash-out on the flutter speed are then discussed and plotted.

Chapter 9 presents the free vibration and flutter analysis of the real composite wing box of the Cranfield A1 aerobatic aircraft for different fibre angles θ (-90 to 90 degree). The analysis was done for two structure configurations, the Circumferentially asymmetric Stiffness (CAS) and Circumferentially Uniform Stiffness (CUS). In each configuration, both symmetric and asymmetric laminates were used as shown in table (9.2-9.5) for a fibre angle from –90 to 90 degree. The composite material used in this section was simplified by using only Unidirectional Carbon/epoxy and two types of polymethylacrylate foams presented in table (9.1). The effect of fibre orientations, wash-in and wash-out and bending-torsion coupling is discussed. In addition, the effect of the structural damping on the flutter speed is investigated.

The final conclusions and some recommendations for future work are summarized in chapter 10. The input data file of the following wing models used for flutter analysis were presented in appendix A.:

- The simplified of the Cranfield metal wing box
- Wing 1 model simulating (CAS) configuration at fibre angle of 30^o.

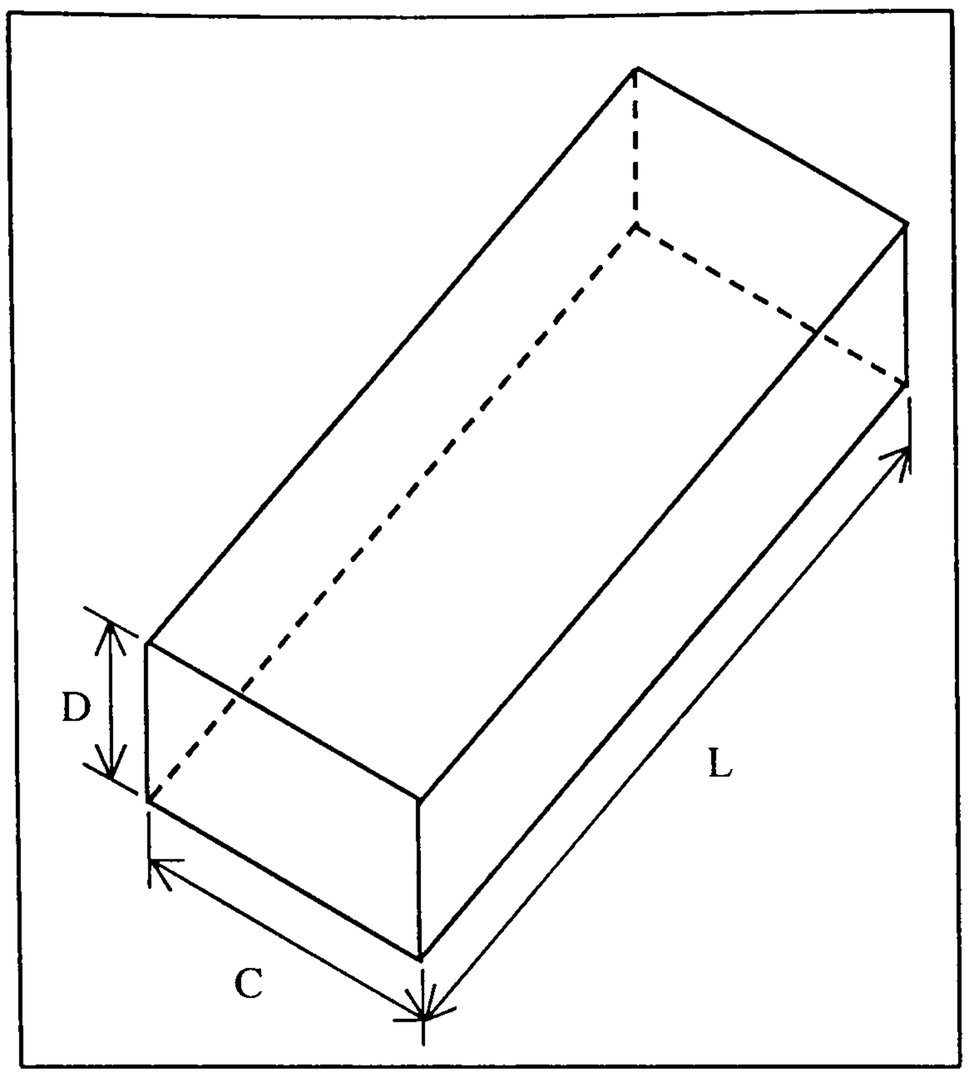

Fig. 1.1 Geometry of the first thin-walled structure.

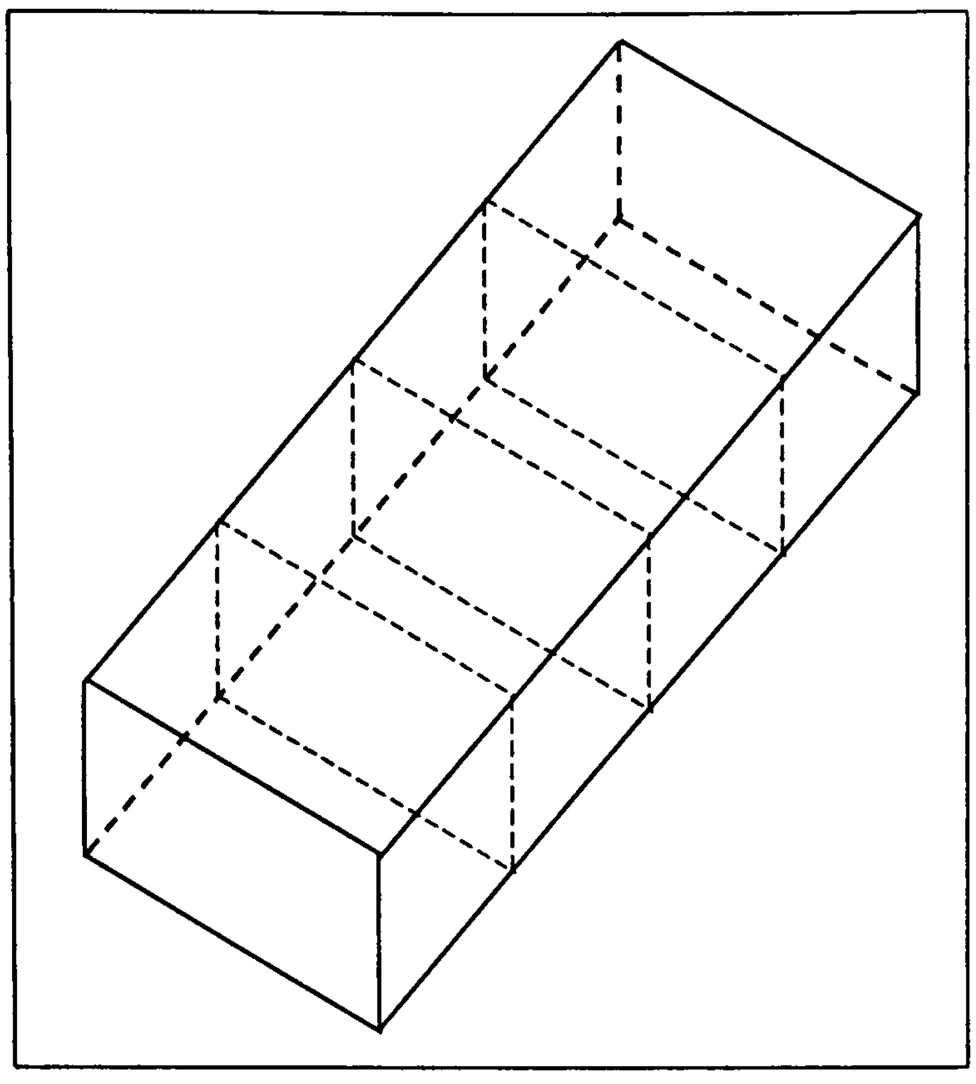

Fig. 1.2 Geometry of the second thin-walled structure.

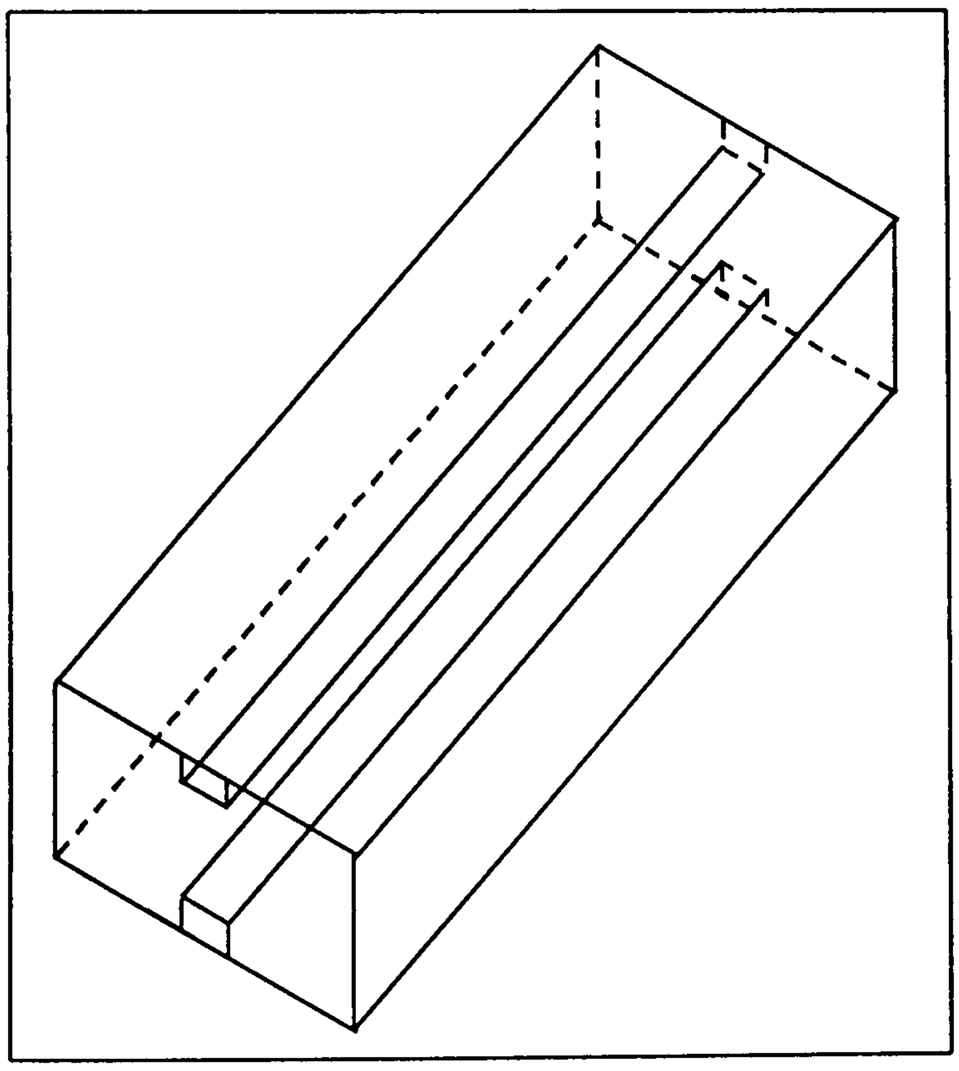

Fig. 1.3 Geometry of the third thin-walled structure.

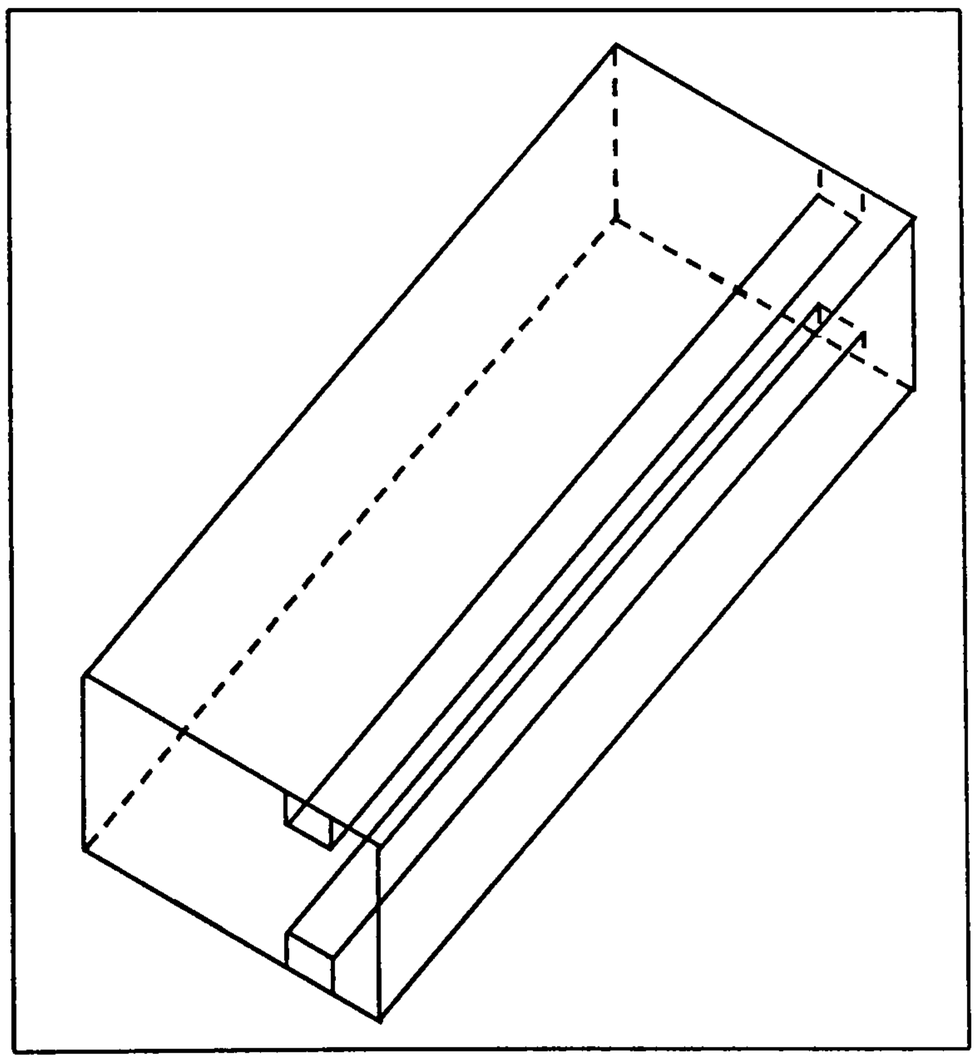

Fig. 1.4 Geometry of the fourth thin-walled structure.

References

1.1 Shanley, F. R. (1960). *Weight-Strength analysis of aircraft structures*. Dover Publications.

1.2 Shirk, M. H., Hertiz, T. J. and Weisshaar, T. A. (1986). "Aeroelastic tailoring-Theory, Practice and promise". Journal of Aircraft, vol. 23, no. 1, p 6-18.

1.3 Battoo, R. S. (1997). A beginners guide to literature in the field of aeroelasticity. Cranfield University, College of Aeronautics, Report no. 9712.

1.4 Garrick, I. E. and Reed III, W. H. (1981). "Historical development of aircraft flutter". Journal of Aircraft, vol. 18, no. 11, p 897-912.

1.5 Souahi, A. (1986). Structural optimization of aircraft lifting surfaces to satisfy flutter requirements. PhD thesis, Cranfield University.

1.6 Freberg, C. R. and Kemler, E. N. (1944). *Aircraft vibration and flutter*. John Wiley and Sons, Inc., New York.

CHAPTER 2

LITERATURE SURVEY

2. LITERATURE SURVEY

2.1 Introduction:

The design of aircraft often aims at lighter components, resulting in flexible structures prone to distortion due to loads. Aerodynamic loads are essentially due to the geometry of the lifting surface structures. If somehow these loads cause deformations in the structure and vary the geometry, they will give rise to totally different aerodynamic loads. These loads will produce further distortion in the shape of the lifting surface. This interaction between aerodynamic, elastic and inertia forces is classified as the subject of AEROELASTICITY. Various aeroelastic phenomena can be classified by means of Collar's triangle of forces [2.53]. Three types of forces, namely (i) aerodynamic forces, (ii) elastic forces, and (iii) inertial forces are placed at the vertices of the triangle. Then every aeroelastic phenomenon can be located according to its relation to the three vertices. Static aeroelastic phenomena due to interaction of aerodynamic and elastic forces (such as lifting surface divergence or control surface efficiency), whereas dynamic aeroelastic phenomena (such as flutter, dynamic response and buffeting), since they involve all the three kind of forces. The interaction of elastic and inertial forces gives a rise to mechanical vibrations, being important for the analytical treatment of dynamic aeroelastic problems, where as the interaction between the aerodynamics and the inertial forces will introduce rigid body dynamics.

The use of composite materials has been increased in many applications in the real life such as aircraft and space structures and automotive structures, which provides a higher performance. This is mainly due to high strength to weight and high stiffness to weight ratios, which is offered by composite materials. The increasing need of lightweight aircraft structures has inspired a quest for a better understanding of the vibration properties of composite materials, which is very important in the analysis of dynamic aeroelastic problem such as flutter phenomena which is considered in this research.

There are many studies have been done on the vibration and then on the flutter analysis of the cantilevered composite aircraft wings, which are close enough to the

fuselage-wing attachment on the actual aircraft. The summary of these studies on the vibration and flutter of composite wings are presented in the next section.

2.2 Vibration and Flutter analysis of composite aircraft wings:

Jensen, D. W. et al. [2.1] calculated the natural frequencies and mode shapes of the cantilevered Graphite/Epoxy plates including the bending-torsion coupling in the analysis. This analytical analysis was done using two methods, the first method was the Ralyleigh-Ritz and the second was the finite element method. The plate was modelled using the unbalanced laminated in the form of $[\theta_2/0]_s$. The analysis was done for different fibre angles θ. The analytical results were compared with the experimental work, which was carried out as well and the variation of the natural frequency against the fibre angle θ was presented. It was concluded that the chordwise bending played an important factor in Rayleigh-Ritz vibration analysis.

An analytical and experimental investigation was conducted by Hollowell and Dugundji [2.2] to determine the aeroelastic flutter and divergence behaviour of unswept, rectangular cantilevered plate made from Graphite/Epoxy with various bending-torsion coupling stiffness. The laminate lay ups of the plate was in the form of unbalanced laminate $[\theta_2/0]_s$ and for $[\pm 45/0]_s$. The analytical and experimental analysis was done for six plate models with the fibre angle of θ = 0, 30, -30, 45, -45 degrees. Two types of flutter were analysed, the first type was a potential flow (low angle of attack) and the second type was a stall flutter.

The analytical approach was incorporated a Rayleigh-Ritz energy formulation and unsteady, incompressible two-dimensional aerodynamic theory. The flutter and divergence velocities were estimated using V-g method.

The obtained results were compared and tabulated with the experimental results. The flutter and divergence velocities were plotted against the root angle of attack for different laminate configurations. It was concluded that the bending torsion coupling can be used in eliminating aeroelastic instability such as divergence.

Lakshminarayana et al. [2.3] presents theoretical analysis with experimental verifications of the free vibration characteristics of a swept composite wing panel. The wing panel was made from graphite/epoxy and E-glass/epoxy composite materials. The finite element technique was used in the analysis modelling of the wing panel. A shear flexible triangular laminated composite plate finite element (TRIPL T) was employed in the modelling of the wing composite panel. The laminate lay ups of the cantilevered wing panel was in the form of $[\theta_2/0]_s$. The effect of the fibre angle θ and the material composite system on the natural frequency was investigated. A comparison was made between the obtained results using TRIPL T elements and the experimental analysis. It was found ply orientation and composite material systems have a significant effect on the natural frequencies of swept laminated composite wing panel.

Chunan-Qi et al. [2.4] deals with the flutter analysis of composite aeronautical structures. A computer programme was written and based on the finite element method and using Lanczos method to calculate the eigenvalues and eigenvectors of the free vibrating of the aeronautical composite structure. The generalised aerodynamics coefficients were based on the improved supersonic kernel functions method. An automatic technique (Lagrange Interpolation process) was used instead of V-g method to estimate the critical flutter point. A test example was carried out on a vertical empennage at Mach number of 0.85, the obtained results were then compared with those results calculated using the commonly used subsonic doublet-lattice method. It was found that for a complex structure the flutter mode is not always the second mode.

Lee, L. and Lee, J. [2.5] analysed and examined the vibration characteristics including the natural frequency and mode shapes for various shapes of composite swept back wing panel using finite element technique based on the shear deformable theory was adopted. The wing panel was idealised as a thin plate, which was composed of multilayered composite laminates. The laminate configuration was in the form of $[\theta_2/0]_s$. Eight node quadrilateral isoparametric elements were chosen and used in the modelling of the wing panel. The degrees of freedom at each node were one translation and two rotations about two perpendicular inplane axes. The effects of the on fiber orientation θ,

taper ratio and sweep back angle on the natural frequency were investigated and plotted. A comparison of natural frequencies obtained from this analysis and the natural frequencies obtained from [2.3] was presented for E glass/epoxy material. It was found that, the natural frequencies and mode shapes of a composite wing are greatly influenced by the aspect ratio and the fiber orientation.

Chuanqui, H. et al. [2.6] presents the aeroelastic tailoring of composite wing surfaces. In this analysis, combined design variables were applied to the problem of wing structure. A bi-cubic polynomial was used to describe each ply thickness of the wing skin and its coefficient was taken as design variable. For the other components such as ribs and webs, the cross-section area or thickness was used as design variable. The analysis was carried out using finite element approach. The structural mode shapes and unsteadies generalised aerodynamics were calculated using the spectral transformation Lanczos method of very high efficiency and subsonic double lattice method respectively. The critical flutter speed was calculated using V-g method. The wing optimal problem was then analysed using feasible direction method.

Thangjitham, S et al. [2.7] analytically investigated the vibration behaviour of anisotropic laminated composite wing structure taking the warping effects into consideration. The wing structure was idealised as cantilever of eight layer laminated composite plate made of graphite/epoxy whose constituent orthotropic layers were characterised by different orientation angles, thickness and material properties. The exact solutions for the dynamic response problems corresponding to both free warping and warping restraint wing models were obtained using Laplace transform technique. The effects of warping restraint on the first three natural frequencies and dynamic response functions were plotted as a function of the wing aspect ratio. It was found that with the proper selection of fiber orientation in each layer; the warping restraint could be used to improve the dynamic performance of the wing composite structure.

Haisong, A. et al. [2.8] developed finite element programme called "CSAOP" and used in performing the analysis of composite structure, which had the ability to

calculate the effect of temperature and humidity. The vibration analysis; static and dynamic aeroelastic analysis, and optimal designs were carried out in the analysis. The effect of the temperature and humidity on the composite wings static and dynamics aeroelastic performances were considered. The wing structure and control surface structure was modelled as a single structure for structural and aeroelastic analysis. The hinge joint of the control surface was done using two point analogies in the finite element modelling. In the vibration analysis, Lanczos method was used to calculate the natural frequencies and mode shapes of the structure, and for static aeroelastic analysis both subsonic vortex lattice method and supersonic vortex lattice method were used. For flutter analysis, both subsonic doublet lattice method and supersonic kernel function method was used. Two optimisation methods were used in the programme, the first was feasible direct method, and the second was the sequence quadratic programming method. Two practical aircraft composite structures were analysed.

Both flutter and divergence speeds were plotted for different temperature and altitudes. It was found that the humidity effect of aeroelastic performance was very small, but the temperature effect on the composite wing structure at high speed should be considered.

Lee in et al. [2.9] presents the vibration characteristics, including the natural frequency and mode shapes for various composite wings configurations with a tip mass and engine using finite element method based on the shear deformation theory. The analysis presented the effect of the tip mass, engine, sweep angle, fiber orientation and aspect ratio of a composite wing made from a graphite/epoxy with symmetric stacking sequence on the vibration characteristics. The wing of an aircraft was made from a graphite/epoxy and was idealised as a thin plate, which consisted of six layered laminate with $[\theta_2/0]_s$ stacking sequence. The tip mass and engine were located at 1/4 chord at mid-span station. Eight node quadrilateral elements were used for modelling the plate element.

A comparison of natural frequencies of swept wing panel (without mass and engine) was done between the obtained results and the results provided in Ref. [2.3]. The effects of the above parameters were plotted for a wing with and without tip mass

and engine. It was concluded firstly that the natural frequencies of the wing with tip mass and engine are lower than the clean wing and secondly, the location of the added mass was a very important to the variation of the natural frequency and mode shapes.

Librescu, L. et al. [2.10] presented the analytical studies of the vibrational and static aeroelastic response of anisotropic composite aircraft wing modelled as single cell thin-thick walled beams of arbitrary closed cross-section. In this analysis, various ply angles were considered to achieve the best structural coupling mechanism for this analysis. The vibrational and static aeroelastic behaviour of composite swept wing was then analysed using two methods, the first method was based on Laplace Transform technique and the second was based on the extended Galerkin method. Both techniques were applied to the structure, which was modelled as cantilevered thin walled beam of biconvex cross-section for supersonic aircraft constructed from graphite/epoxy composite materials. The ply configuration in this case study was the Circumferentially Asymmetric Stiffness configuration (CAS). The variation of bending-torsion stiffness, natural frequencies and eigenvectors were plotted against the fibre angle θ. The divergence speed was plotted against various ply angles for different sweep angle and wall thickness.

Karpouzian, G et al. [2.11] presented an analytical analysis of a plate-beam structural model for aeroelastic analysis of aircraft wings made of anisotropic composite materials. Hamilton varitional principle was applied to the structure to derive the governing equations of the static and dynamic aeroelastic of the cantilevered swept wing structure tacking the effects of transfer shear, rotary inertia and warping into account. A study example was done for a uniform rectangular swept wing modelled with straight elastic axes coinciding with the reference axes directed along the span of the mid-chord line. The wing was constructed from single transversely isotropic material. The combined and separate effects of warping restraints, free warping and transverse shear deformation on the static aeroelastic response along the span were examined based on the shear deformable theory. These effects were plotted for different wing sweep angle.

Meirovitch, L. et al. [2.12] was concerned with the aeroelastic tailoring of a structural model consisting of a rigid fuselage and a low aspect ratio wing made of composite materials. The effect of shear deformation was taken into account. The structural model should represent the essential physical characteristics required for flutter analysis of modern low aspect ratio composite wings and should be sufficiently accurate to account for all important structural parameters and sufficiently simple. The structural wing model was selected as trapezoidal plate with root and tip chords parallel to the flow with general sweep. The fuselage was capable of plunge and pitch and the wing model includes shear deformations but ignores the rotatory inertia. There were $2k^{th}$ layered symmetrical laminate with variable thickness, generally orthotropic layered in the laminate of the wing model. The wing was assumed to act as elastic plate clamped at the root and free at the end. The dynamic was done using the extended Hamilton's principle and the aerodynamic forces' calculations were based on a variant of the piston theory. Two flutter mechanisms were of primary concern for a symmetric model of a wing with forward or aft sweep. The first was bending-torsion flutter and the second was the behaviour of body freedom flutter was considered. The distribution of tailoring plies over the wing planform was considered.

Kuilin, C. et al. [2.13] presented the concept of the Vibration and Flutter Integration Analysis System (VFIAS), which was an analytical system integrating the vibration calculation, vibration test and the flutter evaluation. The measured data were used to improve the dynamic analysis results of the finite element method, and the corrected results were often based on both calculations of the finite element method and measured natural frequencies and mode shapes. There were two methods used in performing the ground vibration test (GVT), the first method was the multi-input and multi-output (MIMO) technique, while the second method was the sine dwell model tests. The dynamic analysis was based on two basic theoretical relationships, which apply to linear, undamped structure represented by finite element method (FEM), these relationship were the orthogonality of the normal mode shape and the eigenvalue. The flutter analysis was done using K-method. The corrected flutter was obtained from the evaluation based on the corrected frequencies and mode shapes. Two examples were

done; the first was a dynamic analysis of the aircraft wing, horizontal stabiliser and fuselage, which were modelled by elastic beam elements. The results were compared with the test work for the first eight modes and it was found that the maximum error of the initial analysis frequencies was 18.11%, after the second modification (mass matrix), the maximum error of the corrected analytical frequencies was 3.73%. The second example was a wing with the aileron, the analysis was carried out for the flutter. Four wing mode shapes and one torsional mode shape were used in the flutter analysis.

Kuo-Juin, L. et al. [2.14] developed a more general approach for the flutter/divergence analysis of a plate composite structure in subsonic flow. The high-precision 18 D.O.F. triangular plate bending finite element was used to generate the mass and stiffness matrices of the composite plate. The equation of motion for the flutter analysis was obtained through the use of Hamilton's principle. The unsteady aerodynamic forces were calculated using the doublet-lattice method (DLM). The interpolation between the structural nodal and the aerodynamics control points was done using a surface spline function and the flutter was calculated using V-g method. The cantilevered plate laminate configuration of the form of $[\theta_2/0]_s$ was investigated. The effects of composite filament angle (0-180 degrees), orthotropic modules ratio, sweep angle and the aspect ratio (1.5 and 4) on the vibration and flutter/divergence were examined.

Georghiades, G. et al. [2.15] presented an analytical investigation on the aeroelastic behaviour of a composite wing, which was represented as laminated beam (plate) using an exact dynamic stiffness matrix method. The analysis was done without taking the effect of the shear deformation, rotary inertia and warping stiffness into account. The effects of ply orientation and sweep angle were investigated on the flutter speed of a Graphite/Epoxy cantilevered wing. The flutter analysis was done using CALFUN computer programme, which uses the normal mode method and generalised co-ordinates for high aspect ratio aircraft wing. In the structural idealisation of the wing, beam and lumped mass elements are used in CALFUN programme. The natural frequencies, mode shapes and the generalised aerodynamic matrix were calculated using

Wittrick-Williams algorithm and strip theory and the principle of virtual work respectively. The flutter analysis of the wing plate was carried out for the three laminate configurations. The variation of the non-dimensional flutter speed ratio was plotted against the fiber orientation for the three cases with the sweep back angle vary from 0° to 40°.

Robert, V et al. [2.16] presented analytical study with the experimental work of the low speed flutter characteristics for low aspect ratio delta wing. The natural frequencies, mode shapes and generalised masses were calculated using the EISI-EAL engineering analysis computer code. The wing was modelled using the combination of the triangular and quadrilateral plate elements. The effects of sweep angle, root clamping and tip-clipping was considered on the flutter characteristics of simple plate models. The models were constructed from aluminium alloy plate. The generalised aerodynamic forces were obtained by using Kernel function and Doublet-Lattice subsonic unsteady lifting surface theories were compared with the experimental results. The flutter solution was done by P-K method and the results were plotted in a root-locus format. The structural damping ratio of 0.01 was used for all modes. The experimental flutter results were carried out at low speed (Mach no. 0.1-0.35). The variation of flutter frequencies and velocity with percent span reduction, sweep angle and clamping root were plotted for the experimental result, calculated double-lattice method and Kernel function.

Koo, K. et al. [2.17] showed the effects of the structural damping on the flutter boundary for three types of wings: rectangular, swept forward (30°) and swept back (30°). The wing plates structure was modelled using the finite element method based on the shear deformable laminated plate theory and the structural damping was included in the form of a complex modulus. The plate laminate configuration was in the form of $[\theta_2/0]_s$. The unsteady aerodynamics loading on oscillating wings were calculated by the Doublet- Point method. The interpolation between the structural and aerodynamic grids was done using the surface spline function. The effect of the fiber orientation on the natural frequencies and modal loss factor was studied and plotted for the rectangular and

swept back wings. Also the effects of the fiber orientation on the flutter/divergence were investigated and plotted for the three types of wings.

Banerjee, J. et al. [2.18] presented an exact analytical method, called the dynamic stiffness matrix method, to determine the free vibration characteristics of the composite beams or of simple structures assembled from them for which the bending and torsional material coupling which were commonly in aircraft wing. In this analysis, the effects of shear deformation, rotary inertia and warping were neglected. The derived dynamic stiffness matrix was then used in conjunction with Wittrick-Williams algorithm to calculate the natural frequencies and mode shapes of bending-torsion coupling composite beams. The composite beam was considered as solid rectangular cross-section and with a symmetric but unbalanced lay up. The equations of motion of the beam in free vibration were derived using the coupled bending-torsional beam theory for thin walled composites. The natural frequencies were obtained for two case studies using the dynamic stiffness matrix method.

A finite element model based on a higher order shear deformation theory was developed by Chandrashekhara et al. [2.19] to study the free vibration characteristics of laminated composite beams. A generally layered one-dimensional laminated beam equation that accounts for transverse shear deformation and Poisson effect, in-plane inertia and rotary inertia were derived. The natural frequencies and mode shapes for symmetric and un-symmetric laminated beams under various boundary conditions were presented. A comparison of non-dimensional natural frequencies of simply supported orthotropic [0°] graphite/epoxy beam and for symmetrically laminated [0/90/90/0] and [45/-45/-45/45] beams under various boundary conditions was made between the present analysis and the exact solution based on the first order shear deformation theory. A variety of parametric studies were conducted to demonstrate the influence of the beam geometry, Poisson effect, ply orientation, number of layers and boundary conditions on the frequencies and mode shapes.

Kapania, R. et al. [2.20] developed a one dimensional finite element for the study of the aeroelastic behaviour of wings of arbitrary lamination, cross-section planform and sweep distribution ranging from beam plates to built-up structure combining curved laminated cover skins, axial stringers and shear webs. The formulation takes into account the effect of transverse shear and the bending-stretching coupling inherent to un-symmetric composite structures and allows for un-symmetric cross-section. The wing was modelled as beam of arbitrary cross-section distribution using a displacement-based finite element formulation. A one-dimensional beam element with 24 D.O.F was used. A modified aerodynamic strip theory a long with the V-g method was used to solve the flutter equations. Two examples were studied, the first was done for static analysis and the second was done for the dynamic analysis of unidirectional graphite/epoxy cantilevered beam, rectangular symmetrically laminated plate, unsymmetrically laminated square plate and a box beam structure. The effects of the sweep angle and the ply angle on the flutter/divergence speed were done. An introductory study of the bending-stretching coupling introduced by unsymmetry and damage was conducted.

Teboub, Y. et al. [2.21] performed an analytical approach for determining the natural frequencies and mode shapes of generally layered composite beams (plates) using a first order shear deformation theory which includes the effects of in-plane and rotary inertia's. The Poisson effect, width effect, boundary conditions, lay-ups, effect of anisotropic on cross-ply and angle-ply laminates, and the effect of coupling were investigated and plotted. The equations of motion were integrated to arbitrary degree of accuracy by using symbolic computation (with the help of Maple programme).

An analytical investigation was conducted by Lottati, I [2.22] to determine the aeroelastic flutter and divergence behaviour of a cantilevered, composite, forward rectangular wing plate. The influence due to the variations in the bending-torsion stiffness coupling of the tailored wing on the flutter and divergence critical dynamic pressure was performed. The analytical approach uses the incompressible two-dimensional unsteady aerodynamic strip theory. Flutter and divergence velocities were

obtained by using an optimisation procedure that solves the coupled bending-torsion equation for cantilevered swept wing.

Lee, U [2.23] developed analytical new continuum method, which was capable of modelling a cantilevered aircraft wing structure with general airfoil and planform geometry's as an equivalent continuum beam-rod model. The method was based on the concept of energy equivalence. The continuum beam-rod model was derived by determining equivalent structural properties so that the continuum beam-rod model takes the same behaviour of the actual aircraft wing. The cantilevered aircraft wing structure consists of curved top and lower laminated skins, webs and stringers. In this paper, for simplicity reason, the analysis was done for a wing structure with a uniform stiffness a long the span. The finite element stiffness and mass matrices from the finite-element formulation were used in calculating the reduced matrices for the aircraft wing. The free vibration equations of an equivalent continuum beam-rod model for the cantilevered aircraft wing were analysed through the use of Hamilton's Principle. A trail and error process was used to calculate the flutter speed and the frequencies. The continuum method was applied to a rectangular symmetric lay-up box-beam as an aircraft wing model.

Armanios, E. et al. [2.24] presented the free vibration analysis of the anistropic thin closed-section beams. The equations of motion for the free vibration were derived using a variational asymptotic approach and Hamilton's Principle. The static stiffness matrix was derived and expressed in terms of the cross section geometry and material properties. The analysis was applied to two laminated composite structures, namely, the Circumferentially Uniform Stiffness (CUS) and the Circumferentially Asymmetric Stiffness (CAS). The effect of the elastic coupling mechanism on the vibration behaviour of thin-walled composite beams was evaluated analytically. The effect of the stacking orientation on the frequencies associated with coupling vibration modes was investigated.

Banerjee, J. [2.25] presented the flutter characteristics of high aspect ratio tailless aircraft. Two classes of tailless sailplane were investigated, the first was called Ricochet airplane and the second was called Kestrel airplane. The first and the second were constructed from aluminium alloy with aspect ratio of 22.93 and carbon fiber spar reinforcement with aspect ratio of 31.35 respectively. The finite element method was used to obtain the mass, stiffness matrices and the normal modes, whereas a strip theory based on Theodorson expressions for unsteady airfoil motion was employed to form the aerodynamic matrix. The flutter matrix was performed by algebraically summing the generalised mass, stiffness, and aerodynamic matrices. The analysis of both aircraft was done using PAFEC analysis programme.

Karpouzian, G. et al. [2.26] analytically analysed the effects of warping inhibition, transverse shear and anisotropic on the flutter of the straight and swept cantilevered wing structures. The concept of the shear deformation plate-beam was adapted. The wing structure was idealised as a laminated composite plate with different orthotropic angles, materials and thickness properties. The equations were derived using Hamilton's variational principle while the analytical framework in which the flutter was studied was based upon the Laplace Transform Technique.

Karpouzian, G. et al. [2.27] presented an analytical analysis of three-dimensional flutter solution of aircraft wings composed of advanced composite material. The concept of the shear deformable plate beam model was adopted. The wing structure was idealised as a laminated composite plate with different orthotropicity angles and different material and thickness properties. For flutter analysis, the harmonic time dependence for both the unsteady aerodynamic loads and the displacement quantities were postulated. An example was done for untapered wing structure whose inertia and structural properties were spanwise uniform. The wing was considered as single transversely isotropic material. The variation of the flutter speed parameter of unswept and swept wings against the transverse shear flexibility was shown.

Teh, K. et al. [2.28] presented two finite element models for the prediction of the free vibration natural frequencies of fixed-free beams (plates) of general orthotropy. The

effect of the transverse shear deformation and rotary inertia was taken into account. The models were made of graphite/epoxy composite materials. The principle differences between the two discrete models were the prescribed generalised co-ordinates and the assumed displacement functions. The generalises co-ordinates of the first model were prescribed such that the discrete model permits only the applications of geometric boundary conditions to the beam, whereas the second model with more complicated generalised co-ordinates permits the application of all the beam boundary conditions, both natural and geometric. The effect of the fibre orientation on the natural frequencies for both models was presented.

Wu, X. et al. [2.29] developed a thin-walled finite element for laminated composite beam based on the modified assumption of classical isotropic thin-walled theory. A two-noded, 10 degrees of freedom per node, thin-walled element presented was suitable for either open-section or close-section beams of any shape, sticking sequence and boundary conditions. Natural frequencies of several thin-walled composite structures (plates and open section) were calculated and compared with full-scale shell finite element results.

Lottati, I. [2.30] investigated the significant influence the unsteadiness of the wake has on the flutter speed of the system and also studied the influence of the structural damping on the flutter speed as related to the aerodynamic damping modelled by aerodynamic airforces incorporated in the analysis. The analysis was done for a high aspect ratio; rectangular wing idealised as a box beam. The light aerodynamic damping was introduced by the noncirculatory terms of the airforces in the analysis. The variations of the frequencies and damping of the first aeroelastic modes against the airflow velocity with applying steady, quasisteady and noncirculatory aerodynamics were shown. The influence of structural damping on the stability behaviour of the wing in the presence of unsteady and the light aerodynamic damping was shown.

Cesnik, C et al. [2.31] performed an aeroelastic analysis for high aspect ratio composite wings. The structural model was based on an asymptotically correct cross-

sectional formulation and a non-linear geometric exact beam analysis. Both were derived from 3D elasticity. This paper discusses, the important of using the right stiffness formulation in order to model the material couplings, the variation of divergence and flutter speeds with the change in the limination angle of a box beam model of a wing cross-section, and some effects of a non-linear structural model in the aeroelastic stability of a slender wing. A simplified code was written that implements a linearized beam model (solution based on Rayleigh-Ritz method) and 2D Theodorsen's unsteady aerodynamic formulation (Strip theory). As a first configuration test, a thin-walled single cell composite beam made of graphite/epoxy and the ply angle varied from -90 to 90 degrees. Two structural configurations were used, the first one was a Circumferentially Uniform Stiffness (CUS) including different values of the sweep angle, and the second type was the Circumferentially Asymmetric Stiffness (CAS). The variation of the divergence dynamic pressure for (CUS), and the flutter and divergence velocities for (CAS) against the fibre angle. A among other things, the divergence dynamic pressure with non-linear steady state for the composite box beam (CAS θ=-45).

Chattopadhyay, A. et al. [2.32] developed a higher order based theory for structural and aeroelastic analysis of composite wing box sections with moderately thick walls. In this model, each wall was analysed using a refined displacement field to account for the variation in transverse shear strain through the wall thickness. Appropriate boundary conditions were imposed at the corners of the beam cross-sections. Both in plane and out of plane warping deformation were included in the analysis. The structural model was validated through correlation with other existing theories and available experimental data. Aeroelastic analysis was performed for a simple composite box beam with 20 in length, 2 in width and 0.5 in depth. Three-ply orientations [0,45, -45] were used for the top and bottom walls, while the side walls were made from at [0] fibre angle. The Doublet lattice method was used to compute the aerodynamic influence coefficient. A fictitious structural damping factor g was introduced and a simple harmonic motion was assumed. The flutter boundary was predicted in the frequency domain using V-g method. The variations of the damping and

frequency histories against the velocity were shown for the three fibre orientations at Mach. number of 0.7.

A detailed parametric investigation in to the flutter characteristic of upswept cantilevered composite wing modelled as a plate was carried out by Georghiades, G. et al. [2.33]. The free vibration characteristics were studied using the dynamic matrix method while. The flutter speed was calculated using CALFUN programme and the optimization was done using an optimization programme ADS. The effect of varying the structural parameters including the cross-coupling parameter φ, the ratio of (uncoupled) fundamental bending and torsional natural frequencies (ω_h/ω_α), density ratio, non dimensional radius of gyration and the static unbalance x_α expressed as a fraction of the semi-chord. The elastic axis was assumed at 20% of the semi-chord. The flutter speed was calculated using CALFUN programme and the optimization was done using an optimization programme ADS. The non-dimensional flutter speed ($V_f/b\omega_\alpha$) was plotted against the above parameters. Two case studies were carried out on a composite plate; both composite plates were constructed from Hercules ASI/3501-6 graphite/epoxy. The dimensionless flutter speed was plotted against the frequency ratio for various values of static unbalance, cross-coupling parameter and density ratio.

Stanley, C. et al. [2.34] presents theoretical flutter analysis with flutter test using a scaled model of an advanced composite wing in the NASA Langley Research Centre. The finite element model was created and analysed with the ATALS computer program. The analytical model included a detailed representation of the spars, skins and rib structure of the wing box as well as the leading and trailing edge structures. The test model was a wall-mounted half-span wing with a semi-span of 6.63 ft. The wing aspect ratio was 5.31, taper ratio of 0.312 and quarter-chord sweep of 25 degrees. The model was supported in a manner that simulated the load path in the carry-through structure of the aircraft and symmetric boundary condition at the fuselage centreline. The model was capable of carrying external stores from three pylon locations on the wing. Flutter tests were conducted for the wing with and without external stores. No flutter was encountered for the clean wing at test conditions, which simulated the scaled airplane

operating envelope. Flutter boundaries were obtained for several external store configurations.

Schoor, M. et al. [2.35] describes the aeroelastic modelling and analysis of MIT's Michelob Light Eagle (MLE) human powered airplane. The unique structural characteristics of the aircraft namely, very flexible wings, high aspect ratio and low wing loading, are typical of proposed high altitude long endurance aircraft. Beam finite elements were used where the beam properties were obtained from the original structure design. The wing was modelled with 8 finite elements, and the finite element programme ADINA was used to determine the natural frequency and mode shapes of the MLE with apparent mass. The unsteady aerodynamics was calculated using a two-dimensional strip model of the MLE. The effect of one aerodynamic surface on another was also ignored. The MLE was divided into four structural surfaces namely, wing, elevator, rudder and cockpit, and for each surface a separate two-dimensional spline was fitted to the mode shapes obtained from the structural dynamic model. The results of the aeroelastic stability analysis were presented.

Weisshaar, T. et al. [2.36] discuss and illustrate several dynamic effects that may be obtained by intentionally coupling together the structural bending and torsional flexibility's of slender, beam-like structure. Other parameters considered in this paper including: modelling of cross-sectional stiffness properties of a beam-like structure and the effect of internal chordwise structural construction or restrains, such as may be provided by ribs, upon stiffness cross-coupling; the effects of stiffness cross-coupling on beam free-vibration mode shape and frequencies and their impact upon aeroelastic characteristics of lifting surfaces; and, the identification of parameter set that is useful for preliminary aeroelastic design.

Schweiger, J. et al. [2.37] describe the aeroelastic analysis for the design, the ground verification tests, and the flight test programme for the RANGER 2000 training aircraft. The structural dynamic analysis was based on a NASTRAN finite element model. Dynamic analysis a subspace method was chosen. The flutter analysis method

developed allows interpolating between reduced frequencies and mach numbers. Doublet Lattice Method was used to generate the required aerodynamic influence coefficient matrices for all mach numbers and reduced frequencies. The same aerodynamic model and method was used for static aeroelastic investigations. Several ground vibration tests were performed for the complete aircraft or for individual components. A flutter flight test was done on the aircraft. Both flutter sensitivities and aerodynamic sensitivities with respect to flutter were done.

Green, J. [2.38] studied the aeroelastic performance of aft-swept high aspect ratio wing using integrating matrix method. Aeroelastic stability boundaries were shown as function of fiber and dimensionless modulus parameters for straight wings of aspect ratio of 14. The bending-torsion coupling that was beneficial for forward-swept wings was shown to be of no advantage for aft-swept wings, for which torsional stiffness was much more significant. Both symmetric and nonsymmetric ply orientations were studied.

Weisshaar, T. [2.39] developed algebraic expressions to predict the static aeroelastic divergence characteristics of unswept and forward swept tapered and untapered wings constructed from composite materials using the laminate beam box model to describe the wing structure. The aerodynamic strip theory was used to calculate the air loads. Two illustrative examples were considered, and the variation of the material coupling, sweep angle and the normalizing divergence speed against the fibre angle for the two illustrative examples.

Weisshaar, T. [2.40] discusses the static aeroelastic problems such as spanwise lift redistribution's, lift effectiveness, and aileron effectiveness. Two theoretical models are commonly used, the first one was the laminate plate theory with elementary strip theory airloads, and the second was a more general representation of the laminated wing structural, in a matrix form, with a discrete-element aerodynamics (Weissinger L method). In the second case, the box beam is characterised by bending stiffness, torsional stiffness and the bending-torsional coupling stiffness. The structural model of

the wing assumes the loads to be carried by the box-beam arrangement in which laminated composite plates form the upper and the lower sheets of the wing box. The laminates themselves should be symmetrical in their lay-up. These are derived from the classical plate theory applied to the top and bottom flanges. The example wing has a layup of some plies of 0°, some of 45°, some of –45°, and some with a variable angle θ. It also discusses the concept of "aeroisocline" as the flexible deforms in such a way that the span center of pressure does not move, nor is the wing lift-curve slope changed from its rigid wing value.

Blair, M. et al. [2.41] illustrate by experimental rather than analysis, the potential effects of laminate design on wing divergence speed. In this work eleven composite wing models (plates) are tested for aeroelastic divergence at a number of fore and aft sweep angles. These fixed-root models incorporate sectioned aerodynamic shells mounted to interchange internal graphite/epoxy plates. These plates provide wing structural stiffness and simulate various off-axis composite structural configurations. Test results obtained from subcritical testing using a modified Southwell method, which was used to study the relationships between wing sweep, composite fibre orientation, and wing divergence speed.

Weisshaar, T. et al. [2.42] extend the study of ref. [2.36] with tailoring the fibre angle for the flutter analysis of moderate to high aspect ratio wings. The flutter and divergence analysis of the composite wing modelled as plate was carried out. The wing was modelled with having, both structural and bend-twist coupling. In the case of structural coupling, two cases are considered the first case the center of mass was located behind the flexural axis, while the second case the center of mass was located a head of the flexural axis. The aerodynamic loads and the solution of the flutter equations were calculated using a modified strip theory together with the two-dimensional, unsteady incompressible aerodynamics and the K-method respectively. The analysis was carried out for unswept wing, 30° sweptback wing and 30° sweptforward wing. In each case the effect of fibre angle was investigated on the flutter and divergence speed.

Also, the effect of the laminate tailoring upon rigid body/elastic model coupling was studied for both clamped root and free-free conditions.

Landsberger, B. et al. [2.43] performed an analytical and experimental investigation of the aeroelastic deflections, divergence, and flutter behaviour of both unswept and 30° forward-swept rectangular, graphite/epoxy, cantilevered plate-type wing with various a mount of bending-torsion stiffness coupling. The analytical investigation used a Rayleigh-Ritz formulation together with incompressible three-dimensional Weissinger L-method aerodynamics for the divergence, and incompressible two-dimensional unsteady strip theory for the flutter analysis. A semi-empirical attempt was also made to obtain the steady airload deflections of the wing including the nonlinear stall behaviour. Experiments on 13 flat plate wing with different ply configurations at 0 and 30 forward sweep were conducted.

Striz, A. et al. [2.44] investigate the flutter behaviour of various fully built up finite element wing models in subsonic and supersonic flow using the automated structural optimization system (ASTROS). First, the performance of the flutter module was tested against other codes. Models of various wings made from isotropic materials with different aspect ratios were investigated for the influence on the free vibration and flutter characteristics of such modelling factors as finite element selection, structural grid refinement, number of selected modes, retention of in-plane and breathing modes, aerodynamic panel size and placement, splining, solution procedures, reduction schemes.

Banerjee, J. et al. [2.45] presented the results of the free vibration analysis, flutter and subsequent flutter sensitivity analysis of a high capacity future aircraft. The free vibration analysis was carried out using the dynamic stiffness method as applicable to a stick model of an aircraft using CALFUNOPT program and the finite element programme MSC/NASTRAN. The first six modes in both symmetric and antisymmetric are presented for the whole aircraft. A flutter analysis was then carried out. Both the symmetric and antisymmetric flutter behaviour of the aircraft were investigated using

selected normal modes through the use of the generalized coordinates and two-dimensional unsteady aerodynamics of Theodorsen type. The flutter matrix was formulated by summing algebraically the generalized dynamic stiffness and the aerodynamic matrices. The V-g method was then used to solve the flutter matrix, yielding to flutter speed and flutter frequency. After the above analysis, the flutter sensitivity analysis was carried out and the effect of the variation of the structural and inertia properties on the flutter speed was performed.

Weisshaar, T. et al. [2.46] developed an idealized aeroelastic tailoring model to assess the effects of the significant changes in directional stiffness orientation upon the flutter and divergence behaviour of swept and unswept wings. The effect of the variation of the nondimensional stiffness cross-coupling parameter and the stiffness ratio on the flutter and divergence speed was investigated.

Georghiades, G. et al. [2.47] carried out an analytical investigation into the effects of wash-in and wash-out on the flutter of composite wing-like plate with the laminate configuration of $[\beta]_{14}$. The analysis was done using CALFUN program. It was concluded that the wash-in behaviour improves the flutter speed as opposed to the wash-out behaviour.

Butler, R. et al. [2.48] present the new features of a computer program (CALFUNOPT) for the conceptual, minimum mass design of high aspect ratio, composite wings subjected to constrains on flutter and divergence speed. The natural frequencies of the wing, modelled as a series of box beams, were obtained using an efficient and accurate Dynamic Stiffness Matrix method whilst aeroelastic loads are based on strip theory. The effect of rotatory inertia, shear deformation and warping stiffness were neglected. The wing was constructed from upper and lower skin, two spars and an attached engine. The flutter and divergence speeds of the wing were then found using the normal mode approach. Design sensitivities, obtained by a very efficient technique were used to direct the optimizer ADS. Different design variables

were includes such as engine location, spar positions and the ply thickness. An illustrative example was presented.

Lillico, M. et al. [2.49] presents the aeroelastic optimization of aircraft wings with high aspect ratios at subsonic speed using CALFUNOPT program. The natural frequencies of the wing, modelled as a series of connected uniform beam elements, were obtained using an efficient and accurate Dynamic Stiffness Matrix method, whilst aeroelastic loads are calculated using strip theory based on Theodorsen expressions. The effect of rotatory inertia, shear deformation and warping stiffness were neglected. The flutter speed of the wing was then found using the normal mode approach. Design sensitivities obtained from a very efficient technique, are used to direct the optimizer ADS. Typical optimization results for unswept metal and composite wings were presented.

Shirk, M. et al. [2.50] presents the historical background of aeroelastic tailoring and the theory underlying the technology. A summary of trend studies that have been performed and a discussion of more specific applications are also presented.

Weisshaar, T. et al. [2.51] discusses the important of including aircraft rigid-body modes in the aeroelastic analysis of forward swept wing aircraft. Several examples were used to show that body-freedom flutter and aircraft aeroelastic divergence, are the primary vehicle aeroelastic instabilities to be encountered by forward swept wing aircraft. It was shown from the analysis that these instabilities are close to the wing divergence speed, but depend upon the aircraft geometry and inertial characteristics as well as wing stiffness.

Lillico, M. et al. [2.52] describe the capability of a program called CALFUNOPT for the optimum (minimum mass) design of high aspect ratio, composite wings at the conceptual structural design stage, subject to constrains on flutter speed, divergence speed and material stress. A simplified wing was used, which contains upper and lower skin and front and rear spar. The wing was modelled as series of uniform

beam elements with, cantilevered at the root and both flutter speed and divergence speed was calculated using a normal mode approach. The composite laminates used for the wing model consist of eight symmetric layers with identical skins. Modal analysis was carried out by applying the Wittrick-Williams algorithm to the dynamic stiffness method, whereas the unsteady aerodynamic loads were calculated using the strip theory with an option of using the lifting surface theory was presented. Validation of the program was done by analysing a published wing result. Single level optimization was carried out using a sequential quadratic programming strategy combined with the modified methods of feasible directions optimizer, for which flutter sensitivities were obtained by an efficient determinant interpolation technique. Design variables include topological variables such as engine positions as well as layer thickness, which were modelled using quadratic functions.

2.3 Concluding remarks:

From the above section of the literature review in the area of vibration and flutter of cantilevered composite wings, and to the best of the author's knowledge most of the presented studies of the composite wings of the aircraft were considered and modelled as cantilevered plate. This is not a practical representation of composite aircraft wings. A few studies considered the wing as a closed single cell structure with uniform stiffness along the span and the chord of the structure, in which there was no offset between the elastic axis and the inertia axis which was not a practical representation of real aircraft wings. In the case of the wing as a single cell structure, the laminate lay ups used in the analysis were unpractical. In both of the above wing models (plate and a uniform single cell structure), the effects of the following parameters on the free vibration characteristics and flutter speed were investigated:

- Fibre orientations,
- Sweep angle,
- Aspect ratios,
- Cross-coupling parameter with fixing the bending to torsion ratio (GJ/EI).

From section 2.2, the terminology of the Circumferentially Asymmetric Stiffness (CAS) was used in [2.31 and 2.32]. Cesnik, C et al. [2.31] shows the variation of the flutter speed versus the fibre orientations (-90 to 90 degrees) of the single cell wing model constructed from a single ply. While in [2.32], the variation of the flutter speed versus the fibre orientations of 0°, 45° and –45° were done using a single ply as well.

From the above discussion, the effects of the following parameters on the free vibration and flutter speed of physical such as Aerobatic aircraft composite wing box or more realistic composite wing models need to be investigated in this work, which has not been considered on practical wing model:

- Structural geometrys,
- Inclusion of structural coupling,
- Fibre orientations (-90° to 90°), and
- Material coupling or the combination of all.
- Wash-in and Wash-out

The composite wing models simulated both Circumferentially Asymmetric Stiffness (CAS) and Circumferentially Uniform Stiffness (CUS) using symmetric and asymmetric laminate lay ups.

The methodical approach used in this research was started by first generating a less representation of a wing model structure (see figure 1.1 of chapter 1), then to more representative models (see figures 1.2-1.4) and finally to physical or real wing box composite model (see figure 7.1 of chapter 7). The methods of investigating the listed parameters were illustrated in section 1.3 of chapter1.

References

2.1 Jensen,D.W, Crawley,E.F. and Dugundji, J. (1982). 'Vibration of Cantilevered Graphite/Epoxy Plates with Bending-Torsion coupling'. Journal of Reinforced Plastics and Composites, vol.1, 254-269.

2.2 Hollowell,S.J.and Dugundji J. (1984). 'Aeroelastic flutter and divergence of stiffness coupled, graphite/epoxy cantilevered plates'. Journal of Aircraft, vol.21, no.1, 69-76.

2.3 Lakshminarayana, H.V., Rajagopal, P., Ramamurthy, M.R. and Jashi, A. (1985). 'Vibration Characteristics of a Swept Composite Wing Panel:Finit Element analysis and Experimental Verification'. Journal. of Aero. Soc. of India, vol.37, no.4, 289-295.

2.4 Chunan-Qi, H.,Chen Jing-Song and Chiao Shing. (1987). 'Flutter analysis of aeronautical composite structures by improved supersonic kernel function method'. Chinese Journal of Aeronautics.

2.5 Lee, L and Lee J. (1990). 'Vibration analysis of composite plate wing'. Computes & Structures, vol.37, no.6, 1077-1085.

2.6 Chuanqi, H and Qiao Xin. (1991). 'Aeroelastic tailoring of aeronautical composite wing structures'. Chinese Journal of Aeronautics, vol.4, no.2, 245-256.

2.7 Thangjitham, S. and Librescu, L. (1991). Vibration characteristics of anisotropic composite wing structures. AIAA 91-1185-cp.

2.8 Haisong, A., Shing, C, Liping, J and Yin, Y. (1992). 'Aeroelastic analysis of composite wing with control surface'. Chinese Journal of Aeronautics, 1971-1922.

2.9 In Lee and Jinglee, J. (1993). 'Vibration analysis of composite wing with tip mass using finite elements'. Computers& Structures, vol.47, no.3, 495-504.

2.10 Librescu, L., Meirovitch, L. and Song, O. (1993). A refined structural model of composite aircraft wings for the enhancement of vibrational and aeroelastic response characteristics. AIAA 93-1536.

2.11 Karpouzian, G. and Librescu, L. (1994). 'Comprehensive model of anisotropic composite aircraft wings suitable for aeroelastic analysis'. Journal of Aircraft, vol.31, no.3, 703-712.

2.12 Meirovitch, L. and Seitz, T.J. (1993). Structural modelling of low-aspect ratio composite wings. AIAA 93-1371.

2.13 Kuilin, C. and Ming, X. (1992). Application of vibration and flutter integration analysis system for a Trainer. Icas, Congress, 18th, Beijing, China, Sept. 20-25, 1992, vol.2, 1258-1262.

2.14 Kuo-Juin, L.; Pong-jeu, L. and Jiann-quo, T. (1989). 'Flutter analysis of cantilever composite plates in subsonic flow'. AIAA Journal, vol.27, no.8, 1102- 1109.

2.15 Georghiades, G.; Guo, S. and Banerjee, J.R. (1995). Flutter analysis of composite wings using an exact dynamic stiffness matrix method. AIAA 95-1488-CP, 3019-3027.

2.16 Robert, V. and Soistmann, D. (1992). 'Low-speed flutter characteristics of some simple low-aspet-ratio delta wing models'. Journal of Aircraft, vol.29, no.2, 273-279.

2.17 Koo, K. and Lee, I. (1994). 'Aeroelastic behaviour of a composite plate wing with structural damping'. Computers&Structures, vol.50, no.2, 167-176.

2.18 Banerjee, J.R. and Williams, F.W. (1995). 'Free vibration of composite beams-an exact method using symbolic computation'. Journal of Aircraft, vol.32, no.3, 636-642.

2.19 Chandrashekhara, K. and Bangera, K. (1992). 'Free vibration of composite beams using a refined shear flexible beam element'. Computers&Structures, vol.43, no.4, 719-727.

2.20 Kapania, R. K. and Francois, C. (1990). 'A simple element for aeroelastic analysis of undamaged and damaged wings'. AIAA Journal, vol.28, no.2, 329-337.

2.21 Teboub, Y. and Hajela, P. (1994). Free vibration of generally layered composite beams using symbolic computations. AIAA 94-1330-CP, 182-192.

2.22 Lottati, I. (1985). 'Flutter and Divergence aeroelastic characteristics for composite forward swept cantilevered wing'. Journal of Aircraft, vol.22, no.11, 1001-1007.

2.23 Lee, U. (1994). Equivalent continuum beam-rod models of aircraft wing structures for aeroelastic analysis. AIAA 94-1695-CP, 191-199.

2.24 Armanios, E. A. and Badir, A. M. (1994). Free vibration analysis of anisotropic thin-walled closed-section beams. AIAA 94-1327-CP, 164-171.

2.25 Banerjee, J. R. (1984). 'Flutter characteristics of high aspect ratio tailless aircraft'. Journal of Aircraft, vol.21, no.9, 733-736.

2.26 Karpouzian, G. and Librescu, L. (1993). Exact flutter solution of advanced anisotropic composite cantilevered wing structures. AIAA 93-1535-CP, 1961-1966.

2.27 Karpouzian, G. and Librescu, L. (1994). Three-Dimensional flutter solution of aircraft wings composed of advanced composite materials. AIAA-94-1490-CP. 2851-2857.

2.28 Teh, K. K. and Huang, C.C. (1979). 'The vibrations of generally orthotropic beams, a finite element approach'. Journal of Sound and Vibration, vol.62, no.2, 195-206.

2.29 Wu, X. X. and Sun, C. T. (1991). 'Vibration analysis of laminated composite thin-walled beams using finite elements'. AIAA Journal, vol.29, no.5, 736742.

2.30 Lottati, I. (1986). 'The role of structural and aerodynamic damping on the aeroelastic behaviour of wings'. Journal of Aircraft, vol.23, no.7, 606-608.

2.31 Cesnik, C.E.; Hodges, D.H. and Patil, M.J. (1996). Aeroelastic analysis of composite wings. AIAA 96-1444-CP. 1113-1123.

2.32 Chattopadhyay, A.; Zhang, S. and Ratneshwar, J. (1996). Structural and aeroelastic analysis of composite wing box sections using higher order laminate theory. AIAA 96-1567-CP. 2185-2198.

2.33 Georghiades, G.A. and Banerjee, J.R. (1996). A parametric investigation into the Flutter Characteristics of Composite Wings. AIAA 96-1351-CP., 300-310.

2.34 Stanley, C.R. and Rivera, Jr. (1987). Flutter study of an advanced composite wing with external stores. AIAA 87-0880., 480-490

2.35 Schoor, M.C.; Zerweckh, S.H. and Flotow, A.H. (1989). Aeroelastic stability and control of a highly flexible aircraft. AIAA 89-1187-CP., 254-264.

2.36 Weisshaar, T.A. (1985). 'Vibration tailoring of advanced composite lifting surfaces'. Journal of Aircraft, vol.22, no.2, 141-147.

2.37. Schweiger, J. and Dobbs, S. (1995). 'Aeroelastic design and flight test evaluation of the ranger 2000 training aircraft'. *International Forum on Aeroelasticity and Structural Dynamics 1995, Manchester Business School*, UK, June 26-28, 1995 Proceedings. vol. (A95-42316 11-39), London, Royal Aeronautical Society, p. 23.1-23.11.

2.38 Green, J. (1987). 'Aeroelastic tailoring of aft-swept high-aspect-ratio composite wings'. Journal of Aircraft, vol.24, no.11, 812-819.

2.39 Weisshaar, T.A. (1980). 'Divergence of forward swept composite wings'. Journal of Aircraft, vol.17, 443-448.

2.40 Weisshaar, T.A. (1981). 'Aeroelastic tailoring of forward swept composite wings'. Journal of Aircraft, vol.18, no. 8, 669-676.

2.41 Blair M. and Weisshaar T.A. (1982). 'Swept composite wing aeroelastic divergence experiments'. Journal of Aircraft, vol.19, no. 11, 1019-1024.

2.42 Weisshaar, T.A. (1983). Vibration and flutter of advanced composite lifting surfaces. A83-29861, 498-508.

2.43 Landsberger, B.J.and Dugundji, J. (1985). 'Experimental aeroelastic behaviour of unswept and forward swept cantilever graphite/epoxy wings'. Journal of Aircraft, vol.22, no.8, 679-686.

2.44 Striz, A.G. and Venkayya, V.B. (1994). 'Influence of structural and aerodynamic modelling on flutter analysis'. Journal of Aircraft, vol.31, no.5, 1205-1211.

2.45 Banerjee, J.R., Patel, M.H., Done, G.T., Butler, R. and Lillico, M. (1998). Free vibration and flutter sensitivity analysis of large transport aircraft. AIAA 98-4765, 465-473.

2.46 Weisshaar, T.A. and Ryan, R. (1986). 'Control of aeroelastic instabilities through stiffness cross-coupling'. Journal of Aircraft, vol.23, no. 2, 148-155.

2.47 Georghiads, G.A. and Banerjee, J.R. (1997). Flutter modes of composite wings exhibiting wash-in and wash-out. AIAA 97-1267, 749-758.

2.48 Butler, R., Lillico, M., Banerjee, J.R. and Guo, S. (1995). Optimum design of high aspect ratio wings subject to aeroelastic constrains. AIAA 95-1223-CP, 558-566.

2.49 Lillico, M., Butler, R., Banerjee, J.R. and Guo, S. (1994). Aeroelastic optimization of high aspect ratio wings using an exact dynamic stiffness matrix method. AIAA 94-4401-CP, 1301-1309.

2.50 Shirk, M.H. and Hertz, T.J. (1986). 'Aeroelastic Tailoring-Theory, Practice, and Promise'. Journal of Aircraft, vol.23, no. 1, 6-18.

2.51 Weisshaar, T.A. and Zeiler, T.A. (1983). 'Dynamic stability of flexible fordward swept wing aircraft'. Journal of Aircraft, vol.20, no. 12, 1014-1020.

2.52 Lillico, M., Butler, R., Guo, S. and Banerjee, J.R. (1997). 'Aeroelastic optimization of composite wings using the dynamic stiffness method'. The Aeronautical Journal, vol. 101, no. 1002, pp. 77-86.

2.53 Collar, A.R. (1946) 'The expanding domain of aeroelasticity'. Journal of the Royal Aeronautical Society, vol. 50, pp. 613-636.

CHAPTER 3

BASIC THEORY FOR THE ANALYSIS OF COMPOSITE LAYERED STRUCTURE

3.1 INTRODUCTION:

This chapter deals with the micromechanical properties of composites, which is very important in the design analysis. The successful prediction of dynamic characteristics of a structure like an aircraft wing depends on adequate knowledge of the static structural properties such as bending, torsional and bending-torsion coupling stiffnesses. The mass per unit length and polar mass moment of inertia of the structure are also important parameters, which influence the dynamic behaviour of the structure. The material properties of isotropic materials, such as Young's modulus and Shear modulus, are independent of the cross-section of the structure and the loading conditions and thus the rigidity properties depend on the geometrical properties of the cross-section.

In the case of composite materials, the material and, in consequence the rigidity properties vary with the fibre orientation (see figures (8.2-8.4) of chapter 8), the stacking of the plies, the geometrical properties of the cross-section, and loading conditions. Thus, an alternative and as it turns out, more complicated theoretical analysis is required to predict the rigidity properties of a composite structure.

The aim of this chapter is to discuss and compare the most popular stiffness models that have been developed for the modelling of laminated composite thin-walled structure (box-beam) and the mathematical expressions of the structural rigidities (EI, GJ and K) were presented. The application and the calculation of the structural stiffnesses using the two methods [3.5 and 3.8] on wing 1 and wing 6 models were illustrated in figures (8.2-8.4) of chapter 8 versus the fibre angle θ. Using two different methods in the stiffness modelling will show the modelling differences and will provide a clear understanding of the influence of the parameters such as fibre orientations on the stiffnesses rigidities. Subsequently this will help the structural designer in understanding of the mechanics of the composite structure and in the selection of the optimum fibre angle, which leads to better dynamic characteristics and then to the maximum flutter speed as illustrated in chapter 8.

3.2 STRESS-STRAIN EQUATIONS FOR COMPOSITE LAYERED PLATES AND SHELLS.

A composite layered plate or shell usually consists of a number of layers (Ni) bonded firmly with each other. Each layer is a lamina and it is flat for plates and curved for shells, and it represents an assemblage of reinforcing fibres in a supporting isotropic matrix. From a macroscopic scale, the layer is considered homogeneous and orthotropic. The material properties of the layer are defined with respect to the material principle axes x, y, z such that

- The z axis is normal to the midsurface of the layer and in direction 3.
- The x, y axes are normal to the z axis, in another wards they are in the midplane of the layer in case of plates and tangential to the midsurface of the the layer in case of shells, the x axis is in the direction 1 which is parallel to the fibre and y axis in the direction 2 which is in the matrix.

The material properties which are required for an elastic analysis are:-

E_x, E_y, E_z Young's moduli in the x, y, z directions respectively.

ν_{xy}, ν_{yz}, ν_{zx} Poisson's ratios, with respect to x, y, z axes.

G_{xy}, G_{yz}, G_{zx} shear moduli, with respect to x, y, z axes.

The stress and strain states at any point inside a layer may be defined in terms of the following engineering stress and stain vectors:-

$$\sigma = \left\{\sigma_x \sigma_y \sigma_z \tau_{yz} \tau_{zx} \tau_{xy}\right\}$$

$$\varepsilon = \left\{\varepsilon_x \varepsilon_y \varepsilon_z \gamma_{yz} \gamma_{zx} \gamma_{xy}\right\}$$

and for an orthotropic layer, the elastic stress-strain equations may be expressed in the following matrix form as given in [3.2]:-

$$\varepsilon_i = S_{ij}\sigma_j \qquad \text{where} \qquad i,j = 1,\ldots..,6$$

and $$\sigma_i = C_{ij}\varepsilon_j$$

where $$C_{ij} = S^{-1}{}_{ij}$$

The compliance matrix S_{ij} components in terms of the engineering constants are

$$[S_{ij}] = \begin{bmatrix} \frac{1}{E_1} & -\frac{\upsilon_{21}}{E_2} & -\frac{\upsilon_{31}}{E_3} & 0 & 0 & 0 \\ -\frac{\upsilon_{12}}{E_1} & \frac{1}{E_2} & -\frac{\upsilon_{32}}{E_3} & 0 & 0 & 0 \\ -\frac{\upsilon_{13}}{E1} & -\frac{\upsilon_{23}}{E_2} & \frac{1}{E_3} & 0 & 0 & 0 \\ 0 & 0 & 0 & \frac{1}{G_{23}} & 0 & 0 \\ 0 & 0 & 0 & 0 & \frac{1}{G_{31}} & 0 \\ 0 & 0 & 0 & 0 & 0 & \frac{1}{G_{12}} \end{bmatrix}$$

The stiffness matrix, C_{ij}, in terms of the engineering constants is obtained by the inverse of the compliance matrix S_{ij}

$$C = \frac{1}{\Delta}\begin{bmatrix} E_1(1-\upsilon_{23}\upsilon_{32}) & E_1(\upsilon_{21}+\upsilon_{31}\upsilon_{23}) & E_1(\upsilon_{31}+\upsilon_{21}\upsilon_{32}) & 0 & 0 & 0 \\ E_2(\upsilon_{12}+\upsilon_{32}\upsilon_{13}) & E_2(1-\upsilon_{13}\upsilon_{31}) & E_2(\upsilon_{32}+\upsilon_{12}\upsilon_{31}) & 0 & 0 & 0 \\ E_3(\upsilon_{13}+\upsilon_{12}\upsilon_{23}) & E_3(\upsilon_{23}+\upsilon_{21}\upsilon_{13}) & E_3(1-\upsilon_{12}\upsilon_{21}) & 0 & 0 & 0 \\ 0 & 0 & 0 & G_{23} & 0 & 0 \\ 0 & 0 & 0 & 0 & G_{31} & 0 \\ 0 & 0 & 0 & 0 & 0 & G_{12} \end{bmatrix}$$

Where $$\Delta = 1-\upsilon_{12}\upsilon_{21}-\upsilon_{23}\upsilon_{32}-\upsilon_{31}\upsilon_{13}-2\upsilon_{21}\upsilon_{32}\upsilon_{13}$$

The constitutive relations for the orthotropic materials were written in terms of the stress and strain components that are referred to the co-ordinate system which coincide with the principle material co-ordinate system. The co-ordinate system used in the solution of a problem, in general, does not coincide with material co-ordinate system. Further, composite laminates have several layers, each with different orientation of their material co-ordinates with respect to the laminate co-ordinates.

The transformation equations for expressing stress in x-y co-ordinate system (Global) in terms of stress in a 1-2 co-ordinate system are:

$$\begin{Bmatrix}\sigma_x\\ \sigma_y\\ \tau_{xy}\end{Bmatrix}=\begin{bmatrix}\cos^2\theta & \sin^2\theta & -2\sin\theta\cos\theta\\ \sin^2\theta & \cos^2\theta & 2\sin\theta\cos\theta\\ \sin\theta\cos\theta & -\sin\theta\cos\theta & \cos^2\theta-\sin^2\theta\end{bmatrix}\begin{Bmatrix}\sigma_1\\ \sigma_2\\ \tau_{12}\end{Bmatrix}$$

Where θ is the angle from the x-axis to the (1)-axis as shown in Figure (3.1).

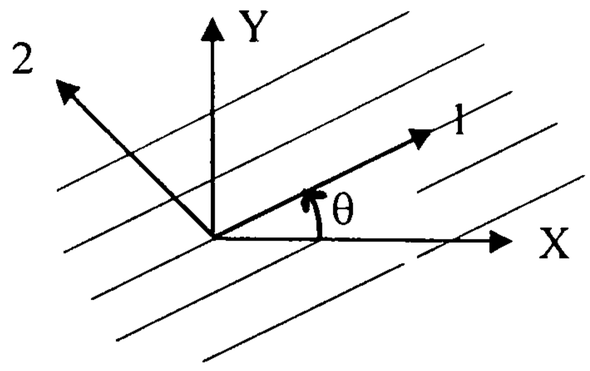

Fig. 3.1 Positive rotation of principle material axes.

Similarly, the strain transformation equations are

$$\begin{Bmatrix}\varepsilon_x\\ \varepsilon_y\\ \frac{\gamma_{xy}}{2}\end{Bmatrix}=\begin{bmatrix}\cos^2\theta & \sin^2\theta & -2\sin\theta\cos\theta\\ \sin^2\theta & \cos^2\theta & 2\sin\theta\cos\theta\\ \sin\theta\cos\theta & -\sin\theta\cos\theta & \cos^2\theta-\sin^2\theta\end{bmatrix}\begin{Bmatrix}\varepsilon_1\\ \varepsilon_2\\ \frac{\gamma_{12}}{2}\end{Bmatrix}$$

For the specially orthotropic lamina is one whose principle material axes are aligned with the natural body axis.

$$\begin{Bmatrix}\sigma_x\\ \sigma_y\\ \tau_{xy}\end{Bmatrix}=\begin{Bmatrix}\sigma_1\\ \sigma_2\\ \tau_{12}\end{Bmatrix}=\begin{bmatrix}Q_{11} & Q_{12} & 0\\ Q_{21} & Q_{22} & 0\\ 0 & 0 & Q_{66}\end{bmatrix}\begin{Bmatrix}\varepsilon_1\\ \varepsilon_2\\ \gamma_{12}\end{Bmatrix}$$

Where the Q_{ij}, the so- called reduced stiffness, are

$$Q_{11}=\frac{E_1}{1-\upsilon_{12}\upsilon_{21}}$$

$$Q_{12}=\frac{\upsilon_{12}E_2}{1-\upsilon_{12}\upsilon_{21}}=\frac{\upsilon_{21}E_1}{1-\upsilon_{12}\upsilon_{21}}$$

$$Q_{22}=\frac{E_2}{1-\upsilon_{12}\upsilon_{21}}$$

$$Q_{66}=G_{12}$$

The transformation relationships for the elastic constants for an orthotropic material in a plane stress state and the transformed reduced stiffness matrix $\left[\overline{Q}_{ij}\right]$ are as follows:

$$\begin{Bmatrix} \sigma_x \\ \sigma_y \\ \tau_{xy} \end{Bmatrix} = \begin{bmatrix} \overline{Q}_{11} & \overline{Q}_{12} & \overline{Q}_{16} \\ \overline{Q}_{21} & \overline{Q}_{22} & \overline{Q}_{26} \\ \overline{Q}_{16} & \overline{Q}_{26} & \overline{Q}_{66} \end{bmatrix} \begin{Bmatrix} \varepsilon_x \\ \varepsilon_y \\ \gamma_{xy} \end{Bmatrix} \tag{3}$$

in which

$$\overline{Q}_{11} = Q_{11}\cos^4\theta + 2\left(Q_{12} + 2Q_{66}\right)\sin^2\theta\cos^2\theta + Q_{22}\sin^4\theta$$
$$\overline{Q}_{12} = \left(Q_{11} + Q_{22} - 4Q_{66}\right)\sin^2\theta\cos^2\theta + Q_{12}\left(\sin^4\theta + \cos^4\theta\right)$$

$$\overline{Q}_{22} = Q_{11}\sin^4\theta + Q_{22}\cos^4\theta + 2\left(Q_{12} + 2Q_{66}\right)\sin^2\theta\cos^2\theta$$
$$\overline{Q}_{16} = \left(Q_{11} - Q_{12} - 2Q_{66}\right)\sin\theta\cos^3\theta + \left(Q_{12} - Q_{22} + 2Q_{66}\right)\sin^3\theta\cos\theta$$
$$\overline{Q}_{26} = \left(Q_{11} - Q_{12} - 2Q_{66}\right)\sin^3\theta\cos\theta + \left(Q_{12} - Q_{22} + 2Q_{66}\right)\sin\theta\cos^3\theta$$
$$\overline{Q}_{66} = \left(Q_{11} + Q_{22} - 2Q_{12} - 2Q_{66}\right)\sin^2\theta\cos^2\theta + Q_{66}\left(\sin^4\theta + \cos^4\theta\right)$$

3.3 LAMINATE CONSTITUTIVE EQUATIONS

The laminate macro-mechanics can be found in [3.1], [3.2] and [3.3] or in other standard text books on the mechanics of composite materials. Composite can be categorised in to several different types depending upon ply thickness, fibre orientation and number of layers as shown in figure (3.1).

The general laminate constituve equations for load-deformation relationships as provided in [3.2] and [3.3] are as follows:

$$\begin{Bmatrix} N_x \\ N_y \\ N_{xy} \end{Bmatrix} = \begin{bmatrix} A_{11} & A_{12} & A_{16} \\ A_{12} & A_{22} & A_{26} \\ A_{16} & A_{26} & A_{66} \end{bmatrix} \begin{Bmatrix} \varepsilon^o{}_x \\ \varepsilon^o{}_y \\ \gamma^o{}_{xy} \end{Bmatrix} + \begin{bmatrix} B_{11} & B_{12} & B_{16} \\ B_{12} & B_{22} & B_{26} \\ B_{16} & B_{26} & B_{66} \end{bmatrix} \begin{Bmatrix} k_x \\ k_y \\ k_{xy} \end{Bmatrix} \tag{3.1}$$

$$\begin{Bmatrix} M_x \\ M_y \\ M_{xy} \end{Bmatrix} = \begin{bmatrix} B_{11} & B_{12} & B_{16} \\ B_{12} & B_{22} & B_{26} \\ B_{16} & B_{26} & B_{66} \end{bmatrix} \begin{Bmatrix} \varepsilon^o{}_x \\ \varepsilon^o{}_y \\ \gamma^o{}_{xy} \end{Bmatrix} + \begin{bmatrix} D_{11} & D_{12} & D_{16} \\ D_{12} & D_{22} & D_{26} \\ D_{16} & D_{26} & D_{66} \end{bmatrix} \begin{Bmatrix} k_x \\ k_y \\ k_{xy} \end{Bmatrix} \tag{3.2}$$

and

$$A_{ij} = \sum_{k=1}^{N} (\overline{Q}_{ij})_k (z_k - z_{k-1}) \tag{3.3}$$

$$B_{ij} = \frac{1}{2} \sum_{k=1}^{N} (\overline{Q}_{ij})_k (z^2{}_k - z^2{}_{k-1}) \tag{3.4}$$

$$D_{ij} = \frac{1}{3} \sum_{k=1}^{N} (\overline{Q}_{ij})_k (z^3{}_k - z^3{}_{k-1}) \tag{3.5}$$

where

N_x, N_y = Normal forces per unit length in x and y direction respectively.

N_{xy} = shear force per unit length.

ε_x, ε_y = normal strain in x and y directions

γ_{xy} = shear strain

M_x, M_y, M_{xy} = moments per unit length

k_x, k_y, k_{xy} = twist curvatures of the middle surface

A_{ij} = extensional stiffness

B_{ij} = coupling stiffness

D_{ij} = bending stiffness.

In the case of symmetric laminates with multiple generally orthotropic layers, the coupling terms in this configuration (B matrix) are zero and the equations (3.1) and (3.2) will be as follows:

$$\begin{Bmatrix} N_x \\ N_y \\ N_{xy} \end{Bmatrix} = \begin{bmatrix} A_{11} & A_{12} & A_{16} \\ A_{12} & A_{22} & A_{26} \\ A_{16} & A_{26} & A_{66} \end{bmatrix} \begin{Bmatrix} \varepsilon^o{}_x \\ \varepsilon^o{}_y \\ \gamma^o{}_{xy} \end{Bmatrix} \tag{3.3}$$

$$\begin{Bmatrix} M_x \\ M_y \\ M_{xy} \end{Bmatrix} = \begin{bmatrix} D_{11} & D_{12} & D_{16} \\ D_{12} & D_{22} & D_{26} \\ D_{16} & D_{26} & D_{66} \end{bmatrix} \begin{Bmatrix} k_x \\ k_y \\ k_{xy} \end{Bmatrix} \tag{3.4}$$

The presence of some terms in A and D matrices will cause coupling between various deformations. For example A_{16}, A_{26}, D_{16} and D_{26} will cause coupling between normal forces and shear strain, shearing force and normal strain, normal moments and twist, and twist moment and normal curvatures respectively.

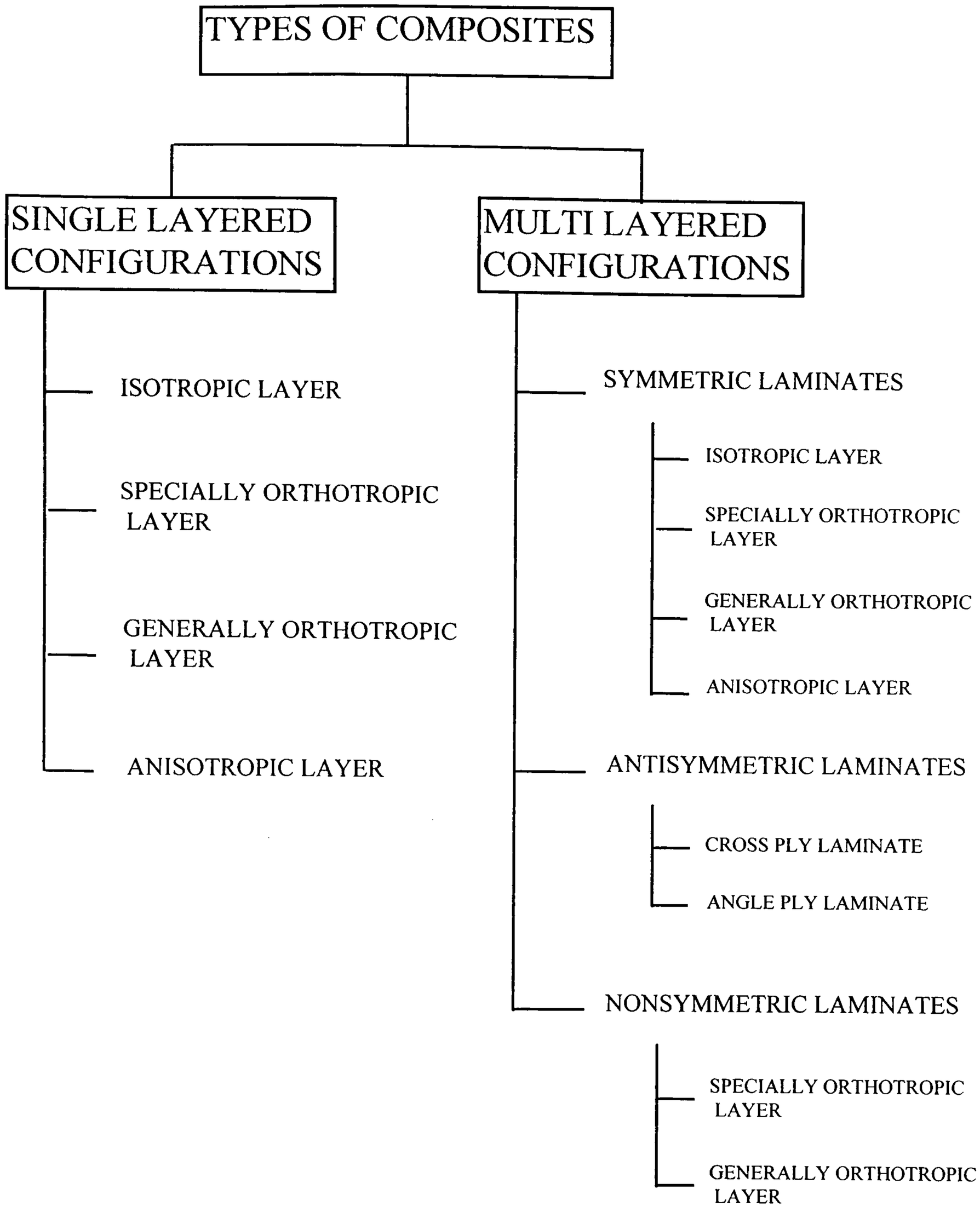

Fig. (3.2) Types of composites

3.4 STRUCTURAL STIFFNESS

The stiffness of a structure is its resistance to the displacement as an unbalanced system of forces and moments are applied to the structure. It basically depends on the material properties and geometry of the structure. Therefore, a desired amount of stiffness can be achieved by selecting from a range of materials and varying the

geometrical parameters such as size and shape of the cross-section. In the case of composite materials the fibre orientation and the stacking sequence provide a wide number of possibilities in achieving certain amount of stiffness.

In the case of thin-walled beams, bending stiffness EI, torsional stiffness GJ, extensional stiffness EA, and warping stiffness EΓ are often considered. In composite materials, the bend-twist coupling stiffness K for symmetric laminates and extension-twist coupling K_{pa} for anti-symmetric laminates are added additional stiffness to the above stiffness. The accurate determination of the above stiffness will give a correct prediction of the natural frequencies of the structure.

3.4.1 STIFFNESS CALCULATION OF COMPOSITE STRUCTURES

The right handed Cartesian axes in the discussion to follow are assigned in such way that x, y and z-axes refers to the chordwise and spanwise (along the flexural axis of the structure) direction and that orthogonal to both x and y-axes respectively. The composite fibre axes 1, 2, and 3 refers to longitudinal, transverse and out of the plane of the lamina respectively. The macro-mechanics of composite materials assume that if the laminate is especially orthotropic then the fibre axis 1 is along the x-axis of the structure. Thus is case of generally orthotropic laminate the fibre angle is measured from the x-axis as shown in figure (3.3).

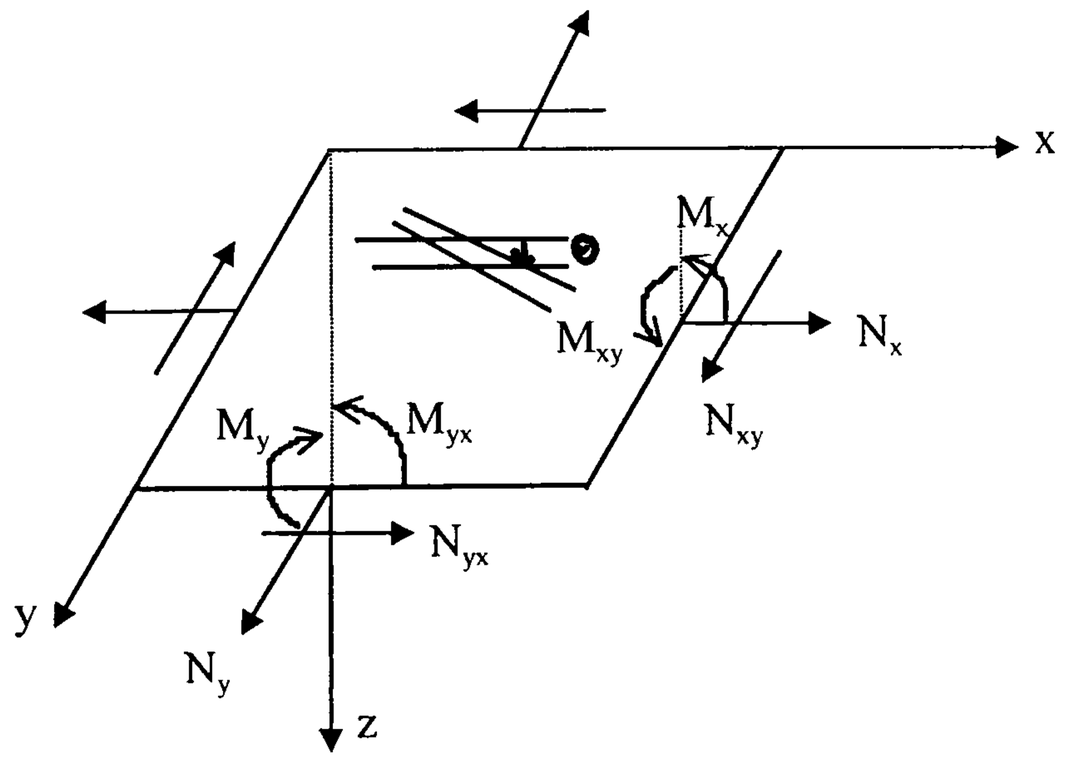

Fig. 3.3 Orientation of axis for plate structure.

A summary of the theoretical prediction of bending, torsional and bending-torsional material coupling stiffnesses will be discussed for various structural elements as follows:

(i) BEAM ELEMENT

The moment-curvature and the in plane stress-strain realtions for the general case of laminate are (given in equations (3.1) and (3.2) of this chapter) as follows:

$$\begin{Bmatrix} N \\ M \end{Bmatrix} = \begin{bmatrix} A & B \\ B & D \end{bmatrix} \begin{Bmatrix} \varepsilon \\ k \end{Bmatrix} \tag{3.5}$$

where $N = \begin{Bmatrix} N_x \\ N_y \\ N_{xy} \end{Bmatrix}$ = in plane forces

$M = \begin{Bmatrix} M_x \\ M_y \\ M_{xy} \end{Bmatrix}$ = bending and twisting moments

$k = \begin{Bmatrix} k_x \\ k_y \\ k_{xy} \end{Bmatrix}$ = bending and twisting curvatures

where A_{ij}, B_{ij}, D_{ij} = inplane, coupling and flexural moduli respectively.

For symmetric laminate B_{ij} is equal to zero. Therefore, flexural and longitudinal modes will uncouple. If a beam as shown in figure (3.4) is subjected to the bending moment M_x, and an torque M_{xy} and with out the chordwise bending moment M_y, then the equation (3.5) will be

$$\begin{Bmatrix} M_x \\ 0 \\ M_{xy} \end{Bmatrix} = \begin{bmatrix} D_{11} & D_{12} & D_{16} \\ D_{21} & D_{22} & D_{26} \\ D_{61} & D_{62} & D_{66} \end{bmatrix} \begin{Bmatrix} k_x \\ k_y \\ k_{xy} \end{Bmatrix} \tag{3.6}$$

or

$$M_x = D_{11}k_x + D_{12}k_y + D_{16}k_{xy} \tag{3.7a}$$

$$0 = D_{21}k_x + D_{22}k_y + D_{26}k_{xy} \tag{3.7b}$$

$$M_{xy}=D_{61}k_x+D_{62}k_y+D_{66}k_{xy} \tag{3.7c}$$

The second equation will yield to

$$k_y= -(D_{21}k_x+D_{26}k_{xy})/ D_{22} \tag{3.7d}$$

Therefore,

$$M_x = \left(D_{11} - \frac{D^2{}_{12}}{D_{22}} \right) k_x + \left(D_{16} - \frac{D_{12} D_{26}}{D_{22}} \right) k_{xy} \tag{3.7e}$$

and similarly

$$M_{xy} = \left(D_{16} - \frac{D_{12} D_{26}}{D_{22}} \right) k_x + \left(D_{66} - \frac{D^2{}_{26}}{D_{22}} \right) k_{xy} \tag{3.7f}$$

Therefore, in matrix form

$$\begin{Bmatrix} M_x \\ M_{xy} \end{Bmatrix} = b \times \begin{bmatrix} \left(D_{11} - \frac{D^2{}_{12}}{D_{22}} \right) & 2 \times \left(D_{16} - \frac{D_{12} D_{26}}{D_{22}} \right) \\ 2 \times \left(D_{16} - \frac{D_{12} D_{26}}{D_{22}} \right) & 4 \times \left(D_{66} - \frac{D^2{}_{26}}{D_{22}} \right) \end{bmatrix} \begin{Bmatrix} k_x \\ k_{xy} \end{Bmatrix}$$

or

$$\begin{Bmatrix} M_x \\ M_{xy} \end{Bmatrix} = \begin{bmatrix} EI & K \\ K & GJ \end{bmatrix} \begin{Bmatrix} k_x \\ k_{xy} \end{Bmatrix} \tag{3.8}$$

where EI = bending stiffness

GJ = torsional stiffness

K = bending-torsional coupling stiffness

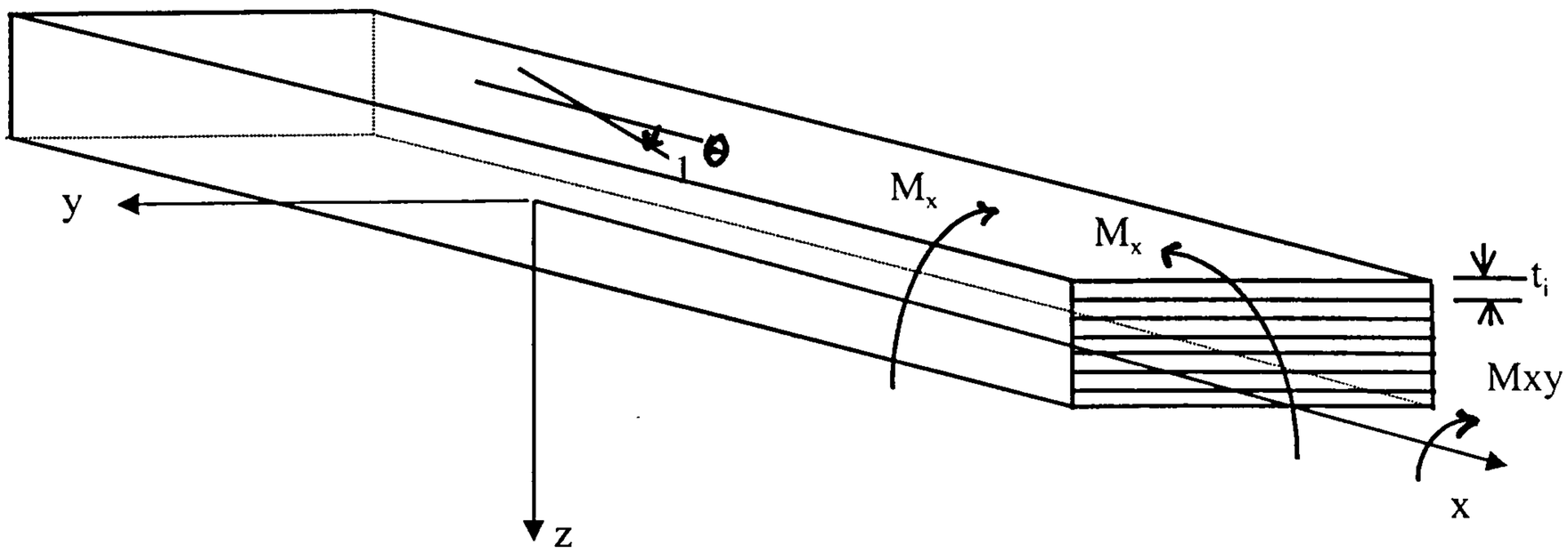

Fig. 3.4 Orientation of axes for beam structure.

(ii) THIN-WALLED BEAM ELEMENT:

Thin-walled composite cylindrical structure can be divided into two major categories, namely symmetric and anti-symmetric. In symmetric configuration, the ply lay-ups on opposite sides are mirror images with respect to the mid-axis. But in the case of anti-symmetric, the play lay-ups are opposite sign.

For a symmetric laminate, the B matrix will vanish, and the bending and longitudinal modes of deformation will uncouple.

Moreover, thin-walled beams can be divided in to closed and open sections. In this work, the stiffness estimation of the closed section will be discussed only as it is considered to be representative of the aircraft wing sections.

CLOSED SECTIONS:

(1.1) GENERAL CASE WITH ARIBITRARY CROSS-SECTION

There are different methods used in the analysis of a cylindrical tube subjected to different loading conditions. Some of these methods will be discussed as follows:

METHOD (1): This method was developed by [3.4]. In this method, a cylindrical tube subjected to torsion, bending and longitudinal tension using cylindrical coordinates system as shown in figure (3.5) and in the absence of circumferencial stresses and strains i.e. $N_{ys}=0$ and $\varepsilon_s=0$, equations (3.1) and (3.2):

$$\begin{Bmatrix} N_y \\ N_{ys} \end{Bmatrix} = \begin{bmatrix} A_{11} & A_{13} \\ A_{13} & A_{33} \end{bmatrix} \begin{Bmatrix} \varepsilon_y \\ \gamma_{ys} \end{Bmatrix}$$

or

$$\begin{Bmatrix} \varepsilon_y \\ \gamma_{ys} \end{Bmatrix} = \begin{bmatrix} A_{11} & A_{13} \\ A_{13} & A_{33} \end{bmatrix}^{-1} \begin{Bmatrix} N_y \\ N_{ys} \end{Bmatrix} = \begin{bmatrix} A^*_{11} & A^*_{13} \\ A^*_{13} & A^*_{33} \end{bmatrix} \begin{Bmatrix} N_y \\ N_{ys} \end{Bmatrix} \tag{3.9}$$

or

$$\begin{Bmatrix} N_y \\ N_{ys} \end{Bmatrix} = \begin{bmatrix} H_{11} = \dfrac{1}{A^*_{11}} & -H_{12} = \dfrac{A^*_{13}}{A^*_{11}} \\ H_{12} = \dfrac{A^*_{13}}{A^*_{11}} & H_{22} = A^*_{33} - \dfrac{A^{*2}_{13}}{A^*_{11}} \end{bmatrix} \begin{Bmatrix} \varepsilon_y \\ \gamma_{ys} \end{Bmatrix}$$

where

$$P = \varepsilon_o \oint H_{11} ds - N_{ys} \oint H_{21} ds \text{ = resultant tensile load P in the cylinder} \qquad (3.10)$$

similarly the bending moment about the x-axis is :

$$M_x = k_x \oint z^2 H_{11} ds - N_{ys} \oint z H_{21} ds \qquad (3.10.1)$$

and the chordwise moment about the z-axis is :

$$M_z = k_z \oint x^2 H_{11} ds + N_{ys} \oint x H_{21} ds \qquad (3.10.2)$$

Finally the resultant torque about the y-axis is :

$$M_y = 2 N_{ys} \oint P ds \qquad (3.10.3)$$

where $A = \oint P ds$ = cross-sectional area of the tube

P = perpendicular distance from the origin to the tangent at s.

combining equations (3.10) to (3.10.3) in a matrix form :

$$\begin{Bmatrix} \varepsilon_o \\ k_x \\ k_z \\ \tau \end{Bmatrix} = \begin{bmatrix} F_{11} & 0 & 0 & F_{14} \\ 0 & F_{22} & 0 & F_{24} \\ 0 & 0 & F_{33} & F_{34} \\ F_{14} & F_{24} & F_{34} & F_{44} \end{bmatrix} \begin{Bmatrix} P \\ M_x \\ M_z \\ M_y \end{Bmatrix} \qquad (3.10.4)$$

where

$$F_{11} = \frac{1}{\oint H_{11} ds} \quad , \quad F_{22} = \frac{1}{\oint z^2 H_{11} ds} \quad , \quad F_{34} = F_{43} = \frac{-\oint x H_{21} ds}{2A \oint x^2 H_{11} ds}$$

$$F_{14} = F_{41} = \frac{\oint H_{21} ds}{2A \oint H_{11} ds} \quad , \quad F_{24} = F_{42} = \frac{\oint z H_{21} ds}{2A \oint z^2 H_{11} ds} \quad , \quad F_{33} = \frac{1}{\oint x^2 H_{11} ds}$$

$$F_{44} = \frac{1}{4A^2} \left[\oint H_{22} ds + \frac{\left(\oint H_{21} ds \right)^2}{\oint H_{11} ds} + \frac{\oint \left(x H_{21} ds \right)^2}{\oint x^2 H_{11} ds} + \frac{\left(\oint z H_{21} ds \right)^2}{\oint z^2 H_{11} ds} \right]$$

Equation (3.10.4) gives the flexibility matrix for the general cylindrical tube under the applied torsion, longitudinal tension and bending forces. In the case of mirror-wise tubes, the equation (3.10.4) uncouples to give the stiffness matrix of a symmetrically laminated thin-walled structure with bending-torsional coupling.

$$\varepsilon_o = F_{11} P \quad , \quad k_z = F_{33} M_z \quad \text{and} \quad \begin{Bmatrix} k_x \\ \tau \end{Bmatrix} = \begin{bmatrix} F_{22} & F_{24} \\ F_{24} & F_{44} \end{bmatrix} \begin{Bmatrix} M_x \\ M_y \end{Bmatrix} \tag{3.10.5}$$

METHOD (2): An evaluation of the variationally consistent theory developed by [3.5] and [3.6]. The theory is applied to a beam with arbitrary closed cross-sections made of laminated composite materials. Two coordinate systems for the description of the state of stress in thin-walled beams. The first is the Cartesian system x, y and z. The second coordinate system is the curvilinear system x, s and ξ as shown in figure (3.6). In this method, both axial strain and bending related out of plane warping were identified in the developed theory in addition to the torsional related warping. The theoretical development of the method is presented in [3.6]. The global stiffness matrix of the beam with arbitrary closed cross-sections made composite materials is:

$$\begin{Bmatrix} T \\ M_x \\ M_y \\ M_z \end{Bmatrix} = \begin{bmatrix} C_{11} & C_{12} & C_{13} & C_{14} \\ C_{21} & C_{22} & C_{23} & C_{24} \\ C_{31} & C_{32} & C_{33} & C_{34} \\ C_{41} & C_{42} & C_{43} & C_{44} \end{bmatrix} \begin{Bmatrix} U_1' \\ \varphi' \\ U_3'' \\ U_2'' \end{Bmatrix} \tag{3.11}$$

where

$$C_{11} = \oint \left(A - \frac{B^2}{C} \right) ds + \frac{\left[\oint \left(\frac{B}{C} \right) ds \right]^2}{\oint \left(\frac{1}{C} \right) ds} \quad , \quad C_{33} = \oint \left(A - \frac{B^2}{C} \right) z^2 ds + \frac{\left[\oint \left(\frac{B}{C} \right) z ds \right]^2}{\oint \left(\frac{1}{C} \right) ds}$$

$$C_{44} = \oint \left(A - \frac{B^2}{C} \right) y^2 ds + \frac{\left[\oint \left(\frac{B}{C} \right) y ds \right]^2}{\oint \left(\frac{1}{C} \right) ds} \quad , \quad C_{13} = -\oint \left(A - \frac{B^2}{C} \right) z ds - \frac{\oint \left(\frac{B}{C} \right) ds \oint \left(\frac{B}{C} \right) z ds}{\oint \left(\frac{1}{C} \right) ds}$$

$$C_{14} = -\oint \left(A - \frac{B^2}{C} \right) y ds - \frac{\oint \left(\frac{B}{C} \right) ds \oint \left(\frac{B}{C} \right) y ds}{\oint \left(\frac{1}{C} \right) ds} \quad , \quad C_{22} = \frac{1}{\oint \left(\frac{1}{C} \right) ds} A^2{}_e$$

$$C_{34} = \oint \left(A - \frac{B^2}{C} \right) yz ds + \frac{\oint \left(\frac{B}{C} \right) y ds \oint \left(\frac{B}{C} \right) z ds}{\oint \left(\frac{1}{C} \right) ds} \quad , \quad C_{12} = \frac{\oint \left(\frac{B}{C} \right) ds}{\oint \left(\frac{1}{C} \right) ds} A_e$$

$$C_{23} = -\frac{\oint\left(\frac{B}{C}\right)zds}{\oint\left(\frac{1}{C}\right)ds}A_e \quad , \qquad C_{24} = -\frac{\oint\left(\frac{B}{C}\right)yds}{\oint\left(\frac{1}{C}\right)ds}A_e$$

where

$$A = A_{11} - \frac{A^2{}_{12}}{A_{22}} \quad , \qquad B = 2\left[A_{16} - \frac{A_{12}A_{26}}{A_{22}}\right] \quad , \qquad C = 4\left[A_{66} - \frac{A^2{}_{26}}{A_{22}}\right]$$

The above parameters A, B and C are defined in terms of the axial stiffness coefficients A_{ij} as shown in equation (3.3).

There are other methods, which are deals with the same structural configuration as the above theories. One of these methods developed by [3.7].

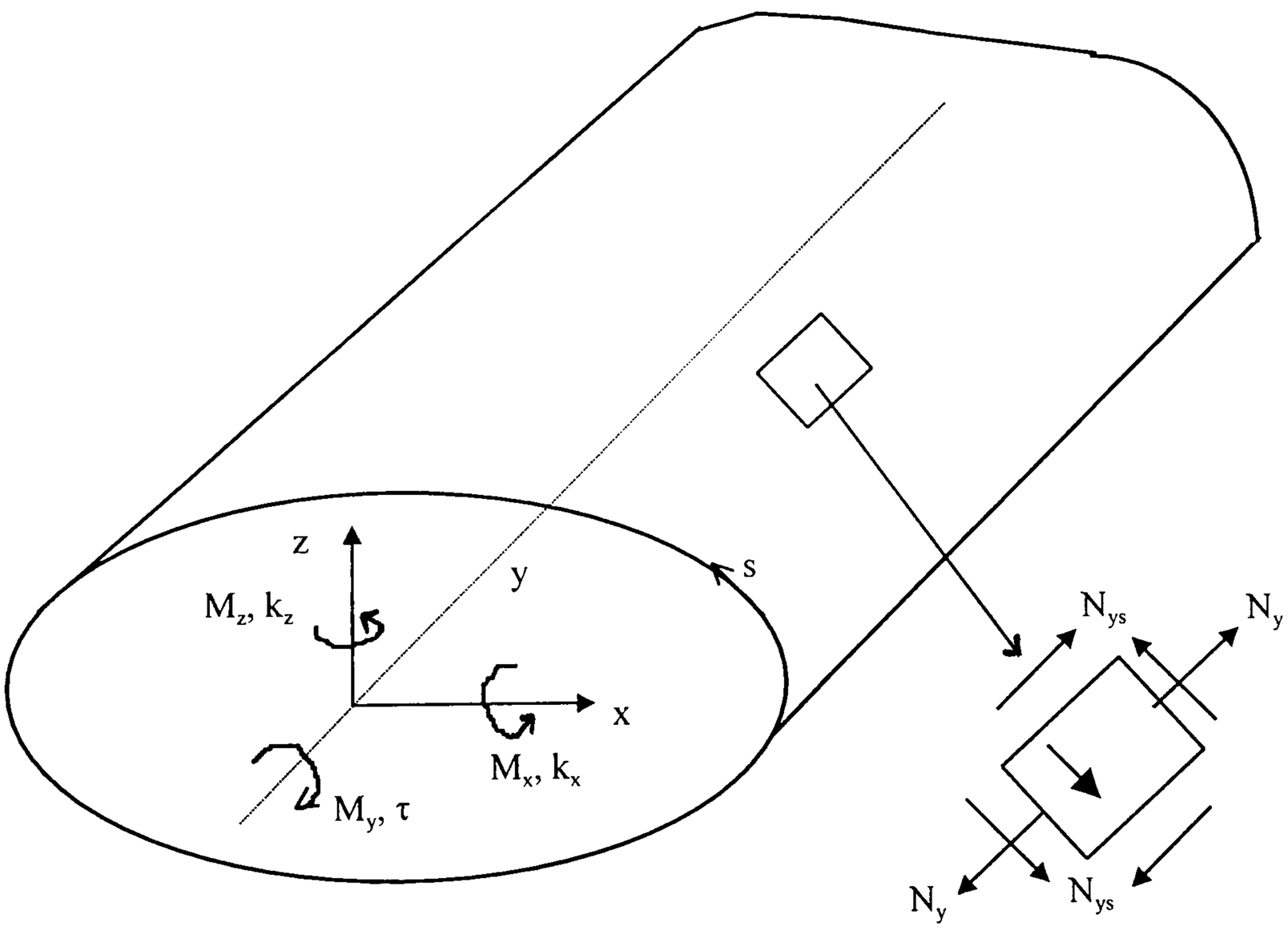

Fig. 3.5 The cylindrical tube coordinate system

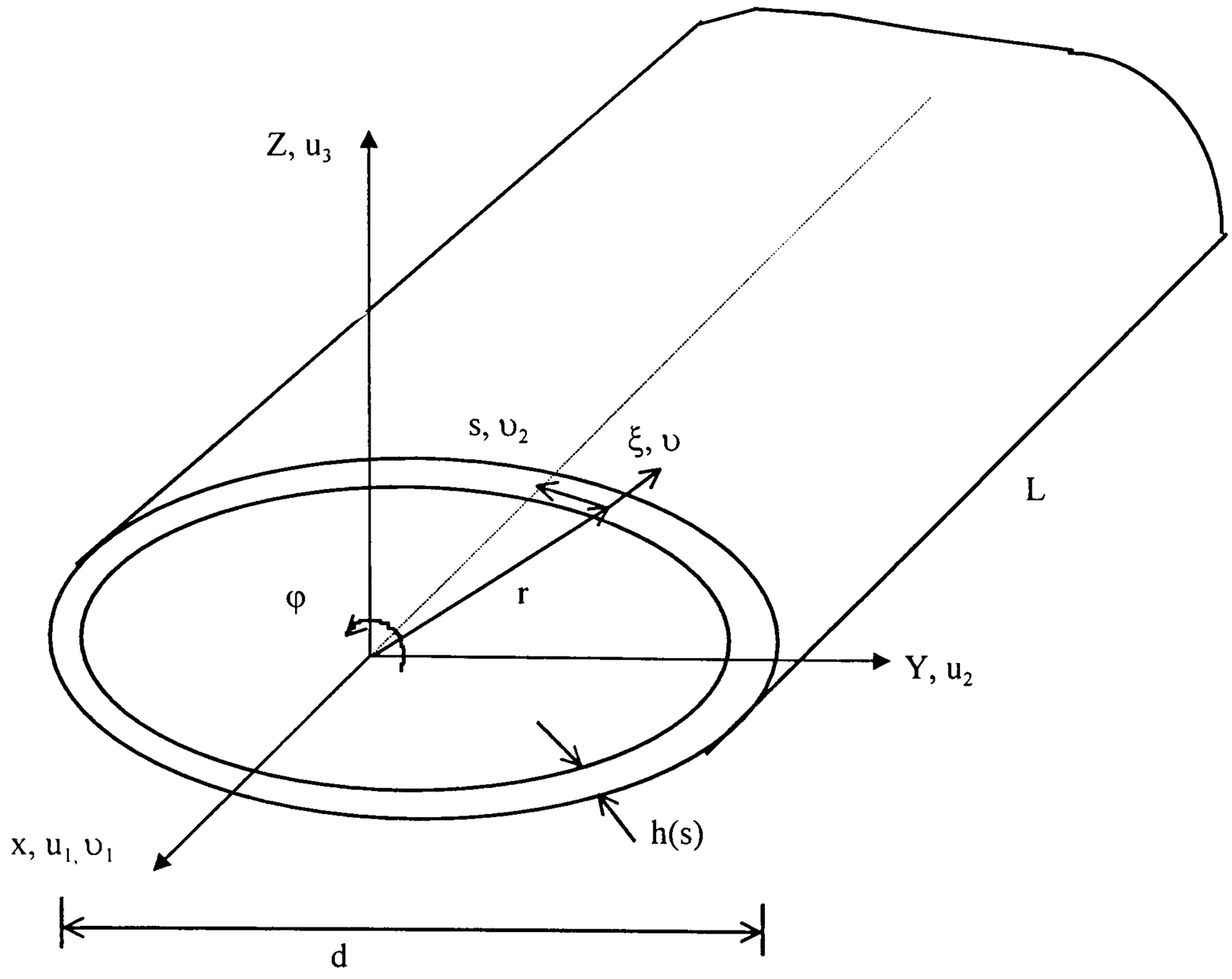

Fig. 3.6 Cylindrical shell coordinate system

(1.2) BOX BEAM CROSS SECTION:

A similar analysis for the prediction of stiffnesses applicable to box beam structure has been developed by [3.8]. The circumferencial strain are not assumed to be zero as compared with [3.4]. The x and y axes are aligned with the spanwise and chordwise axes of the structure respectively. The deformed structure is represented by the orthogonal coordinate system ξ, ζ and η as shown in figure (3.7) and given in [3.9]. By using the stress-strain relationship which given in equation (3) and with assuming that $\sigma_{xx} = \sigma_{\xi\xi}$, $\sigma_{x\eta} = \sigma_{\xi\eta}$, and $\sigma_{x\zeta} = \sigma_{\xi\zeta}$ and the similar assumption for strain was made. The stress-strain relationship for the top flanges of the box beam shown in figure (3.8) is given by the following expression:

$$\begin{Bmatrix} \sigma_{\xi\xi} \\ \sigma_{\eta\eta} \\ \tau_{\xi\eta} \end{Bmatrix} = \begin{bmatrix} \overline{Q}_{11} & \overline{Q}_{12} & \overline{Q}_{16} \\ \overline{Q}_{21} & \overline{Q}_{22} & \overline{Q}_{26} \\ \overline{Q}_{16} & \overline{Q}_{26} & \overline{Q}_{66} \end{bmatrix} \begin{Bmatrix} \varepsilon_{\xi\xi} \\ \varepsilon_{\eta\eta} \\ \gamma_{\xi\eta} \end{Bmatrix} \tag{3.12}$$

where $\overline{Q}$ = transformed reduced stiffness matrix of the kth lamina in the (ξ-η) or (ξ-ζ) plane. Since $\sigma_{\eta\eta}$=0, equation (3.12) can be simplified by solving for $\varepsilon_{\eta\eta}$ as shown below:

$$\begin{Bmatrix} \sigma_{\xi\xi} \\ \tau_{\xi\eta} \end{Bmatrix} = \begin{bmatrix} \overline{C}_{11} & \overline{C}_{16} \\ \overline{C}_{16} & \overline{C}_{66} \end{bmatrix} \begin{Bmatrix} \varepsilon_{\xi\xi} \\ \gamma_{\xi\eta} \end{Bmatrix} \tag{3.13}$$

where

$$\overline{C}_{11} = \overline{Q}_{11} - \frac{\overline{Q}^2{}_{12}}{\overline{Q}_{22}} \quad , \qquad \overline{C}_{16} = \overline{Q}_{16} - \frac{\overline{Q}_{12}\overline{Q}_{26}}{\overline{Q}_{22}} \quad , \qquad \overline{C}_{66} = \overline{Q}_{66} - \frac{\overline{Q}^2{}_{26}}{\overline{Q}_{22}}$$

Similarly for left and right sides with $\sigma_{\zeta\zeta}$= 0, the following relation can be obtained:

$$\begin{Bmatrix} \sigma_{\xi\xi} \\ \tau_{\xi\zeta} \end{Bmatrix} = \begin{bmatrix} \overline{C}_{11} & \overline{C}_{16} \\ \overline{C}_{16} & \overline{C}_{66} \end{bmatrix} \begin{Bmatrix} \varepsilon_{\xi\xi} \\ \gamma_{\xi\zeta} \end{Bmatrix} \tag{3.14}$$

A simplified linear analysis is presented for bending and torsion of thin-walled composite structure based on the coupling non-linear analysis presented in [3.9] for a composite helicopter rotor blade subjected to flap bending, lag bending, elastic twist and axial deflection.

$$\begin{Bmatrix} M \\ T \end{Bmatrix} = \begin{bmatrix} EI & K \\ K & GJ \end{bmatrix} \begin{Bmatrix} w'' \\ \phi' \end{Bmatrix}$$

Where

$$EI = \sum_{k=1}^{N} \iint_{1,2} \overline{C}_{11}{}^{(k)} \zeta^2 d\eta d\zeta + \sum_{l=1}^{M} \iint_{3,4} \overline{C}_{11}{}^{(k)} \zeta^2 d\eta d\zeta \tag{3.15}$$

$$GJ = \sum_{k=1}^{N} \iint_{,2} \overline{C}_{66}{}^{(k)} \hat{\zeta}^2 d\eta d\zeta + \sum_{l=1}^{M} \iint_{3,4} \overline{C}_{66}{}^{(k)} \hat{\eta}^2 d\eta d\zeta \tag{3.16}$$

$$K = \sum_{k=1}^{N} \iint_{,2} \overline{C}_{16}{}^{(k)} \hat{\zeta}\zeta d\eta d\zeta \tag{3.17}$$

Subscripts 1,2 respectively represent the top and bottom laminates of the box beam and 3,4 respectively represent the left and right side of the laminates of the box beam.

N = number of layers in laminate 1 or 2

M = number of layers in laminate 3 or 4

η, ζ = coordinates in the plane of the cross section

$$\hat{\zeta} = \zeta + \lambda, \eta \quad , \qquad \hat{\eta} = \eta - \lambda, \zeta$$

Where λ is the warping function given in approximate manner in [3.8] as,

βζη

$$\beta = \frac{(c-d)}{(c+d)}$$

Where c and d are the beam width and depth respectively.

There are other methods developed for the analysis of box composite beam cross-section. Some of these methods were developed by [3.10] and [3.11] as examples.

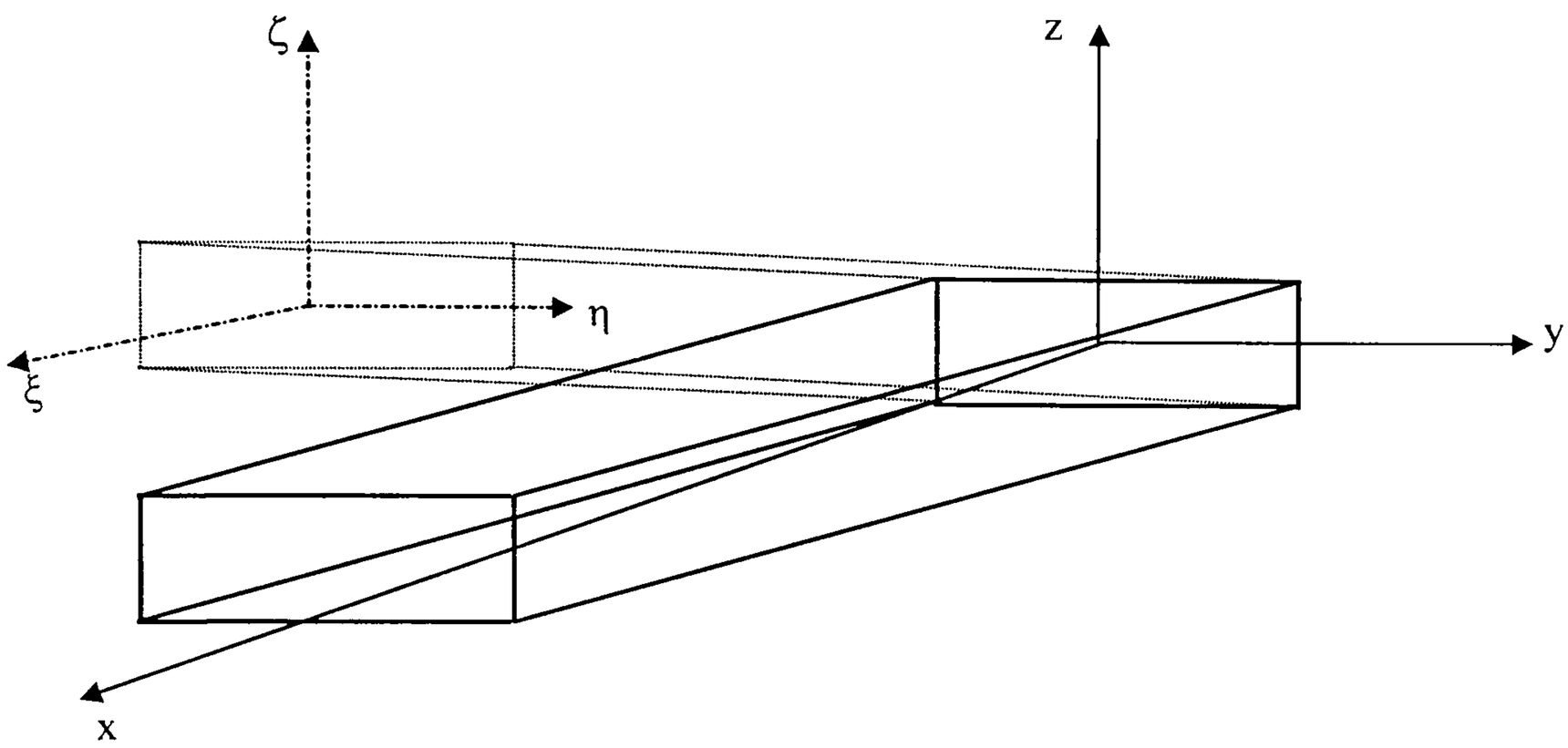

Fig. 3.7 Box beam coordinate system

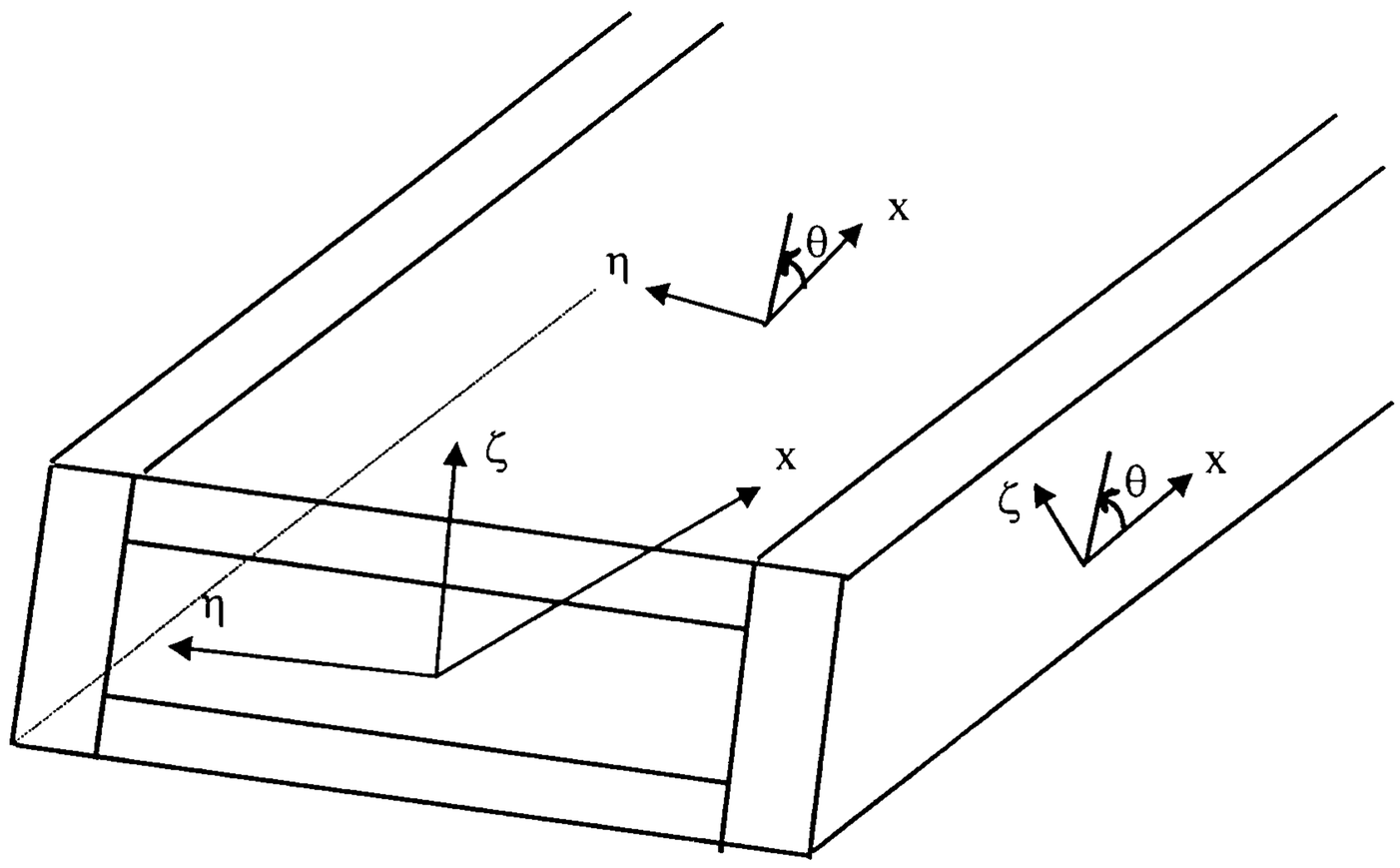

Fig. 3.8 Ply angle with reference axis

References

3.1 Tasi, S.W. and Hahn, H.T., *Introduction to composite materials*, Technomic, CT. 1980.

3.2 Jones, R.M., *Mechanics of composite materials*, Hemispher, 1975

3.3 Reddy, J.N., *Mechanics of laminated composite plates theory and analysis*, CRC, 1997.

3.4 Mansfield, E.H. and Sobey, A.J. The fibre composite helicopter blade, part 1stiffness properties, part 2 : prospects for aeroelastic tailoring, Aeronautical quarterly, May 1979,pp. 413-449.

3.5 Armanios, E.A. and Badir A.M. Free vibration analysis of anistropic thin-walled closed-section beams. AIAA-94-1327-CP, pp 164-171.

3.6 Badir, A.M. Analysis of advanced thin-walled composite structures. PhD thesis, Georgia Institute of Technology, February, 1992.

3.7 Librescu, L., Meirovitch, L. and Song, O. Refined structural modelling for enhancing vibrational and aeroelastic characteristics of composite aircraft wings. La Recherche Aerospatiale, 1996, no. 1, pp 23-35.

3.8 Chandara, R., Stemple, A.D. and Chopra, I. Thin-walled composite beams under bending, torsional, and extensional loads. Journal of Aircraft, July 1990, Vol. 27, No. 7, pp 619-626.

3.9 Hong, Chang-Ho and Chopra, I. Aeroelastic stability analysis of a composite rotor blade. Journal of the American Helicopter Society, April 1985, Vol. 30, No. 2, pp 57-67.

3.10 Smith, E.C. and Chopra, I. Formulation and evaluation of an analytical model for composite box-beams. Journal of the American Helicopter Society, July 1991, Vol. 28, No. 3, pp 23-35.

3.11 Weisshaar, T.A. Aeroelastic tailoring of forward swept composite wings. Journal of Aircraft, August 1981, Vol. 18, No. 8, pp 669-676.

CHAPTER 4

FINITE ELEMENT APPROACH USED IN MSC/NASTRAN

4. Finite element approach used in MSC/NASTRAN:

4.1 Introduction:

MSC/NASTRAN is a computer program for structural analysis that is based on the finite element method. It is an advanced version of the NASTRAN program that was developed under the sponsorship of the National Aeronautics and space administration (NASA). The NASTRAN development, which was based on the requirements of aerospace industry, began in 1966. The name of NASTRAN is derived from NASA STRuctural Analysis. The MacNeal-Schwendler Corporation (MSC) was involved with NASTRAN from the beginning, and MSC has been marketing their own advanced version, MSC/NASTRAN, since 1972. This undertaking involved the extension of the program to provide for the needs of general industry and the maintenance of these many extensions in capability and performance. MSC/NASTRAN, are the worlds most comprehensive and a large-scale general purpose digital program, which solves a wide variety of engineering problems by the finite element method. The program uses a finite element structural model, wherein the distributed physical properties of a structure are represented by a finite number of structural elements which are interconnected at a finite number of grid points to which the loads are applied and for which the displacements are calculated. The program capabilities including linear and non linear static and dynamic structural analysis, aeroelasticity, design sensitivity and optimization, heat transfer, acoustics, electromagnetism and other types of field problems.

MSC/NASTRAN element library offers an extensive variety of general purpose and specialty finite elements. The elements including the one, two and three-dimensional elements, scalar elements, axisymmetric elements, rigid elements, mass and damping elements, and fluid elements. Many of these elements may also be used in heat transfer analysis as well as structural analysis. The materials represented by finite elements may be linear or nonlinear, isotropic or anisotropic, and they may be temperature dependent.

In this chapter, a brief account of the normal mode analysis and the flutter solutions analysis and the methods provided by MSC/NASTRAN for performing the

analysis is presented. For comprehensive details, the reader should refer to MSC/NASTRAN documents [4.1] and [4.3].

4.2 Normal mode analysis:

Normal mode analysis is the calculation of the natural frequencies and mode shapes of the structure with damping neglected. The natural frequencies of the structure are the frequencies at which the structure naturally tends to vibrate if it is subjected to a disturbance. The mode shape is the deformed shape of the structure at a specific natural frequency of vibration. Natural frequencies and mode shapes are functions of the structural properties and boundary conditions.

The solution of the equation of motion for natural frequencies and mode shapes requires a special reduced form of the equation of motion. If there is no damping and no applied loading, the equation of motion in matrix form reduced to

$$[M]\{\ddot{U}\}+[K]\{U\}=0$$

Where $[M]$ is the mass matrix

$[K]$ is the stiffness matrix

MSC/NASTRAN offers seven methods of real eigenvalue extraction in order to solve the wide variety of problems arising in finite element analysis applications. These methods are numerical approaches to solving for natural frequencies and mode shapes.

In structural analysis, the representation of stiffness and mass in the eigenequation result in the physical representations of natural frequencies and mode shapes. Therefore, the eigenequation is written in terms of stiffness matrix and mass matrix. The equation of the normal mode analysis is of form:

$$([K]-\lambda[M])\{X\}=0 \qquad \text{where} \quad \lambda=\omega^2$$

The methods of eigenvalue extraction belong to one or both of the following two groups [4.1]:

- Transformation methods.
- Tracking methods.

In the transformation method, the eigenvalue equation is first transformed into a special form which eigenvalues may easily be extracted, while in the tracking method, the eigenvalues are extracted one at a time using an iterative procedure [4.1].

Four of the real eigenvalue extraction methods available in MSC/NASTRAN are transformation methods. These methods are:

- Givens method
- Householder method
- Modified Givens method
- Modified Householder method

Two of the real eigenvalue extraction methods available in MSC/NASTRAN are classified as tracking methods. These methods are:

- Inverse power method
- Sturm modified inverse power method

The last and the recommended eigenvalue extraction MSC/NASTRAN is the Lanczos method. The Lanczos method combines the best characteristics of both the tracking and transformation methods. This is an efficient method, and does not miss roots and computes accurate eigenvalues and eigenvectors. It is the recommended method for most medium-to large sized problems [4.1]. Comparison of eigenvalue methods provided in MSC/NASTRAN is presented in table (4.1). The solution number 103 can be used in the executive control section in the input data file for conducting a normal mode analysis. The set identification number specified by the METHOD case control command refers to the set identification number of an EIGR or EIGRL entry in the bulk data section of the input data file. The EIGR entry is used to select the modal extraction parameters for the Givens; Householder, Modified Givens, Modified Householder, Inverse power, and Sturm modified inverse power methods. The EIGRL entry is used to select the modal extraction parameters for the Lanczos method.

The detailed information about the theory and the algorithms behind each method can be found in [4.2].

Table (4.1) Comparison of Eigenvalue Methods.

	Method				
	Givens, Householder	Modified Givens, Householder	Inverse Power	Sturm Modified Inverse Power	Lanczos
Reliability	High	High	Poor (can miss modes)	High	High
Relative Cost: Few modes Many Modes	 Medium High	 Medium High	 Low High	 Low High	 Medium Medium
Limitations	Cannot analyse singular [M] Expensive for problems that do not fit in memory	Expensive for many modes Expensive for problems that do not fit in memory	Can miss modes Expensive for many modes	Expensive for many modes	Difficulty with massless mechanism
Best Application	Small, dense matrices that fit in memory Use with Dynamic Reduction	Small, dense matrices that fit in memory Use with Dynamic Reduction	To determine a few modes	To determine a few modes Backup method	Medium to large models

4.3 Flutter analysis:

4.3.1 Aerodynamic influence coefficients:

In MSC/NASTRAN, there are six aerodynamic theories used to create the aerodynamic finite elements and hence the aerodynamic influence coefficients. There are three matrix equations summarize the relationships required to define a set of aerodynamic influence coefficients. These are the basic relationships between the lifting pressure and the dimensionless vertical or normal velocity induced by the inclination of the surface to the airstream; i.e., the downwash (or normal wash),

$$\{W_j\} = [A_{jj}]\left\{\frac{f_j}{\bar{q}}\right\} \tag{4.1}$$

The substantial differential matrix of the deflections to obtain downwash,

$$\{W_j\} = [D^1_{jk} + ikD^2_{jk}]\{U_k\} + \{W^g_j \tag{4.2}$$

and the integration of the pressure to obtain forces and moments [4.3-4.4],

$$\{P_k\} = [S_{kj}]\{f_j\} \tag{4.3}$$

where

W_j = downwash (dimensionless)

W^g_j = static aerodynamic downwash; it includes, primarity, the static incidence distribution that may arise from an initial angle of attack, camber, or twist

f_j = pressure on lifting element j

$\bar{q}$ = flight dynamic pressure

k = reduced frequency, $k = \frac{\omega \times b}{v}$, where ω is the angular frequency, b is the reference semicord, and v is the free - stream velocity

$A_{jj}(m, K)$ = aerodynamic influence coefficient matrix, a function of Mach number (m), and reduced frequency (k)

U_k, P_k = displacements and forces at aerodynamic grid points

D^1_{jk}, D^2_{jk} = real and imaginary parts of substantial differentiation matrix, respectively (dimensionless)

S_{kj} = integration matrix

The three matrices of equation (4.1), (4.2), and (4.3) can be combined to give an aerodynamic influence coefficient matrix [4.3]:

$$[Q_{kk}] = [S_{kj}][A_{jj}]^{-1}[D^1_{jk} + ikD^2_{jk}] \tag{4.4}$$

All the aerodynamic methods compute the S, D^1, and D^2 matrices at user-supplied Mach numbers and reduced frequencies. The Doublet-Lattice and ZONA51 theories compute the A matrix. Then, matrix decomposition and forward and backward substitution are used in the computation of the Q matrix. The remaining methods compute A^{-1} directly and use matrix multiplication's to form Q.

4.3.2 Aerodynamic Theories:

In MSC/NASTRAN, there are six aerodynamic methods used in the modeling and calculations of the aerodynamic influence coefficients and the generalized aerodynamic forces. These methods are:

- Doublet-Lattice subsonic lifting surface theory (DLM)
- ZONA51 supersonic lifting surface theory
- Subsonic wing-body interference theory (DLM with slender bodies)
- Mach Box method
- Strip theory
- Piston theory

In this section, brief description of the DLM is described in this section and for detailed description of the other methods refers to [4.3] and [4.4].

The theoretical basis of the DLM is linearized aerodynamic potential theory. The undisturbed flow is uniform and is either steady or varying (gusting) harmonically. All the lifting surface is assumed to lie nearly parallel to the flow. This method (DLM) is an extension of the steady Vortex-Lattice method to unsteady flow. Each of the interfering surfaces (or panels) is divided into small trapezoidal lifting elements (boxes) such that the boxes are arranged in strips parallel to the free stream with surface edges, fold lines, and hinge lines lying on box boundaries as shown in figure (4.1). The unknown lifting pressures are assumed to be concentrated uniformly across the one-quarter chord of each box.

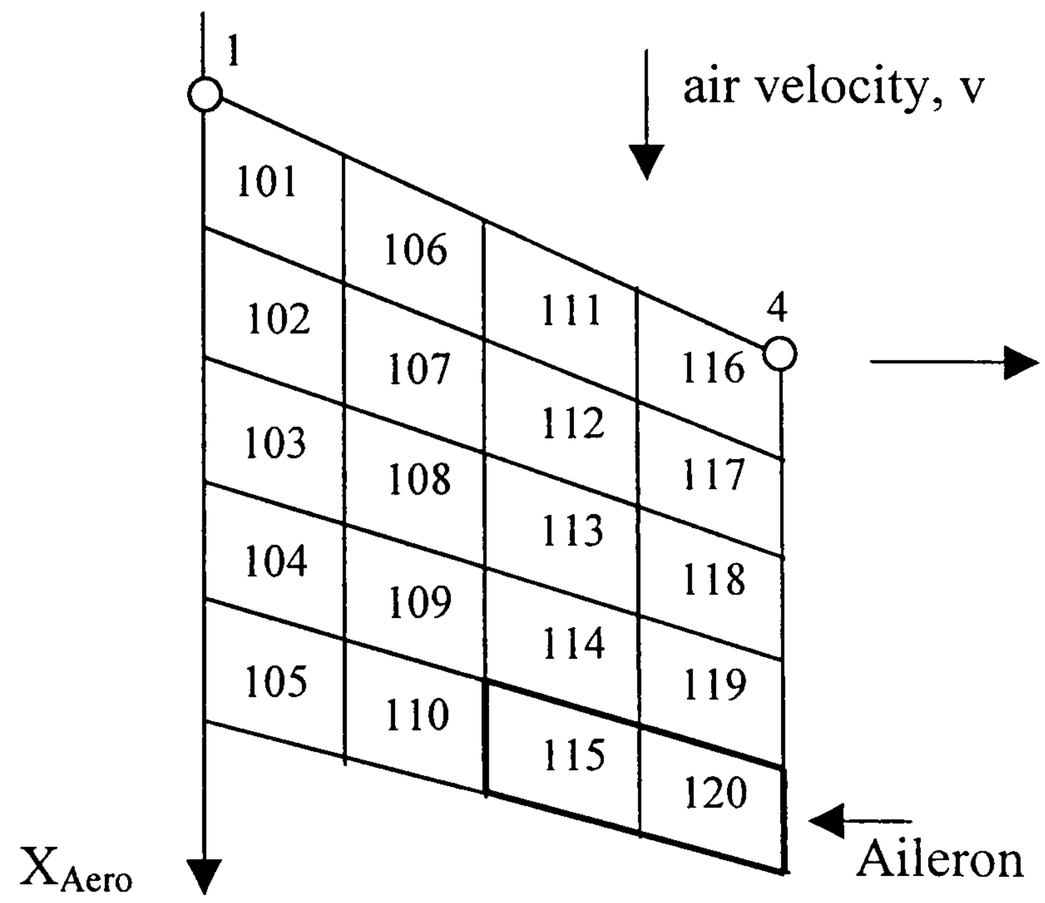

Fig. 4.1 An aerodynamic Doublet-Lattice Panel subdivided into boxes.

There is one control point per box, centered spanwise on the three-quarter chord line of the box, and the surface normal downwash boundary condition is satisfied at each of these points. If a surface lies in (or nearly in) the wake of another surface, then its spanwise divisions should lie along the division of the upstream surface. The aspect ratio of the boxes should be approximate unity; less than three is acceptable in the subsonic case and no less than four boxes per chord should be used. The chord lengths of adjacent boxes in the streamwise direction should change gradually. Aerodynamic panels are assigned to interference groups. All panels within a group have aerodynamic interaction. The purpose of the groups is to reduce the computational effort for aerodynamic matrices when it is known that aerodynamic interference is important within the group but otherwise is negligible or to allow the analyst to investigate the effects of aerodynamic interference. The Aerodynamic elements in MSC/NASTRAN are presented in table (4.2). The description of each panel with the flight conditions were presented in appendix A through the use of CAER01, PAERO1, AERO and MKAERO1 bulk data entries for the DLM. The theory of the DLM is presented in [4.5, 4.6, and 4.7] and will not present here.

Table (4.2) Aerodynamic elements used in MSC/NASTRAN.

	Aerodynamic Theory					
Attribute	Doublet-Lattice panel	Lifting Body (Interference)	ZONA51 Panel	Mach Box Surface	Strip Theory	Piston Theory
Bulk Data Entries	CAER01 PAER01	CAER02 PAER02	CAER01 PAER01	CAER03 PAER03	CAER04 PAER04	CAER05 PAER05
Mach Number	Subsonic	Subsonic	Supersonic	Supersonic	All	High Supersonic
Symmetry Options	Two Planes Y=0 Z=0	Two Planes Y=0 Z=0	One Planes Y=0	One Plane Required	None	None
Interaction	Panels and Bodes in the Same Group		Panels in the Same Group	Boxes on one Surface	None	None
Interconnection to Structure	Box centers	Slender Body centers	Box Centers	User Specified Locations	Strip 1/4-Chord	Strip 1/4-Chord
Displacement Components used at Connection Points	3,5	3,5 Z-Bodies 2,6 Y-Bodies	3,5	3,5	3,5 and 6 for Control	3,5 and 6 for Control

4.3.3 Interpolation methods:

Structural and aerodynamic grids are connected by interpolation. This allows the independent selection of grid points of the structure and aerodynamic elements of the lifting surfaces/bodies in a manner best suited to the particular theory. The structural model for a wing may involve a one, two or three-dimensional array of grid points. The aerodynamic theory may be a lifting surface theory or a strip theory. A general interpolation method is available that will interconnect the various combinations. Any aerodynamic panel or body can be subdivided into subregions for interpolation, using separate function for each.

The interpolation method is called splining. The theory involves the mathematical analysis of beams and plats. Three methods are available in MSC/NASTRAN [4.3-4.4]:

- Linear splines, which are a generalization of an infinite beam and allow torsional as well as bending degrees of freedom
- Surface splines, which are solutions for an infinite uniform plates
- An explicit user-defined interpolation

Several splines, including combinations of the three types, can be used in one model. The structural degrees of freedom have been chosen in MSC/NASTRAN as the independent degree of freedom; the aerodynamic degrees of freedom are dependent. A matrix form that relates the dependent degrees of freedom to the independent ones. The structural degree of freedom may include any grid components. Two transformations are required: the interpolation from the structural deflections to the aerodynamic deflections and the structurally equivalent forces acting on the structural grid points. The derivation of elements of the interpolation matrix for the above methods is presented in [4.3-4.4].

4.3.4 Flutter solution techniques:

Flutter is the dynamic aeroelastic stability problem. It may be solved in any speed regime; this is by selecting the appropriate aerodynamic method. Three different flutter solutions techniques were provided in MSC/NASTRAN. These techniques are:

- The American K-method of Flutter Solution
- The American KE-method of Flutter Solution
- The British PK-method of Flutter Solution

Comparisons between the three methods are shown in table (4.3). The main advantages of the PK method was that the it produces results directly for a given values of velocity, where as the American methods require iteration to determine the reduced frequency of flutter and that the damping values obtained at subcritical flutter conditions appear to be more representative of the physical damping [4.3]. Therefore, the PK method was selected to calculate the flutter speed and frequency in this research. The Pk method of flutter analysis follows the "lined-up" British method as described in refs. [4.8-4.9]. A brief description of the PK method is presented below and for comprehensive details see [4.3]

4.3.4.1 The PK-method of Flutter Solution:

The fundamental equation for modal flutter analysis by the PK method is

$$\left[M_{hh}P^2+\left(B_{hh}-\frac{1}{4}\times\frac{\rho\,\bar{c}\,V\,Q^{I}{}_{hh}}{k}\right)P+\left(k_{hh}-\frac{1}{2}\times\rho\,V^2\,Q^{R}{}_{hh}\right)\right]\{u_h\}=0$$

Where

M_{hh} = modal mass matrix

B_{hh} = modal damping matrix. An equivalent viscous structural damping matrix is usually diagonal.

k_{hh} = modal structural stiffness matrix.

$Q^{I}{}_{hh}$ = modal aerodynamic damping matrix, a function of reduced frequency, k and Mach numbers, m

$Q^{R}{}_{hh}$ = modal aerodynamic stiffness matrix, a function of reduced frequency, k and Mach numbers, m

P = $\omega(\gamma \pm i)$

ω = circular frequency

γ = transient decay rate coefficient

ρ = density

V = Velocity

$\bar{c}$ = reference chord

k = reduced frequency

u_h = modal amplitude vector

The matrix terms in the equation above are all real. Q^R_{hh} and Q^I_{hh} are respectively the real and imaginary parts of Q_{hh} (m,k). An appropriate root finding algorithm is used, see ref. [4.3]. With specifying the flight conditions of mach no., density ratio on the outer loops and the velocities of interest on the inner loop. The output of the PK method will provide a summary of the variation of the induced frequency (k) and the velocities with damping and frequencies for each structural modes and from there the flutter speed identified with the zero damping (damping sign change from negative to positive). The plots of the frequency and damping versus velocity may be requested in the case control of the MSC/NASTRAN.

Table (4.3) Features of Flutter analysis methods used in MSC/NASTRAN.

Feature	Method		
	American K-method	American KE-method	British PK-method
Structural Matrices	K (complex)	K (complex)	K (real)
	B (complex)		B (real)
	M (complex)	M (complex)	M (real)
Aerodynamic Matrices	M (complex)	M (complex)	K (real)
			B (real)
User Input Loops	ρ– Density	ρ– Density	ρ– Density
	m- Mach Number	m- Mach Number	m- Mach Number
	k- Reduced	k- Reduced	v - Velocity
	Frequency	Frequency	
Output	V-g Curves	V-g Curves	V-g Curves
	Complex Modes		Complex Modes
	Displacements		Displacements
	Deformed Plots		Deformed Plots
Method	Computes roots for user input ρ, m, k	Computes roots for user input ρ, m, k	For each ρ, m, v
		Reorder output so	Iterate on each
		a "curve" refers to	root to find
		a Mode	consistent results
Eigenvalue Method	Several methods	Complex upper*	Real upper*
	available, selected	Hessenberg	Hessenberg
	by user via CMETHOD		
	in case control		

*No CMETHOD entry is used

References

4.1 Blakely, K. "MSC/NASTRAN Basic Dynamic analysis user's guide, V68" The MacNeal-Schwendler Corporation.

4.2 Komzsik, L. "MSC/NASTRAN Numerical Methods user's guide, V70.5, Chapter 6" The MacNeal-Schwendler Corporation.

4.3 Rodden, W. P. and Johnson, E. H. "MSC/NASTRAN Aeroelastic analysis user's guide, V68" The MacNeal-Schwendler Corporation.

4.4 Rodden, W. P., Harder, R. L. and Bellinger E. D. "Aeroelastic addition to MSC/NASTRAN" NASA CR 3094.

4.5 Albano, E., and Rodden, W.P., "Adoublet-Lattice Method for Calculating Lift distributions on Oscillating Surfaces in Subsonic Flows" AIAA Journal, Vol. 7, No. 2, 1969 and No. 11, 1969.

4.6 Rodden, W. P., Giesing, J. P. and Kalman. T. P. "Refinement of the Nonplanar aspects of the Subsonic Doublet-Lattice Surface Method" Journal of Aircraft, Vol. 9, No. 1, 1972

4.7 Giesing, J. P., Kalman. T. P. and Rodden, W. P. "Subsonic Unsteady Aerodynamics for General Configurations; Part I, Vol. I – Direct application of the Nonplanar Doublet-Lattice Method" Air Force Flight Dynamics Laboratory Report No. AFFDL-Tr-71-5, Part I, Vol. I, 1971.

4.8 Lawrence, A. J. and Jackson, P. "Comparison of Different Methods of Assessing the Free Oscillatory Characteristics of Aeroelastic System" British Aeronautical Research Council, ACR C. P. No. 1084, 1970.

4.9 Woodcock, D. L. and Lawrence, A. J. "Further Comparisons of Different Methods of Assessing the Free Oscillatory Characteristics of Aeroelastic System" Royal Aircraft Establishment, TR No. 72188, 1972.

CHAPTER 5

EXPERIMENTAL ANALYSIS OF THE CRANFIELD-A1 COMPOSITE WING BOX

5 Experimental analysis of the Cranfield A1 composite wing box.

5.1 Introduction:

Modern light aircraft are required to fly in different manner during the flight (i.e. steady and maneuver flight). If the test or a theoretical dynamic analysis does not considered the vibration characteristics of the structure, then that could lead to a significantly reduced fatigue life of the aircraft and to flutter speed to occur within the desired operational envelope of the aircraft. Therefore, the vibration analysis is an important first step in the design of the aircraft structure and in the calculation the flutter speed. For this purpose the vibration test was done for the composite wing box of the Cranfield A1 aerobatic aircraft. Also it is gaining experience via this practical approach in setting up the wing, proper locations of accelerometers and exciter, retrieval and understanding of the data and some other aspects presented in the papers which were prepared by the author of this thesis and presented by the supervisor [5.6-5.8]. The vibration characteristics obtained will be compared with the finite element model and then using the vibration characteristics obtained from the finite element model for further investigation on the flutter characteristics of the wing box.

The composite wing box was constructed from carbon fibre reinforced plastic (CFRP) and is representative of a real Cranfield A1 composite wing box for studying the post buckling behaviour of the wing box [5.1]. The wing box root was attached to the large thick wall made from concrete. This is done to simulate the cantilevered boundary condition. The wing box was excited using random and sinusoidal excitation methods under the frequency range from 0-300 Hz. A total of five test locations were conducted in order to measure the response of the entire wing box. The frequency, gain, mode shapes and structural damping were calculated and identified using a computer program analyzer provided by Cranfield university environmental sciences group.

The structural mode shapes were plotted using UNIMAP 2000 software installed in the Unix machines in the college of aeronautics as shown in figures (5.9-5.14).

5.2 Description of the Composite Wing box:

The composite wing box, which represented the A1 Cranfield aerobatic aircraft was made from Carbon fibre reinforced plastic and was constructed for the study of the post buckling behavior of the wing box. The structure of the wing box was consisted of a front spar and rear spar, tip rib, (seven) intermediate ribs positioned between the wing root and tip of the wing box, stringers and top and bottom skins. The spars, stringers made from hat section along the semi-span and the two ribs, which are located at 1981 mm and 3706 mm from the aircraft center line are filled with the form. Some strain gauge wires were left attached to the web of the ribs and the top skin since the post buckling tests conducted on the wing box. The wires passed through the four holes made in the web of the rear spar of the wing box. The airfoil section of the wing box at the root was NACA 23015 and at the tip was NACA 23012. The approximate dimension of the tested wing box are Semi-span of 4050 mm (up to the last rib at 4281 mm from the aircraft center line), 812 mm root chord, 369 mm tip chord. For more information, the reader should refer to [5.1] where a comprehensive discussion is conducted.

5.3 Modal analysis equipment and requirements:

The initial step in undertaking a modal analysis test is to have a clear set of objectives in order that suitable testing equipment may be selected that will maximize the desired output [5.2].

Choosing the location and the appropriate form of support for the test structure is an important criterion. Normally, one of two support conditions is used, either free or grounded. A free support means that the structure is not attached in any way to the ground and thus, in effect, freely suspended in space [5.3]. In practice, of course, it is not possible to achieve a truly free condition; however, it is feasible to provide a suspension system that closely approximates it [5.2 and 5.3]. This can be achieved by supporting the structure on a soft springs, such as might be provided by elastic bands, so that the rigid body mode is significantly less than the lower bending mode [5.2 and 5.3].

Theoretically, a freely supported structure would have six rigid body modes, each with a natural frequency of 0 Hz. A precaution that may be taken to minimize any distortion in the fundamental bending mode is to suspend the structure from as close as possible to the nodal points of that particular mode [5.2].

A grounded support occurs when the structure is taken to be fixed rigidly to the support structure. Although this condition is easy to model theoretically, it is much more difficult to implement in the practical case because it is very difficult to provide a base or foundation on which to attach the test structure which is sufficiently rigid to provide the necessary grounding [5.2 and 5.3].

In a grounded case, care must be taken to ensure that no local stiffening or other distortion is introduced by the attachment other than that which is an integral part of the structure itself.

Various devices are available for exciting the structure and several of these are widespread use. Basically, they can be divided into two types [5.2 and 5.3]:

1. Contacting and.
2. Non-contacting.

The first type involves the connection of an exciter of some form which remains attached to the structure throughout the test, whether the excitation type is continuous (sinusoidal, random, etc.) or transient (pulse, chirp).

The second type includes devices which are either out of contact throughout the vibration (such as provided by a non-contacting electromagnet) or which are only in contact for a short period of time, while the excitation is being applied (such as a hammer blow).

There are three different forms of excitation available, mechanical, electromagnetic and electrohydraulic. Of these, the electromagnetic type is the most commonly used, which was used in this test work.

An electromagnetic exciter operates by connecting an input signal to an alternating magnetic field, in which is placed a coil which is attached to the drive part of the device and hence to the structure [5.2]. Although the difference is normally small, it is possible that the force input at the coil will be different than the input at the test structure. The shaker and its attachment can add mass to the structure under test as well

as otherwise constraining the structure. Attaching the shaker to the structure through a stinger can minimize mass and other constraints. A stinger consists of a short thin rod running from the driving point of the shaker to a force transducer mounted directly on the structure. This stinger serves to isolate the shaker from the structure, reduced the added mass, and causes the force to be transmitted along the stinger, controlling the direction of the applied force [5.4]. It is important as well that the force applied to the structure is as close as possible to the surface in order to obtain a reliable and accurate indication of the excitation level [5.3].

Transducers are used to measure the force input and the nodal displacement/acceleration on the test structure. A transducer is a device, which produces an output signal in response to different input signal. The basic principle makes use of the fact that an element of piezoelectric material generates an electric charge across its end forces when subjected to a mechanical stress. A force transducer thus operates by generating a charge that is proportional to the force that is being transmitted across it.

Therefore by connecting a force transducer to the connecting rod between the exciter and the test structure, the input force may be measured. The nodal displacement on a point on the test structure is measured using an accelerometer. The transduction in an accelerometer is indirect use and is achieved using auxiliary or seismic mass that is connected to the test structure in such a manner that they move as one. Therefore, the output measured from it during a test will be proportional to the acceleration at the nodal to which it is connected. This acceleration may be connected into a displacement and by taking readings at a number of nodal positions, an interpretation of the mode shape may obtained. The selection of a suitable accelerometer is governed by two parameters:

Firstly, the required sensitivity, obviously, the greater the sensitivity, the more accurate the results. However, with increased sensitivity comes increased mass and bulk. This will cause it to interfere with the test structure and lower the maximum permissible working frequency [5.3].

Secondly, the addition of the accelerometer mass to the test structure will impose additional force on the structure. This will give a misrepresentation to the result and in order to minimize the effect, the mass should be kept to a minimum. There are

numerous methods of attaching an accelerometer to the test structure and none is particularly superior to the other. A choice should be made that interferes the least with the structural integrity of the test structure.

Locating an accelerometer can cause difficulties, since if it is placed at or near a nodal point, then this particular mode will not picked up. A way of overcoming this problem is by taking readings at a number of locations on the test structure, so that by pooling the results a realistic representation of the structure may be obtained. The output from these measuring devices may be analyzed using a PC program as analysis to obtain the amplitude of the response to force input ratio and the phase difference between the force and the response and the structural damping at each natural frequency.

5.4 Experimental setup and equipment used:

In this section, the location of the test and the structure support selected for the vibration test of the composite wing box and the equipment used in conducting the test were shown in figures (5.1-5.5). The dimension of the concrete structure was about 3000 mm height and 3000 mm width. The wing box was attached to the two thick plates made of steel attached to the rigid structure made from concrete. The dimension of the concrete structure was about 3000 mm height and 3000 mm width. Eleven bolts on the upper section of the root chord and eleven bolts on the lower section of the root chord attached the wing box. The selection of the structure support (concrete structure) was satisfied the grounded condition explained in section 5.3, which simulate the wing-fuselage attachment on the actual aircraft.

Equipment used for excitation of the wing box is illustrated in figure (5.2) which shows the power amplifier, signal generator and filter unit connected to the shaker. These implements provide the input needed to shake the structure. Standard Bruel & Kjaer equipment was used extensively. An electromagnetic exciter "Goodmans vibrator model 309" was used to shake the composite wing box, the location of the exciter was placed at the tip of the wing box at the intersection of the tip rib and the middle stringer. The vibrator was attached to the bottom surface of the wing box through a sting as recommended by [5.4] as shown in figure (5.3).

A force transducer type 8200 was connected to the sting and a mounting block, the load cell being glued directly onto the lower surface of the wing box with standard setting car body filler. An inexpensive and effective method of attachment used extensively in industry. The sting will allow only the force to be transmitted in the vertical direction.

Figures (5.1 and 5.5) also show the location of the reference accelerometer, which was directly opposite to the force transducer at the top surface of the wing box.

A total of eleven accelerometers type 4374 including the reference accelerometer were calibrated and used in a total of five complementary tests to measure the response of the entire wing box as shown in figure (5.1). The accelerometers were attached at the intersection of each rib with the stringers and spars over the composite wing box using "blue-tac". Again an inexpensive and effective means of attachment, which is not permanent but secure enough for the duration of the test. The electrical leads of the accelerometers to the junction/splitter box were securely tapped on the wing box so as to avoid any drumming of the leads. The locations of the accelerometers on the wing box are shown in figure (5.6).

Two different sizes of accelerometers of the same type were used in the test, the smaller sizes were numbered from 2 to 6 and the other size was numbered from 21 to 26 as shown in figure (5.1). The strain gauge cables attached to the rib webs were carried by the high stand on the side of the wing box, this was done to avoid the inertia mass of the cables. The transducers cable were connected to the FSML Signal Conditioner Unit, which is designed and build at Cranfield University. The signal conditioner contains 26 channels numbered from 1 to 26; each accelerometer was connected to the same calibrated channel number on the signal conditioner.

The signal conditioner was connected to a Dc power generator and to the Multicore to Single channels, which contains all the transducers channels and located behind the oscilloscope as shown in figures (5.3 and 5.5). An external sixteen channel PC anti-aliassing filter with switched gain amplifier (SGA) unit was connected to the

Figure (5.1) Structure support and accelerometers attached to the composite wing box for one test location.

Figure (5.2) Power amplifier, Signal generator and filter unit.

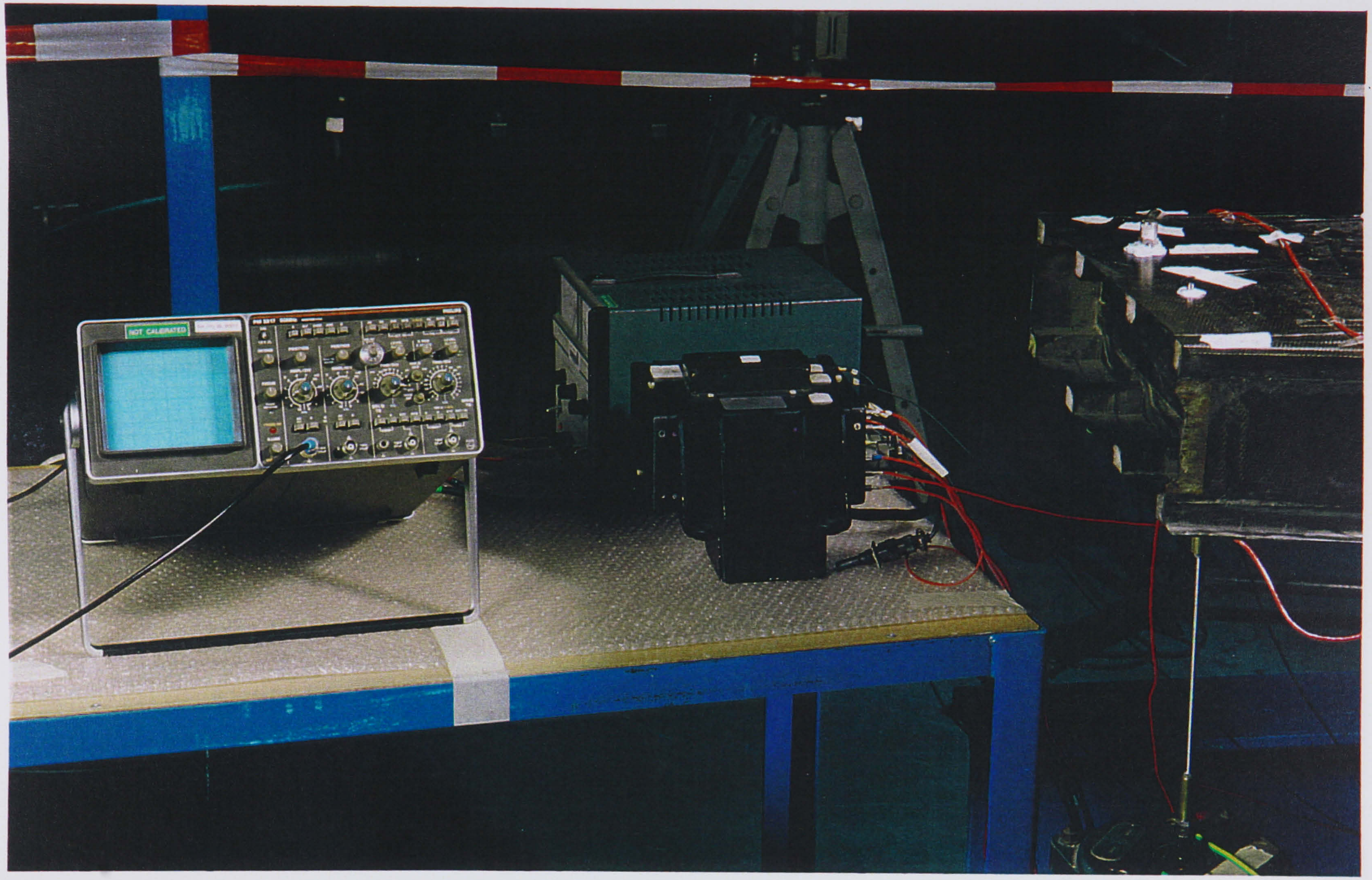

Figure (5.3) FSML signal conditioning unit, DC power supply and Multicore signal channels.

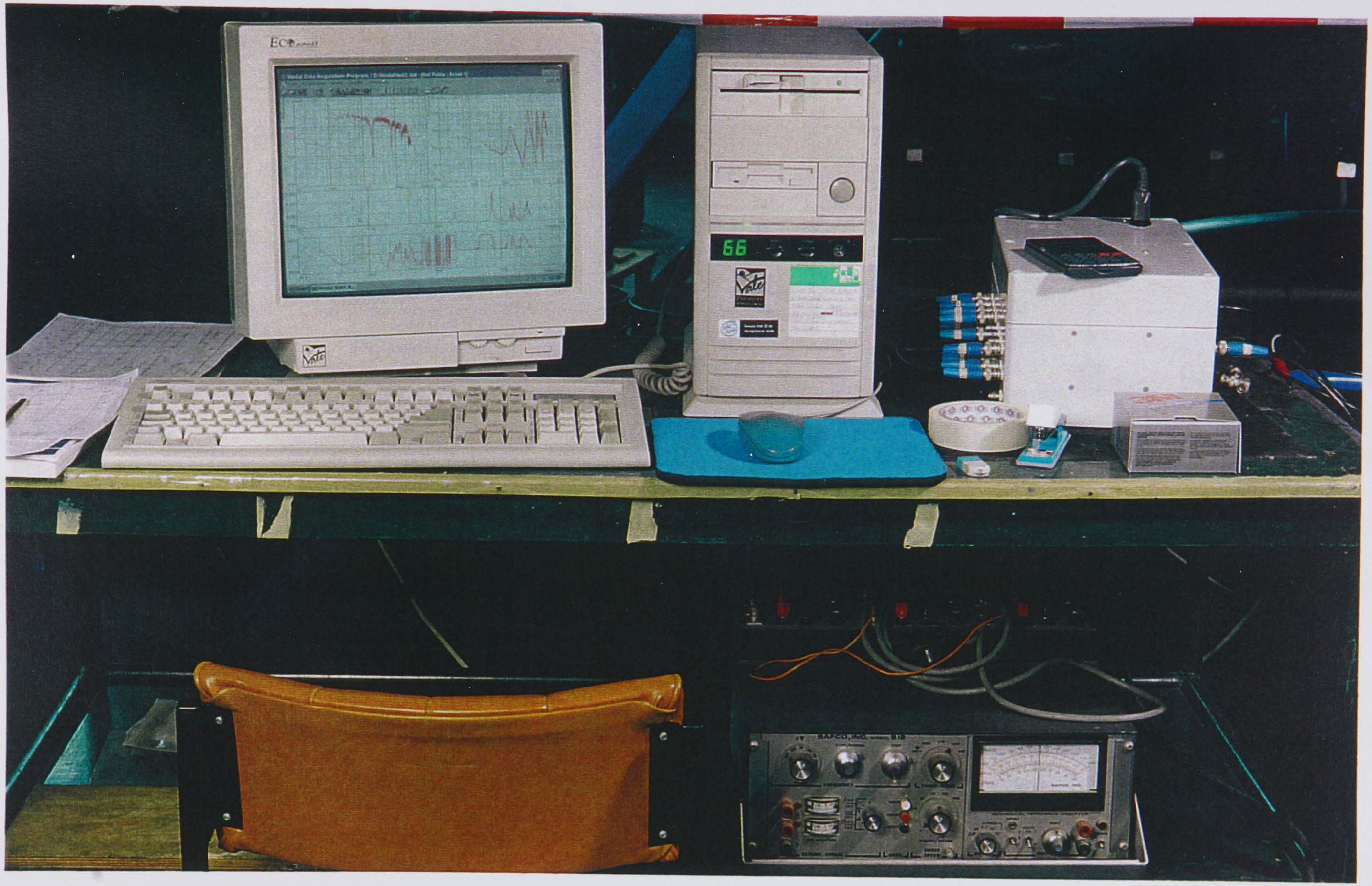

Figure (5.4) PC interface filter + SGA and PC modal analysis software.

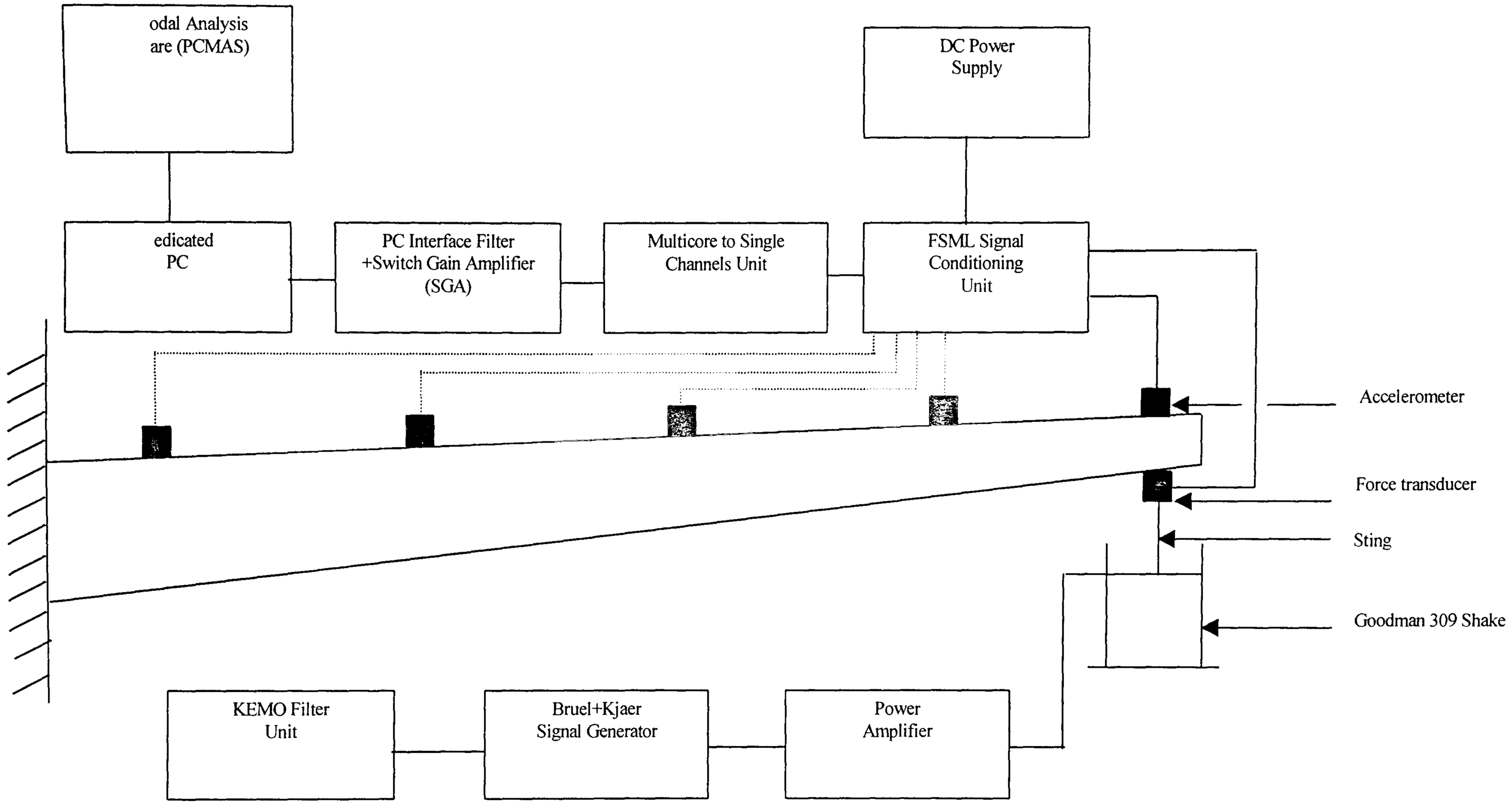

Figure (5.5) Schematic of experimental equipment used.

Multicore Single channels and oscilloscope "Philips" from each side and then to the computer analyzer from the back of the filter as shown in figures (5.3-5.5). The gain and input signal can be checked using the switched monitor on the filter for each transducer channel through the oscilloscope. The filter unit was calibrated before the test and set up to 300 HZ. The three sides of the filter unit are shown in figure (5.4).

The analysis of the test data was done using a desk-top personal computer running a sixteen channel data acquisition, processing and data storage-retrieval software. This system known as PC Based Modal Analysis System (PCMAS). A sixteen channel ADC board, housed within the PC. This board is a proprietary Blue Chip Technology ADC 42 interface board, providing sixteen channels of ADC input. The system supports stepped sine, random, impact and structural relaxation analysis test types. Capabilities includes:

1- Acquisition of calibrated signals and storage/retrieval previously saved calibrations.
2- Acquisition of time series data.
3- Acquisition of cross-spectral data
4- Acquisition of time or spectral data using pre-trigger channel
5- Analysis to extract modal parameters, including natural frequency, damping, gain and phase at each accelerometer location

Graphical display of mode shapes at user defined frequencies

5.5 Tests Conducted:

The accelerometers were located on the entire wing box at five different locations as shown in figure (5.6) to cover the entire wing box. After fixing the accelerometers and connecting them to the right channel number on the signal conditioner unit and checking all the connection of the accelerometers to the signal conditioner and to the filter unit. The next step is to select the right type of excitation from the noise and sine generator. The random and sinusoidal excitation was selected for the first location only and the rest were done using random excitation only. By switching all the instruments on, the signal of the transducers can be checked using the switched monitor on the filter unit through the oscilloscope.

All dimensions are in millimeters

Where L2/4 Location No. 2 and using accelerometer No. 4

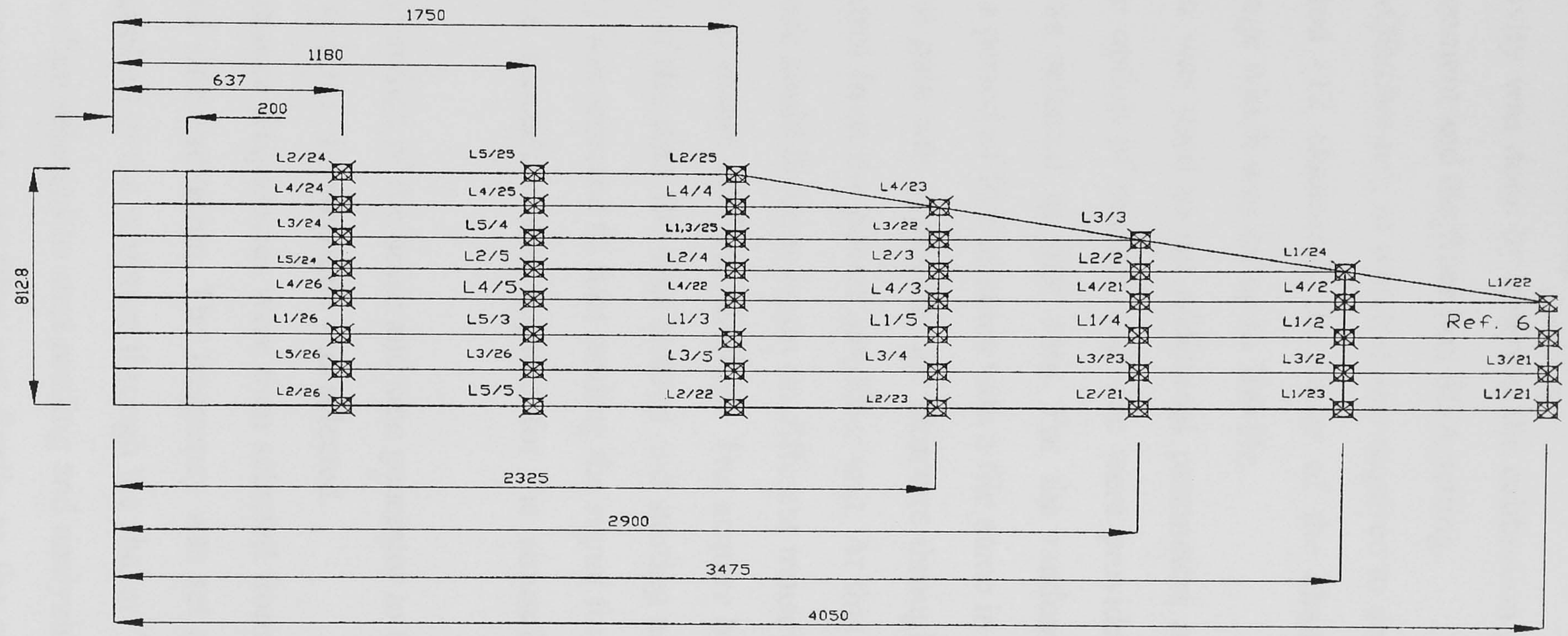

Fig. (5.6) Plan view of composite wing box test

This is to make sure that all the accelerometers are attached properly to the structure of the wing box without leakage.

Using the acquisition menu of the software, the following must be done before the test to insure a reliable reading:

1. Setup sensitivity was done by entering the calibration parameter of the transducers, unit's measurement and the filter box SGA setting.
2. Setting the AQR/channel, in which it was required to defined the number of channels to be acquired (12 channels), the order of the channel to be sampled and the frequency range which was set up to 300 Hz.
3. Setup spectra was used to set additional parameters necessary to conduct spectral analysis. The option of random and sine were provided in this setup. The random excitation was selected as first case. For the random excitation cases, data was acquired for a period of five minutes with a file name in each location test.

The input gain was applied to the structure through the shaker by adjusting the gain switch control from the power amplifier unit. At this stage before starting reading the signal, a check could be done again on different transducers amplifiers gain through the oscilloscope to insure uniform readings. The acquire button was then selected from which the name of the data file was entered and starting acquisition button for location number one (L1) was selected to start reading the signal for L1.

The same procedure was applied for the sinusoidal excitation with the two changes:

1- Adjusting the switch of the noise and sine generator to the sine excitation

2- In the setup spectra, the step sine was selected.

The resonance frequencies were then selected from the random test and applied using the stepped sine excitation. The frequency was set on the sine generator and the gain input was applied to the structure through the shaker. The test analysis button from the analyzer was then selected to start reading and analyzing the signal initially coming from the accelerometers to the filter and finally to the analyzer. This procedure was done for all the resonance frequencies of the location number one only.

The tests of the other locations were done using random excitation and using the same procedure explained above.

5.6 Retrieval of data:

Once the test is completed and the data was stored in a file, the software allowed the user to retrieve and display the data file. The software can generate the gain, phase, coherence, Nyquist and spectra plots against the frequencies. The gain, phase and coherence plots for the reference accelerometers (Accl.6) and (Accel.22) against the frequency was generated by the software as shown in figure (5.7 and 5.8) respectively.

The frequency, gain and structural damping were calculated using a single degree of freedom root mean square (rms) curve fit through a resonance frequency of each accelerometer of the entire wing box by selecting the required frequency points.

5.7 Results and Discussion:

A frequency sweep was applied to the structure from 0-300 Hz. The response was measured on the entire wing box. Since there were a total of 46 separate locations for the five sets of tests conducted there were a considerable amount of data acquired. Hence the reference accelerometer (Accel.6) and accelerometer (Accel.22) which are located at the tip (with maximum displacements) of the wing box as shown in figures (5.1 and 5.6) are taken as typical sample of the results obtained which are representative of the whole set acquired. There was a good agreement between the frequencies obtained from the two methods of excitation, and therefore the rest of the test was done using the random excitation. From figure (5.7 and 5.8), it can be seen from the gain plots that there are some distinct peaks visible. The gain is defined as the ratio of the output to the input response. From the plots of the gain against frequency, it was possible to identify each resonance frequency by peaks in the response. The peak, resonant locations on the gain plot can be corroborated with the phase diagram, which illustrates clearly the change in phase at the resonant condition. Further confirmation can also be obtained by the inspection of the Coherence plot, which should show a drop off at the resonant condition. Similar results were obtained for all the other locations mentioned above. The average of the six main resonance frequencies of the wing box was identified as indicated in table (5.1).

The reference accelerometer (Accel.6) was used to normalize all the other accelerometer response values and the relative phase angle with all the accelerometer on the entire wing box. The relative phase angles between -90 degree through 0 degree to +90 degree were taken as in phase (positive), and phase angles outside this range were taken as out of phase (negative).

Table (5.1) Average frequencies between the test locations.

Mode No.	Location 1 Average Frequency (Hz)	Location 2 Average Frequency (Hz)	Location 3 Average Frequency (Hz)	Location 4 Average Frequency (Hz)	Location 5 Average Frequency (Hz)	Average Frequency (Hz)
1	19.608	19.831	19.761	19.822	19.806	19.7350
2	73.475	74.242	73.924	74.233	74.239	73.8500
3	142.592	142.047	142.821	142.592	142.592	142.415
4	158.480	157.905	158.393	158.249	158.270	158.081
5	229.884	232.142	234.917	231.861	231.731	232.430
6	252.916	256.099	254.845	256.536	256.536	254.720

The structural modes were identified by their mode shapes and frequencies. The first six natural frequencies and mode shapes of the composite wing box are shown in figures (5.9-5.14). From these figures, it can be seen that the first mode was the first bending mode, at 19.74 Hz as shown in figure (5.9). The second bending mode was found at frequency 73.85 Hz, figure (5.10). There is evidently a large frequency separation between these two frequencies (see figs. 5.7 and 5.8). The third mode was the third bending mode was found at frequency 142.415 Hz, figure (5.11). The fourth mode was the coupled bending-torsion mode was found at frequency 158.081 Hz as presented in figure (5.12). The third and forth modes are close to each other as shown from the Gain and coherence plots of (Accel. 6) and (Accel. 22) are shown in figures (5.7 and 5.8). The fifth mode was the fourth bending mode at frequency 232.34 Hz, figure (5.13). Finally the sixth mode was at 254.72 Hz, which representing the tip bending and torsion mode as shown in figure (5.14).

5.8 Conclusions:

The vibration test was conducted on the Cranfield A1 aerobatic composite wing box. A good agreement between the two methods (random and sine), upon which the rest of the locations were excited with random excitation. The vibration experiments can be seen to be successful, yielding six resonant frequencies and associated eigen modes. These results are representative of the carbon fibre reinforced plastic (CFRP) wing box structure with root fixed end conditions and provide useful initial data. This work has also provided a useful teaching; understanding and learning exercise allowing the application of taught material. The results obtained will be used for comparison with the results obtained from the finite element analysis (chapter 7).

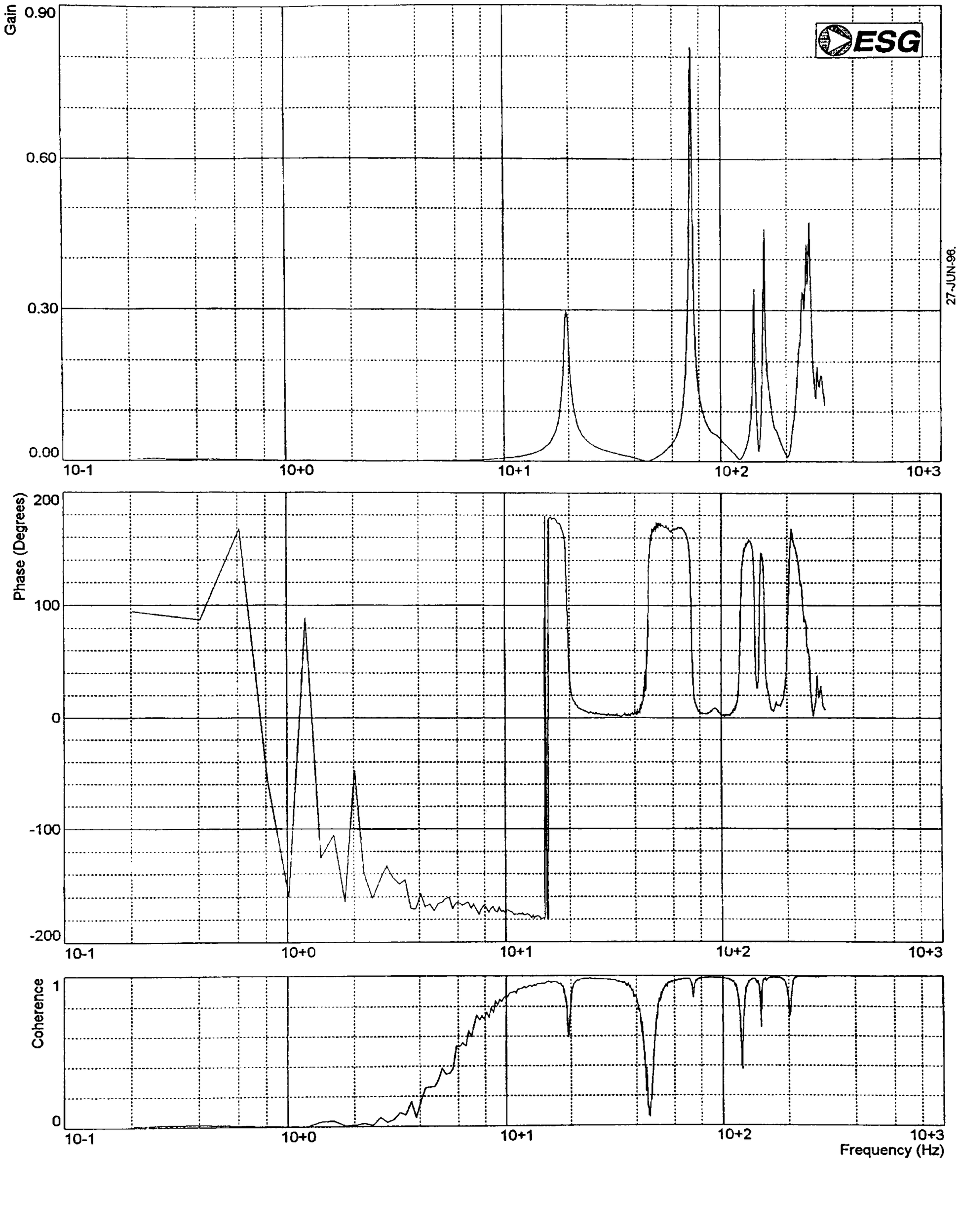

Figure (5.7) Gain, Phase and Coherence plots for reference accelerometer (Accl. 6).

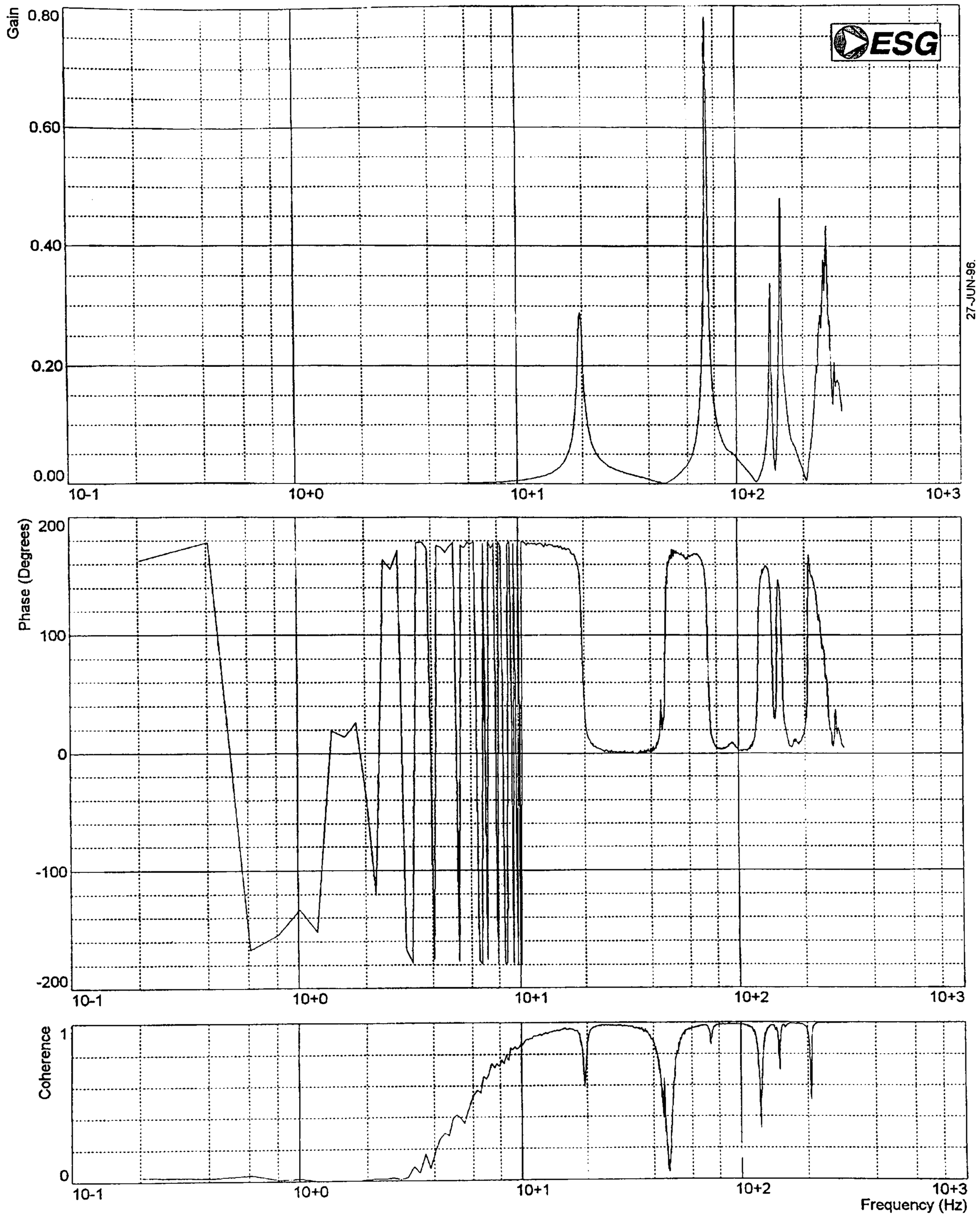

Figure (5.8) Gain, Phase and coherence plots at tip station (Accl. 22).

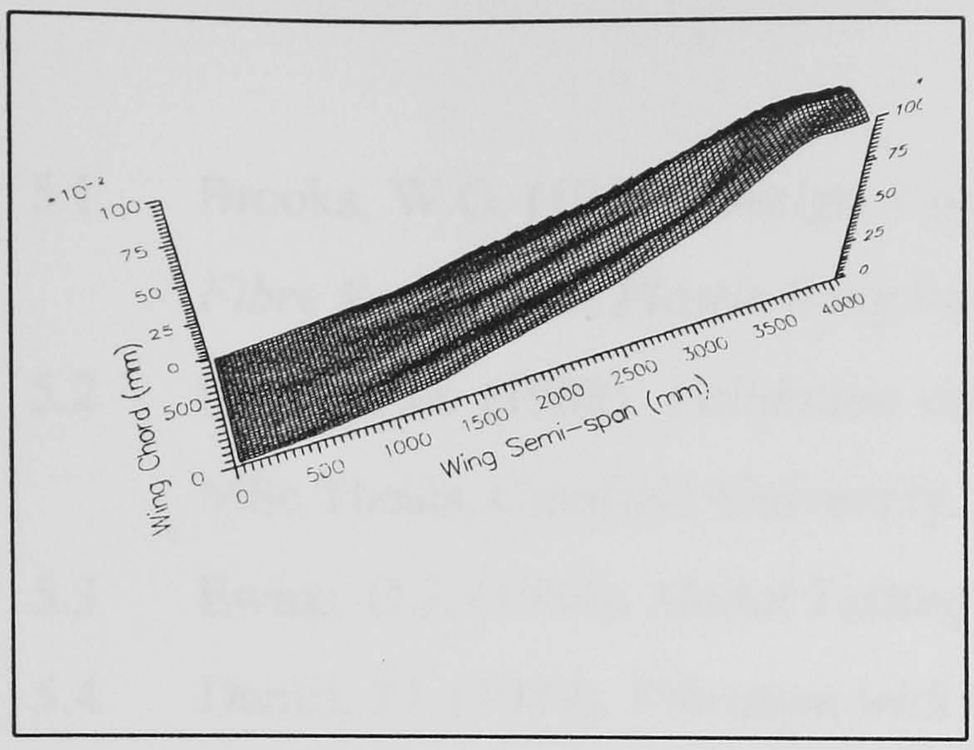

Fig. (5.9) 1st Bending Mode (19.735 Hz).

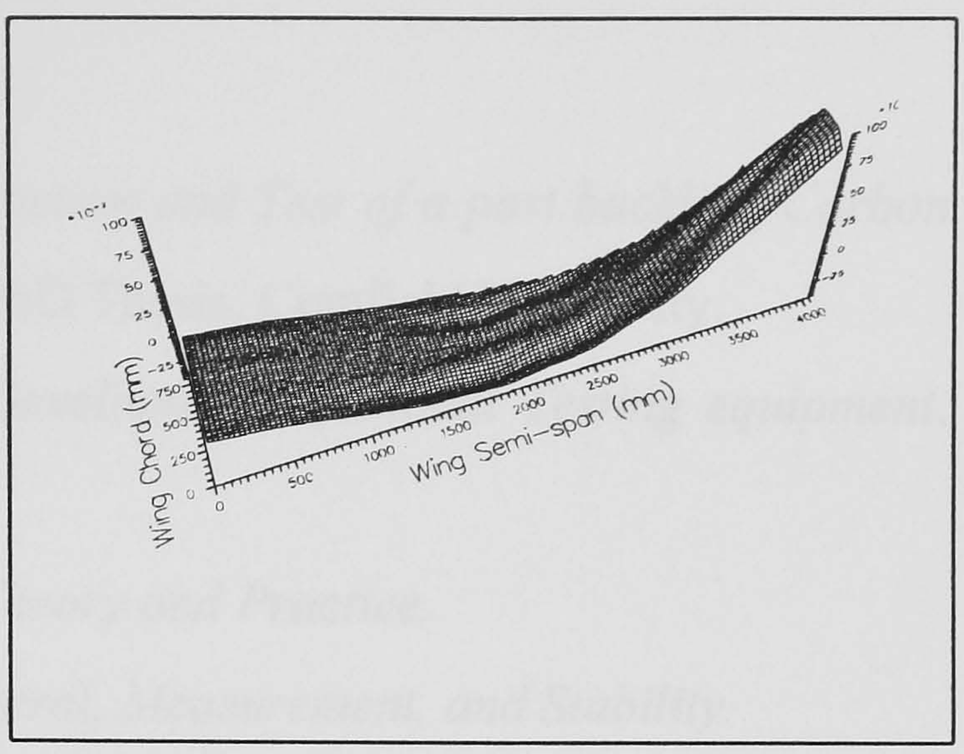

Fig. (5.10) 2nd Bending Mode (73.85 Hz).

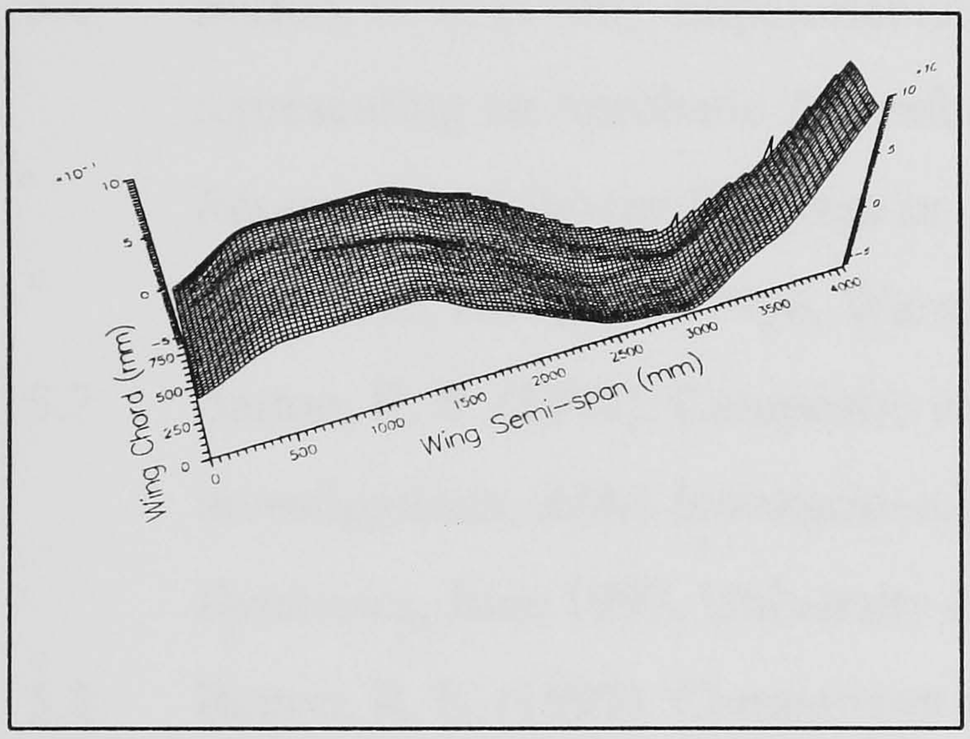

Fig. (5.11) 3rd Bending Mode (142.415 Hz).

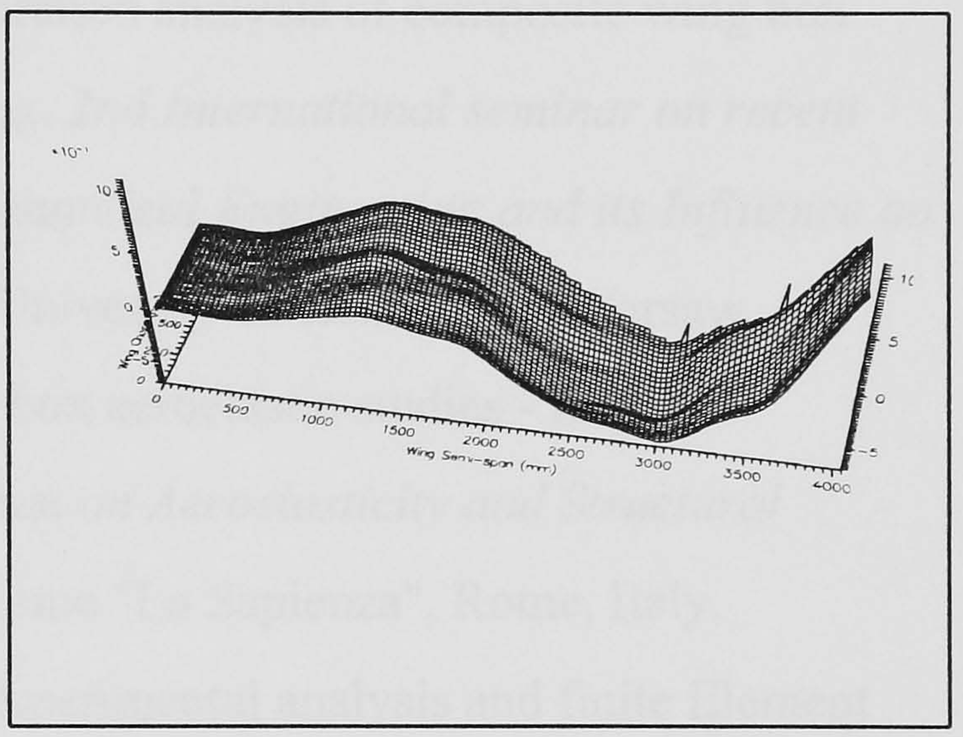

Fig. (5.12) Coupled Bending-Torsion Mode (158.081 Hz).

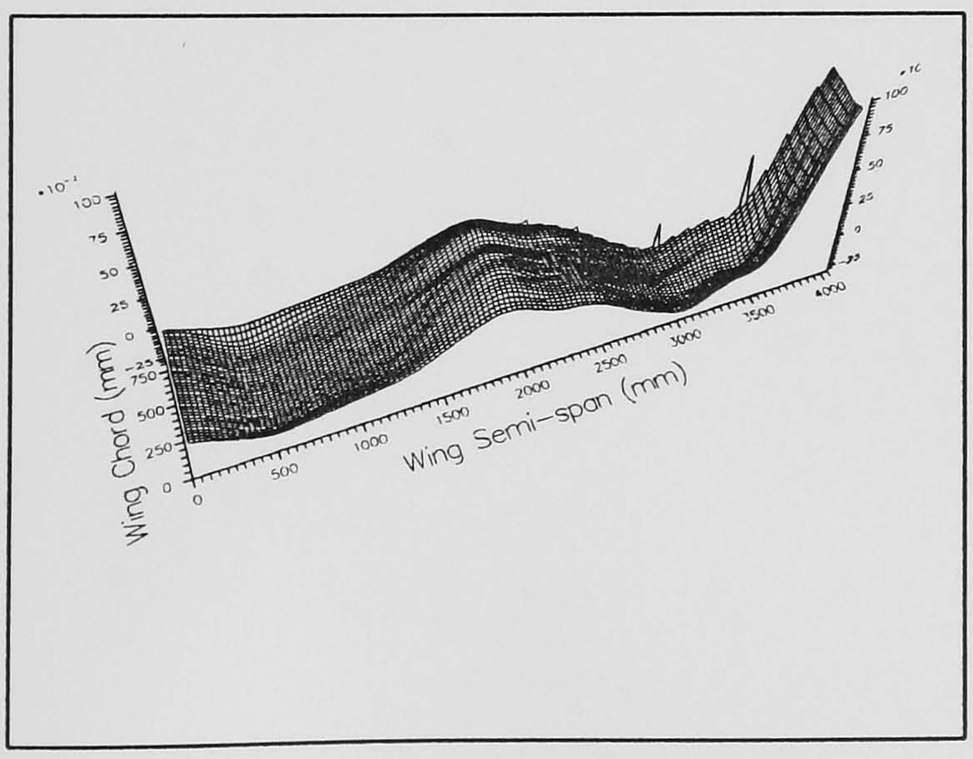

Fig. (5.13) 4th Bending Mode (232.43 Hz).

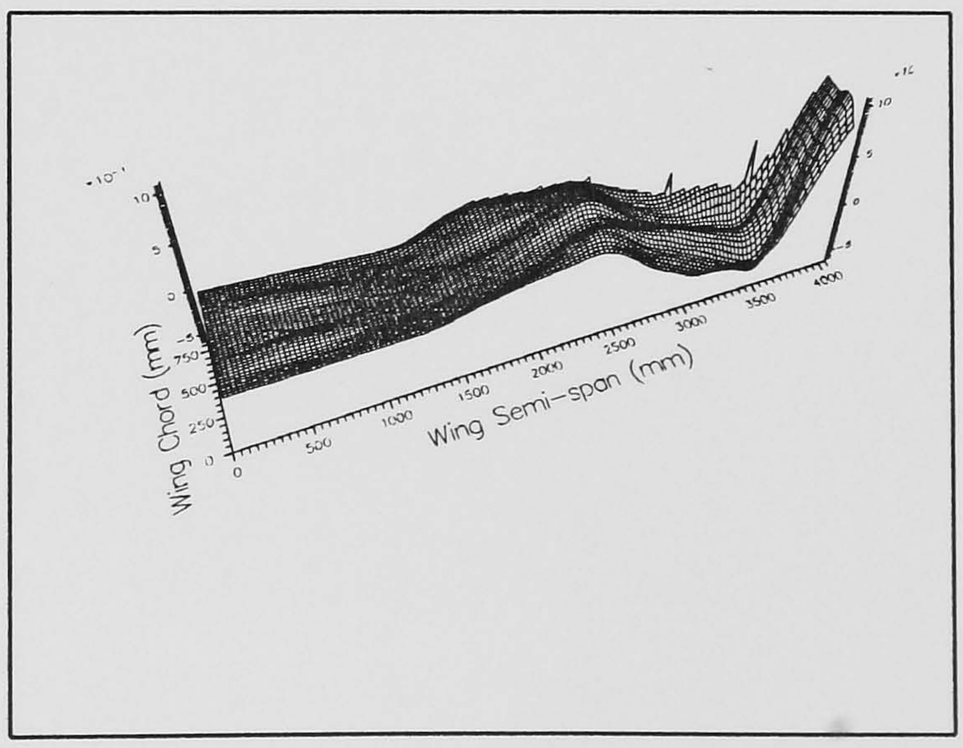

Fig. (5.14) Tip Bending-Torsion Mode (254.72 Hz).

References

5.1 Brooks, W.G. (1987). *Design, Construction and Test of a post buckling Carbon Fibre Re-inforced Plastic Wing box*. PhD Thesis, Cranfield University.

5.2 David, J.D. (1988). *Validation and Development of Modal Testing equipment*. MSc Thesis, Cranfield University.

5.3 Ewins, D.J. (1984). *Modal Testing : Theory and Practice*.

5.4 Danirl, J.I. (1989). *Vibration with Control, Measurement, and Stability.*

5.5 Iyanalu, O.F. (1986). *Design, Development and Testing of Vibration Model of an aircraft*. Msc Thesis, Cranfiled University.

5.6 Battoo, R. S. (1996). Experimental vibration analysis of composite wing box representing an Aerobatic Aircraft wing. *2nd International seminar on recent Research and Design Progress in Aeronautical Engineering and its Influence on Education*, November 1996, Warsaw University of technology, Warsaw.

5.7 Battoo, R. S. (1997). Composite wing box aeroelastic studies - initial investigations, *AIAA International forum on Aeroelasticity and Structural Dynamics*, June 1997, University of Rome "La Sapienza", Rome, Italy.

5.8 Battoo, R. S. (1997). Comparison of experimental analysis and finite Element analysis results for a composite aircraft structure, Aviation - 2000 Prospect, TsAGI, Shukovsky, Moscow.

CHAPTER 6

DYNAMIC AND AEROELASTIC ANALYSIS OF THE CRANFIELD A1 METAL WING BOX

6. Dynamic and Aeroelastic analysis of the detailed metal wing box of the Cranfield A1 Aerobatic Aircraft:

6.1 Introduction:

This chapter describes, the normal mode analysis carried out for the Cranfield A1 metal wing box. The analysis was done using the finite element code MSC/NASTRN [6.1] for the detailed and simplified wing models and CALFUN program [6.2] for the simplified wing model of the metal wing box. The airfoil sections of the wing geometry at the root were taken as NACA 23015 and at the tip NACA 23012 [6.3 and 6.4].

The first simplified model was constructed using the pre-postprocessor MSC/XL and analyzed using MSC/NASTRAN. In this model, the wing box was modeled using beam elements with lumped masses as shown in figure (6.5). The second simplified model of the wing box was modeled using CALFUN [6.2], which used beam elements with distributed masses. The structural properties of wing box required for the normal mode analysis were given in table (6.1) for CALFUN program and in figure (6.4 and 6.5) and in appendix A (A1) for MSC/NASTRAN. The finite element modeling of the detailed metal wing box was constructed using MSC/PATRAN V6.0, which is the pre and postprocessor for MSC/NASTRAN. The material properties of the metal wing box were aluminum (L72). The dimension and the thickness of the metal wing box components such as top and bottom skins were taken from the original drawing of the Cranfield A1 Aerobatic aircraft [6.13]. For comprehensive details the reader should refer to these drawings in [6.13]. The metal wing box was modeled to simulate the cantilever boundary condition, which is close enough to the wing-fuselage attachment. The eigenvalues and eigenvectors (with zero structural damping) of the metal wing was calculated using the Lanczos method through solution number 103 available in MSC/NASTRAN. The mode shapes are plotted using the postprocessor MSC/PATRAN V6.0 as shown in figures (6.13-6.16) for the detailed metal wing model and the Microsoft EXCEL for the simplified models as shown in figures (6.6-6.9). In the case of using CALFUN program, the eigenvalues were calculated using the dynamic stiffness method, and the natural frequencies are presented in table (6.4).

The flutter analysis of the metal wing box was done using MSC/NASTRAN for the simplified and detailed models. This was done because it is more powerful compared with the limited applications of the CALFUN program.

Aerodynamic modeling of both wing models was done using the subsonic method provided by MSC/NASTRAN called the Doublet-Lattice Method (DLM). Artificial structural damping of 2% was assumed as complex stiffness matrix in the flutter analysis through the use of the SDAMP card in the case control deck and both PARAM (KDAMP –1) and TABDMP1 in the input bulk data deck of the metal wing box model.

The PK method was selected to solve the flutter equation of motion through the use of the flutter solution number 145. The flutter speed and flutter frequency were identified from the plots of the flight velocity against the total damping and frequency respectively as shown in figure (6.10-6.11) for the simplified wing model.

6.2 Description of the A1 metal wing box:

The metal wing box, which represented the A1 Cranfield Aerobatic wing, was made from Aluminum. The Cranfield aerobatic aircraft was designed by the students with the help of the staff of college of aeronautics and were given as student design project in 1968/1969 that resulted in an Aerobatic aircraft that even today flies. Figure (6.1) shows the whole of the A1 Aerobatic with salient wing parameters. As mentioned in chapter 5, the airfoil sections of the metal wing box were NACA 23015 and NACA 23012 at the root and the tip of the wing box respectively. The dimensions of the modeled metal wing box are span of 4.902 m, 0.8128 m root chord, 0.254 m tip chord. As in real aircraft wings, the wing box consists of upper and lower skin, front and rear spars, stringers, spar caps and ribs. The wing was constructed from a total of seventeen ribs including the root and tip ribs. The wing box was designed with 3 degree dihedral angle for the rear spar and 2.76 degree dihedral for the front spar. The over all dimensions with the ribs and stringers spacing in the metal wing box are shown in figure (6.2). For more information the reader is referred to [6.3] and to the original drawing of the Cranfield A1 Aerobatic aircraft [6.13].

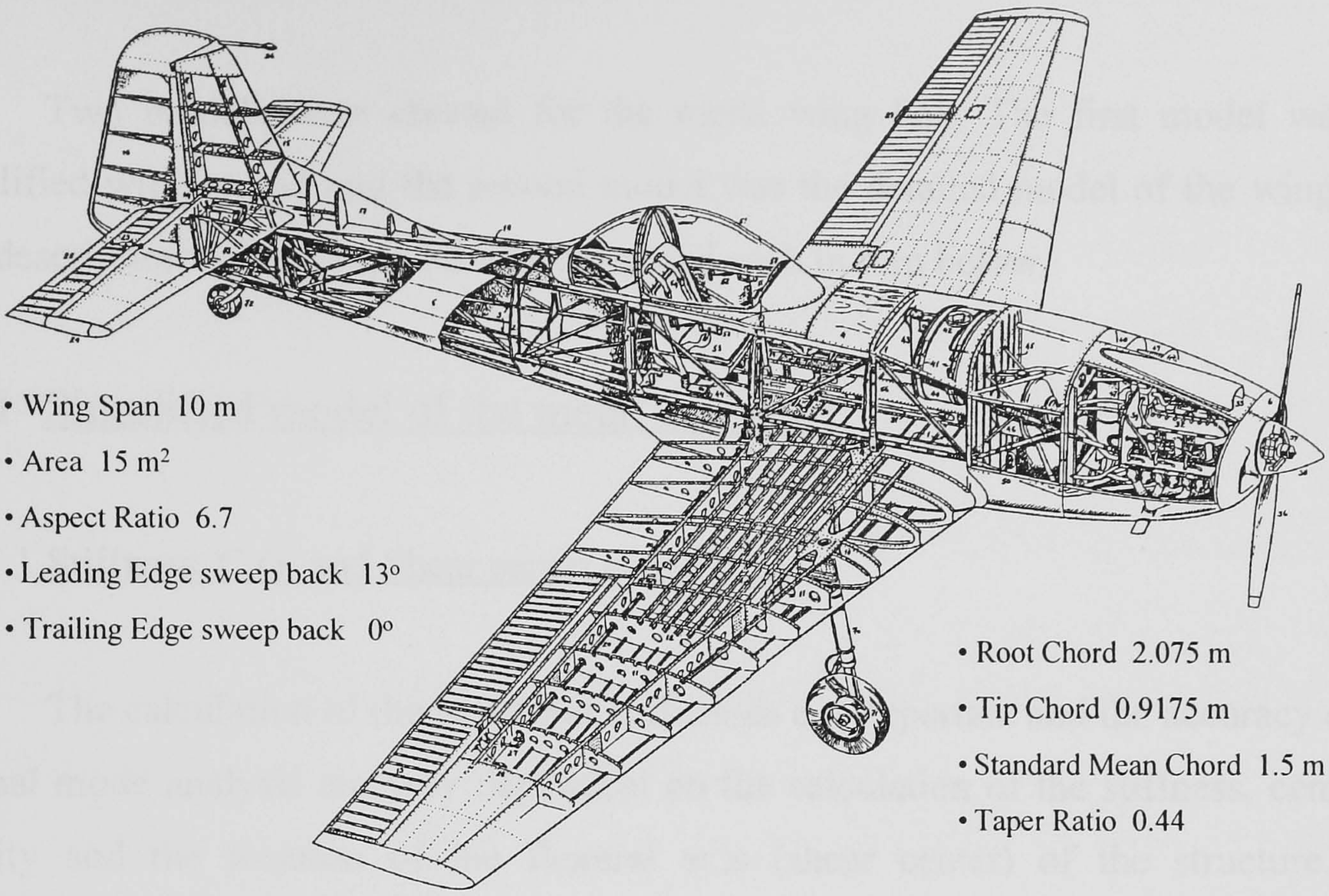

Figure (6.1) Cranfield A1 Aerobat with salient wing parameters.

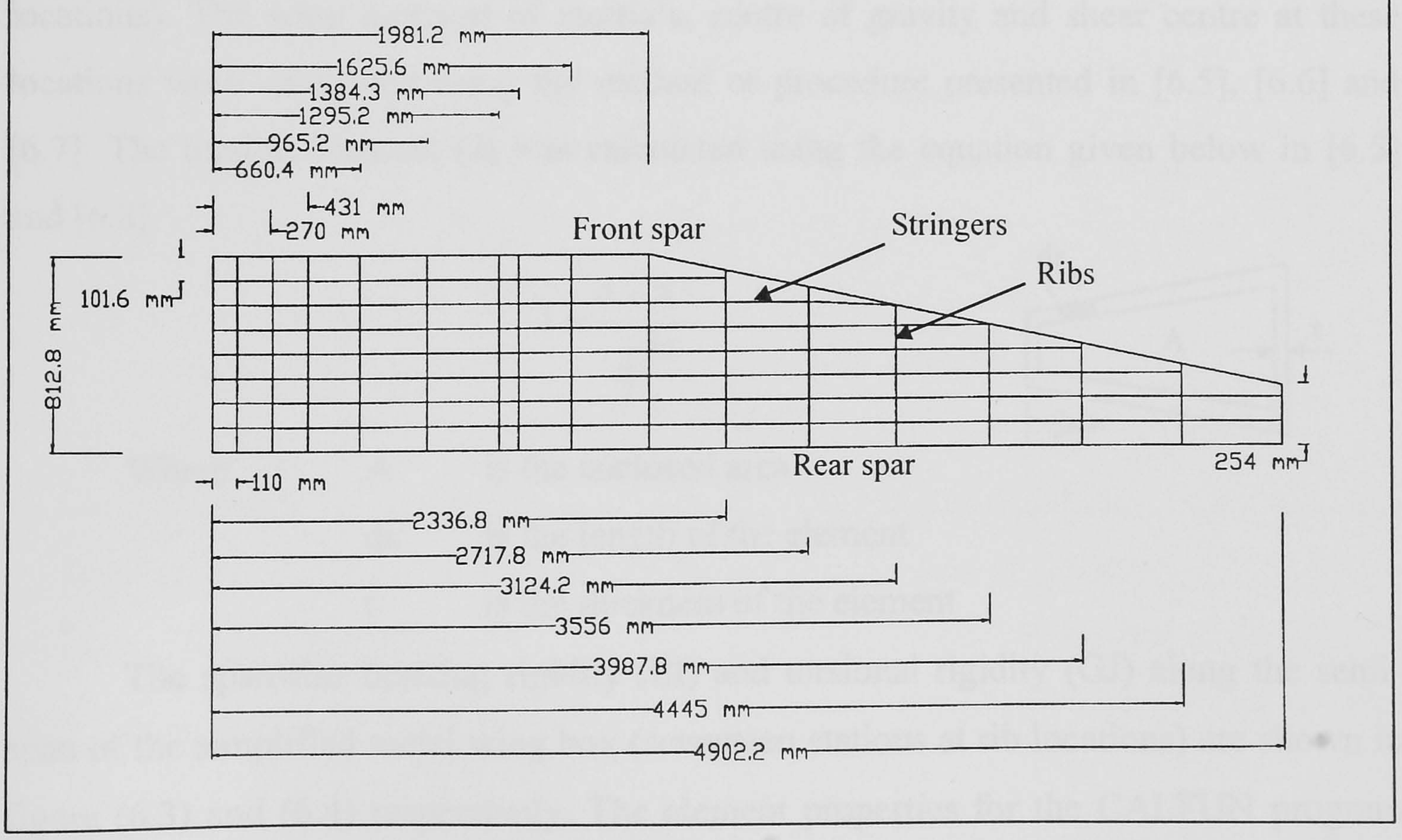

Fig. (6.2) Plan view of the A1 metal wing box.

6.3 Modeling of the metal wing box:

Two models were created for the metal wing box. The first model was the simplified wing model and the second model was the detailed model of the wing box. The descriptions of these models are discussed each in turn below.

6.3.1 Simplified model of the metal wing box:

6.3.1.1 Stiffness, C.G. and Shear center calculations:

The calculation of the structural stiffnesses are important and the accuracy of the normal mode analysis are very dependent on the calculation of the stiffness, center of gravity and the location of the flexural axis (shear center) of the structure. The dimensions of the wing box at each rib location were calculated using [6.3] and [6.4]. Also the dimensions and thickness of the upper and lower skin, stringers and spar webs and caps are taken from the original drawing of the A1 aircraft and [6.3]. The area and the center of gravity of each stringer and spar cap with effective skins along the span of the metal wing box were then calculated along the semi-span for seventeen stations (ribs locations). The wing moment of inertia's, centre of gravity and shear centre at these locations were calculated using the method or procedure presented in [6.5], [6.6] and [6.7]. The torsion constant (J) was calculated using the equation given below in [6.5] and [6.8].

$$J = \frac{4 \times A^2}{\oint \frac{ds}{t}}$$

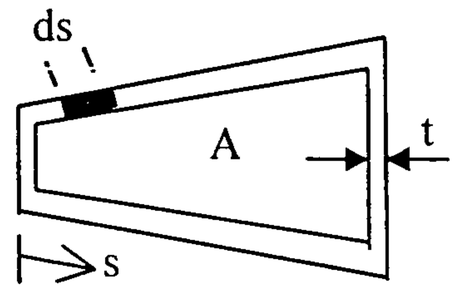

Where A is the enclosed area

ds is the length of the element

t is the thickness of the element

The spanwise bending rigidity (EI) and torsional rigidity (GJ) along the semi-span of the simplified metal wing box (seventeen stations at rib locations) are shown in figure (6.3) and (6.4) respectively. The element properties for the CALFUN program are presented in table (6.1). The bending and torsional rigidities for each element were

6.3.1.2 Finite element modeling:

The flexural axis of the metal wing box (shear center) and the center of gravity were calculated along the semi-span of the wing as mentioned in the above section. In the structural idealisation, the wing box was modeled using the beam elements and lumped masses provided in [6.1]. The beam elements are located along the flexural axis of the metal wing box and the lumped masses are located along the center of gravity of the wing section as shown in figure (6.5). A total of 32 beam elements and sixteen lumped masses at the rib locations are created using MSC/XL and analysed using MSC/NASTRAN [6.1] as drawn in the sketch shown in figure (6.5). The bending moment of inertias and torsion constant are specified through the use of PBEAM card and the material properties of the isotropic material through the use of MAT1 card in MSC/NASTRAN. The inertia properties of the lumped masses are applied through the use of the CONM2 card.

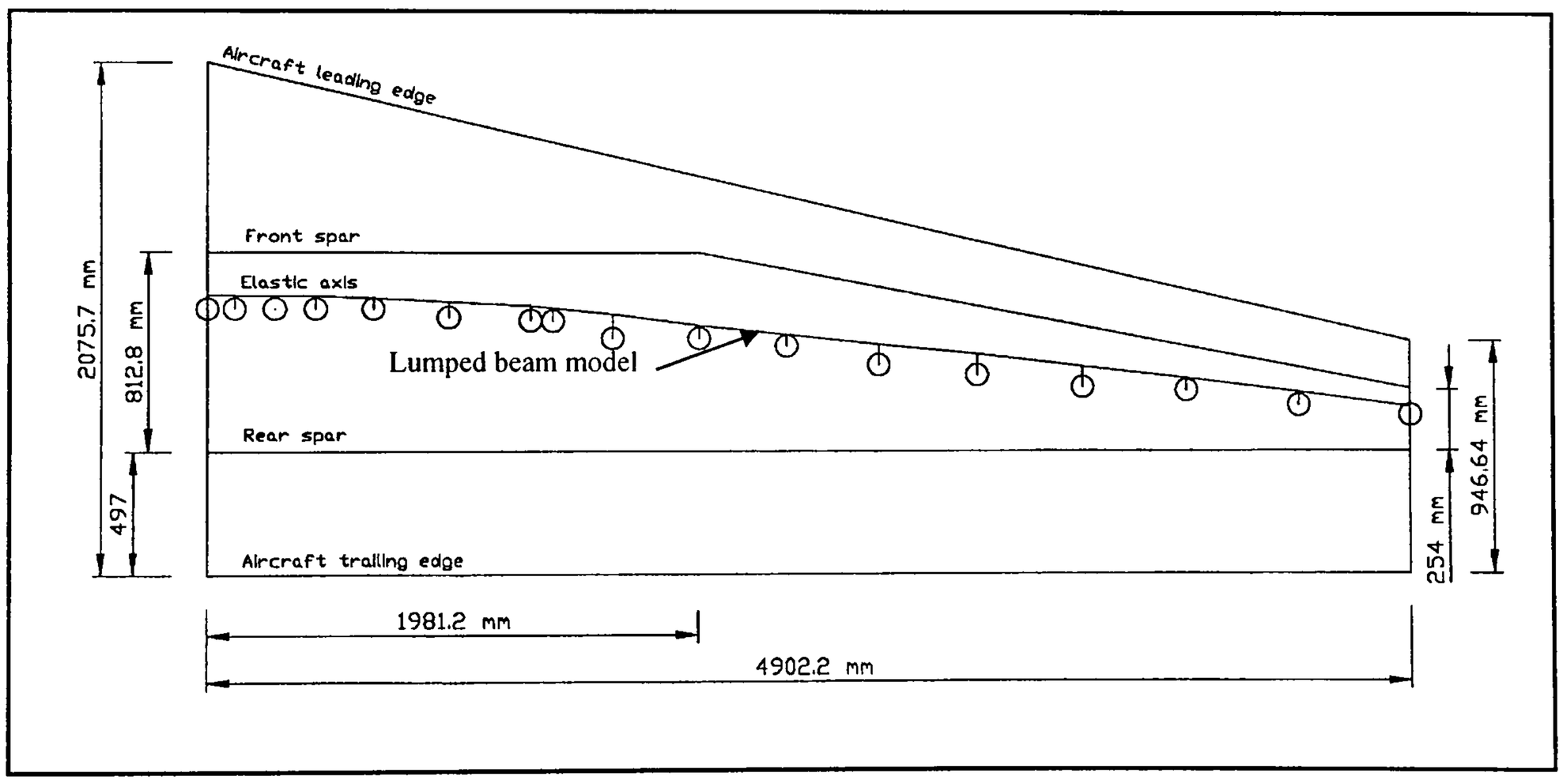

Figure (6.5) Lumped beam model of the simplified metal wing box.

In the case of using CALFUN program, a total of sixteen beam elements are used with the structural properties of the elements representing the metal wing box presented in table (6.1) in the normal mode analysis using the dynamic stiffness matrix

taken in the analysis as the average value between the rigidity at the first and second nodes.

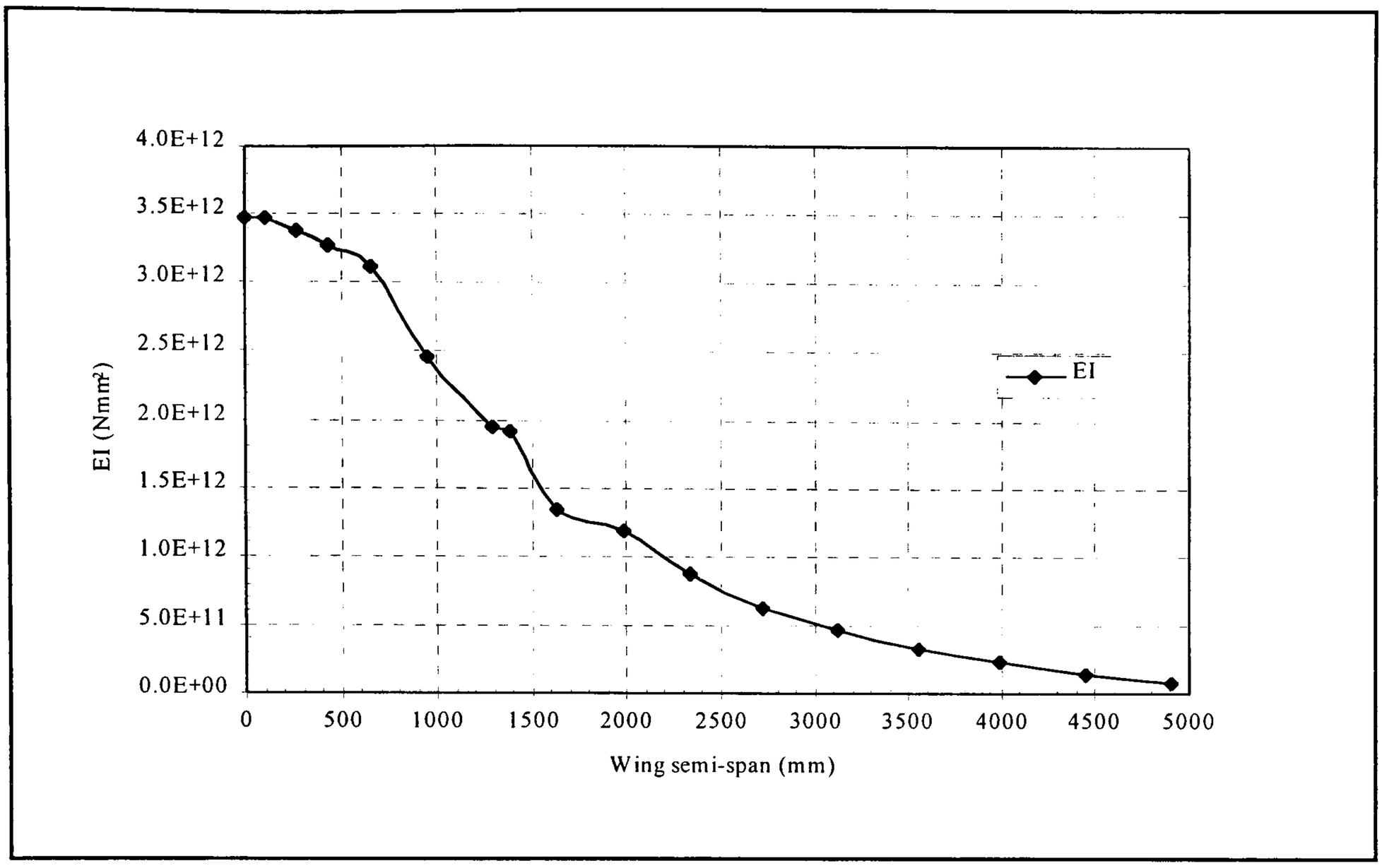

Figure (6.3) Variation of the wing spanwise bending rigidity (EI) along the semi-span of the metal wing box.

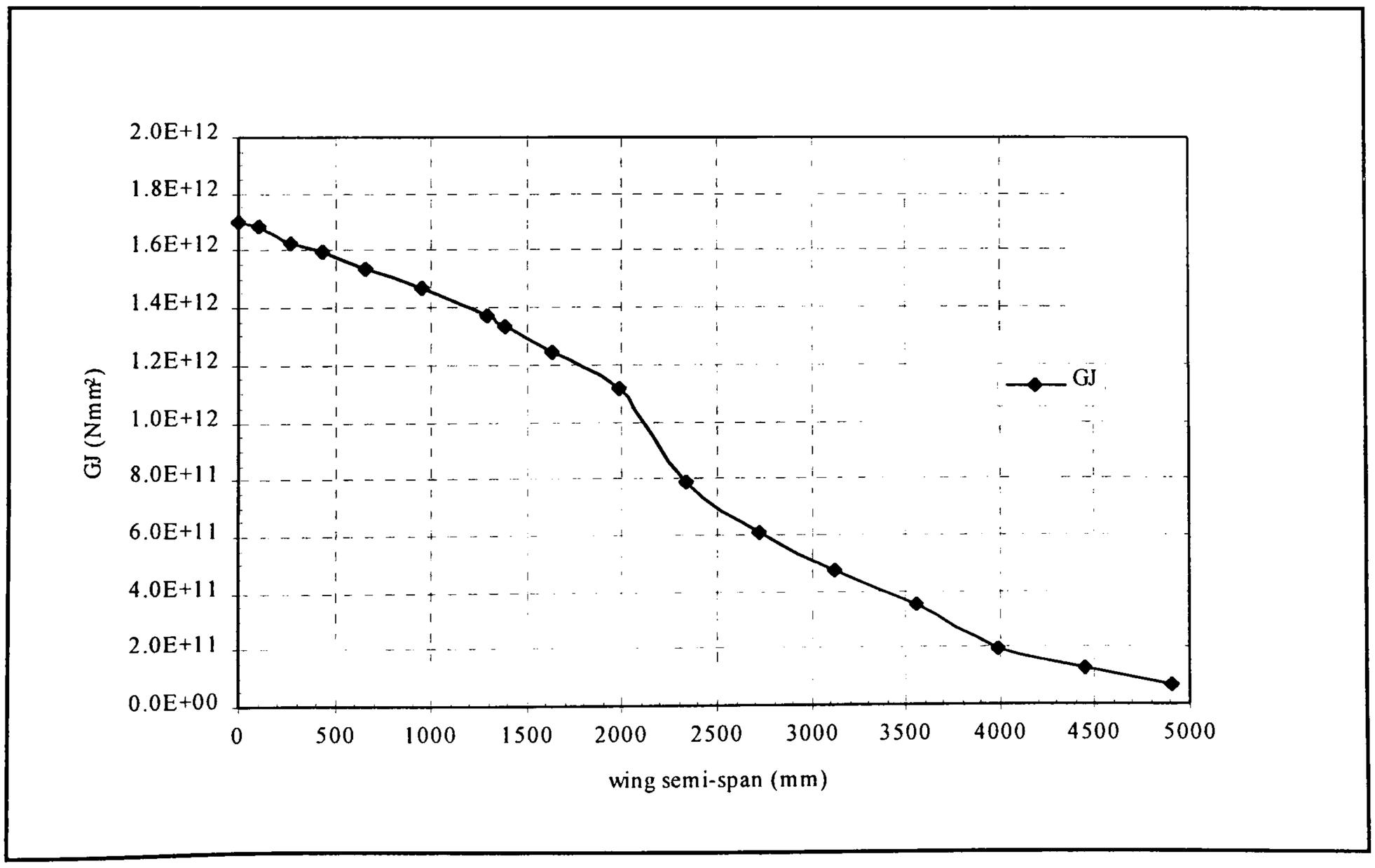

Figure (6.4) Variation of the torsional rigidity (GJ) of the metal wing box.

approach. The input data file created by MSC/XL programs is presented in section A1 of appendix (A). The simplified wing model was modeled to simulate the cantilevered boundary condition. The material properties (aluminum) with the Young modulus E=72400 N/mm^2, Shear modulus G=27000 N/mm^2, Poisson ratio of 0.33 and density of 2.8×10^{-6} Kg/mm^3 was used in the analysis.

6.3.1.3 Normal mode analysis:

The free vibration analysis (no damping) was carried out for the simplified metal wing box using the finite element MSC/NASTRAN [6.1] and CALFUN [6.2] programs. The average spanwise bending and torsional rigidities were used in the normal mode analysis in both programs. The methods of each program used in the analysis are as follows:

- In MSC/NASTRAN, this was done through the use of Solution 103 for normal mode analysis. The Lanczos method was applied to calculate the natural frequency and mode shapes in the frequency range of (0-300 Hz) of the simplified metal wing box model.
- In the case of CALFUN program, it uses the dynamic stiffness approach to calculate the natural frequency and mode shapes, in this approach, the mass and stiffness are combined in one matrix and the program is written for the unswept cantilever aircraft wing using finite element method as well.

6.3.1.3.1 Results and discussion:

The eigen values for the first four resonant frequencies for the metal wing box (FE models) were presented in table (6.2) for simplified metal wing using both MSC/NASTRAN and CALFUN programs. The results obtained from both programs have a very good agreement in both natural frequencies and mode shapes even though CALFUN program is mainly for unswept wing. In this metal wing there is a kink in the front spar at 1981.2 mm from the aircraft center line, hence the flexural axis and the center of gravity are not straight lines.

Table (6.1) Structural properties of the elements representing the simplified metal wing using CALFUN program.

Element No.	EI (Nm^2)	GJ (Nm^2)	M/L Kg/m	Ip/L Kgm	X m	L m
1	0.1144×10^6	0.9725×10^5	3.0630	0.03102	-0.035	0.4572
2	0.1879×10^6	0.1601×10^6	3.6146	0.06315	-0.052	0.4572
3	0.2780×10^6	0.2700×10^6	4.7036	0.11389	-0.049	0.4318
4	0.3901×10^6	0.4099×10^6	5.3974	0.17218	-0.084	0.4318
5	0.5413×10^6	0.5400×10^6	6.4300	0.25265	-0.085	0.4064
6	0.7486×10^6	0.7722×10^6	7.8215	0.40320	-0.085	0.3810
7	0.1035×10^7	0.1088×10^7	8.8724	0.49561	-0.047	0.3556
8	0.1258×10^7	0.1220×10^7	10.4137	0.65023	-0.053	0.3556
9	0.1622×10^7	0.1304×10^7	11.8900	0.84081	-0.093	0.2413
10	0.1926×10^7	0.1342×10^7	15.7127	0.83983	-0.049	0.0891
11	0.2201×10^7	0.1439×10^7	12.0780	0.85094	-0.056	0.3300
12	0.2751×10^7	0.1512×10^7	13.1185	0.99668	-0.060	0.3048
13	0.3186×10^7	0.1566×10^7	14.7870	1.08871	-0.040	0.2294
14	0.3316×10^7	0.1593×10^7	15.7800	1.11166	-0.040	0.1610
15	0.3425×10^7	0.1647×10^7	15.8125	1.12144	-0.051	0.1600
16	0.3472×10^7	0.1674×10^7	15.0727	1.12196	-0.055	0.1100

Where

- The elements are numbered from the tip wing to the root.
- EI and GJ are the spanwise bending and torsional rigidities respectively.
- M/L is the mass per unit length.
- Ip/L is the polar mass moment of inertia per unit length.
- X is the distance between the mass axis and the flexural axis (negative if the mass axis is behind the flexural axis).
- L is the length of the element.

Table (6.2) Comparison of results obtained from MSC/NASTRAN and CALFUN programs for the simplified model of the metal wing box.

Mode No.	FE (MSC/NASTRAN) Frequencies (Hz)	FE (CALFUN) Frequencies (Hz)	Structural mode
1	15.7	15.88	1st Bending mode
2	55.6	57.2	2nd Bending mode
3	119.0	126.5	1st Torsion mode
4	129.0	136.0	3rd Bending mode

After close inspection of the mode shapes of the simplified metal wing box, it was found that figure (6.6) shows the fundamental mode at 15.7 Hz is representative of the 1st bending mode. The second mode, at 55.6 Hz, represents the 2nd bending mode, figure (6.7). The third mode, at 119.0 Hz, represents the 1st torsion mode, figure (6.8). The fourth mode, at 129.0 Hz, represents the 3rd bending mode, figure (6.9).

It is interesting to find similar structural behaviour as in the composite wing box in chapter 5 except that, in chapter 5, the torsion-bending frequency mode was higher than the third bending frequency mode. However, in the simplified metal model the first torsion mode was lower than the third bending mode. Also there is a similar large frequency separation as well between the first bending mode (15.7 Hz) frequency and the second bending mode (55.6 Hz) frequency of the metal wing. Similarly, there is also a large separation between the second bending frequency mode (55.6 Hz) and the third mode which is the first torsion mode (119 Hz) frequency. It was noticed as well that the first torsion frequency mode (119 Hz) and the third bending frequency mode (129 Hz) of the metal model are close to each other as shown in figure (6.8) and (6.9).

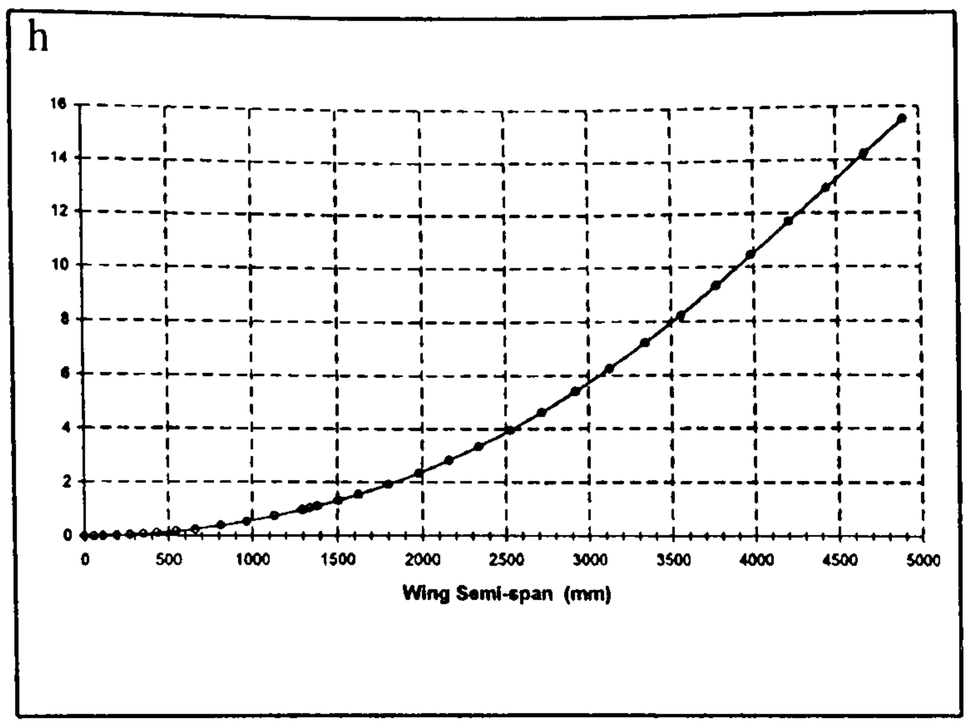

Fig. (6.6) 1st Bending Mode (15.7 Hz) for the simplified metal wing box (lumped beam).

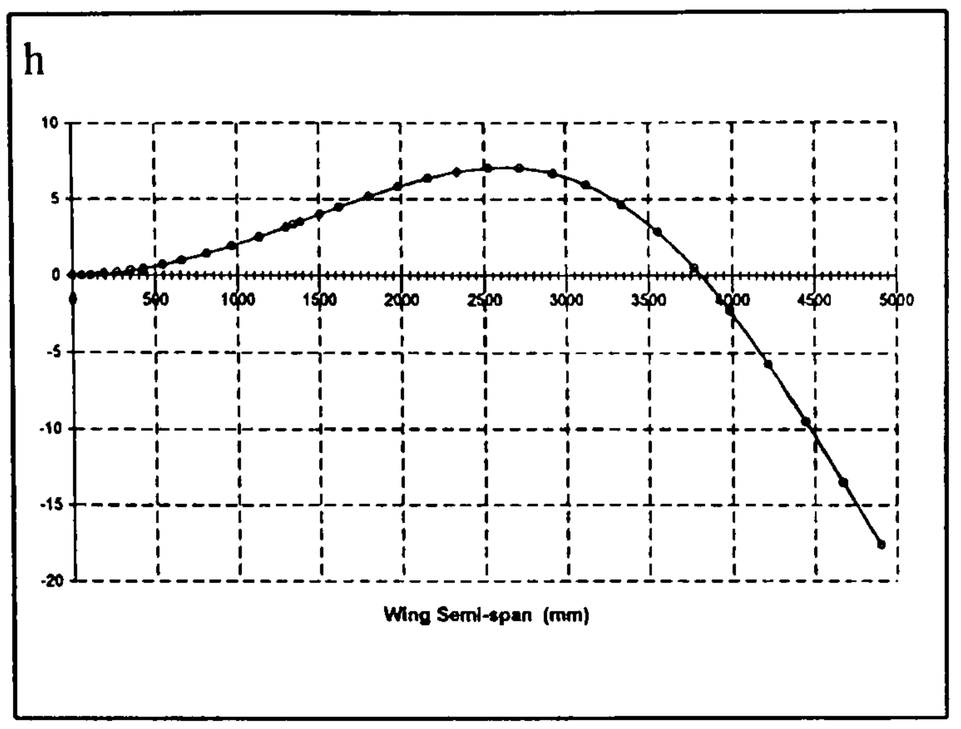

Fig. (6.7) 2nd Bending Mode (55.6 Hz) for the simplified metal wing box (lumped beam).

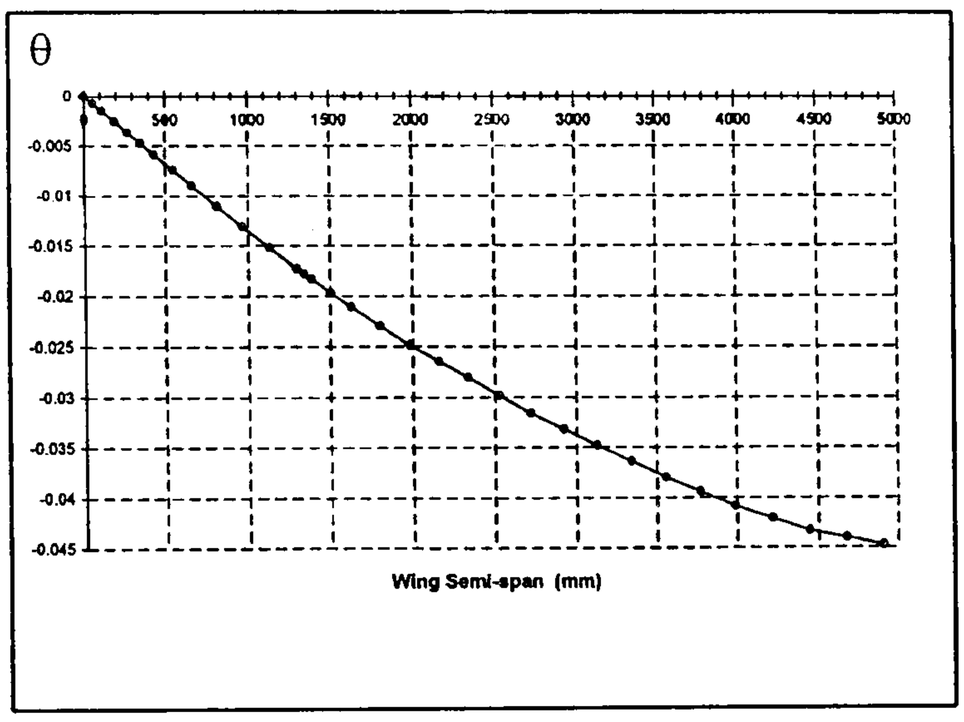

Fig. (6.8) 1st Torsion Mode (119.0 Hz) for the simplified metal wing box (lumped beam).

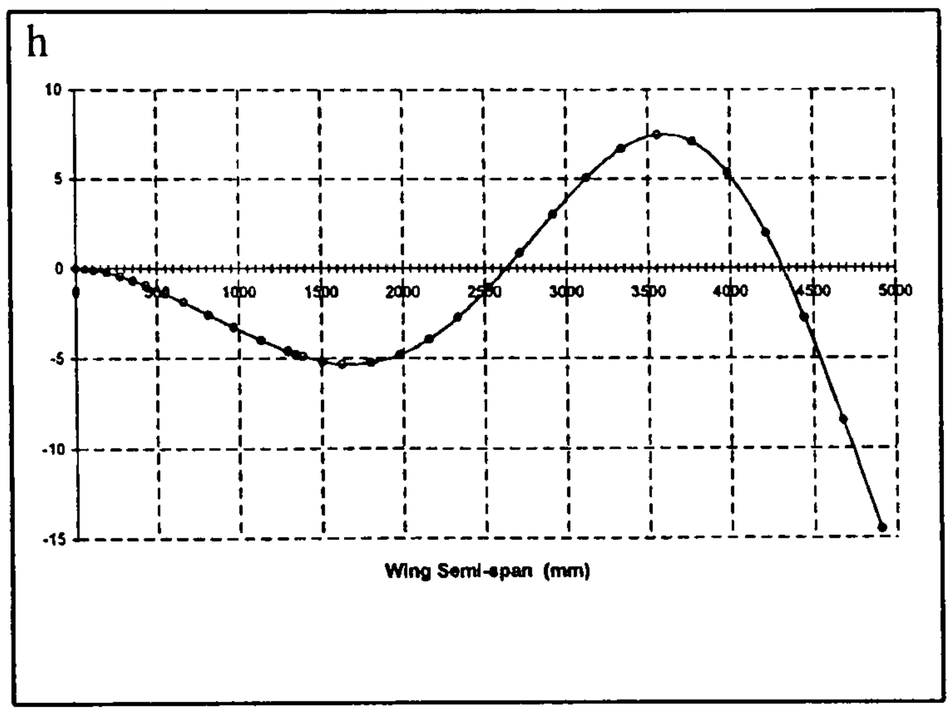

Fig. (6.9) 3rd Bending Mode (129 Hz) for the simplified metal wing box (lumped beam).

6.3.1.4 Flutter analysis:

6.3.1.4.1 Introduction:

In this section, the flutter analysis of the simplified metal model of the physical metal wing box of the Cranfield A1 aerobatic aircraft was carried out. The flutter speed was calculated using the finite element package MSC/NASTRAN V69. The Doublet-Lattice Method (DLM) was used to generate the aerodynamic coefficient matrix, and the interpolation of the structural grids with the aerodynamic grids was done using the theory of beam splines (SPLINE2 card).

Artificial structural damping of 2% was used as complex stiffness matrix in the flutter equation of motion.

The flutter solution method used to solve the flutter equations was the PK method and the relation of the flight velocity versus the total damping (structural and aerodynamic damping) and frequency were taken from the output file of the PK method and plotted using Microsoft EXCEL program.

6.3.1.4.2 Aerodynamic Modeling:

The aerodynamic modeling of the simplified metal model of the real A1 metal wing box configurations and the calculation of the aerodynamic forces was done using the Doublet-Lattice Method (DLM) for subsonic flow. The flutter input data file was created using the first four frequency modes shown in figures (6.6-6.9). A total of 40 aerodynamic elements, ten along the span and four along the chord with a reduced frequency (k) range from 0.001 to 0.8.

Two aerodynamic cards are used with the DLM, AERO card which specified the pertinent basic flight and geometric parameters for the dynamic aeroelastic analysis (flutter analysis). The other card was the CAER01, which is used to specify the location of the inner leading and the outer edge points of the structure and the mesh density along the wing span and chord.

A reference chord of 1207 mm (chord at 75% of the semi-span), fluid density at sea level and the default aerodynamic coordinate system No. 0 was specified through the AERO card. The aerodynamic coordinates system was with the X-axis is parallel and positive in the direction of the flow, Y-axis was along the span and Z-axis pointing positive upward.

The total semi-span including the tip fairing was 5029.2 mm from the aircraft center line. The inner leading edge of the metal wing at the aircraft center line with the chord of 2075.7 mm and the outer leading edge at 5029.2 mm a long the semi-span with the chord of 917.5 mm.

The aerodynamic and structural grids are connected through the use of the linear SPLINE2 and SET1 cards. All the aerodynamic elements were used in the interpolation with the selected structural grids.

The aerodynamic conditions, which are listed in the MKAER01 card, are used to specify the Mach number (0.4) and the reduced frequency range.

The selection of the structural grids to be involved in the interpolation with the aerodynamic grids is very important in the flutter analysis. Also the selection of the number of the aerodynamic boxes and the range of the induced frequency parameter to be used in the analysis is important in getting the optimum flutter point. All the above parameters are considered in the flutter analysis.

6.3.1.4.3 Flutter solution parameters:

The flutter analysis was carried out for the simplified A1 metal wing box with including the first four of the vibration modes (PARAM LMODES 4). Artificial structural damping of 2% was used as a complex stiffness matrix for the first four modes in the flutter equation of motion using the PARAM KDAMP-1 and TABDMP1 cards. The flutter equation was solved using the PK method [6.1].

The density ratio of 0.738609 (3.048 Km altitude), Mach number of 0.4 and a range of selected flight velocities were used in the flutter analysis through the use of solution number (145). The flutter input data file of the simplified metal wing box is presented in section A1 of appendix A.

6.3.1.4.4 Results:

Figure (6.10) and (6.11) show the variation of the flight velocity against the total damping and frequency respectively using MSC/NASTRAN. The flutter analysis of a cantilevered unswept wing modeled as isotropic plate is presented in chapter 8 using both MSC/NASTRAN and CALFUN. The flutter speed is identified from figure (6.10) and the corresponding mode called the flutter or critical mode (fourth mode). The flutter frequency was that of the critical mode at the flutter speed as shown in figure (6.11). The flutter speed and frequency of the simplified metal wing box was 658.031 m/sec and 41.995 Hz respectively as shown in figures (6.10-6.11).

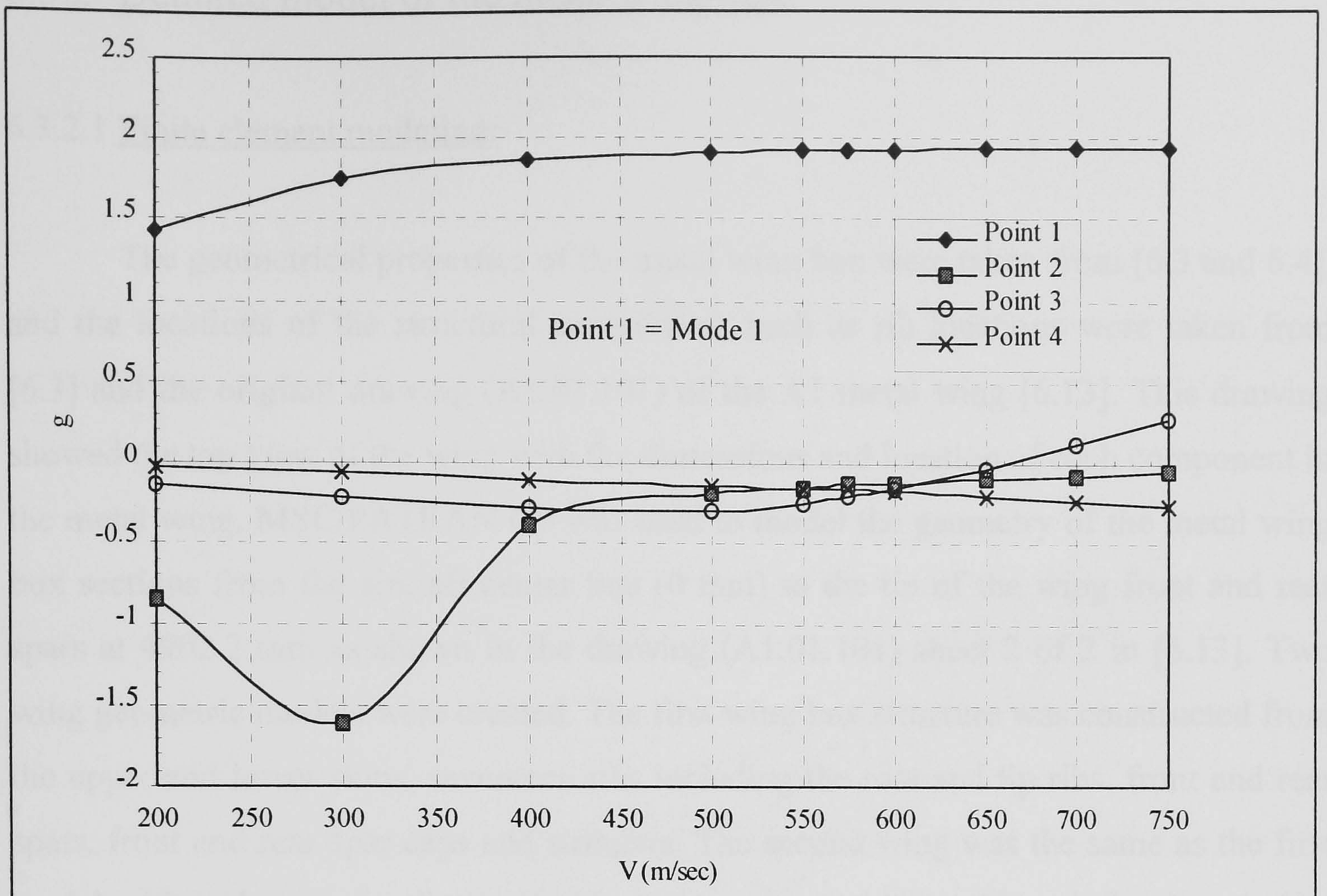

Fig. 6.10 Velocity vs Damping for the simplified metal wing box (lumped beam).

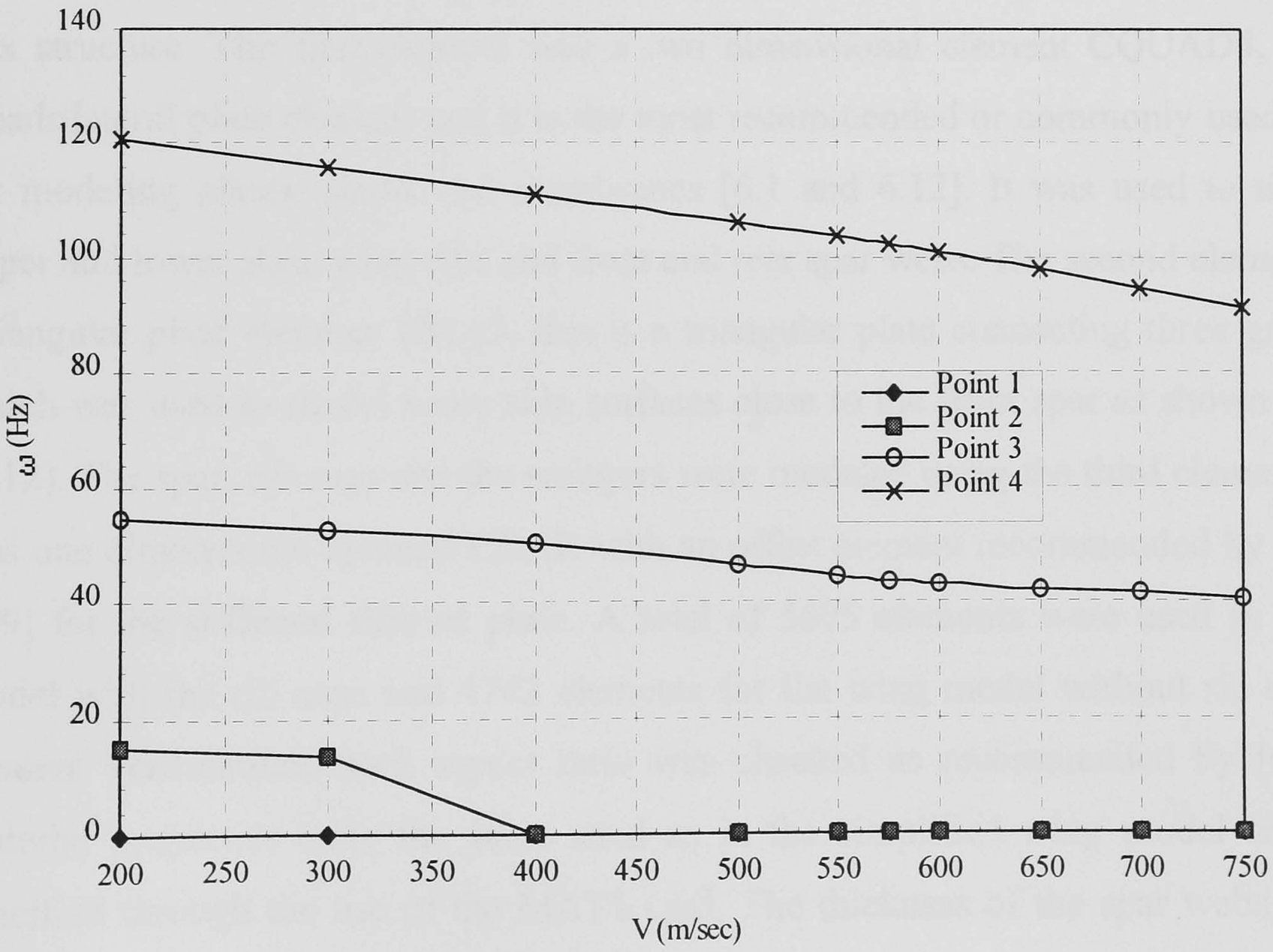

Fig. 6.11 Velocity vs Frequency for the simplified metal wing box (lumped beam).

Where Point 1 = Mode

6.3.2 Detailed model of the metal wing box:

6.3.2.1 Finite element modeling:

The geometrical properties of the metal wing box were taken from [6.3 and 6.4], and the locations of the structural components such as rib locations were taken from [6.3] and the original drawing (A1.01.101) of the A1 metal wing [6.13]. This drawing showed the top view of the wing with the dimensions and location of each component in the metal wing. MSC/PATRAN 6.0 was used to model the geometry of the metal wing box sections from the aircraft center line (0 mm) to the tip of the wing front and rear spars at 4902.2 mm as shown in the drawing (A1.01.101) sheet 2 of 2 in [6.13]. Two wing geometric models were created. The first wing box structure was constructed from the upper and lower skins, seventeen ribs including the root and tip ribs, front and rear spars, front and rear spar caps and stringers. The second wing was the same as the first model with including the rib caps (without the upper and lower ribs reinforcement plate A1.01.66). The lighting holes in the front and rear spar and in the ribs were not modeled in the wing geometry. Three different types of elements are used to mesh the metal wing box structure. The first element was a two dimensional element CQUAD4, this is a Quadrilateral plate element and it is the most recommended or commonly used element for modeling plates, shells and membranes [6.1 and 6.12]. It was used to model the upper and lower skin, wing ribs and front and rear spar webs. The second element was a Triangular plate element TRIA3, this is a triangular plate connecting three grid points which was used to model some skin surfaces close to the front spar as shown in figure (6.12). The spar, rib caps and the stringers were modeled using the third element, which was one dimensional element CBAR with an offset element recommended by [6.1] and [6.9] for the stiffened skin or plate. A total of 5695 elements were used in the wing model with the rib caps and 4742 elements for the wing model without rib caps. The element verifications such aspect ratio was checked as recommended by [6.1]. The material properties were the same used as in the simplified wing model and it was specified through the use of the MAT1 card. The thickness of the spar webs, ribs and skins were taken from the original drawing of the A1 metal wing [6.13] and specified through the use of the PSHELL card for the CQUAD4 and TRIA3 elements.

The area, moment of inertias about both axis and non structural mass of the spar and rib caps and stringers are calculated using the detailed geometry given by the original drawing of the metal wing. The above data's were then specified through the use of PBAR card, while the grids numbers, the components of orientation vector of the bar element and the offset were specified in the CBAR entry as presented in the input data file in appendixA. Both wing models are modeled to simulate the fixed free boundary condition.

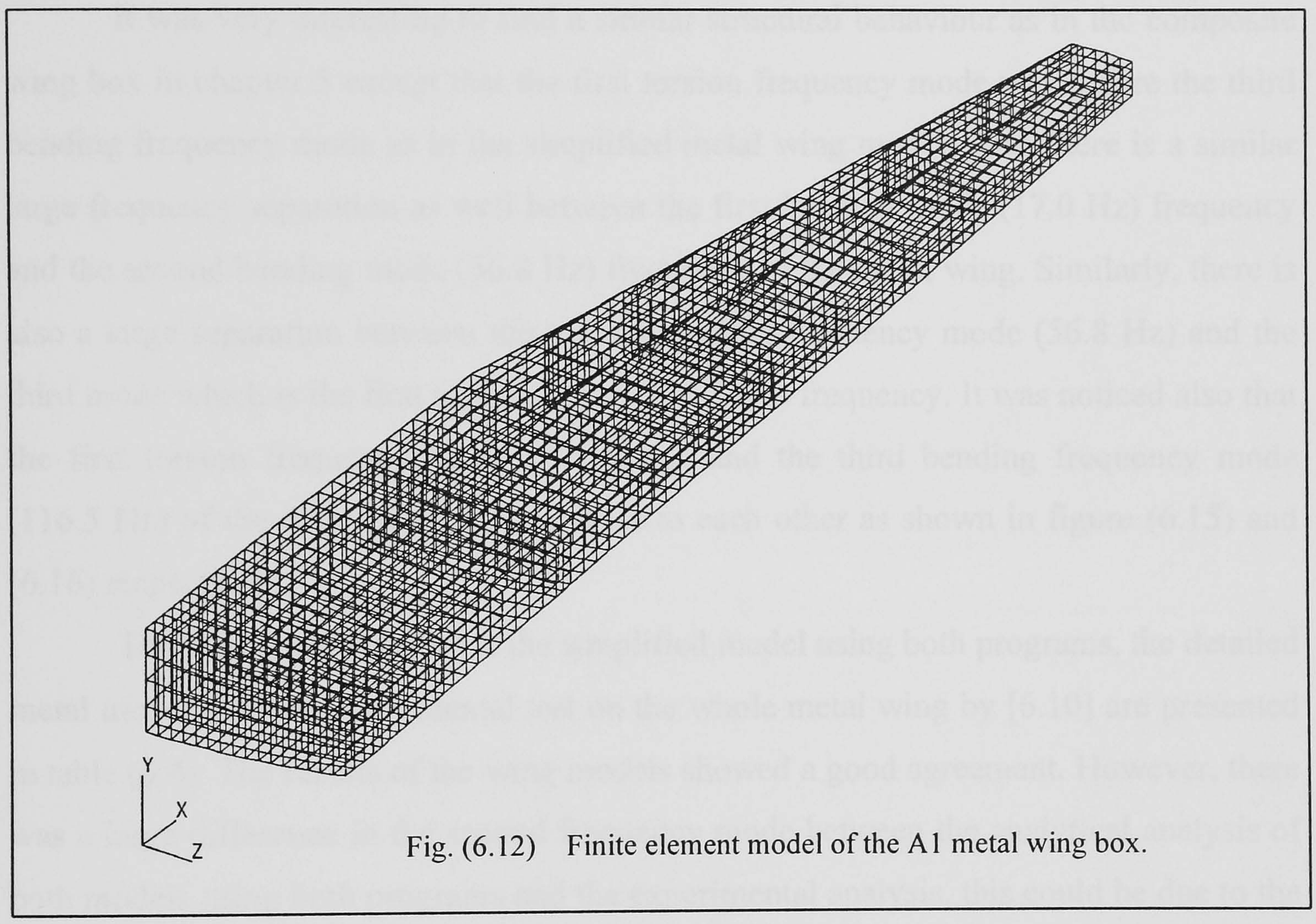

Fig. (6.12) Finite element model of the A1 metal wing box.

6.3.2.2 Normal mode analysis:

The natural frequencies and mode shapes with zero damping was found for both detailed models of the metal wing box using the finite element code MSC/NASTRAN through the use of Sol. 103. The analysis was done using the same method used in the simplified model of the metal wing box.

6.3.2.2.1 Discussion of results:

Table (6.3) presented the first four natural frequencies for the two wing models of the detailed metal wing box. After looking to the mode shapes of the wing structure, it appears that the first frequency mode was the fundamental bending mode, the second frequency mode was the second bending mode, the third frequency mode was the first torsion mode and the fourth frequency mode was the third bending mode as shown in figures (6.13-6.16) respectively.

It was very interesting to find a similar structural behaviour as in the composite wing box in chapter 5 except that the first torsion frequency mode was before the third bending frequency mode as in the simplified metal wing model. Also there is a similar large frequency separation as well between the first bending mode (17.0 Hz) frequency and the second bending mode (56.8 Hz) frequency of the metal wing. Similarly, there is also a large separation between the second bending frequency mode (56.8 Hz) and the third mode which is the first torsion mode (111.5 Hz) frequency. It was noticed also that the first torsion frequency mode (111.5 Hz) and the third bending frequency mode (116.5 Hz) of the detailed model are close to each other as shown in figure (6.15) and (6.16) respectively.

The results obtained from the simplified model using both programs, the detailed metal model and the experimental test on the whole metal wing by [6.10] are presented in table (6.4). The results of the wing models showed a good agreement. However, there was a large difference in the second frequency mode between the analytical analysis of both models using both programs and the experimental analysis, this could be due to the following as mention in [6.10]:

- The simplicity or the method used was not therefore particularly precise.
- The very limited time was available for conducting an extensive experimental analysis on the A1 aerobatic metal wing.

From table (6.4), it can be seen that a good agreement was obtained even with simplifying the wing model structure. Therefore, simplifying the wing structure will be very useful and give a good representation of the real structure especially at early stage of the structural design. This leads to a good representation of dynamic characteristics

(natural frequency and mode shapes) and then to the Aeroelastic behaviour of the wing structure.

Table (6.3) Comparison of natural frequencies between the two detailed metal model.

Mode No.	Detailed model[1] (MSC/NASTRAN) Frequency (Hz)	Detailed model[2] (MSC/NASTRAN) Frequency (Hz)
1	17.22	17.0
2	57.60	56.80
3	112.11	111.50
4	118.01	116.50

Table (6.4) Comparison of natural frequencies of the metal wing box.

Mode No.	Simplified model (MSC/NASTRAN) Frequency (Hz)	Simplified model (CALFUN) Frequency (Hz)	Detailed model[2] (MSC/NASTRAN) Frequency (Hz)	Experimental analysis [6.10] Frequency (Hz)
1	15.70	15.88	17.0	16.70
2	55.6	57.20	56.80	45.4
3	119.0	126.5	111.50	-
4	129.0	136.0	116.50	120.0

1 This is with out including the rib caps into the metal model.
2 This is with including the rib caps into the metal model.

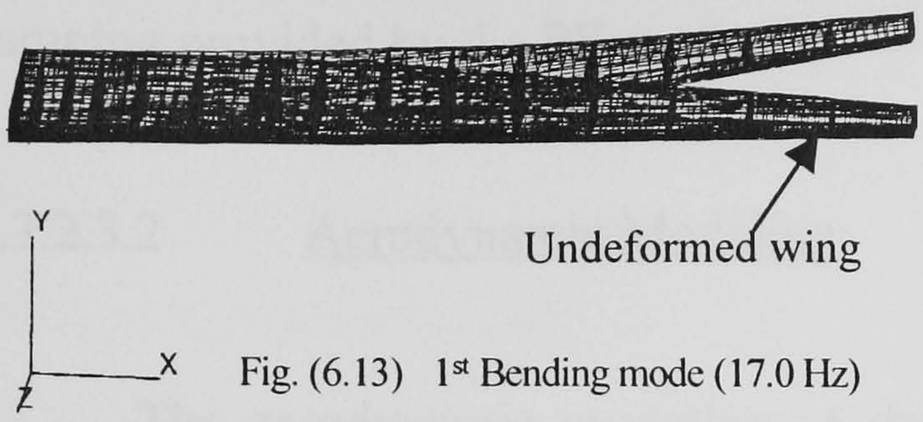

Fig. (6.13) 1st Bending mode (17.0 Hz)

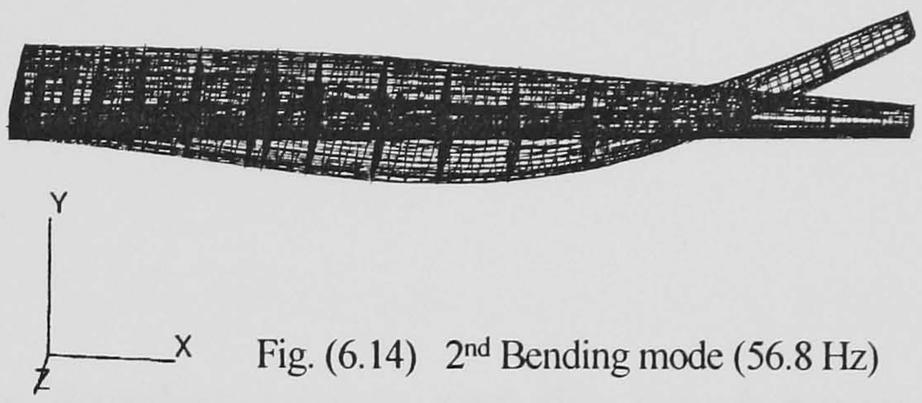

Fig. (6.14) 2nd Bending mode (56.8 Hz)

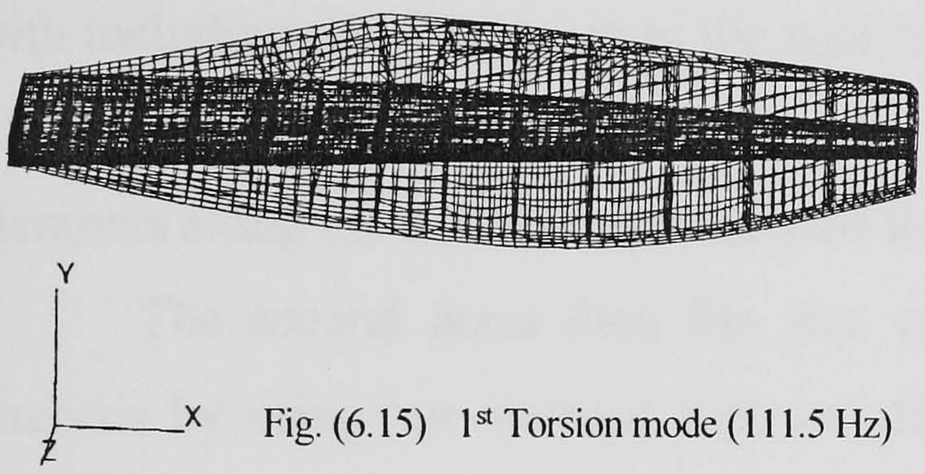

Fig. (6.15) 1st Torsion mode (111.5 Hz)

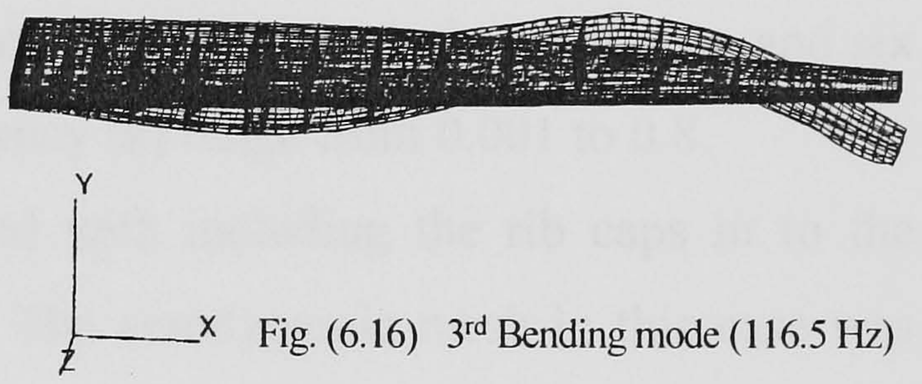

Fig. (6.16) 3rd Bending mode (116.5 Hz)

6.3.2.3 Flutter analysis:

6.3.2.3.1 Introduction:

The analysis of the two detailed A1 metal wig box was performed using the finite element code MSC/NASTRAN. The aerodynamic modeling was done using the same method used in the simplified metal wing model (DLM). The Doublet-Lattice Method (DLM) was used to generate the aerodynamic coefficient matrix, and the interpolation of the structural grids with the aerodynamic grids was done using the theory of surface splines (SPLINE1 card).

The same value of structural damping (2%) as in the simplified model was used as complex stiffness matrix in the flutter input data file through the same card mentioned in the simplified model.

PK method was used to solve the flutter equations and the flutter speed was then identified from out put results, which show the variation of the flight speed and the total damping provided by the PK method.

6.3.2.3.2 Aerodynamic Modeling:

The aerodynamic modeling of the two detailed models and the aerodynamic forces were calculated using the same method used in simplified model. The first four vibration modes shown in figures (6.13-6.16) are used in the flutter analysis. Three input data files were created for the flutter analysis. The first input data file was created with including the rib caps in to the analysis by using bar element with an offset. In this file, a total of 120 aerodynamic elements, twenty elements along the semi-span and six elements along the chord with a reduced frequency (k) range from 0.001 to 0.8.

The second input data file was created with including the rib caps in to the analysis by using bar element with an offset. The aerodynamic mesh in this case was with a total of 320 aerodynamic elements, forty elements along the semi-span and eight elements along the chord with a reduced frequency (k) range from 0.001 to 0.8.

The third input data file was created with out including the rib caps in to the analysis. In this case, a total of 120 aerodynamic elements, twenty elements along the semi-span and six elements along the chord with a reduced frequency (k) range from 0.001 to 0.8.

An aerodynamic coordinates system No. 1 was created using CORD2R card with the X-axis is parallel and positive in the direction of the flow, Y-axis was along the span and Z-axis pointing positive upward. The locations of the inboard and outboard leading edge points were identified using coordinate system No. 1 in the AERO card; reference chord and the flight conditions were the same as in the simplified metal model.

The aerodynamic and structural grids are connected through the use of the surface SPLINE1 and SET1 cards. All the aerodynamic elements were used in the interpolation with the selected structural grids.

The selection of the structural grids in the flutter analysis is very important. Also the selection of the number of the aerodynamic boxes to be used in the analysis is

important in getting the optimum flutter point. All the above parameters are considered in the flutter analysis as presented in table (6.5).

6.3.2.3.3 Flutter solution parameters:

The flutter analysis was performed using Sol. (145) for the three input data files for the detailed metal wing box. The analysis was done using the first four of the vibration modes (PARAM LMODES 4). Artificial structural damping of 2% was used as a complex stiffness matrix for the first four modes in the flutter equation of motion using the PARAM KDAMP-1 and TABDMP1 cards. The flutter equation was solved using the PK method [6.1].

6.3.2.3.4 Discussion of results:

Table (6.5) presented the variation of the flutter speed with changing the aerodynamic mesh and induced frequency parameter for the detailed metal wing box. This was identified from the variation of the flight speed with the total damping and frequency given by the out put file of the PK method provided by MSC/NASTRAN. This is the speed at which the total damping is zero [6.1and 6.11].

It can be seen from table (6.5) that the differences between the four input data files are very small and less than 2%. The flutter speed obtained from the simplified model was agreed very well with the flutter speed obtained from the detailed model with less than 1% error and less than 4% for the flutter frequencies. As seen from the results, simplifying the structure will gave a good results and representation of the detailed structure at minimum cost providing that the right method was used to calculate the structural properties. This approach will be very useful to the structural designer at the early design stage of the structure.

Table (6.5) Flutter speed of the detailed A1 metal wing box.

Aerodynamic Elements		Induced Frequency Parameter (k)	Flutter speed (m/sec)	Flutter Frequency (Hz)	Type of wing model
Spanwise	Chordwise				
20	6	0.001 to 0.8	665.30	42.345	Model[1]
40	8	0.001 to 0.8	662.552	40.399	Model[2]
40	8	0.001 to 1.8	662.560	40.40	Model[2]
20	6	0.001 to 0.8	655.231	41.546	Model[2]

Where Model[1] Metal wing box model without including the rib caps.

Model[2] Metal wing box with including the rib caps.

References

6.1 MSC/NASTRAN Hand book for Aeroelastic analysis, R.H. MacNeal (ed), The MacNeal-Schwendler Corporation, California U.S.A.

6.2 Banerjee, J.R. "CALFUN is a program for CALculation of Flutter speed Using Normal modes.", The city University, London, 1988.

6.3 Potter, J.G. Design of aerobatic aircraft wing. MSc Thesis, 1968/1969, Cranfield University.

6.4 Abbot, I.H. and Von Doenhoff, A.E. Theory of wing sections. 1959, Dover Publications, New York.

6.5 Bruhn, E.F. Analysis and design of flight vehicle structures June 1973, Jacobs Publishing Inc, U.S.A.

6.6 DES 8733 Shear flows in Unsymmetrical two-cell box section. 1987, Cranfield University.

6.7 Niu, M.C. Airframe stress analysis and sizing. 1997, Hong Kong Conmilit Press Ltd.

6.8 Gere, J.M. and Timoshenko, S.P. Mechanics of materials. 2nd ed., 1985, PWS Publishers.

6.9 Taig, I.C. Modeling for the finite element method. In AGARD Practical application of finite element analysis to aircraft structure design, 1986, 18p.

6.10 Stacey, J.A. The development of finite element aeroelastic calculation package and its application to the Cranfield Aerobatic Aircraft –A1. MSc Thesis, 1976, Cranfield University.

6.11 Loring, J.S. General approach to the flutter problem. AIAA selected reprint series, Aerodynamic flutter, Volume V, March 1969.

6.12 Miller M.P. Getting started with MSC/NASTRAN 1st edition, 1993, The MacNeal-Schwendler Corporation, U.S.A.

6.13 Original drawing of the Cranfield A1 aerobatic wing structure. (1978) "A1.01.02, A1.01.03, A1.01.11, A1.01.17, A1.01.23, A1.01.66, and A1.01.101" College of aeronautic, Cranfield University.

CHAPTER 7

DYNAMIC AND AEROELASTIC ANALYSIS OF THE CRANFIELD A1 COMPOSITE WING BOX

7 Dynamic and Aeroelastic analysis of the detailed composite wing box of the Cranfield A1 Aerobatic Aircraft:

7.1 Introduction:

In this section, the normal mode analysis and flutter analysis was carried out for the Cranfield A1 composite wing box with the original laminates lay-up, as used in the construction of the composite wing box for the post buckling analysis (as mentioned in chapter 5). The analysis was done using the finite element code MSC/NASTRN [7.1]. The airfoil sections of the wing at the root were taken as NACA 23015 and at the tip as NACA 23012 [7.2] and [7.3], as stated in chapter 5.

The finite element modeling of the composite wing box was conducted using MSC/PATRAN 7.0, the pre and postprocessor for MSC/NASTRAN. The material properties and laminate lay-ups of the composite wing box were taken from [7.2] as presented in table (7.1) and (7.2). The wing box was modeled to simulate the cantilevered boundary condition, which is closed to the physical fuselage-wing attachment. The natural frequencies and mode shapes (with zero structural damping) of the wing were calculated using the Lanczos method through solution number 103 available in [7.1]. The mode shapes were plotted using UNIMAP 2000 software as shown in figures (7.4-7.9) for the coarse model.

Aerodynamic modeling of the wing as a first step towards the flutter analysis after the structural modeling was done applying the Doublet-Lattice Method (DLM) in the subsonic speed. Structural damping was calculate from the experimental work using the PC Modal Analysis Software (PCMAS). The damping characteristics were then used in the flutter analysis as complex stiffness matrix through the use of the SDAMP card in the case control deck and both PARAM (KDAMP –1) and TABDMP1 in the input bulk data deck of the composite wing box.

The PK method was selected to solve the flutter equation of motion through the use of the flutter solution number 145. The flutter speed (velocity at which the damping is zero) was identified from the variations of the flight velocity against the total

damping. Subsequently the flutter frequency (at flutter speed for particular mode) was identified from the variations of the flight velocity against frequency for the coarse model, which was illustrated in figure (7.10-7.11).

7.2 Description of the Composite wing box:

A description of the composite wing box was given in chapter 5. For further details the reader is referred to [7.2]. Figure (5.6) of chapter 5 illustrates the primary dimensions of the composite wing box. The description of the actual wing, which was made from aluminum and other wing parameters were presented in figure (6.1) of chapter 6 and will not be repeated here.

7.3 Finite Element model development of composite wing box:

To meet design requirements, the aircraft wing is essentially constructed as a structure composed of a upper and lower skins, front and rear spars, ribs and stringers and some times intercastol stringers are embedded to stiffen the wing structure.

A methodical approach was applied, by first generating a model that simulated the physical, material and the geometric properties of the wing box, but was represented as a beam with a lumped masses modeled along the flexural axis of the model using MSC/NASTRAN and CALFUN programs (see chapter 6). This was then replaced by a more detailed and consequently more representative wing model having metallic properties. Both of these wing boxes made from isotropic material were compared and were in a good agreement (chapter 6). Then three wing models for the composite wing box were generated in the same way as in the metal wing box with modification in the material and geometric properties with the same airfoil sections as in the metal wing box.

The first of the three models of the composite wing box was created starting with the simplified model to the fine detailed wing model. The simplified wing box was constructed from the upper and lower skins, front and rear spars webs filled with a foam, front and rear spars stiffeners (caps) filled with a foam as well and a total of eight

ribs. Two of these ribs which are located at 1981 and 3706 mm are filled with a foam in a portion close to the rear spar for the aileron hinge brackets as shown in details in [7.2]. This simplified model was considered as coarse mesh, but was not representing the construction of the real aircraft wings. The second wing model was the same as the simplified model, but in this case with adding all the upper and lower stringers (Hat section). The Hat section was filled with foam including the anti-peel strip at all the stringers as shown in [7.2] and the front and rear spar caps. The third wing box model was the same as the second model, but in this case the model was created with a very fine mesh (more elements used compared with both above models). The trade off between model complexity and simplicity and the cost of the analysis and the accuracy was clearly an important issue considered. The main purpose of this approach was to ensure a consistency in the development and means of verification or checking the results at an early stage of the research starting with the first simplified composite wing box model to the fine detailed composite wing box model. The finite element model for the detailed coarse mesh and the detailed fine mesh of the composite wing box are shown in figure (7.2 and 7.3) respectively.

7.3.1 Types of Elements used in the FE model:

The finite element coarse and fine detailed models of the composite wing box were shown in figure (7.2) and (7.3). In these FE models, three types of elements were used in the modeling of the composite wing box. The first element was CQUAD4 plate element, which was used in modeling of the following components of the wing structure:

- upper and lower skin surfaces of the wing
- stringers (hat sections)
- front and rear spar webs, stiffeners and caps
- wing ribs

The CQUAD4 is a quadrilateral plate element and is represented by the fully coupled laminate equations, which are shown in equations (3.1 and 3.2) of chapter 3 and in Ref. [7.3]. This is a four node element and is the most commonly used and

recommended by [7.1]. The CQUAD4 plate element was represented the above structural components through the use of the PCOMP and MAT8 cards. For more details about the CQUAD4 and other types of elements, the reader shall refer to [7.1].

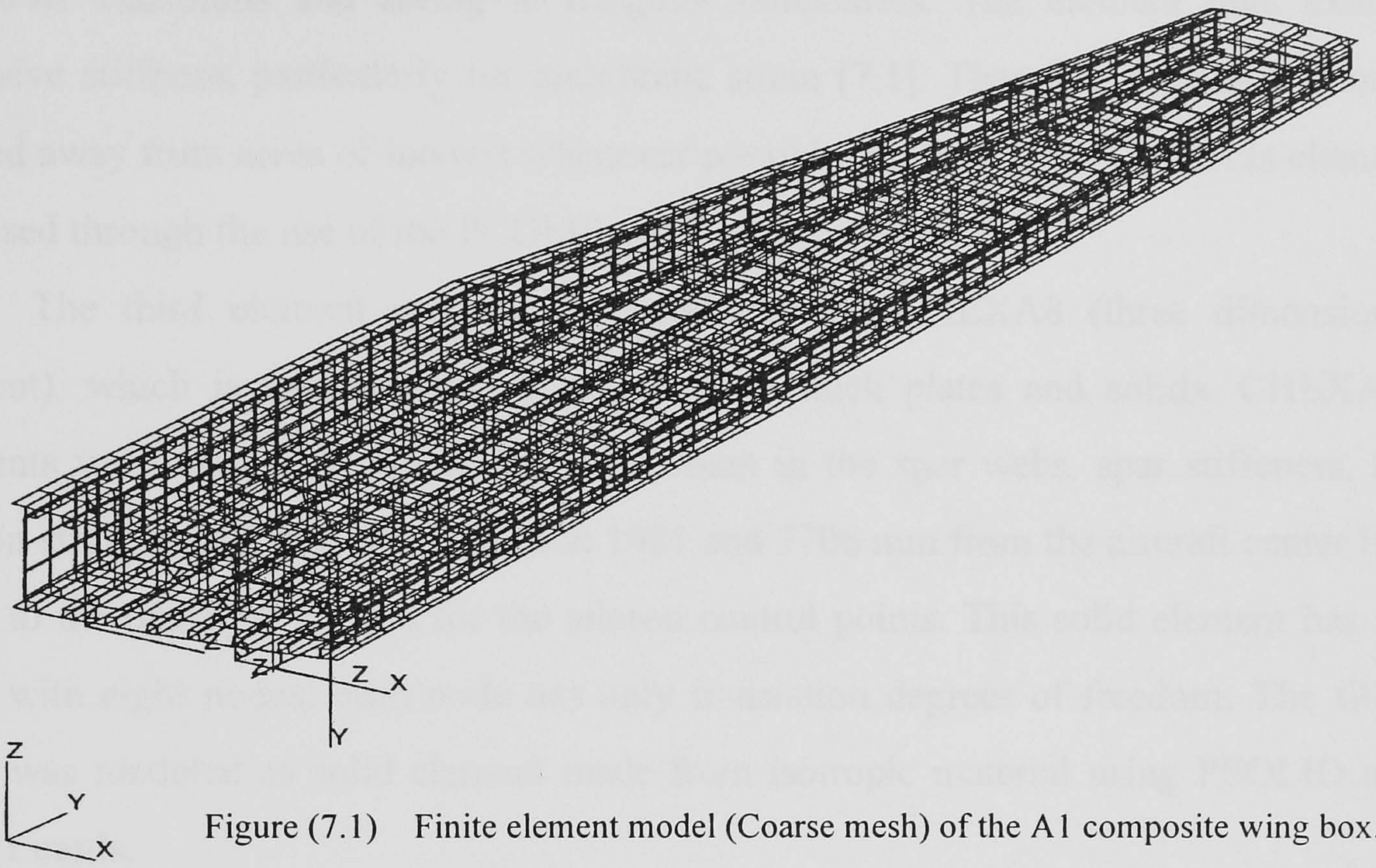

Figure (7.1) Finite element model (Coarse mesh) of the A1 composite wing box.

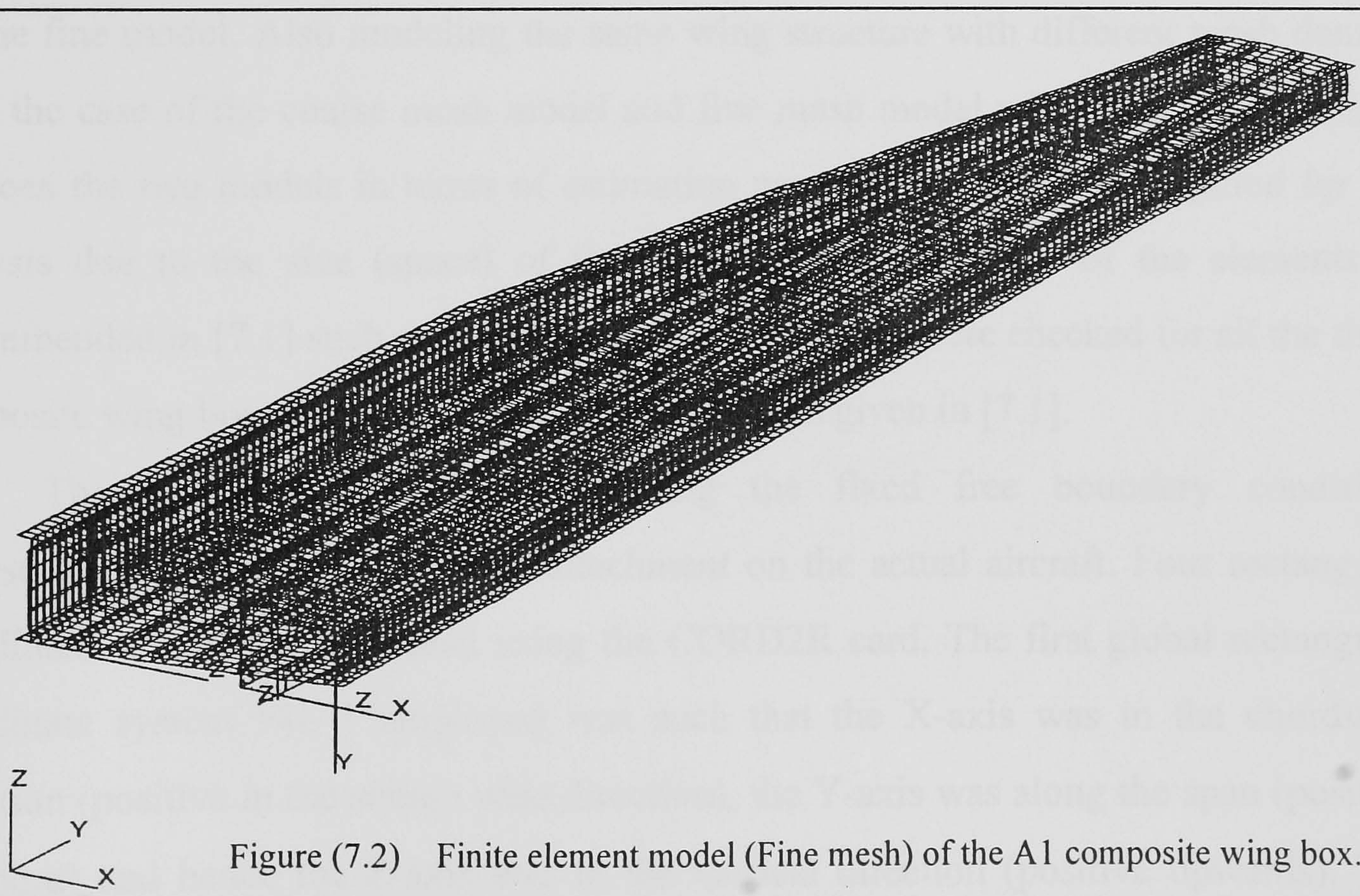

Figure (7.2) Finite element model (Fine mesh) of the A1 composite wing box.

The second type of elements used in the modeling of the composite wing box was the Triangular Plate Element (CTRIA3). It was used in the modeling of the small portions of the upper and lower skin, which close to the front spar due to the kink of the front spar.(see figure 7.2). This is a three node element, which is most commonly used for mesh transitions and filling in irregular boundaries. The element may exhibit excessive stiffness, particularly for membrane strain [7.1]. Therefore CTRIA3s should located away from areas of interest whenever possible. Similarly, the CTRIA3s element was used through the use of the PCOMP and MAT8 cards.

The third element used was a solid element CHEXA8 (three dimensional element), which is usually used in modeling of thick plates and solids. CHEXA8s elements were used to represent the filled foam in the spar webs, spar stiffeners, hat section stringers and two ribs located at 1981 and 3706 mm from the aircraft center line close to the rear spar portion for the aileron control points. This solid element has six sides with eight nodes; each node has only translation degrees of freedom. The filled foam was modeled as solid element made from isotropic material using PSOLID and MAT1 cards.

Different types of mesh seeds were generated along the span and the chord of the composite wing box as shown in figure (7.2) for the coarse wing model and figure (7.3) for the fine model. Also modeling the same wing structure with different mesh density as in the case of the coarse mesh model and fine mesh model will show the difference between the two models in terms of estimation accuracy and the time required for the analysis due to the size (space) of the model. The verification of the elements as recommended in [7.1] such as aspect ratio and skew angle were checked for all the three composite wing boxes with the recommended figures given in [7.1].

The wing models were simulating the fixed free boundary condition, representative of the wing-fuselage attachment on the actual aircraft. Four rectangular coordinate systems were created using the CORD2R card. The first global rectangular coordinate system No. 1 employed was such that the X-axis was in the chordwise direction (positive in the stream wise direction), the Y-axis was along the span (positive outboard) and hence the Z-axis was in the vertical direction (positive upwards). The second Cartesian coordinate system No. 2 employed was such that the X-axis was in the

chordwise direction (positive in the stream wise direction), the Y-axis was along the span (positive outboard) and hence the Z-axis was in the vertical direction (positive upwards). This local coordinate system (2) was used as a material coordinate system (longitudinal axis of the fibre) for the wing ribs in the PCOMP card. The third Cartesian coordinate system No. 3 was used to define the material coordinate system (longitudinal axis of the fibre) through the use of PCOMP card for the upper and lower skin and stringers such that the X-axis was in the spanwise direction (positive outboard), the Y-axis was in the vertical direction (positive upwards) and hence the Z-axis was in the chordwise direction (positive in the streamwise direction). The fourth Cartesian system No. 4 was the same as coordinate No. 3, which was used to define the material longitudinal axis of the fibre for the front and rear spar webs.

The material coordinate system, which shows the direction of the fibre angle θ was identified in [7.1] by the following:

- The longitudinal direction x_m of the fibre is the projection of the x-axis of the coordinate system onto the surface of the element.
- The z_m axis of the material coordinate system is the same as the z_e (element axis).
- The positive y_m axis of the material coordinate system was then found by the right hand rule for a positive fibre angle θ as shown in figure (7.3).

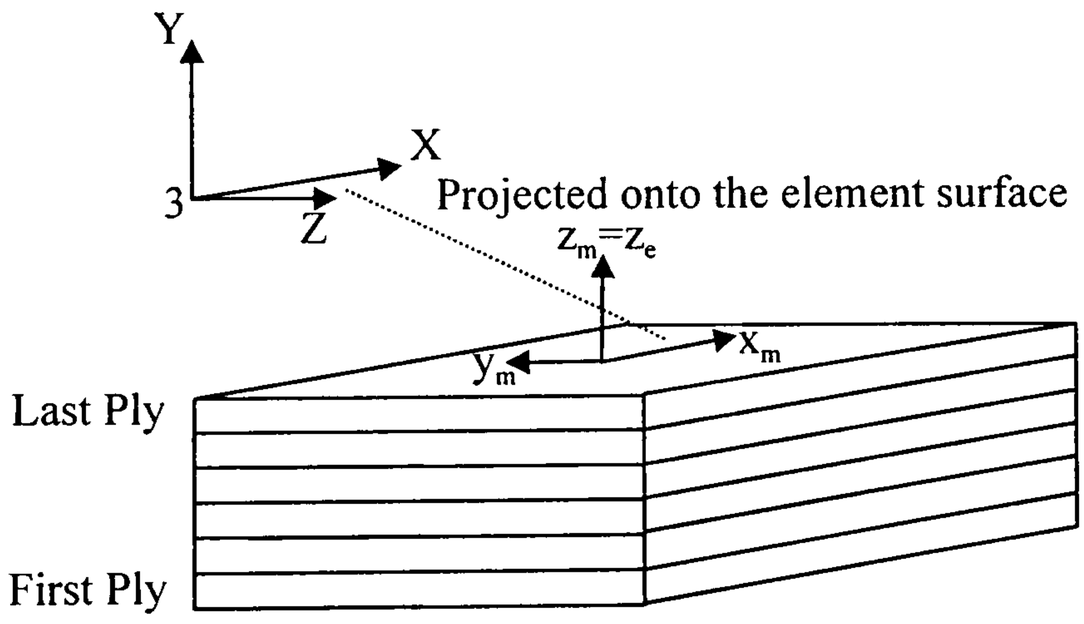

Figure (7.3) Fibre orientation system used in MSC/NASTRAN.

The method of defining the material coordinate systems of the composite elements were identified and explained in [7.1].

7.4 Material Properties:

Four different types of material were used in the modeling of the composite wing box [7.1]. The material properties of the four material used in the construction of the composite wing box are presented in table (7.1). Two of these materials are made from the XAS, which is the Ciba-Geigy 913 carbon/epoxy prepreg for unidirectional material and unidirectional woven material. The other two were made from a polymethylacrylate foams (Rohacell 51 and 71). Table (7.2) shows the laminate configurations used in the A1 composite wing box. The unidirectional woven material was used for all the outer fibre angle of ±45 degrees and for the anti-peel strip made for the top of the Hat stringers (0°/90°) in the original laminates of the composite wing box shown in table (7.2). The unidirectional material was used for all the inner plies of zero degree (longitudinal direction along the span) as presented in table (7.2). The polymethylacrylate foam (Rohacell 51) was considered as isotropic material and it was used to model the form in the front and rear spar webs and the two ribs located at 1981 and 3706 mm from the aircraft center line for the aileron control points. While the polymethylacrylate foam (Rohacell 71) was used in the modeling of the filled foam of the upper and lower stringers, spar stiffeners. The ply thickness of the unidirectional woven material was 0.17 mm and 0.127 mm for the unidirectional material. The generations of the structural materials for the composite components were done through the use of the MAT8 and PCOMP cards, and through the PSOLID and MAT1 cards for the polymethylacrylate foams.

7.5 Normal Mode Analysis:

7.5.1 Introduction:

Normal mode analysis or real eigen value (undamped free vibrations) was conducted by using the Lanczos method, via MASC/NASTRAN, Sol (103) [7.1] for the three composite wing box models using the material properties and the laminates lay-ups presented in table (7.1 and 7.2) respectively. This method was used to determine the

basic dynamic characteristics of the composite wing box (natural frequency and mode shapes) for the three models starting from the simplified to the fine mesh wing model.

Table (7.1) Material properties of the A1 composite wing box.

Material type /Properties	XAS (UD) Materials	XAS (UD WOVEN) Matreials	Rohacell (R51)	Rohacell (R71)
E_{11} (N/mm^2)	130×10^3	69×10^3	0.07×10^3	$.092\times10^3$
E_{22} (N/mm^2)	9.0×10^3	65×10^3	0.07×10^3	0.092×10^3
ν_{12}	0.28	0.10	0.3	0.3
G_{12} (N/mm^2)	4.8×10^3	5.5×10^3	0.021×10^3	0.03×10^3
Density (ρ) Kg/mm^3	1.61×10^{-6}	1.65×10^{-6}	0.05×10^{-6}	0.07×10^{-6}
0 thermal e/c	-0.1×10^{-6}	5.0×10^{-6}	33×10^{-6}	35×10^{-6}
90 thermal e/c	28×10^{-6}	5.0×10^{-6}	33×10^{-6}	35×10^{-6}

Where XAS is Ciba-Geigy 913 carbon/epoxy prepreg,
R51 and R71 are Rohacell 51 and 71 polymethylacrylate foams respectively [7.2].
UD is Uni-Directional

Table (7.2) Laminate lay-ups configurations of the A1 composite wing box.

Span-wise / Laminate	0- 431 mm	431- 868 mm	868 - 1411 mm	1411-1981 mm	1981 - 2556 mm	2556 - 3131	3131 - 3706	3706 - 4281	4281 - 4902
Upper skin	$[\pm 45_2 / 0_2]_s$	$[\pm 45_2 / 0_2]_s$	$[\pm 45_2 / 0_2]_s$	$[\pm 45_2 / 0]_s$	$[\pm 45_2 /0]_s$	$[\pm 45/0]_s$	$[\pm 45/0]_s$	$[\pm 45]_s$	$[\pm 45]_s$
Upper top Hat stringers	$[\pm 45_2 / 0_2]_s/0/90$	$[\pm 45_2 / 0_2]_s/0/90$	$[\pm 45_2 / 0_2]_s/0/90$	$[\pm 45_2 / 0]_s/0/90$	$[\pm 45_2 /0]_s/0/90$	$[\pm 45/0]_s/0/90$	$[\pm 45/0]_s/0/90$	$[\pm 45]_s/0/90$	$[\pm 45]_s/0/90$
lower skin	$[\pm 45_2 / 0]_s$	$[\pm 45_2 / 0]_s$	$[\pm 45_2 / 0]_s$	$[\pm 45_2 / 0]_s$	$[\pm 45/0]_s$	$[\pm 45/0]_s$	$[\pm 45]_s$	$[\pm 45]_s$	$[\pm 45]_s$
Lower top Hat stringers	$[\pm 45_2 / 0]_s/0/90$	$[\pm 45_2 / 0]_s/0/90$	$[\pm 45_2 / 0]_s/0/90$	$[\pm 45_2 / 0]_s/0/90$	$[\pm 45/0]_s/0/90$	$[\pm 45/0]_s/0/90$	$[\pm 45]_s/0/90$	$[\pm 45]_s/0/90$	$[\pm 45]_s/0/90$
Upper stiffeners side wall	$\pm 45_2$	$\pm 45_2$	$\pm 45_2$	$\pm 45_2$	$\pm 45_2$	±45	±45	±45	±45
Lower stiffeners side wall	$\pm 45_2$	$\pm 45_2$	$\pm 45_2$	$\pm 45_2$	±45	±45	±45	±45	±45
upper stiffeners caps	$[\pm 45/0_{15}/\pm 45]$	$[\pm 45/0_{15}/\pm 45]$	$[\pm 45/0_{15}/\pm 45]$	$[\pm 45/0_{15}/\pm 45]$	$[\pm 45/0_{13}/45]$	$[\pm 45/0_{12}]$	$[\pm 45/0_{10}]$	$[\pm 45 /0_9]$	$[\pm 45/0_8]$
Lower stiffeners caps	$[\pm 45 / 0_{13} /\pm 45]$	$[\pm 45 / 0_{13} /\pm 45]$	$[\pm 45 / 0_{12} /\pm 45]$	$[\pm 45 / 0_{12} /\pm 45]$	$[\pm 45 / 0_{12}]$	$[\pm 45 / 0_9]$	$[\pm 45 / 0_9]$	$[\pm 45 / 0_7]$	$[\pm 45 / 0_5]$
Front & Rear Spar webs	$[\pm 45_2/ F51/\pm 45_2]$	$[\pm 45_2/F51/\pm 45_2]$	$[\pm 45_2/F51/\pm 45_2]$	$[\pm 45_2/F51/\pm 45_2]$	$[\pm 45_2/F51/\pm 45_2]$	$[\pm 45_2/F51/\pm 45_2]$	[±45/F51/±45]	[±45 /F51/±45]	[±45 /F51/±45]
Spar flanges	$[\pm 45_2]$	$[\pm 45_2]$	$[\pm 45_2]$	$[\pm 45_2]$	$[\pm 45_2]$	$[\pm 45_2]$	[±45]	[±45]	[±45]

Where $[\pm 45_2/0]_s$ is $[+45/-45/+45/-45/0]_s$

Table (7.2) Laminate lay-ups configurations of the A1 composite wing box.

Span-wise/ Laminate	431 mm	868 mm	1411 mm	1981 mm	2556 mm	3131 mm	3706 mm	4281 mm
Rib	$[\pm 45_2]_s$	$[\pm 45_2]_s$	$[\pm 45_2]_s$	0-127 mm from R.S upper and lower sections $[\pm 45_4/\ 0_4\ /\ F51/\pm 45_2/0_4]$	$[\pm 45_2]_s$	$[\pm 45_2]_s$	0-127 mm from R.S upper and lower sections $[\pm 45_4/\ 0_4\ /\ F51/\pm 45_2/0_4]$	$[\pm 45_2]_s$
Rib				0-127 mm from R.S middle section $[\pm 45_4/\ F51/\pm 45_2]$			0-127 mm from R.S middle section $[\pm 45_4/\ F51/\pm 45_2]$	
Rib				127-481 mm from R.S upper and lower sections $[\pm 45_2]_s\ /\ 0_2$			127-481 mm from R.S upper and lower sections $[\pm 45_2]_s\ /\ 0_2$	
Rib				127-481 mm from R.S middle section $[\pm 45_2]_s$			127-633 mm from R.S middle section $[\pm 45_2]_s$	
Rib				481-812.8 mm from R.S upper and lower sections $[\pm 45_2]_s\ /\ 0$			481-633 mm from R.S upper and lower sections $[\pm 45_2]_s\ /\ 0$	
Rib				481-812.8 mm from R.S middle section $[\pm 45_2]_s$				

- Please refer to Ref. [7.2] for more details.

7.5.2 Results:

The eigen values for the first six resonance frequencies of the composite wing box (FE models) were presented in table (7.3) for the coarse and fine mesh models, which represent the real A1 composite wing box. The output of the coarse model results from MSC/NASTRAN were then used in the UNIMAP2000 software from which the mode shapes of the wing box were plotted as shown in figure (7.4-7.9). After close inspection of the mode shapes of the composite wing box, it was found that figures (7.4, 7.5 and 7.6) show the first fundamental bending natural frequency, the second and third bending frequency mode respectively. The fourth mode shape, which was the coupling bending-torsion mode as shown in figure (7.7). Figures (7.8 and 7.9) show the fourth bending frequency mode and the tip bending-torsion frequency mode respectively.

7.5.3 Discussion and Comparison of results:

Figure (7.2) shows the coarse mesh model of the composite wing box. The size of this model was about 23.4 MB, with a total of 5690 elements used in the analysis and required about 9 minutes to run on the UNIX/Cray system and 13 minutes on the Sun system. The fine mesh mode shown in figure (7.3) required space of about 42 MB, with a total of 19000 elements and required 28 minutes on the UNIX/Cray system and 43 minutes on the Sun system. The results presented in table (7.3) showed that the difference between the coarse mesh and the fine mesh model are very small (0.696% to 2.27%) with reduced cost (time to run and size) of the analysis for the coarse model compared with the fine model. Therefore the coarse mesh was selected for further analysis (flutter analysis).

The results presented in table (7.4) compares the results obtained from the analysis of the coarse, fine mesh models and experimental work. It can be seen on comparing figures (5.9-5.11) with figures (7.4-7.6) and figures (5.12-5.14) with figures (7.7-7.9) that there is a close proximity of the results between the eigen vectors obtained from the finite element analysis (analytical) and the experimental analysis. It will suffice to note that all the mode shapes obtained from both analysis are very similar to each

other except the mode shape shown in figures (5.12 and 7.7) for the experimental and analytical analysis respectively. After close inspection it appears that figure 5.12 represents a coupled mode between the third bending and torsion mode, while figure (7.7) represents a coupled mode between the second bending and torsion mode.

Table (7.3) Comparision of the natural frequencies of the analytical models.

Mode Number	Analytical (FE) Model (1) Frequency (Hz)	Analytical (FE) Model (2) Frequency (Hz)
1	25.85	25.67
2	87.2	86.0
3	174.4	170.43
4	177.9	177.42
5	254.3	253.54
6	269.1	274.94

Where

- Analytical (FE) model (1) is the coarse model of the composite wing box with all the structural components.
- Analytical (FE) model (2) is the fine model of the composite wing box with all the structural components.

Table (7.4) Eigen values for the wing box for experimental and analytical analysis

Mode Number	Experimental analysis Frequency (Hz)	Analytical (FE) Model (1) Frequency (Hz)	Analytical (FE) Model (2) Frequency (Hz)
1	19.74	25.85	25.67
2	73.85	87.2	86.0
3	142.42	174.4	170.43
4	158.08	177.9	177.42
5	232.43	254.3	253.54
6	254.72	269.1	274.94

It is interesting to find the same structural behaviour between the analytical and experimental results. As seen with the experimental results there is a similar large frequency separation between the first mode (25.85 Hz) frequency and the second mode (87.2 Hz) frequency. There is also a large separation between the second mode (87.2 Hz) and the third mode (174.4 Hz) frequencies. The third (174.4 Hz) and the fourth mode (177.9 Hz) are relatively close to each other, as observed in the experimental analysis as well. A similar gap was found as well in the experimental analysis between the fifth mode and sixth mode as shown in figures (5.13 and 5.14) respectively.

It will be noted from the comparison of the eigen values from the experimental and analytical models shown in table (7.4) that the fundamental frequency (first mode) variation is 23%, reducing to a more acceptable 5% for the sixth mode. This is a large difference and it illustrates the complexity, difficulties and the assumption in the analytical modeling of a real composite structure (aircraft wings as an example) compared to experimental work on the real and physical composite structure.

The difference in the magnitude of the natural frequencies might be related to the variation of the stiffness of the actual structure as compared with the analytical model.

In order to verify this, static tests were conducted on both the physical and the analytical model. Loads of increasing magnitudes were applied at the tip rib and the deflections at the tip were measured by a dial gauge as presented in table (7.5) and figure (7.10). From this the appropriate stiffness of the structure was estimated. Reference [7.2] had carried out an experimental test in 1984-1987 to find the tip deflection of the composite wing box under total of ultimate load of 28.25 KN. This load was applied as 2/3 on the front spar and 1/3 on the rear spar along the semi-span of the composite wing box as shown in figure (9.5) of the same reference. The tip deflection was 132 mm at tip rib (at 4281 mm from the aircraft center line). The same loading condition was then applied to the analytical model (coarse model) and the deflection was 124 mm at the tip rib. The difference between Ref. [7.2] and the analytical model was 6.06%, which was acceptable. Referring to the results presented in table (7.5), it was not too surprising to note that the analytical model was 25% stiffer than the physical structure due to the age of the wing box.

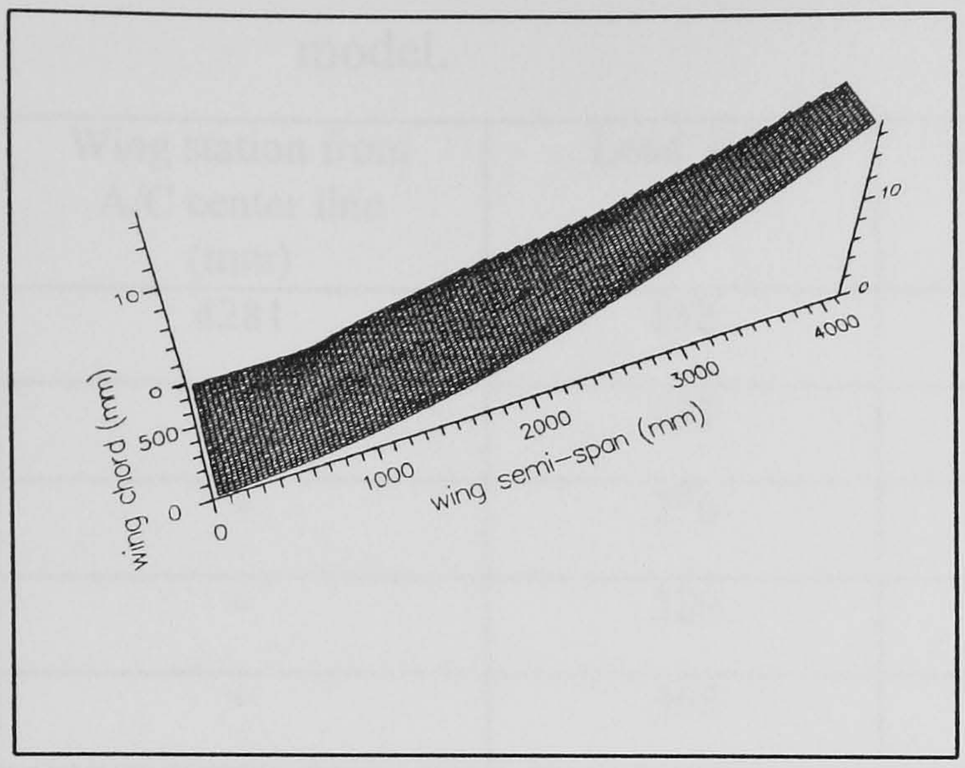

Fig. (7.4) 1st Bending Mode (25.85 Hz)

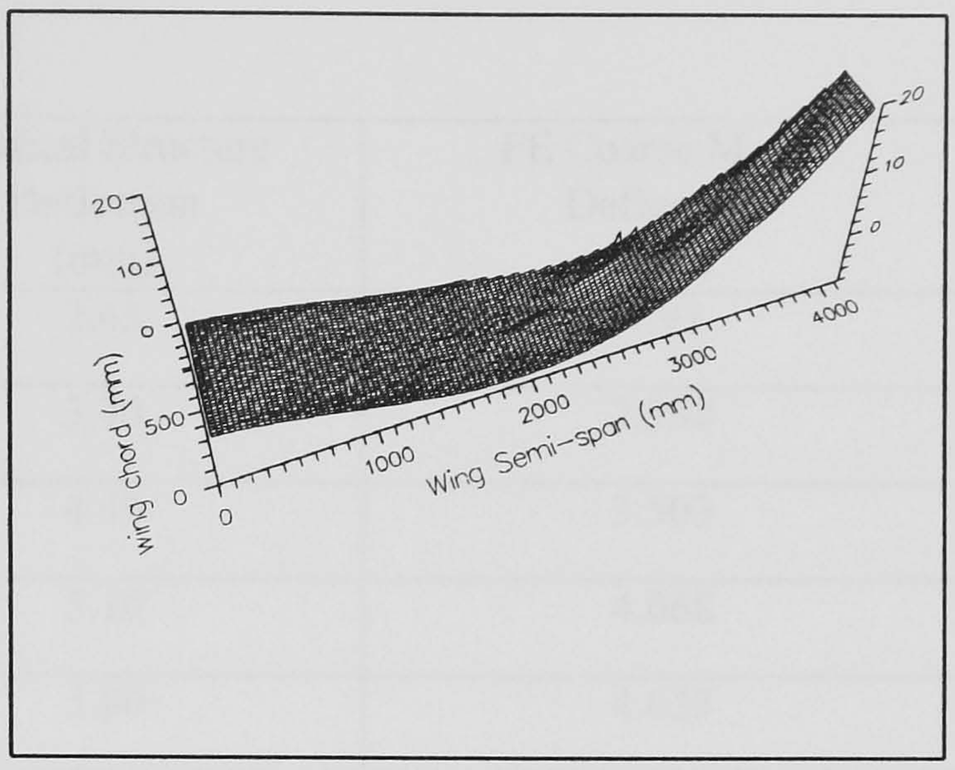

Fig. (7.5) 2nd Bending Mode (87.2 Hz)

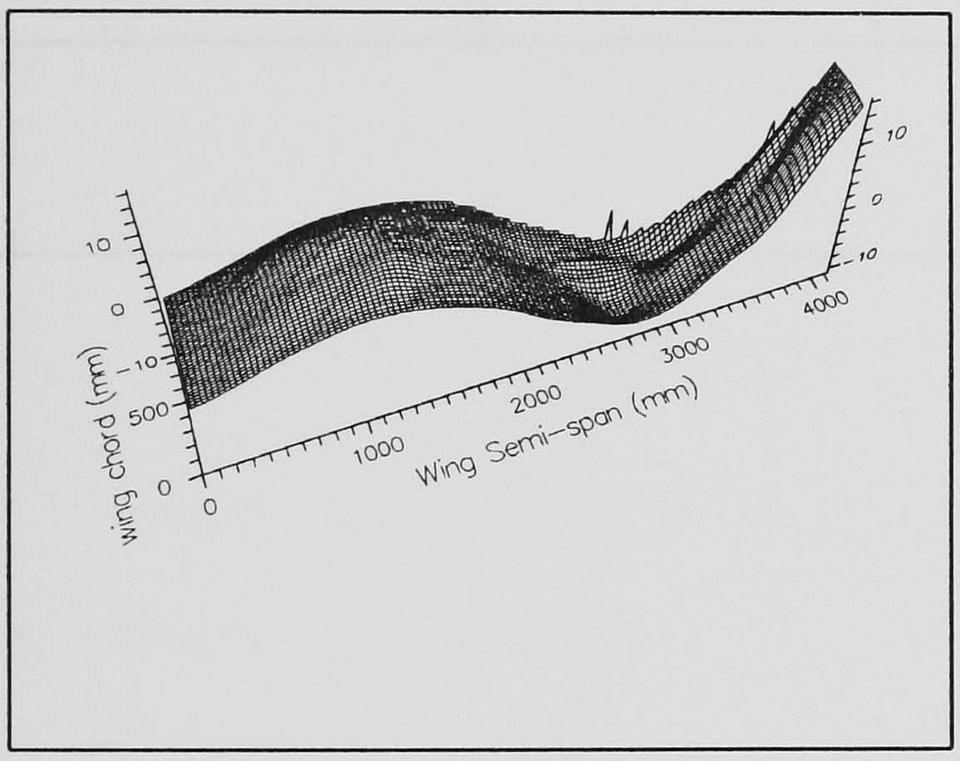

Fig. (7.6) 3rd Bending Mode (174.4 Hz)

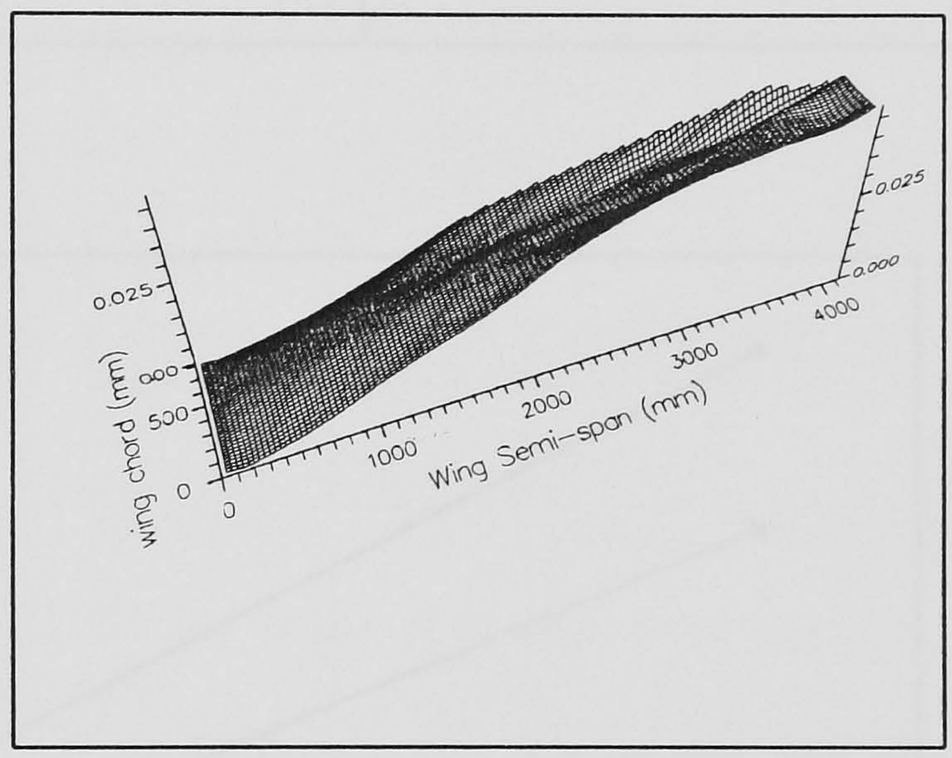

Fig. (7.7) Coupled Bending-Torsion Mode (177.9 Hz)

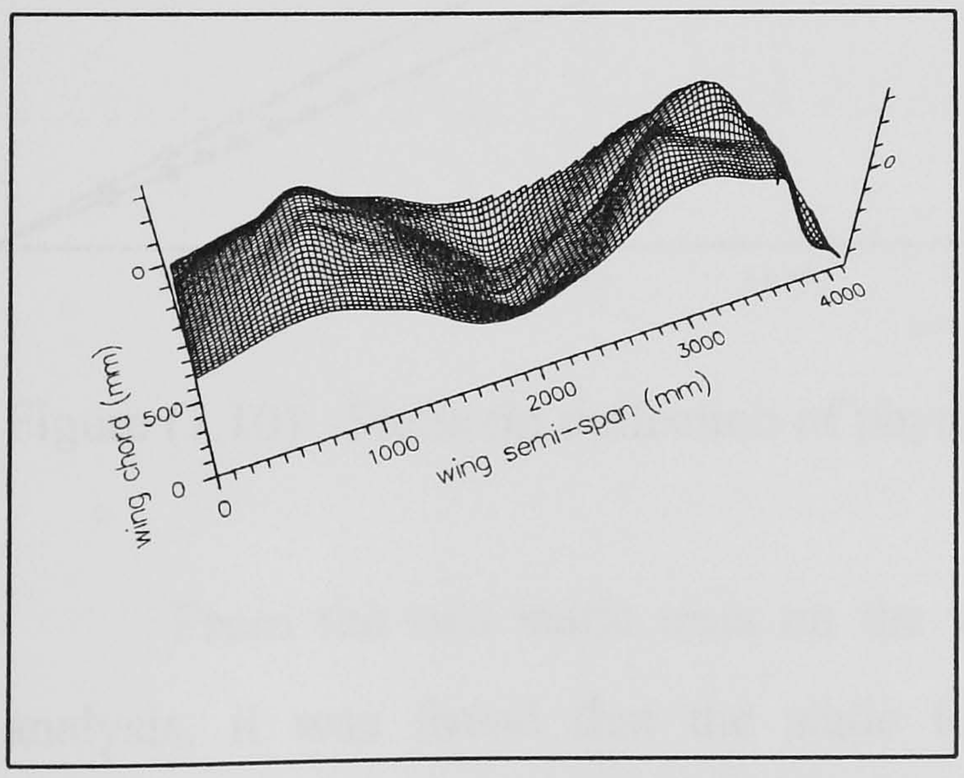

Fig. (7.8) 4th Bending Mode (254.3 Hz)

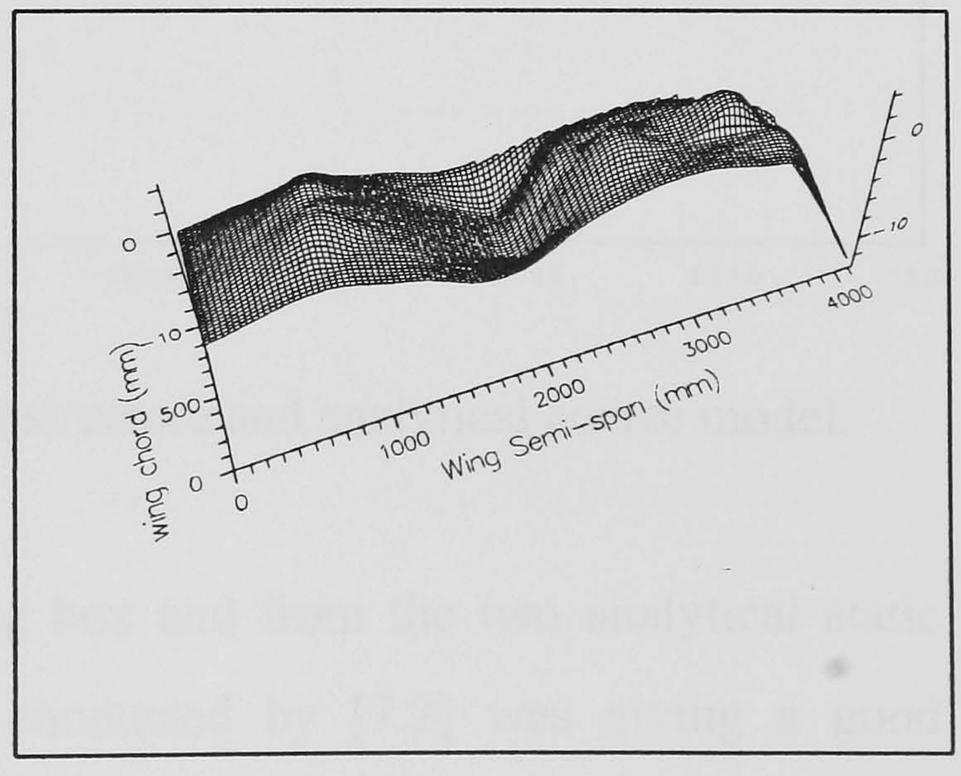

Fig. (7.9) Tip Bending-Torsion Mode (269.1 Hz)

Table (7.5) Comparisons of static tip deflections of physical structure and analytical model.

Wing station from A/C center line (mm)	Load (N)	Physical Structure Deflection (mm)	FE Coarse Model Deflection (mm)
4281	152	2.43	1.93
=	231	3.70	2.938
=	276	4.40	3.503
=	320	5.10	4.068
=	365	5.80	4.633
=	409	6.50	5.198
=	454	7.25	5.763
=	2295	36.25	29.15

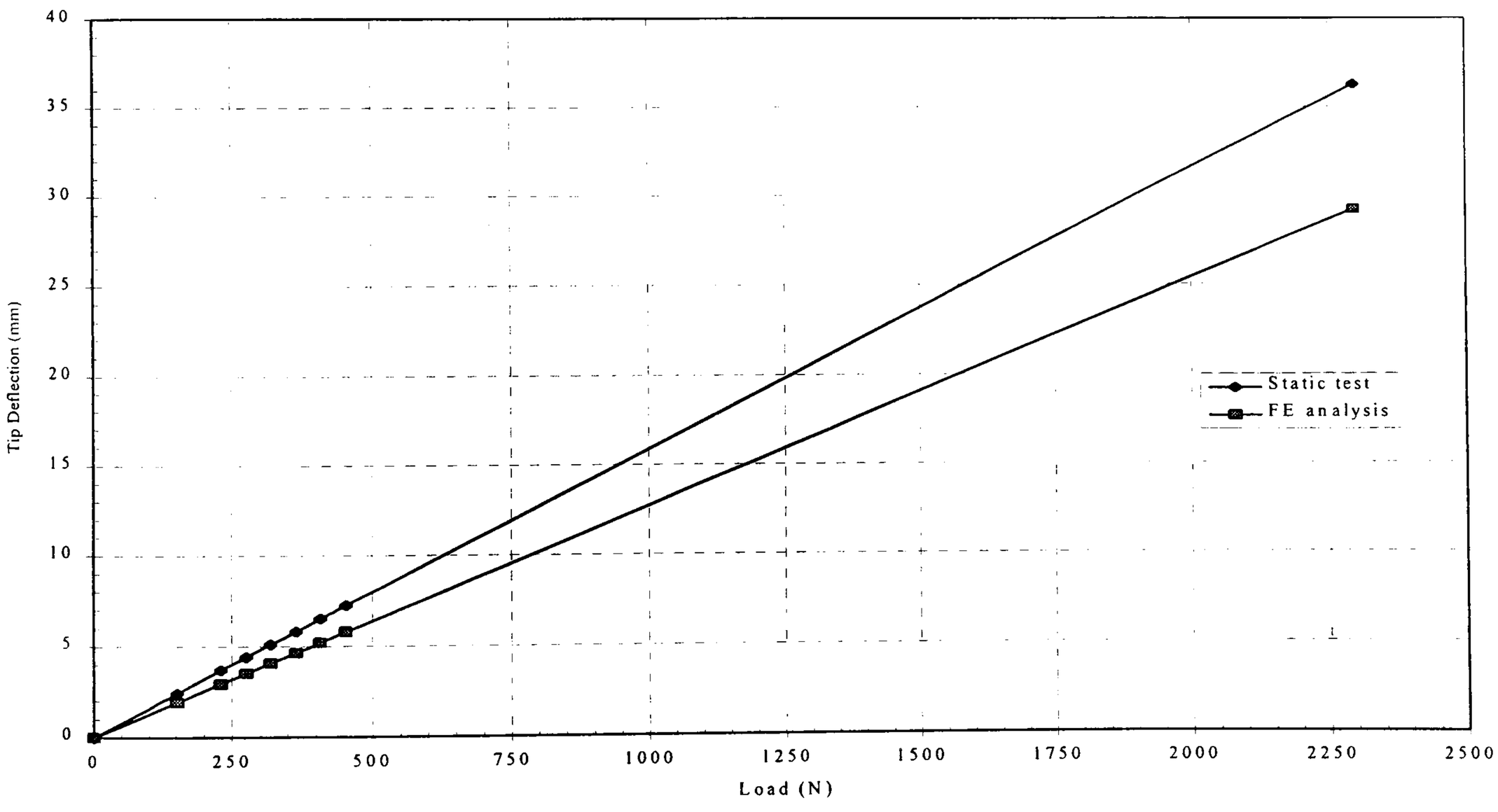

Figure (7.10) Static tip deflection of physical structure and analytical coarse model.

From the two static tests on the wing box and from the two analytical static analysis, it was found that the static test conducted by [7.2] was giving a good agreement compared with analytical static analysis under 28.25 KN, while a large

difference is obtained from the other analytical static analysis and static test as shown in table (7.5).

There are many parameters, which could lead together to this large variation in natural frequency between the experimental and the analytical model.

The first parameter is the stiffness of the structure. From the relation of the natural frequency, it can be said that the natural frequency is proportional to the square root of the wing stiffness. The static test showed that the physical structure is more flexible than the analytical model, which indicated some reduction in the stiffness of the structure. This reduction of stiffness leads to some reduction in the natural frequency of the physical wing. This reduction in stiffness could be related to the following:

- The age of the wing and the fact that extensive tests were carried out at ultimate load over a long period of time could lead to some level of delamination might exist, which will effect and reduce the stiffness in the physical wing box.
- Boundary condition applied on the physical wing box may not simulate the perfect clamped root of the wing box, which will make the structure more flexible and hence give lower frequency.

The second parameter is the mass of the wing structure, as the natural frequency is universally proportional to the square root of the mass. The moisture and the environmental effect could increase the mass of the wing box. As the mass increased, the natural frequency of the physical structure will be decreased.

The third parameter could be due to that, the root flange was not included in the analytical model (FE) of the wing box, which will have additional mass in the analytical model. This elimination will increase slightly the natural frequency of the analytical wing model.

The fourth parameter is the modeling differences between the analytical and physical wing box such as joints of different structure components.

The differences in the natural frequency could be due to the combinations of all or some of the above parameters.

7.6 Flutter analysis:

7.6.1 Introduction:

In this section, the flutter analysis of the coarse wing model of the real A1 composite wing box was done using the original laminate lay-ups presented in table (7.2) with the material properties specified in table (7.1). The flutter speed was calculated using the finite element package MSC/NASTRAN 69. The aerodynamic coefficient matrix was evaluated by of the Doublet-Lattice Method (DLM). The interconnection of the structural grids with the aerodynamic grids was done using the theory of surface splines (SPLINE1 card). The structural damping was taken from experimental analysis and used as complex stiffness matrix.

The same flutter solution method was used as in chapter 6 (PK method) and the relation of the flight velocity versus the total damping (structural and aerodynamic damping) and frequency are taken from the output of the PK method and plotted using Microsoft EXCEL program.

7.6.2 Aerodynamic Modeling:

A total of nine input data aerodynamic models were created using DLM for the flutter analysis. The detailed information and differences between the aerodynamic models were summarized in table (7.6). This was done to investigate the sensitivity of the aerodynamic panels or elements in the spanwise and chordwise directions, range of the induced frequency parameter (k) and the number of vibration modes on the flutter speed. This investigation gives the optimum flutter speed with an acceptable accuracy between the nine models and with reduced model size and time to run.

For every aerodynamic model, pertinent basic flight and geometric parameters are specified on the AERO card for the dynamic aeroelastic analysis (see chapter 6). The aerodynamic element meshes and the locations of the root and tip leading edges were controlled and located using the CAER01 card which was used for the DLM.

A reference chord of 1207 mm (chord at 75% of the semi-span), reference density at sea level and a rectangular aerodynamic coordinate system no.1 were specified through the AERO card for all the configurations. The aerodynamic coordinates system was created using CORD2R card and the x-aero axis is parallel and positive in the direction of the flow.

The total semi-span with the tip fairing was 5029.2 mm from the reference line of the aircraft. The inner leading edge of the composite wing box at 231 mm along the semi-span from the aircraft reference line with a total chord of 2022.5 mm and the outer leading edge at 5029.2 mm along the semi-span with a total chord of 917.5 mm.

Surface spline method was used for the interpolation between the aerodynamic grid and the structural grids through the use of SPLINE1 and SET1cards.

The aerodynamic conditions, which are listed in the MKAER01 card, were used to specify the Mach number (0.4) and the reduced frequency range.

However, the selection and the number of the structural grids to be involved in the interpolation with the aerodynamic grids, selection of the number of the aerodynamic boxes, induced frequency (k) and number of vibration modes are very important parameters in getting the optimum flutter speed (see table 7.6). All the above parameters were investigated and the optimum was then selected and used (see chapter 9) which gives a minimum cost analysis (size and time required for the analysis) and the accuracy (error in % between the input data files).

Table (7.6) Varying the aerodynamic elements on the A1 composite wing box.

Aerodynamic Elements		Induced Frequency	Flutter speed	No. of Modes
Spanwise	Chordwise	Parameter (k)	(m/sec)	(see figs. 7.4-7.9)
20	6	0.001 to 0.8	578.4510	4
20	6	0.001 to 0.8	578.444	6
20	8	0.001 to 0.8	583.7653	4
20	8	0.001 to 1.0	583.76358	4
20	10	0.001 to 1.0	586.00	4
40	8	0.001 to 1.0	583.55540	4
40	16	0.001 to 1.0	590.340	4
20	8	0.001 to 1.8	583.76356	4
40	8	0.001 to 1.8	583.55527	4

7.6.3 Flutter solution parameters:

The flutter analysis was carried out for A1 composite wing box with the laminate lay-ups presented in table (7.2). The structural damping (for the frequency range of 0 to 300 Hz) was taken from the experimental test at each frequency mode shown in figures (7.4-7.9) and used in the equation of motion using the PARAM KDAMP-1 and TABDMP1 cards. The flutter equation was solved using the PK method. The density ratio of 0.738609 (3.048 Km altitude), Mach number of 0.4 and a range of selected velocities were used in the flutter analysis through the use of solution number (145) for all the input data files of the A1 composite wing box.

7.6.4 Results and discussion:

The variation of the aerodynamic elements and its effect on the flutter speed were presented in table (7.6). The effects of the inclusion of structural vibration modes were investigated for two cases, the first case with the first four modes and the second case with the first six modes. It was found that the effect of structural modes was negligible for the A1 composite wing box. The effect of the aerodynamic mesh along the span and the chord was investigated as shown in table (7.6). The variation in flutter speed was found to be about 2% as shown in table (7.6). Therefore, taking into account the size of the model and the time required to get the results and within acceptable accuracy, the first input data file with 20 aerodynamic elements along the span and 6 elements along the chord, including the induced frequency parameter from 0.001 to 0.8 was considered in further flutter analysis.

Figures (7.11-7.12) show the trend of variations of damping and frequency of the first nine natural frequencies as a function of the flight speed of the composite wing box. The damping variation of the first mode started increasing up to 300 m/sec and then started decreasing as the flight speed increasing. The frequency of this mode started decreasing to zero at 350 m/sec, but without changing damping sign. This could be due to the intersection with the sixth mode as shown in figure (7.11). The damping of the second mode was started increasing and then decreasing as negative damping till the

intersection with the zero damping line at 578.45 m/sec with frequency of 65.17 Hz as shown in figures (7.11-7.12) respectively. The damping of the third mode was increasing with the flight speed up to 575 m/sec and then started decreasing with the speed, whereas the frequency decreasing up to 525 m/sec and then started increasing with the flight speed. The damping of the fourth and fifth modes (local modes) was very small with unchanged sign, whereas the frequencies were almost constant with the speeding. The damping and frequency of the sixth mode (local mode) was decreasing as the flight increasing without changing damping sign. The damping variation of the seventh and ninth modes was very small and the frequency was almost constant. The damping variation of the eighth mode (local mode) was increasing with the speed, whereas the frequency was decreasing.

However, from the above discussion, it can be seen that the flutter speed was at 578.49 m/sec of the second mode and its corresponding frequency was at 65.17 Hz. This mode is called the flutter mode or the critical mode.

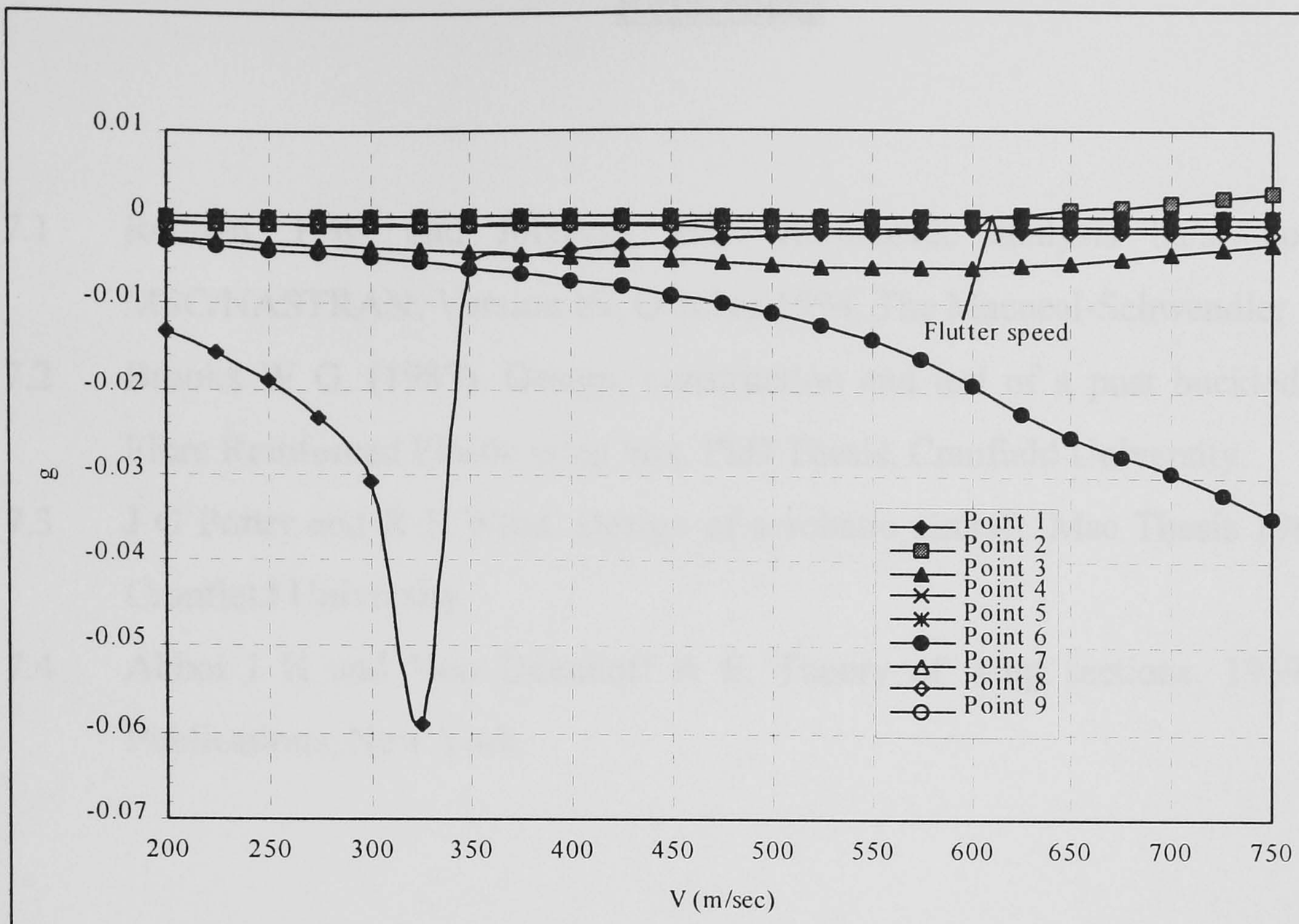

Fig. 7.11 Velocity vs Damping of the A1 compsite wing box.

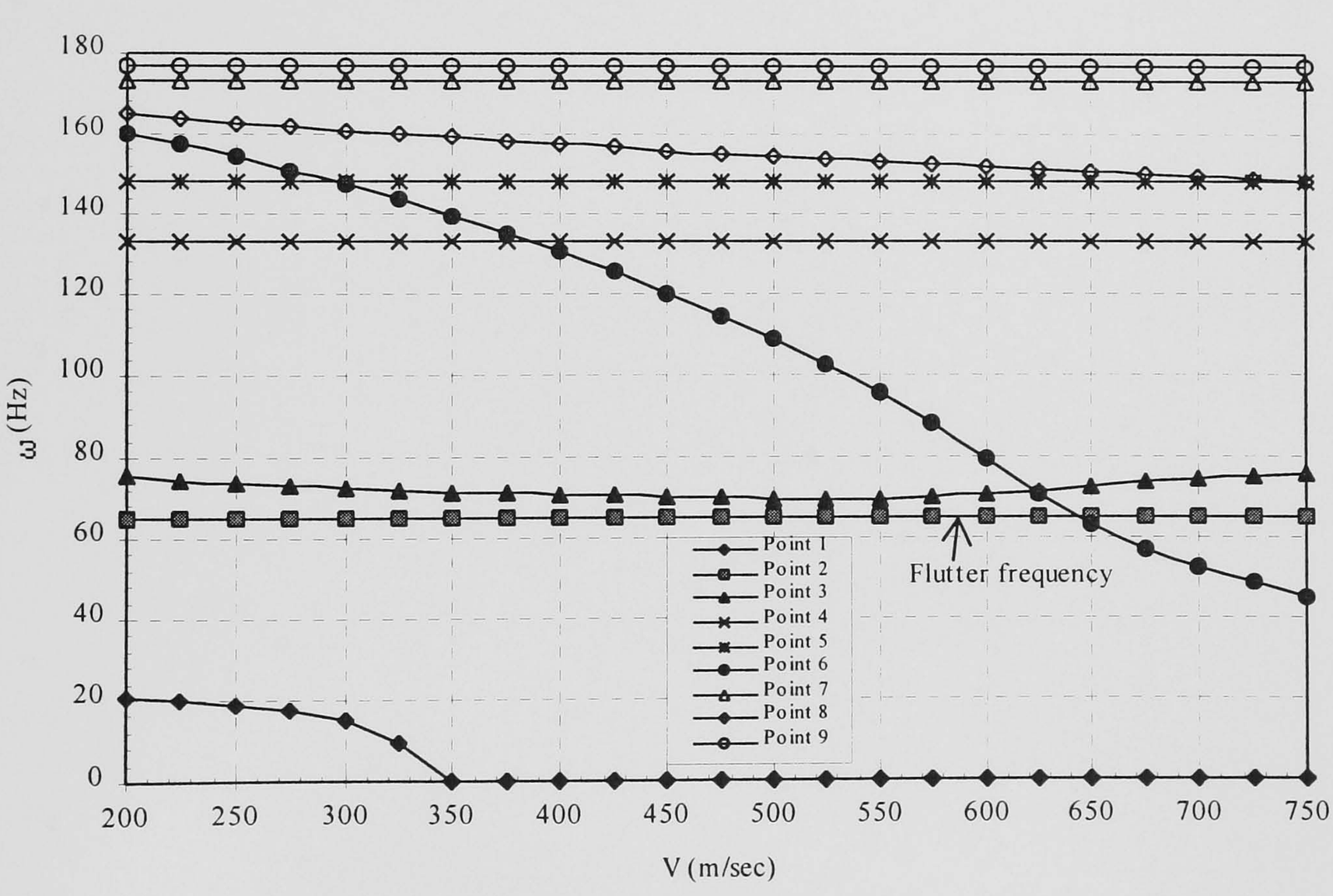

Fig. 7.12 Velocity vs Frequency (ω) of the A1 composite wing box.

References

7.1 Rodden, P.W. and Johnson, H.E. Aeroleastic analysis hand books for MSC/NASTRAN, Version 69, October 1994, The Macneal-Schwendler

7.2 Brooks W G. (1987). Design, construction and test of a post buckled Carbon Fibre Reinforced Plastic wing box. PhD Thesis, Cranfield University.

7.3 J G Potter and R E Ward. Design of aerobatic aircraft. Msc Thesis 1968/1969, Cranfield University.

7.4 Abbot I H and Von Doenhoff A E. Theory of wing sections. 1959, Dover Publications, New York.

CHAPTER 8

DYNAMIC AND FLUTTER ANALYSIS OF THIN-WALLED STRUCTURES

8 Dynamic and Flutter analysis of thin-walled structures:

8.1 Introduction:

The contents of this chapter are divided into three sections. The first section (8.2), a normal mode analysis was carried out for a flat plate and thin-walled structure [8.10] constructed from composite materials using the MSC/NASTRAN as in chapter 7. The results were compared with the results of [8.10] and show a good agreement as shown in tables (8.5-8.6). The purpose of the analysis was to get more experience and confidence in the modelling and analysis of composite structures using MSC/NASTRAN and to investigate the effect of bend-twist coupling stiffness on the natural frequency of both structures.

The second section (8.3) deals with flutter analysis of two different types of wing structures. The first wing model was modelled as a flat plate constructed from isotropic material. The flat plate model was analysed using MSC/NASTRAN and flutter speed and frequency were compared with CALFUN results. The second wing model was a thin-walled structure, which was constructed from aluminium. This wing model was analysed by [8.12] and [8.19-8.20] for the flutter speed using its optimum structural overall dimensions. The flutter speed obtained by [8.12] and [8.19-8.20] were compared with the present results. However, this analysis was done on isotropic material because there is no enough structure details of composite structure presented in the open literature to enable using MSC/NASTRAN. This was done to gain experience in the modelling of flutter input file, analysing in the right way and compare the results with published results, which was considered as a first step towards the complex composite structure.

In the third section (8.4), vibration and flutter analysis of the composite thin-walled structure were carried out for four different thin-walled structures. Two configurations were considered in each thin-walled structure, namely Circumferentially Uniform Stiffness (CUS) and Circumferentially Asymmetric Stiffness (CAS) structural configurations. In the balanced or (CUS) configuration, the top and lower flanges are

constructed from the same laminate lay-up with the fibre angles θ reversed. The sides were made from antisymmetric laminate $[\pm 45]_2$ to avoid the bend-twist coupling produced by the side webs. In the (CUS) configuration of the first thin-walled structure, two laminate lay-ups were used $[\theta_2/0]_s$ and $[\theta_2/0]_2$ for the upper and lower flanges as presented in table (8.9). Where θ is the most outer ply in the laminate stacking sequence and was oriented in the range [-90° to 90°]. This configuration will produce an extension-twist coupling [8.9]. In the second case of the Circumferentially Asymmetric Stiffness (CAS), the upper and lower skins were made from the same laminate lay-up with the same sign of the fibre angle θ. The sides are made from antisymmetric lay-ups $[\pm 45]_2$ for the same above reason. A computer programme using EXCEL software was written to calculate the effective bending (EI), torsional (GJ) and bending-torsional (K) stiffness of the wing 1 model (see table 8.9) using the theories developed by [8.9] and [8.10]. The approach provided in [8.9] was taken into account the stacking sequence of the lay-ups, but in [8.10] method, the in-plane stiffness were used which did not take the effect of ply lay-ups. The effective stiffnesses were shown in figure (8.2-8.4) for the symmetric laminated skins of wing 1 model. The structure was modelled to simulate cantilevered boundary conditions using MSC/NASTRAN. Normal mode analysis was then carried out using Lanczos method provided in MSC/NASTRAN [8.8] for all the models presented in table (8.9).

The generalized aerodynamic forces and flutter determinates were generated and analysed using the same method used previously (see chapter 6 and 7). The flutter analysis was conducted for the wing models (table 8.9) using MSC/NASTRAN. The variation of the flight speed against the damping and the frequency of wing 1 model were shown in figure (8.32-8.39). Also, the variation of the flutter speed and frequency versus the fibre angle θ with and without bend-twist coupling stiffness for all wing models were shown in figure (8.40-8.41, 8.47-8.48, and 8.51-8.54).

The objective was to investigate the effects of fibre angle and subsequent bend-twist coupling and wash-in and wash-out deformations on the flutter speed for different wing models, which was considered as a first step towards the real composite wing.

8.2 Dynamic analysis of the thin-walled structure:

In this section, normal mode analysis was carried out using MSC/NASTRAN on two wing composite structures, namely flat plate and box-beam composite structure [8.10]. The analysis was done to gain experience in the modelling using MAS/NASTRAN and investigate the effect of bend-twist coupling stiffness on the natural frequency and mode shapes of a wing structure modelled as flat plate and thin-walled closed section (box-beam).

8.2.1 Wing plate structure:

The wing was modelled as flat plate using CQUAD4 plate element given in MSC/NASTRAN. The dimensions of the wing plate were 762 mm and 35 mm as semi-span and chord respectively. The unidirectional material properties of the plate were presented in table (8.1) with the ply thickness of 0.17 mm. Symmetrical and anti-symmetrical laminate lay-ups were used in the plate model. The symmetrical laminate was in the form of $[\pm 45]_s$, in which the extension-bending matrix [B] does not exist whereas the bend-twist coupling stiffness is present. The anti-symmetrical laminate was in the form of $[\pm 45]_2$, in this form the bend-twist coupling stiffness does not exist, but the B_{13} and B_{23} of the matrix [B] are present.

The natural frequencies for both symmetrical and anti-symmetrical laminated plates were calculated and presented in table (8.2).

Table (8.1) Material properties of Ciba-Geigy 913 carbon/epoxy prepreg. for the first thin-walled structure.

$E_{11} = 130\times10^3$ N/mm^2	$\rho = 1.60\times10^{-6}$ Kg/mm^3
$E_{22} = 9.0\times10^3$ N/mm^2	$\nu_{12} = 0.28$
$G_{12} = 4.8\times10^3$ N/mm^2	ply thickness = 0.170 mm

Where
E_{11} is the young's modulus of elasticity in the fibre direction,
E_{22} is the young's modulus of elasticity in the matrix direction,
G_{12} is the shear modulus in fibre and matrix directions,
ν_{12} is the Poisson's ratio and
ρ is the density of the material

Table (8.2) Natural frequencies for wing plate models

Mode No.	Frequencies (Hz) $[\pm 45]_s$	Frequencies (Hz) $[\pm 45]_2$
1	0.6085 (BT)	0.63216 (B)
2	3.8149 (BT)	3.9673 (B)
3	10.729 (BT)	11.191 (B)
4	21.193 (BT)	22.203 (B)
5	35.405 (BT)	37.295 (B)
6	44.604 (TB)	51.89 (T)

Where B is pure bending mode,

T is pure torsion mode,

BT is a bending mode with torsional displacement,

TB is a torsional mode with bending displacement.

8.2.2 Thin-walled closed section structures:

Two unswept thin-walled structures were modelled using MSC/NASTRAN. The dimensions of the first thin-walled was of 762 mm, 35 mm and 13.0 mm in length, chord and depth respectively (see fig. 1.1 of chapter 1). The dimensions of the second thin-walled structure was the same as the first structure except that the chord and the depth was 24.21 mm and 13.46 mm respectively [8.10] in the second thin-walled structure. The material properties used in the first structure are given in table (8.1), whereas the material properties of the second structure were taken from [8.10] and shown in table (8.3).

Table (8.3) Material properties of the second thin-walled structure [8.10].

$E_{11} = 142\times10^3$ N/mm^2	$\rho = 1.60\times10^{-6}$ Kg/mm^3
$E_{22} = 9.80\times10^3$ N/mm^2	$\nu_{12} = 0.42$
$G_{12} = 6.0\times10^3$ N/mm^2	ply thickness = 0.127 mm

8.2.2.1 Finite Element Modelling and Analysis:

The thin-walled structures described above were modelled using a structural idealization programme MSC/PATRAN 7.0 and analysed using MSC/NASTRAN. The global Cartesian coordinate system No. 1 was employed such that the x-axis was in the chordwise direction (positive in the stream wise direction), the y-axis along the span and hence the z-axis was in the depth direction (positive up wards). The structure was modelled using CQUAD4 plate elements with four grid points. The CQUAD4 element is represented by fully coupled laminate equation and can count for all coupling effects introduced through unbalanced laminates. The finite element model contained a total of 480 CQUAD4 plate elements. This was done by creating forty elements along the span, five elements along the chord and one element in the spar webs. The verifications of the elements were checked as listed in [8.8] such as aspect ratio, were checked for the model. The model was simulating a cantilevered boundary condition, which approximated to the attachment of the aircraft wings.

The default coordinate system No. 0 was used to define the material coordinate system for both skins and spars. The x, y and z axis are in the span wise, up positive and in the chord wise positive to the flow respectively. The material coordinate system which shows the directions of the fibre angle θ were identified in [8.8] by the following:

1. The longitudinal direction x_m of the fibre angle is the projection of the X-axis of the coordinate system No. 0 to the surface of the element.
2. The z_m axis of the material coordinate system is the same as the element coordinate system.
3. The positive y_m axis of the material coordinate system was then found by the right hand rule (see section 7.3.1 of chapter 7).

Both thin-walled structures were modelled to simulate both Circumferentially Uniform Stiffness (CUS) and Circumferentially Asymmetric Stiffness (CAS). The CUS configuration produces an extension-twist coupling, whereas CAS produces bend-twist coupling.

The laminate lay ups of the first thin-walled structure was in the form of unbalanced symmetric laminate $[\theta_2/0]_s$ for the upper and lower skins and $[90/0]_s$ for the spar webs. In the case of CAS, the bend-twist coupling stiffness will be generated by the upper and lower skins only (all the coupling terms (A_{13}, A_{23}, $[B_{ij}]$, D_{13} and D_{23} are zero in the spar webs).

The laminate lay ups of the thin-walled structure presented in [8.10] was in the form of $[\theta_6]$. The natural frequency and mode shapes were obtained using Lanczos method.

Tables (8.4-8.5) show the frequency results for CAS and CUS configurations of the first and second thin-walled structures respectively. These results (MSC/NASTRAN) were compared with [8.10] and showed a very good agreement.

Table (8.4) Comparison of the natural frequencies of the first thin-walled structure at $\theta = 20°$.

Mode No.	Present (MSC/NASTRAN) CAS (Hz)	Present (MSC/NASTRAN) CUS (Hz)
1	38.599 (BT)	38.43 (B)
2	224.41 (BT)	224.01 (B)
3	473.00 (TB)	441.62 (T)

Table (8.5) Comparison of the natural frequencies for the second thin-walled structure [8.10] at $\theta = 30°$.

Mode No.	Present (MSC/NASTRAN)		Ref. [8.10]	
	CUS (Hz)	CAS (Hz)	CUS (Hz)	CAS (Hz)
1	24.70 (B)	24.9 (BT)	23.8 (B)	24.08 (BT)
2	154.7 (B)	155.2 (BT)	-	150.72 (BT)
3	430.69 (B)	430.8 (BT)	-	421.2 (BT)
4	736.87 (T)	825.08 (BT)	-	-
5	-	856.8 (TB)	-	-

Note: The natural frequency in CUS of Ref. [8.10] was scaled,

The maximum differences in natural frequencies were about 3%.

Table (8.6) Comparison of the first bending frequencies of the thin-walled structure [8.10] for the CUS configuration.

Fibre angle θ°	Present (MSC/NASTRAN) Frequency (Hz)	Ref. [8.10] Frequency (Hz)
0	52.75 (B)	53.0 (B)
5	49.66 (B)	49.8 (B)
30	24.7 (B)	23.8 (B)
45	19.91 (B)	18.9 (B)
60	16.03 (B)	16.0 (B)
90	14.01 (B)	14.0 (B)

Note: All the natural frequencies in [8.10] are scaled.

From table (8.2), it can be said that including the bend-twist coupling in the flat plate model will make the plate model more flexible (lower frequency) compared to the same model without including bend-twist coupling stiffness.

However, in the case of thin-walled closed sections such as wing box structure, the following points can be observed from the results presented in table (8.4-8.5) by MSC/NASTRAN and [8.10]:

- The fundamental bending frequency is slightly lower in the case of CUS as compared to the CAS, which was not the case in the plate model.
- The first torsion frequency mode in the case of CUS was much lower than the first torsion frequency of the CAS, which was not the case of the plate model.

From the above results, it can be said that the structural geometry (plate without spar webs and closed box sections with upper and lower skins and spar webs) has played a very important role in the results presented in table (8.2 and 8.4-8.5) of plate and thin-walled closed section.

8.3 Flutter analysis of the lifting aircraft surfaces:

8.3.1 Aircraft lifting surface (1):

In this case, the aircraft wing was modelled as a cantilevered plate made from aluminium. The structural dimensions are of 5000 mm length, 500 mm chord and 20 mm thickness. The wing plate was modelled using MSC/NASTRAN [8.8] and CALFUN [8.11] programmes for the flutter analysis. In MSC/NASTRAN, the plate was modelled using CQUAD4 elements and all the structural elements were modelled with the Young modulus E = 72400 N/mm^2, Shear modulus G = 27000 N/mm^2 of the aluminium material.

Normal mode analysis was carried out using MSC/NASTRAN and using dynamic stiffness method in [8.11]. Comparisons of the natural frequencies were given in table (8.7) between the two programmes. A strip theory was used in CALFUN [8.11] to calculate the generalized aerodynamic forces, whereas the flutter solution was obtained using the standard egiensolution procedure. Table (8.8), gives the flutter speed and frequency obtained from both programmes which show a good agreement.

Table (8.7) Comparison of the natural frequencies between NASTRAN and CALFUN programmes.

Mode No.	Present (NASTRAN) Natural frequencies (Hz)	Present CALFUN [8.11] Natural frequencies (Hz)
1	0.6627	0.660
2	4.165	4.120
3	11.760	11.530
4	12.592	12.300

Table (8.8) Comparison of the flutter speed and frequencies between NASTRAN and CALFUN programmes.

Present (NASTRAN)		Present CALFUN [8.11]	
V_f (m/sec)	ω_f (Hz)	V_f (m/sec)	ω_f (Hz)
133.379	6.600	130.00	5.95

Where V_f is the flutter speed (m/sec)

ω_f is the flutter frequency (Hz).

8.3.2 Aircraft lifting surface (2):

Two aircraft wing models were modelled as a cantilevered thin-walled structure made from aluminium (L72). The first wing model structure [8.12] shown in figure (8.1) has the following geometrical properties:

L = 1524 mm

H = 101.6 mm

W = 635 mm

The area of spar caps were constant and equal to 214.85 mm^2; the web thickens was equal to 1.49 mm, 1.36 mm and 1.27 mm in the three bays respectively. The top and bottom skins were same i.e., 0.17 mm, 0.24 mm and 0.17 mm in the three bays respectively. The rib thickness was 0.93 mm, 0.86 mm and 0.85 mm in the three bays respectively as shown in figure (8.1).

The second wing model given in [8.19] was made from the same material and same structural geometry as the first wing model. The optimum dimensions were used for the upper and lower skin of 1.016 mm in the three bays, 2.032 mm for the spar webs, 1290 mm^2 for the area of the spar caps. The rib thickness was 1.016 mm, 4.745 mm and 3.097 mm for the first three ribs respectively. Both wing models were modelled using CQUAD4 plate elements and the stringer caps were modelled using one dimensional rod elements. All the structural elements were modelled with the Young modulus E = 68950 N/mm^2, Shear modulus G = 27580 N/mm^2.

Both normal mode analysis and flutter analysis was carried out on the first and second wing models. The flight conditions considered in the analysis for the first wing model were a Mach number of 0.5566, an altitude of 3048 m, and at Mach number of 0.717 and an altitude of 1372 m for the second wing model. The flutter speed and frequency of the first wing model obtained from NASTRAN were 239.8 m/sec and 12.35 Hz respectively, while from [8.12], the flutter speed of the first wing was 243.84 m/sec. Moreover, the flutter speed and frequency obtained from NASTRAN for the second wing model was 242 m/sec and 11.35 Hz respectively, while the flutter speed obtained from [8.19] was 246.0 m/sec. The results obtained showed a good agreement.

This wing model was analysed, as well by [8.20] and the optimum flutter speed was about 238.09 m/sec at Mach number of 0.717 and 1372 m height.

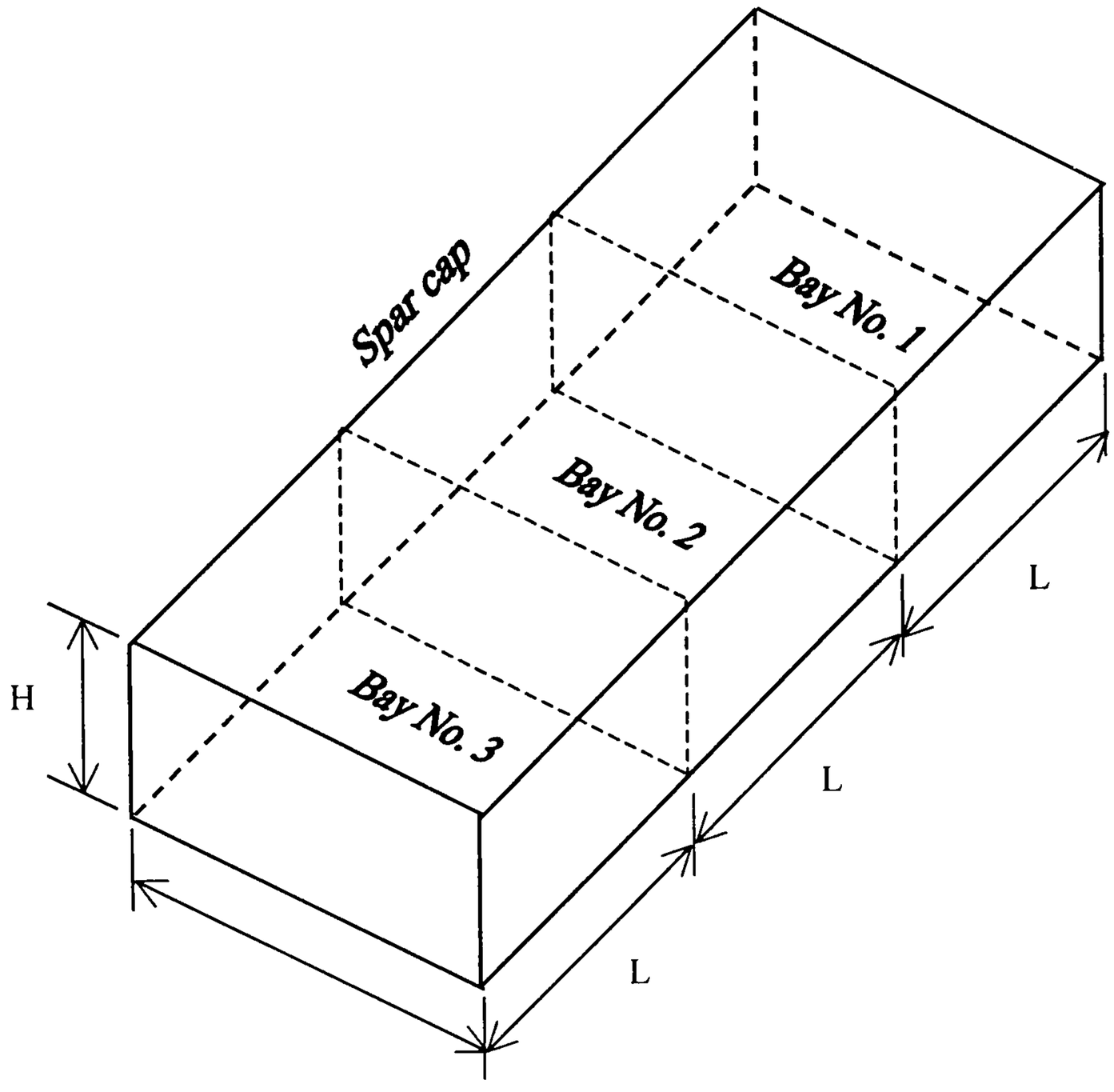

Fig. 8.1 Wing box structural geometry used by [8.12]

8.4 Dynamic and Flutter analysis of composite thin-walled structures:

8.4.1 Description of the thin-walled structure:

Thin-walled close section structure was selected as it is considered to be representative of the aircraft wing sections. The unswept thin-walled structure was made from composite materials and the geometric dimensions are 762 mm length (L) or span, 35 mm chord (C) and 13 mm depth (D). Four thin-walled structures were used, the first thin-walled structure was made from upper and lower skins and front and rear spars as shown in figure (1.1) of chapter 1. The structure configuration of the second thin-walled structure was the same as the first thin-walled structure, but with adding three ribs at three equal spaces from the wing root (190.5, 381 and 571.5 mm) as shown in figure (1.2) of chapter 1. The third thin-walled structure was the same as the first thin-walled structure, but with adding a hat section stringer attached to the middle surface of the upper and lower skin as shown in figure (1.3) of chapter 1. The fourth thin-walled structure was the same as the third thin-walled structure, but with moving the stringer closer to the rear spar as shown in figure (1.4) of chapter 1.

The laminate configurations of the wing models created from the four thin-walled structures were summarised in table (8.9). The fibre ply angle θ was oriented in the range of [-90° to 90°] in steps of 0, 20, 30, 45, 60, 90, -20, -30, -45, -60 and -90 degrees (see figure 7.3 of chapter 7 and figure 8.5).

8.4.2 Effective stiffness of the thin-walled structure:

In normal analysis of composite materials, the bending, torsional and bend-twist coupling stiffness plays a very important role. Therefore, it is very important to understand the mechanics of the composite laminates. There are different methods in calculating the effective stiffness of the thin-walled composite structures as mention in chapter 3. Two different methods of structural modelling were selected. The first method was implying the inplane stiffness of the composite laminate [8.10] and the second method is taking the bending stiffness and hence the stacking sequence into

account [8.9]. Using the basic material properties given in [8.13] and the procedure of both methods outlined in chapter 3, the effective bending stiffness (EI), torsional stiffness (GJ) and the bending-torsional coupling stiffness (K) were calculated for the symmetric lay-ups of the wing 1 model for a wide range of fibre orientation θ as shown in figure (8.2-8.4). The main features and differences between these methods and others are presented in chapter 3.

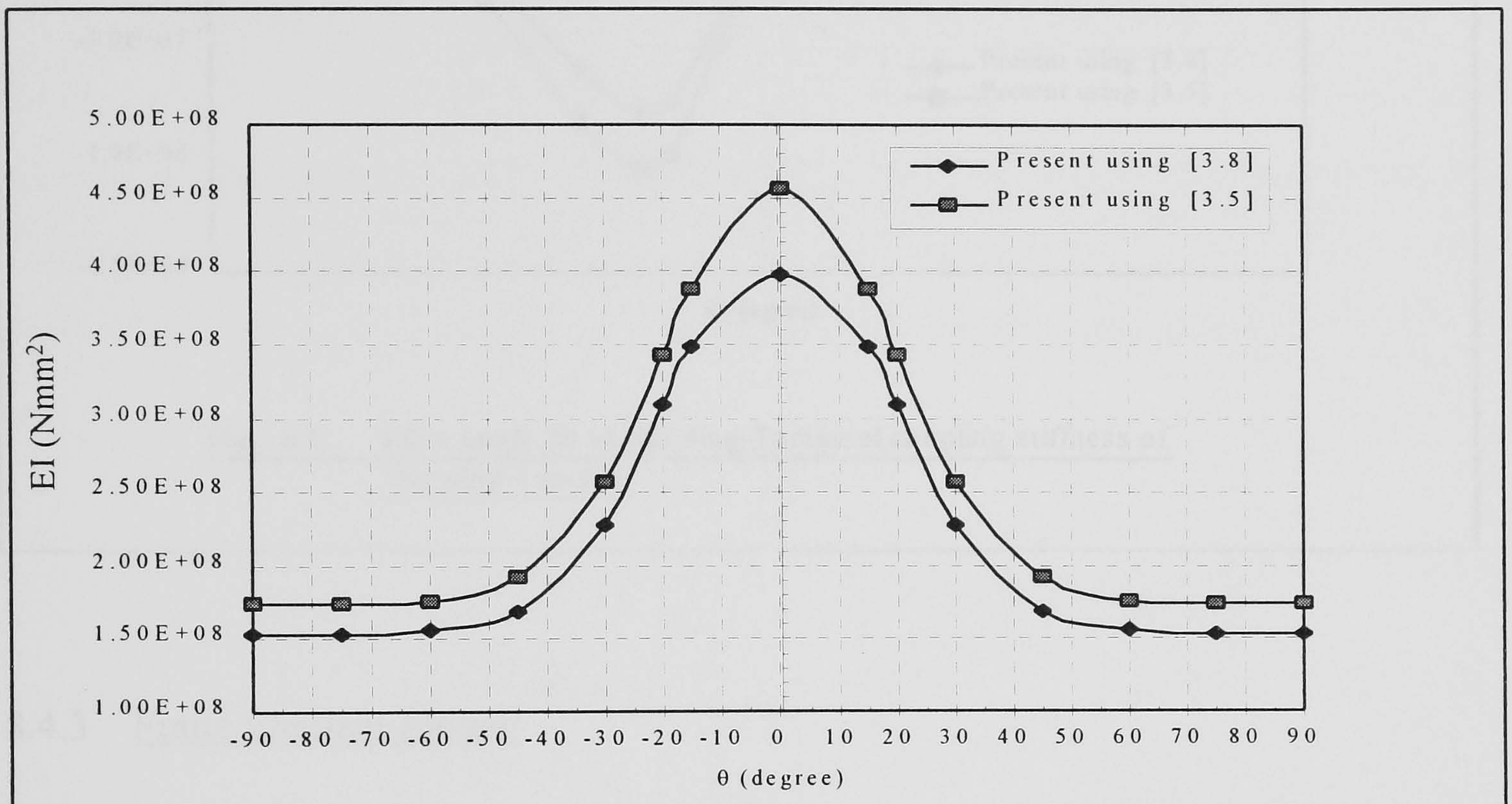

Fig. 8.2 Fibre angle (θ) vs Bending stiffness (EI) of the wing 1 and wing 6 models

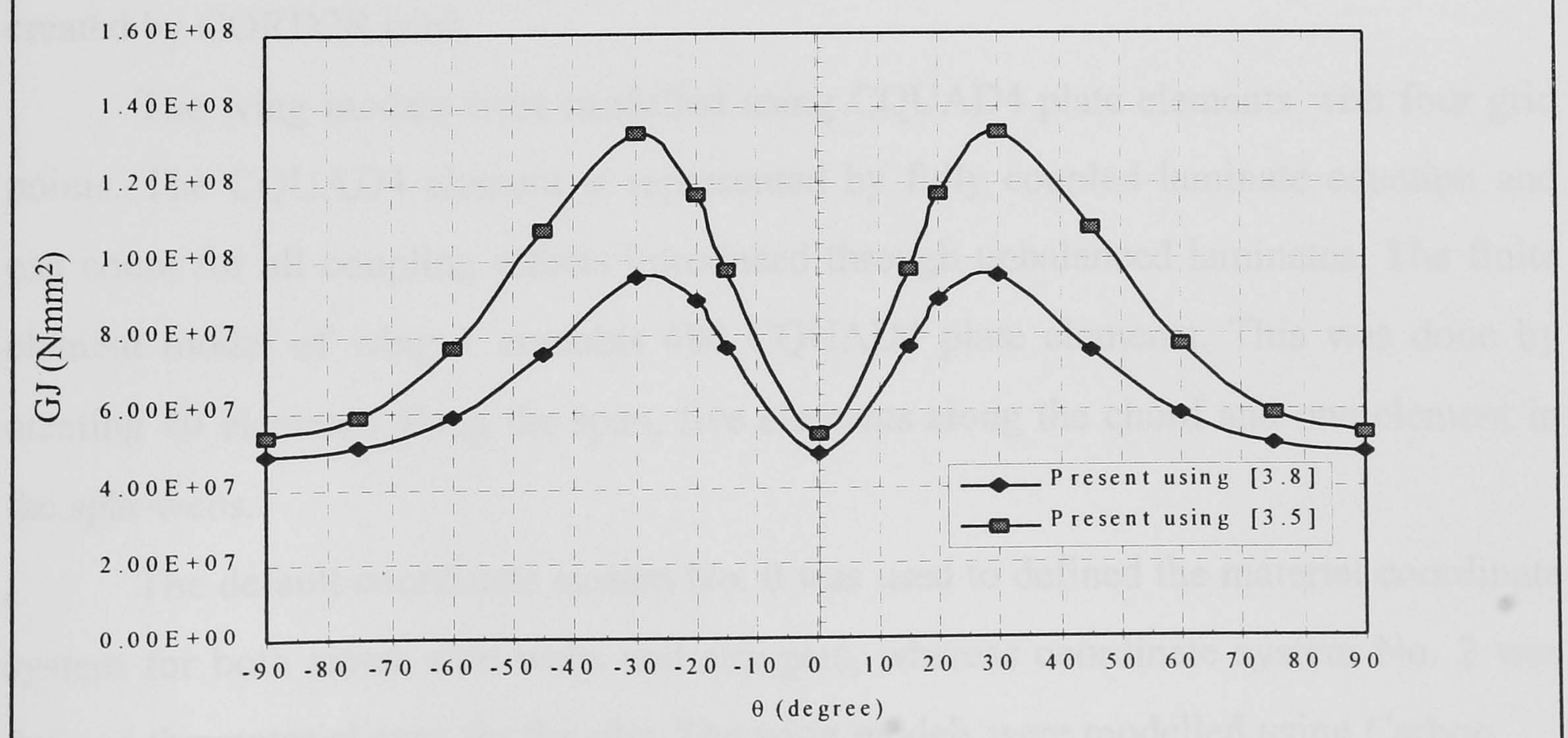

Fig. 8.3 Fibre angle (θ) vs Torsional stiffness (GJ) of the wing 1 and wing 6 models.

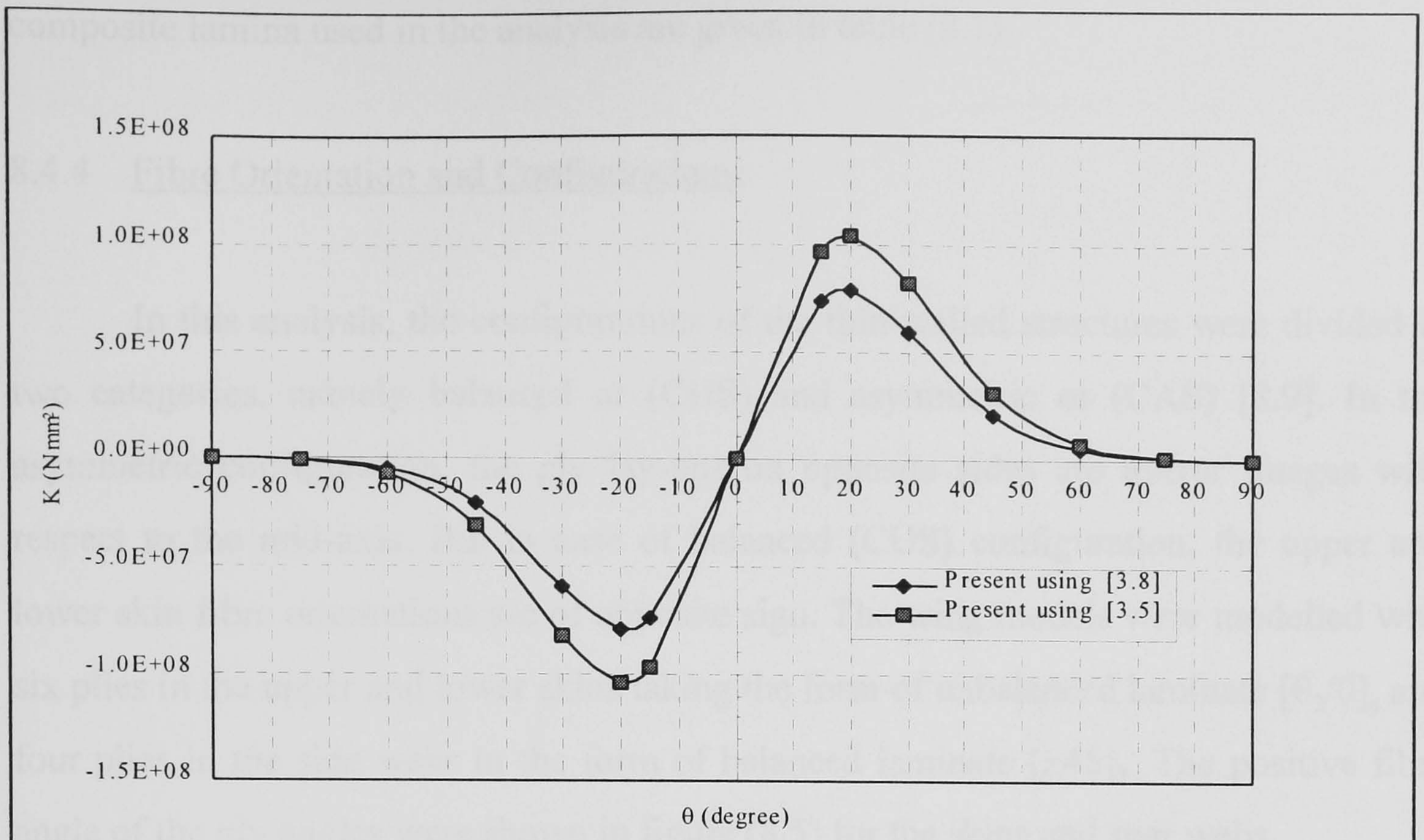

Fig. 8.4 Fibre angle (θ) vs Bending-Torsional coupling stiffness of the wing 1 model.

8.4.3 Finite Element Model:

Ten wing models were given in table (8.9), modelled and analysed using MSC/NASTRAN as in chapter 7. The global Cartesian coordinate system No. 1 was created by CORD2R card.

The wing models were modelled using CQUAD4 plate elements with four grid points. The CQUAD4 element is represented by fully coupled laminate equation and can count for all coupling effects introduced through unbalanced laminates. The finite element model of wing 1 contains 480 CQUAD4 plate elements. This was done by creating 40 elements along the span, five elements along the chord and one element in the spar webs.

The default coordinate system No. 0 was used to defined the material coordinate system for both skins, side webs and stringers, whereas coordinate system No. 2 was defined the material axes for the ribs. The wing models were modelled using Carbon Fibre Reinforced Plastic (CFRP) given in [8.13]. The elastic properties of CFRP

composite lamina used in the analysis are given in table (8.1).

8.4.4 Fibre Orientation and Configurations:

In this analysis, the configurations of the thin-walled structures were divided in two categories, namely balanced or (CUS) and asymmetric or (CAS) [8.9]. In the asymmetric configuration, the ply lay-ups on opposite sides are mirror images with respect to the mid-axis. But in case of balanced (CUS) configuration, the upper and lower skin fibre orientations are of opposite sign. The wing models were modelled with six plies in the upper and lower skins taking the form of unbalanced laminate $[\theta_2/0]_s$ and four plies in the side webs in the form of balanced laminate $[\pm 45]_2$. The positive fibre angle of the ply angles were shown in figure (8.5) for the skins and spar webs.

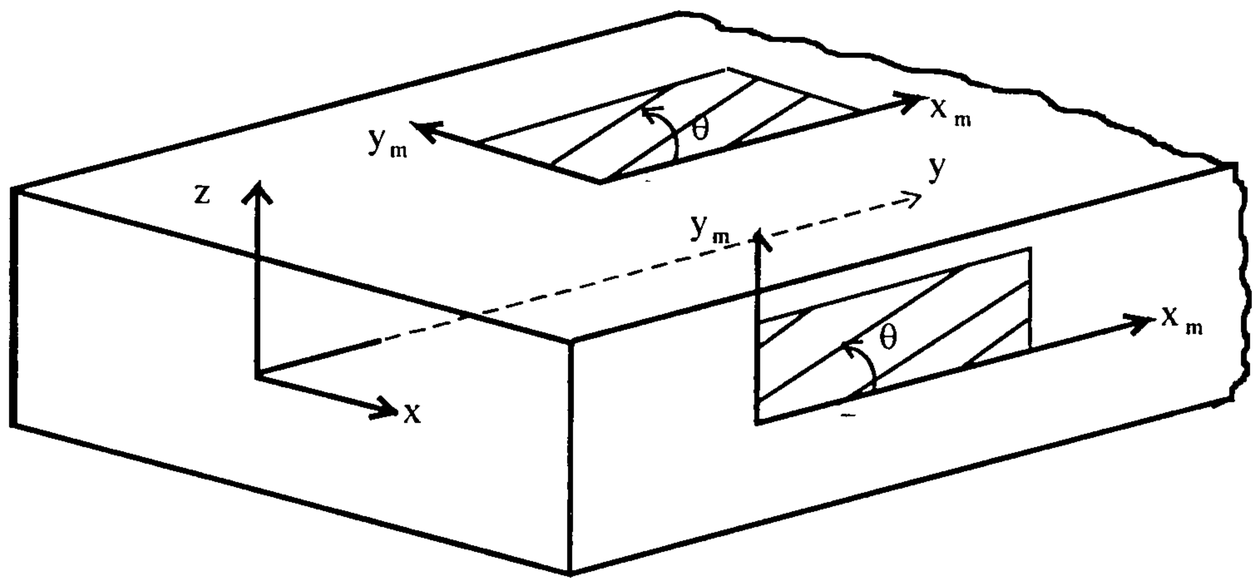

Fig. 8.5 Coordinate system and sign convention for positive angle skin laminates and spar laminates

These are considered to be practical lay-ups as not recommended to keep the outer plies as a unidirectional plies (0 or 90 degrees) [8.5]. These configurations are outlined below:

1. Circumferentially Asymmetric Stiffness (CAS) configuration:

Five different wing models were constructed to simulate (CAS) configurations. From the first thin-walled structure (see figure (1.1) of chapter 1), two wing models were modelled using symmetric and asymmetric laminates for wing 1 and wing 2 models respectively. Similarly from the second, third and fourth thin-walled structures

(see figure (1.2-1.4) of chapter 1), three wing models were constructed using symmetric laminates for the wing 3, wing 4 and wing 5 respectively. The laminate lay-ups forms of the five wing models (CAS) were given in detail in table (8.9). This configuration, which shown in figure (8.6) will produce bend-twist coupling stiffness [8.9 and 8.10] and therefore, the effects of the fibre orientations with a various amount of bending-twist coupling on the natural frequencies, mode shapes of the structure, and hence on the flutter speed will be investigated. This form of unbalanced laminate will represent a wide range of positive and negative bending-twist coupling, torsional stiffness and bending stiffness as shown in figure (8.2-8.4).

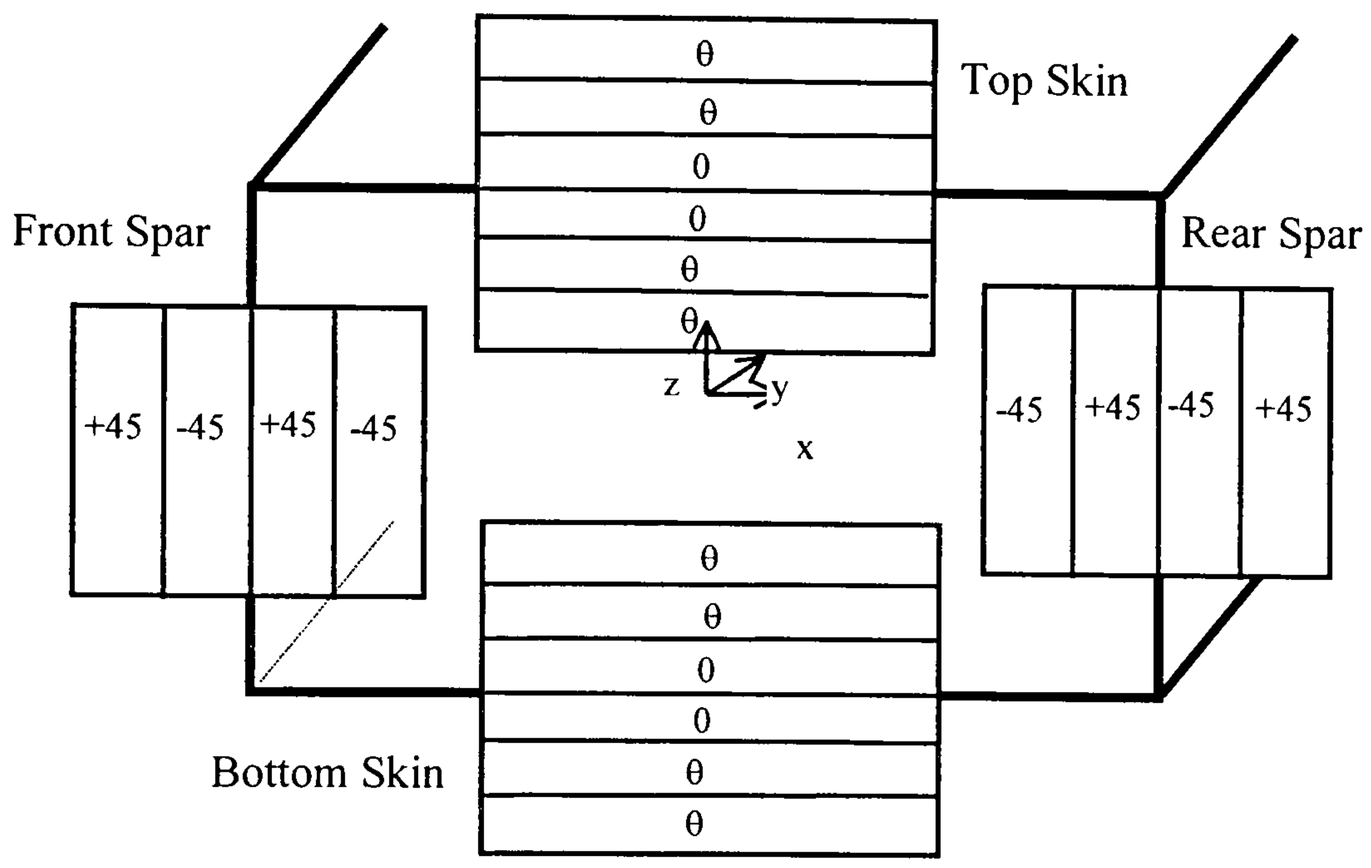

Fig. 8.6 Circumferentially Asymmetric Stiffness (CAS) configuration of the thin-walled Structures.

2. <u>Circumferentially Uniform Stiffness (CUS) configuration</u>:

Five wing models were modelled in the same way above to represent the (CUS) configuration as presented in table (8.9). This configuration shown in figure (8.7) will not produce any bending-torsional stiffness coupling (K = 0), but will produce an extension-twist coupling instead. This configuration will behave as isotropic materials but with having the same bending and torsional stiffness of the composite material as in the CAS configuration. Two types of laminate configurations were used in the

modelling of wing structures (see table 8.9). The cross-section and laminate lay-ups of the hat section stringer were shown in figure (8.8).

Table (8.9) Configurations of the thin-walled structures used in the analysis.

Configuration	Wing model number.	Upper skin	Lower skin	Front and Rear spars	Ribs	Stringer caps	Stringer sides
Asymmetric (CAS)	Wing 1	$[\theta_2/0]_s$	$[\theta_2/0]_s$	$[\pm45]_2$	-	-	-
Asymmetric	Wing 2	$[\theta_2/0]_2$	$[\theta_2/0]_2$	$[\pm45]_2$	-	-	-
Asymmetric	Wing 3	$[\theta_2/0]_s$	$[\theta_2/0]_s$	$[\pm45]_2$	$[\pm45_2]_s$	-	-
Asymmetric	Wing 4	$[\theta_2/0]_s$	$[\theta_2/0]_s$	$[\pm45]_2$	-	[±45/0/±45]	[±45]
Asymmetric	Wing 5	$[\theta_2/0]_s$	$[\theta_2/0]_s$	$[\pm45]_2$	-	[±45/0/±45]	[±45]
Balanced (CUS)	Wing 6	$[\theta_2/0]_s$	$[-\theta_2/0]_s$	$[\pm45]_2$	-	-	-
Balanced	Wing 7	$[\theta_2/0]_2$	$[-\theta_2/0]_2$	$[\pm45]_2$	-	-	-
Balanced	Wing 8	$[\theta_2/0]_s$	$[-\theta_2/0]_s$	$[\pm45]_2$	$[\pm45_2]_s$	-	-
Balanced	Wing 9	$[\theta_2/0]_s$	$[-\theta_2/0]_s$	$[\pm45]_2$	-	[±45/0/±45]	[±45]
Balanced	Wing 10	$[\theta_2/0]_s$	$[-\theta_2/0]_s$	$[\pm45]_2$	-	[±45/0/±45]	[±45]

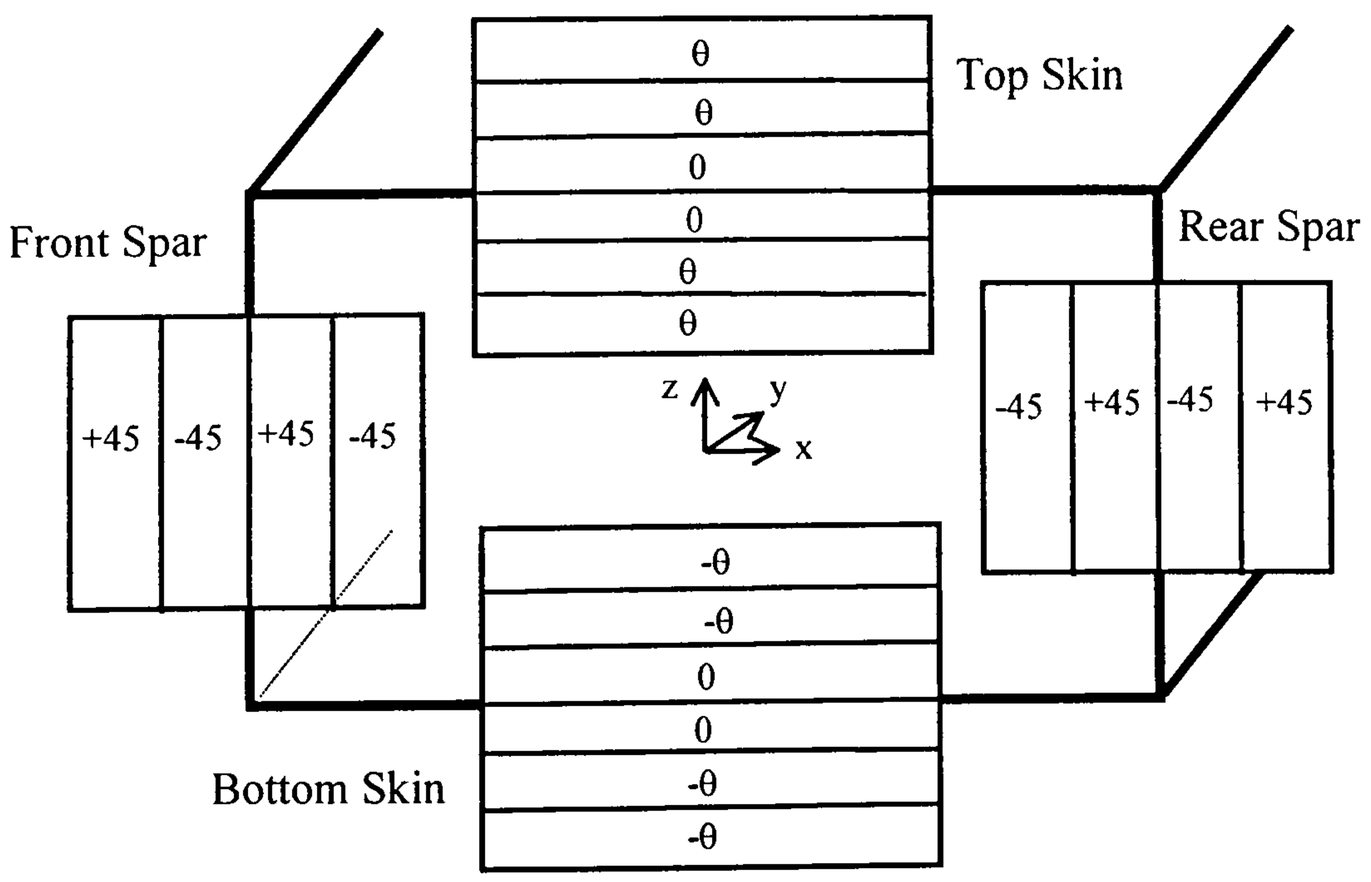

Fig. 8.7 Circumferentially Uniform Stiffness (CUS) configuration of the thin-walled Structures.

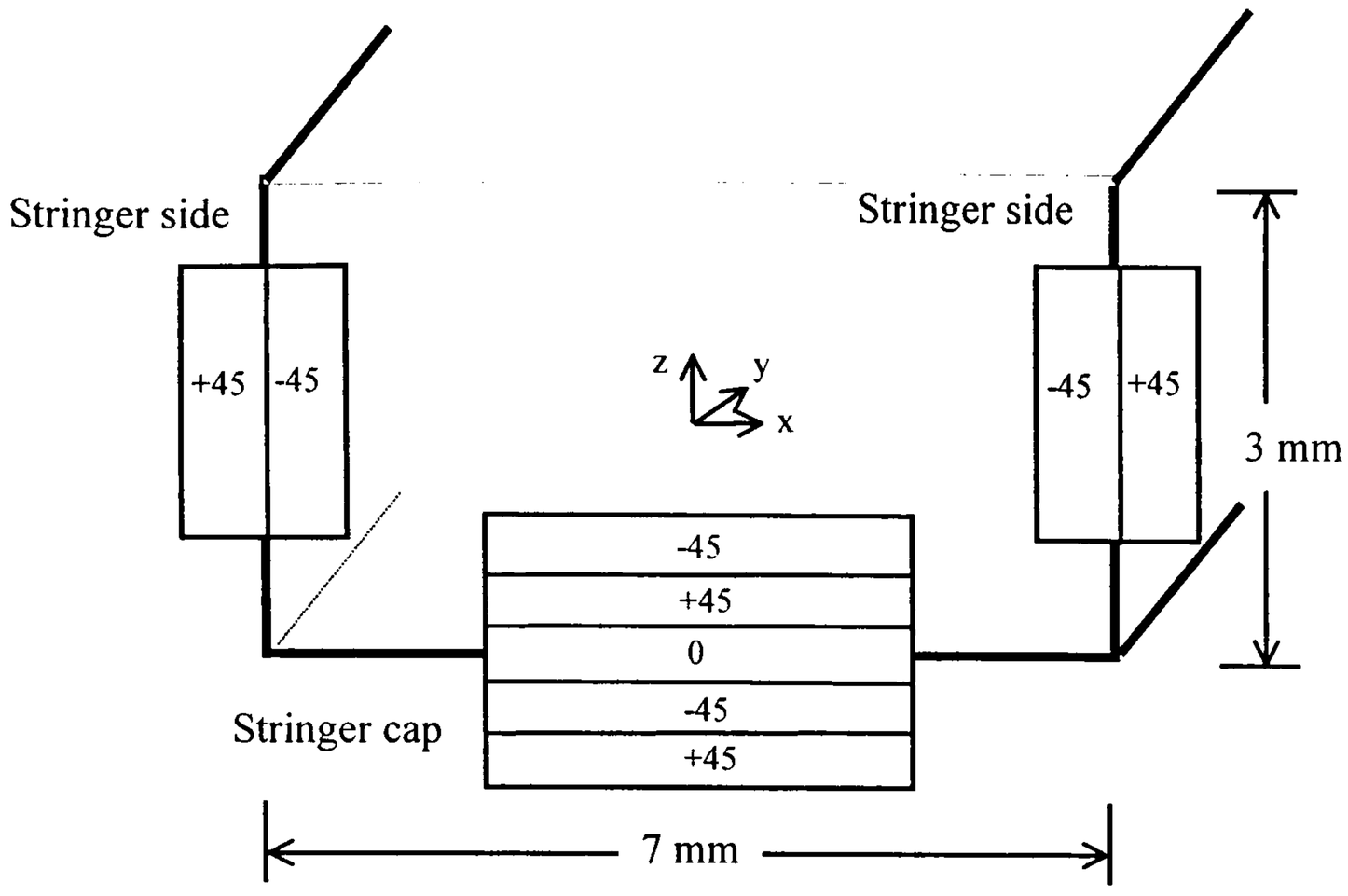

Fig. 8.8 Stringer Configuration and laminate lay-ups.

The effective bending, torsional and bending-torsional coupling stiffnesses were calculated for the symmetric laminated of the wing 1 and wing 6 models using the approach outlined in chapter 3. This will show the effect of the fibre orientations with and without the amount of bend-twist coupling on the natural frequencies and mode shapes of the structure and hence on the flutter speed and frequency.

8.4.5 Normal Mode Analysis:

Normal mode analysis or real eigenvalue (undamped free vibrations) was carried out to determine the basic dynamic characteristics of the structure (natural frequency and mode shapes).

The solution 103 (normal mode analysis) was selected for all wing models and the eigenvalues and eigenvectors are then computed using Lanczos method as in the previous chapters (6 and 7).

8.4.5.1 Results:

The undamped free vibration analysis was done for all the wing models using the same material properties given in [8.13] which are shown in table (8.1). The eigenvalues for the first four bending and torsional resonance frequencies with cantilevered end conditions were investigated for various fibre ply angles of the (CAS) and (CUS) configurations. The variation of the first four bending and torsional natural frequencies as a function of the fibre angle were shown in figure (8.9) and (8.28) for (wing 1 and wing 6) and (wing 2 and wing 7) respectively. Representative results for the first six egienvalues and eigenvectors of wing 1 model when $\theta = 0^{o}$, 30^{o} and 90^{o} were shown in figure (8.10-8.27). Similarly figure (8.29) showed that how the natural frequencies changes with the change of the fibre angle of wing 3 and wing 8 models.

The trend of variation of the natural frequencies versus the fibre angle of (wing 4 and wing 9) and (wing 5 and wing 10) were shown in figure (8.30) and (8.31) respectively.

8.4.5.2 Discussion of results:

The presence of stiffness cross coupling as shown in figure (8.2-8.4) can provide large change in both frequencies and mode shapes of similar, but orthotropic laminates. As shown in figures (8.9 and 8.28-8.31), the effect of ply orientation with different amount of coupling stiffness on the natural frequencies is quite pronounced. The effective stiffness of wing 1 and wing 6 models (see figure 8.2-8.4) show that the bending stiffness (EI) decreasing as the fibre angle increasing, whereas the torsional stiffness (GJ) started increasing up to $\pm 30^{o}$ and then declined.

However, bend-twist coupling stiffness (K) of the wing 1 model shows that the maximum coupling was at $\pm 20^{o}$ and then declined to zero at $\pm 90^{o}$. The values of bending stiffness, torsional stiffness and bend-twist coupling of a laminated plate are very much depends on the value of D_{11}, D_{66} and the sign of D_{16} values of the transformed reduced stiffness matrix respectively in the case of the out of plan stiffness [8.9] as presented in

chapter 3. The difference in both methods is mainly in the difference of the inclusion of the warping and displacement functions in the formulation of the analysis.

However, the essential purpose of figure (8.9) of wing 1 and wing 6 models was to show trends and modal interchanges as a result of ply orientations that can be interpreted as follows:

Looking at the wing 1 model, the first mode is basically a dominated fundamental bending with a small torsion displacement for $0°<\theta<\pm90°$ as shown in figure (8.16) for a selected fibre angle of $\theta = 30°$. The first mode shape at $\theta = 0°$ and $90°$ were purely bending modes as shown in figures (8.10 and 8.22). The second natural frequency was a pure second bending mode at $\theta = 0°$ and $90°$ and as bending mode with various amount of torsion displacement for all the fibre angle between $0°$ and $\pm90°$ as shown in figure (8.9) and (8.12, 8.18 and 8.24) at $\theta = 0°$, $30°$ and $90°$ respectively. It can be seen that the first and second natural frequency decreases as the fibre angle increases due to decrease in spanwise bending rigidity (EI) as shown in figure (8.2). The third natural frequency is the pure first torsion mode for $\theta = 0°$ and then changes to a third bending mode with various amount of torsional displacement at $0°<\theta<\pm90°$ and then back to the pure first torsional mode at $\theta = \pm90°$ as shown in figure (8.13, 8.20 and 8.26) respectively. Similarly, the forth natural frequency is a pure third bending mode at $\theta = 0°$, first torsional mode for with various amount of bending displacement in it at $0°<\theta<\pm90°$, and then back to the pure third bending mode at $\theta = \pm90°$ as shown in figure (8.15, 8.21 and 8.27). The maximum torsional frequency was occurred at $\theta = \pm30°$ as shown in figure (8.9).

The dynamic behaviour of the wing 6 model (CUS) model was the same as the wing 1 model for the first two modes, but as pure bending modes without torsional displacement as bending-torsional coupling (K) equal to zero in this configuration. The third and forth modes were the same as in the wing 1 model, but as pure modes in this wing configuration (CUS) except that there was a modal change at $\theta = \pm20°$ as shown in figure (8.9), due to the elimination of the maximum bending-torsional coupling present in wing 1 model (see figure 8.4). From figure (8.9), the effect of including the bending-torsional coupling stiffness (K) as in the case of wing 1 model (CAS) configuration is that the torsional frequency becomes higher as compared to the case of wing 6 model

(CUS) configuration when (K) was not included. However, the effect of bending-torsional coupling stiffness (K) on the bending frequency was found almost negligible. The effect of bending-torsional coupling stiffness was found pronounced on the mode shapes of the wing 1 model at 30° especially on the second and third bending modes (see figure 8.18 and 8.20). This was observed as well by MSC/NASTRAN and [8.10] in section 8.2 of this chapter.

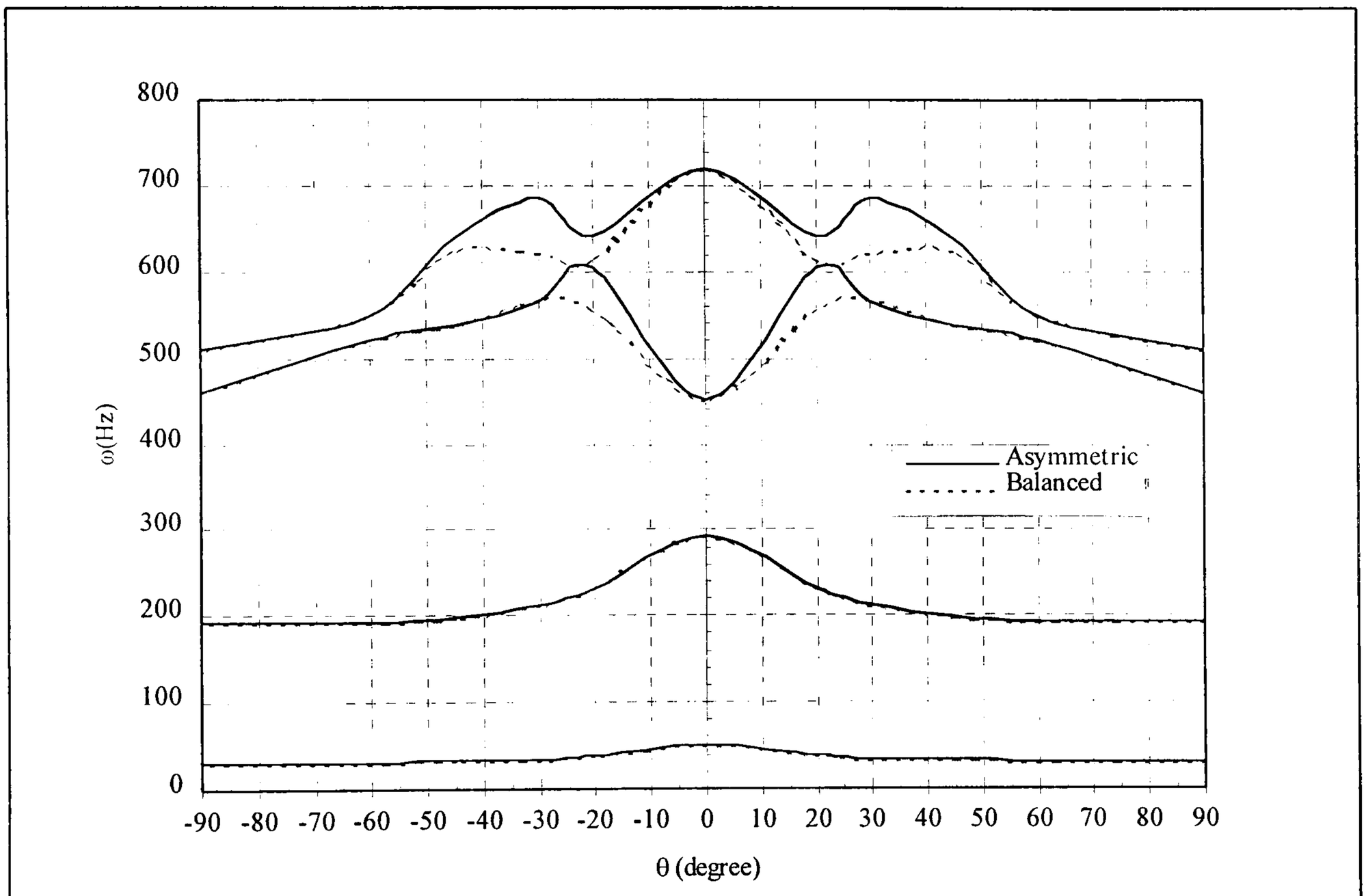

Fig. 8.9 Variation of the first four bending and torsional frequencies of wing 1 and wing 6 models versus ply angle (θ).

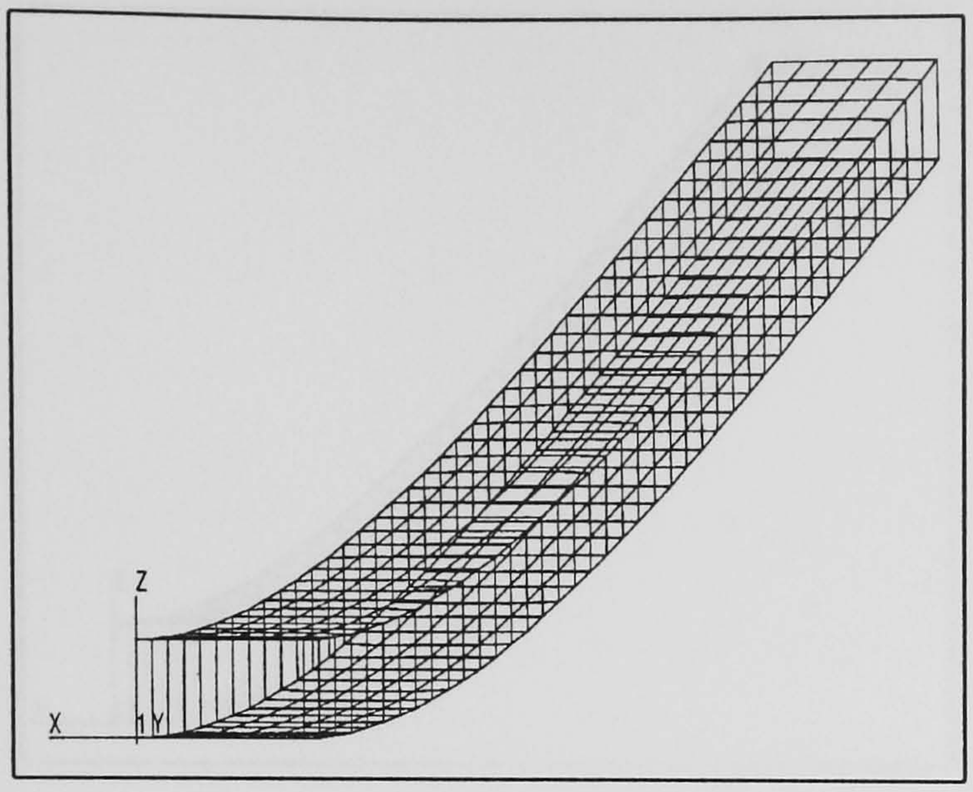

Fig. 8.10 1st Bending mode (50.439 Hz) for the wing 1 model at θ=0 degree.

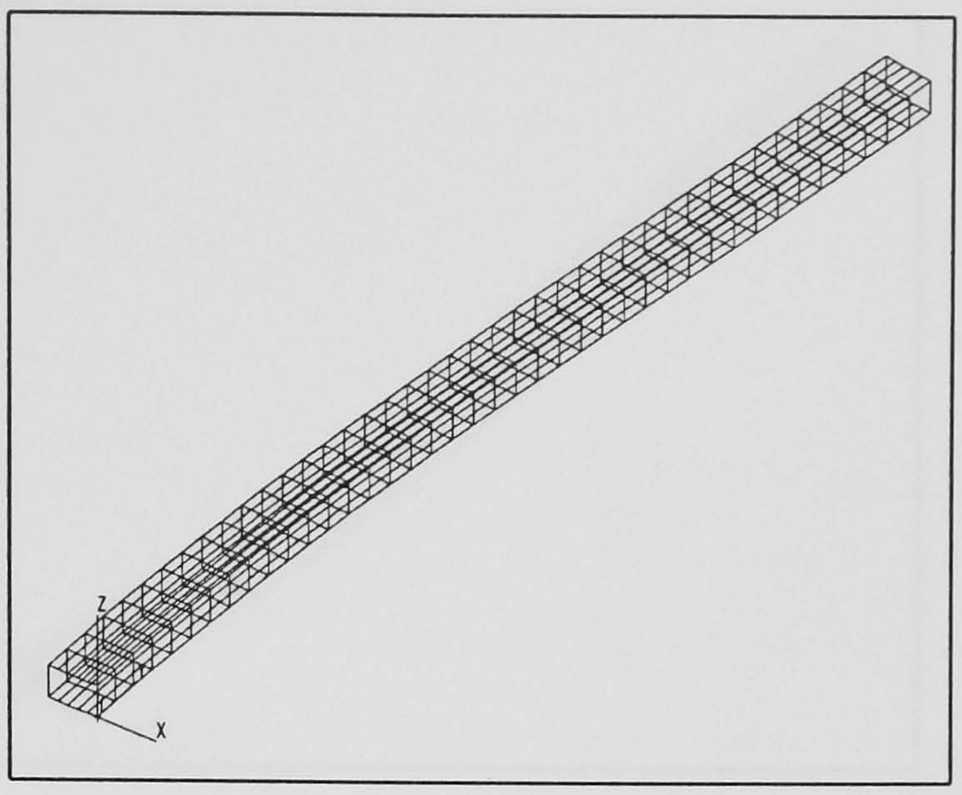

Fig. 8.11 1st Chord wise mode (81.033 Hz) for the wing 1 model at θ=0 degree.

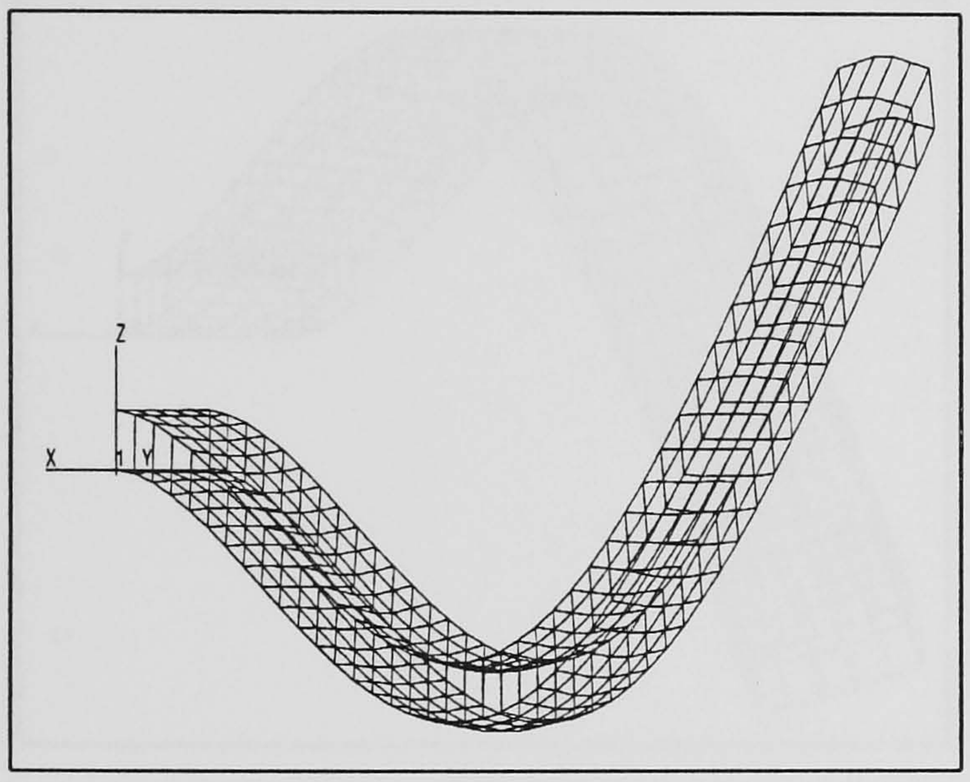

Fig. 8.12 2nd Bending mode (293.522 Hz) for the wing 1 model at θ=0 degree.

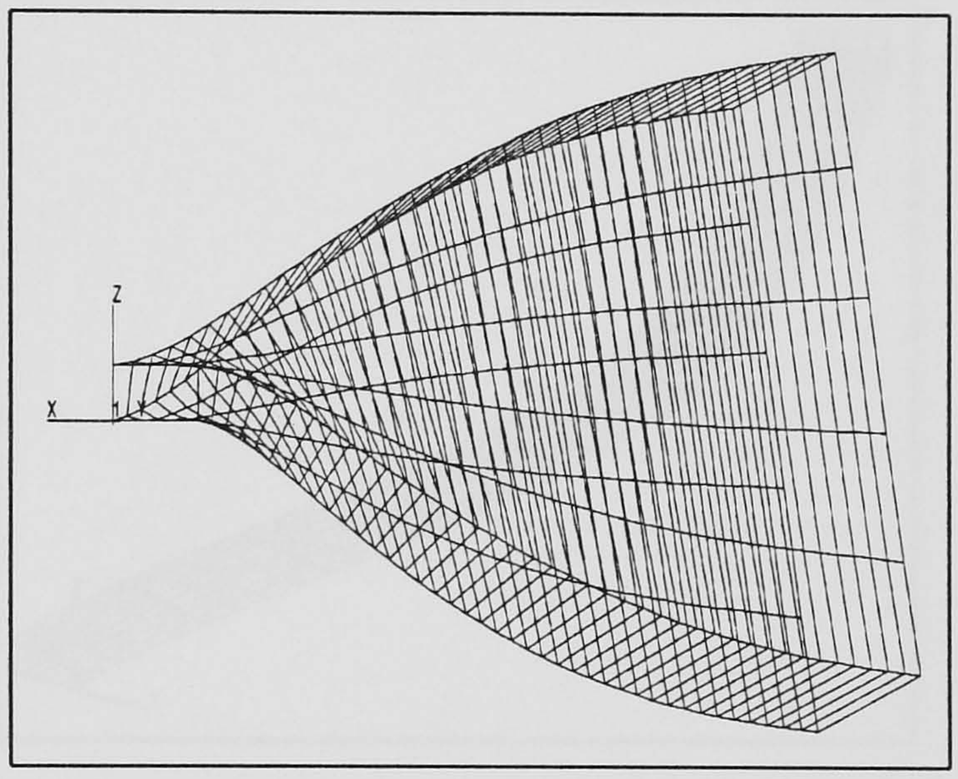

Fig. 8.13 1st Torsion mode (450.583 Hz) for the wing 1 model at θ=0 degree.

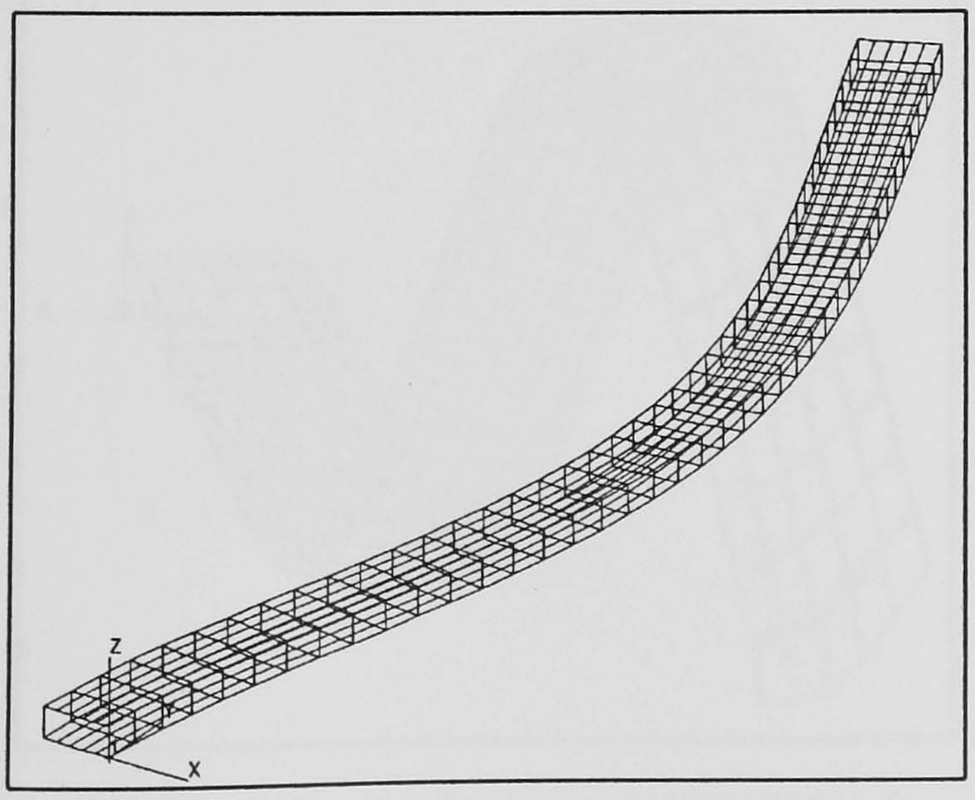

Fig. 8.14 2nd Chord wise mode (470.401 Hz) for the wing 1 model at θ=0 degree.

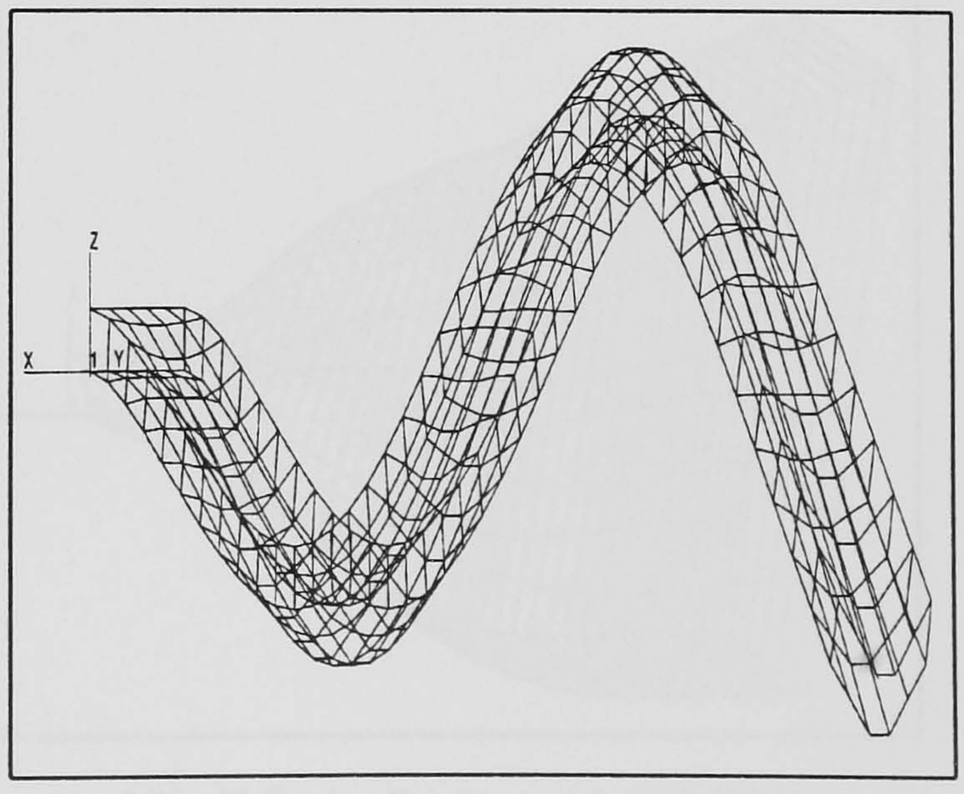

Fig. 8.15 3rd Bending mode (720.451 Hz) for the wing 1 model at θ=0 degree.

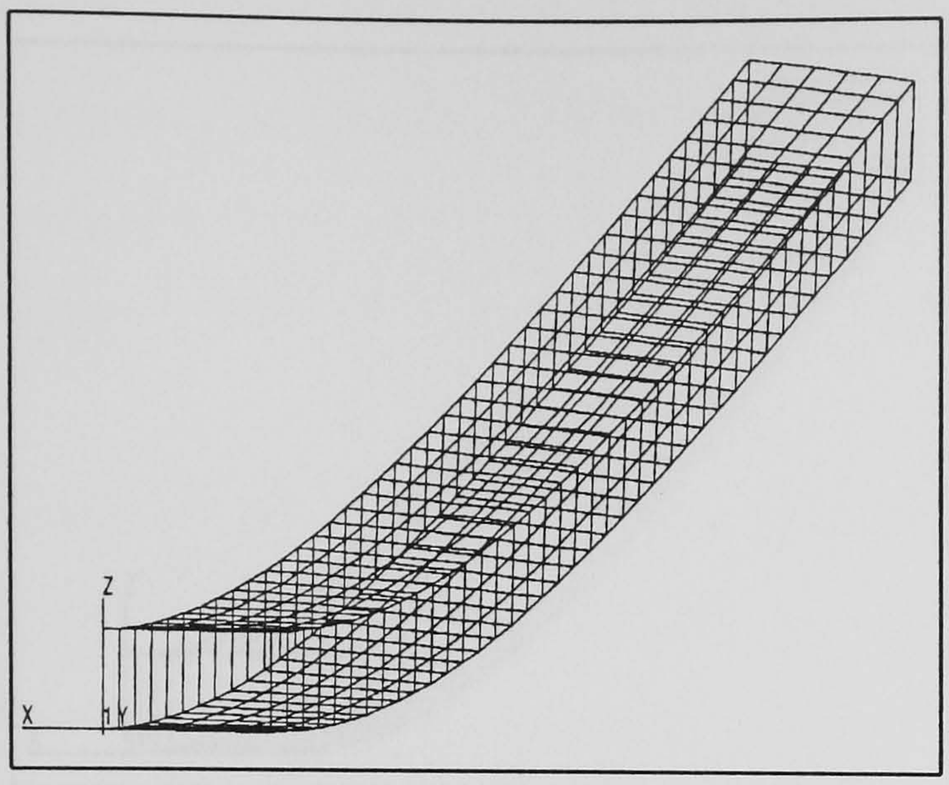

Fig. 8.16 1st Bending-Torsion mode (34.987 Hz) for the wing 1 model at θ=30 degree.

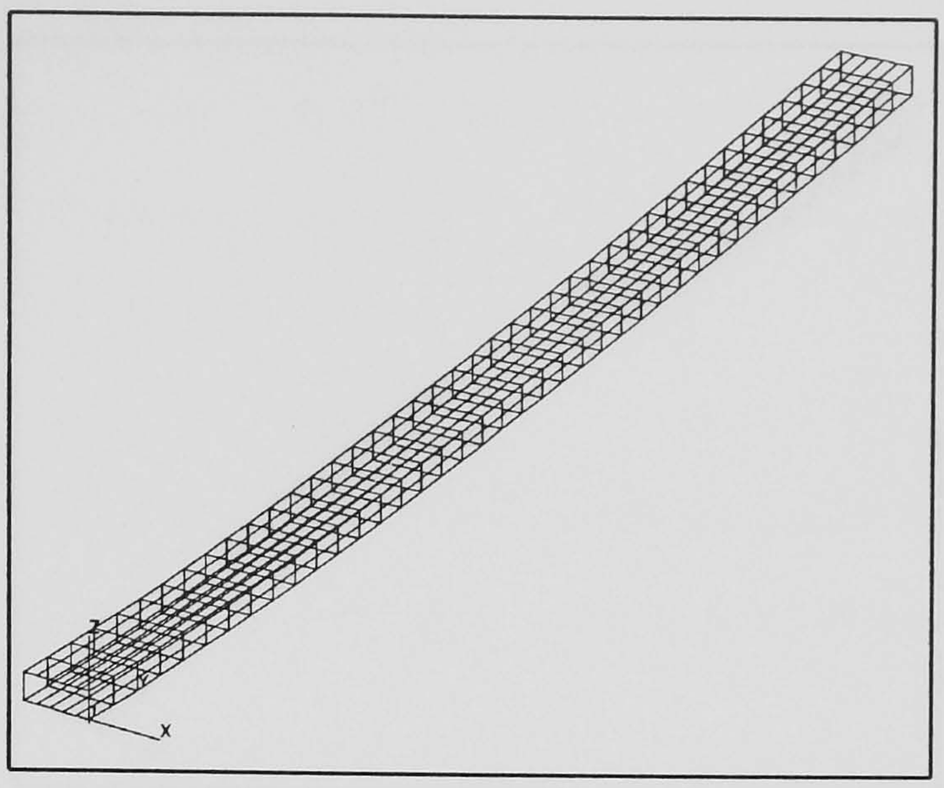

Fig. 8.17 1st Chord wise mode (59.194 Hz) for the wing 1 model at θ=30 degree.

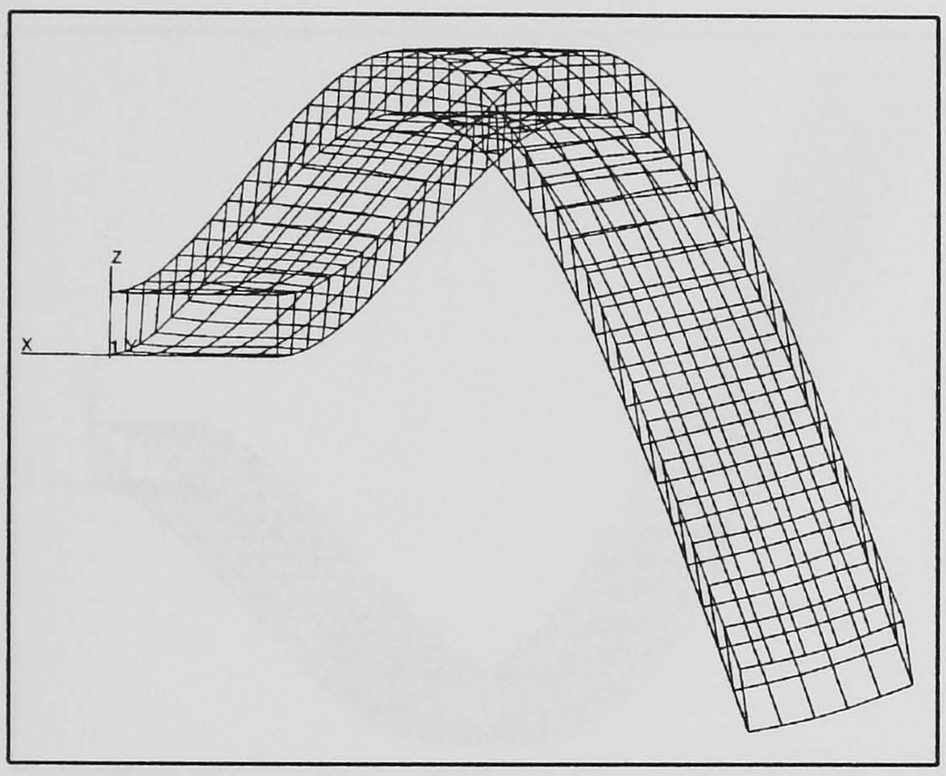

Fig. 8.18 2nd Bending-Torsion mode (215.124 Hz) for the wing 1 model at θ=30 degree.

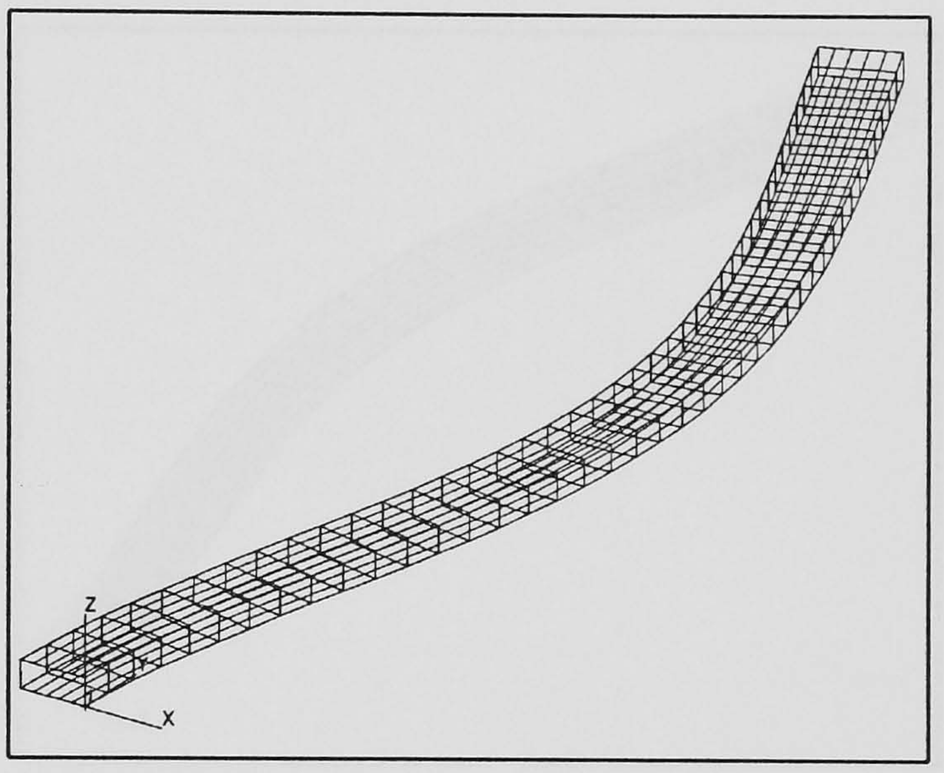

Fig. 8.19 2nd Chord wise mode (363.703 Hz) for the wing 1 model at θ=30 degree.

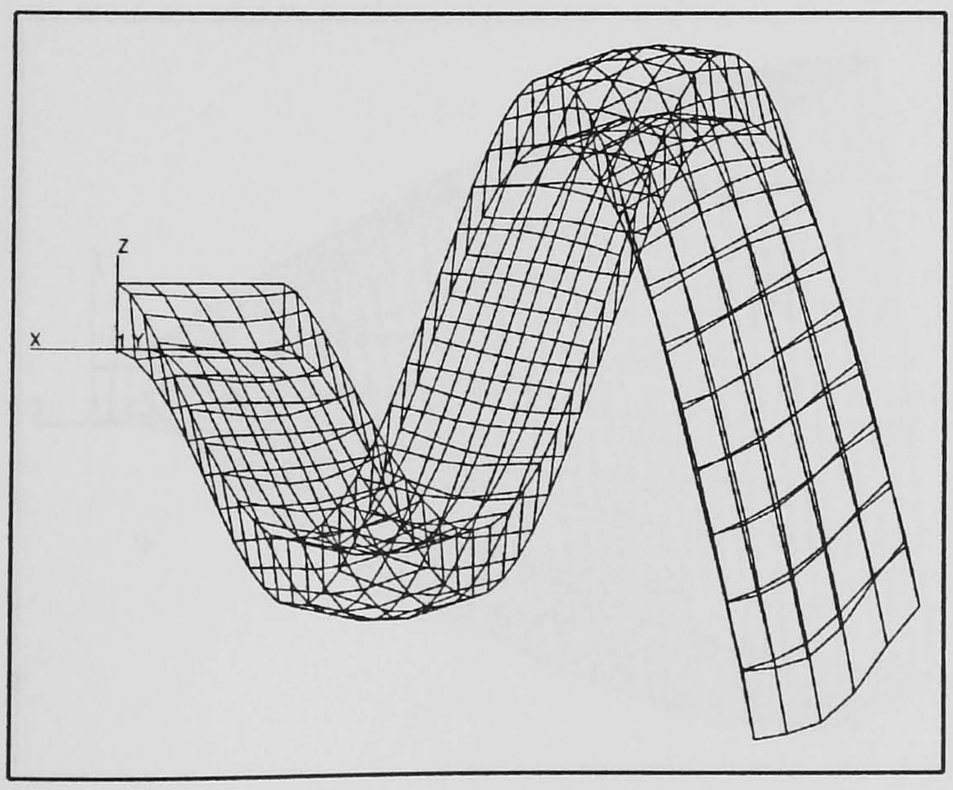

Fig. 8.20 3rd Bending-Torsion mode (578.076 Hz) for the wing 1 model at θ=30 degree.

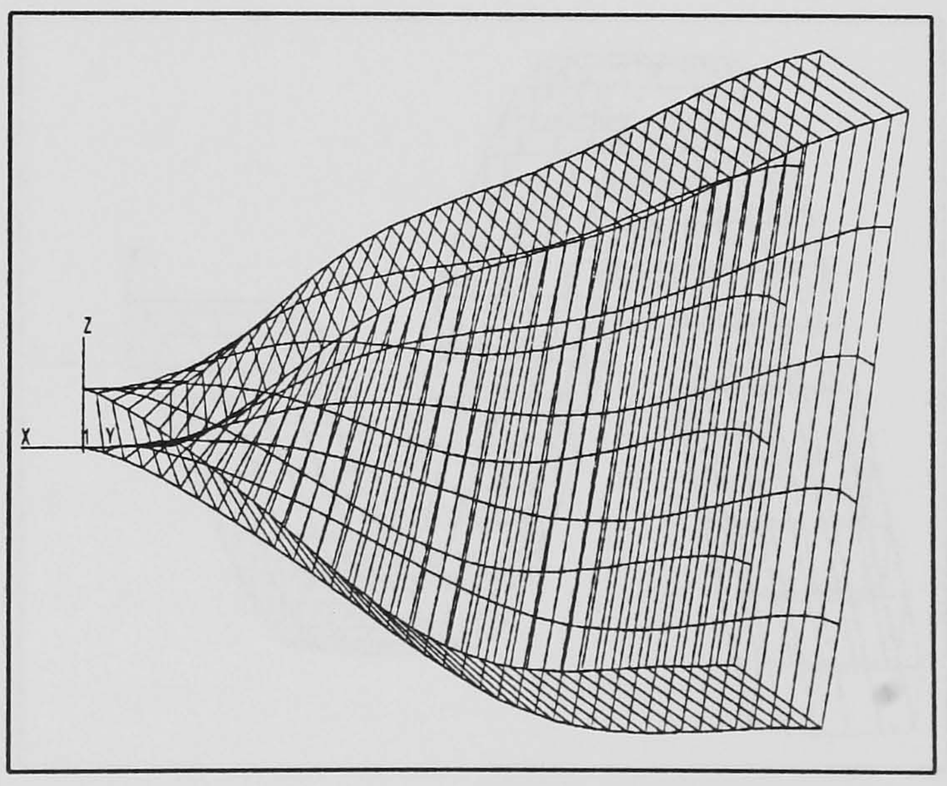

Fig. 8.21 1st Torsion-Bending mode (690.528 Hz) for the wing 1 model at θ=30 degree.

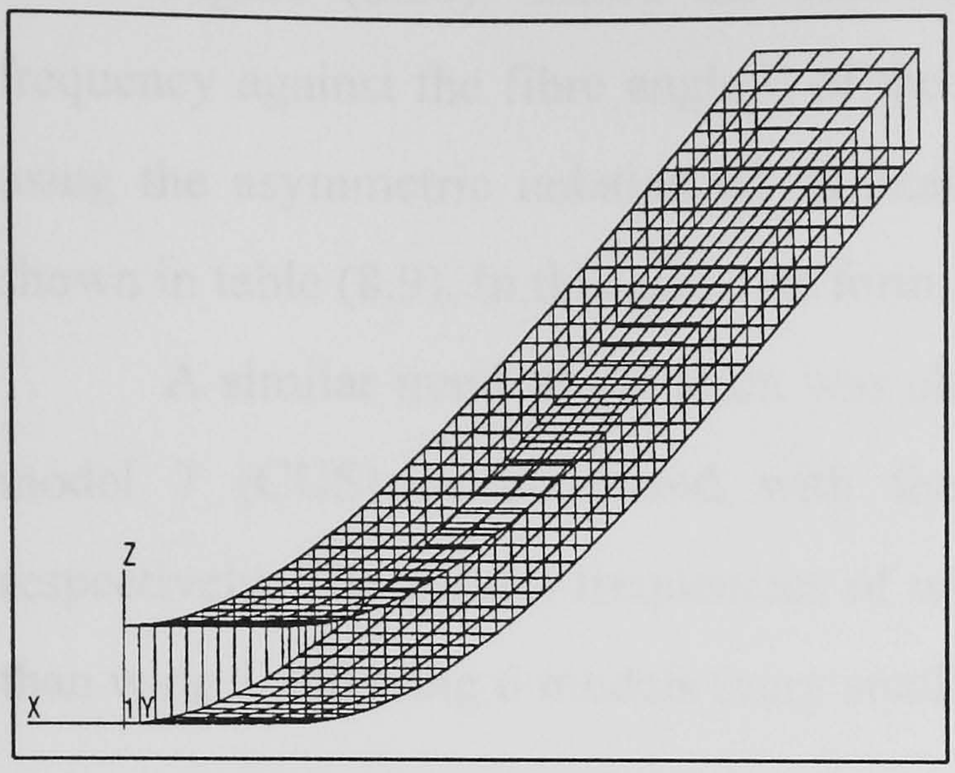

Fig. 8.22 1st Bending mode (31.998 Hz) for the wing 1 model at θ=90 degree.

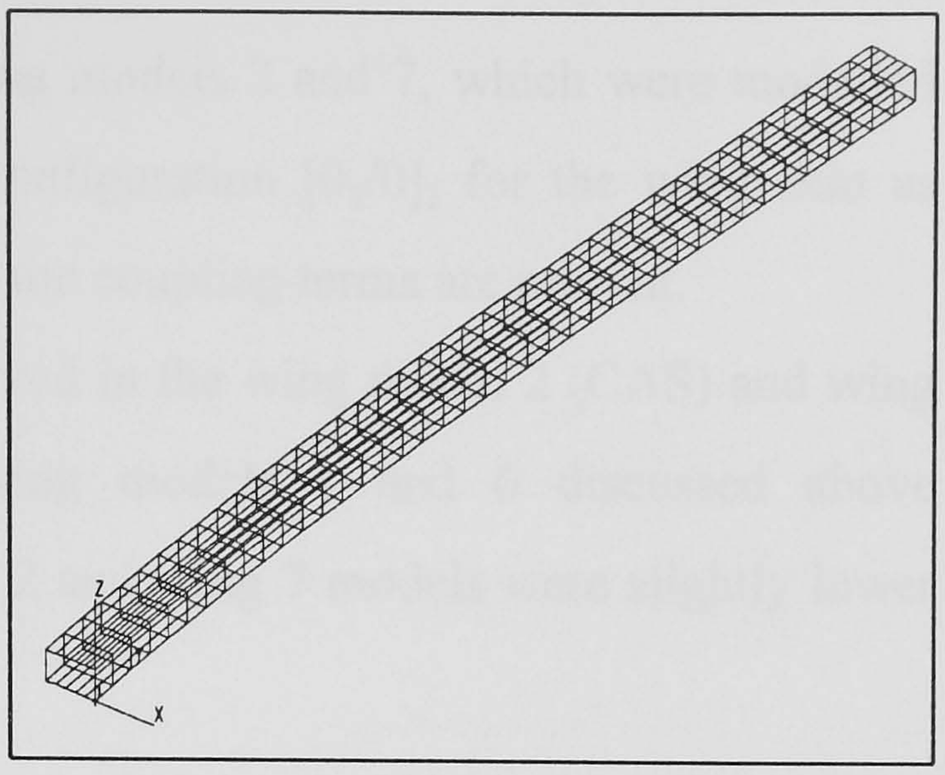

Fig. 8.23 1st Chord wise mode (53.990 Hz) for the wing 1 model at θ=90 degree.

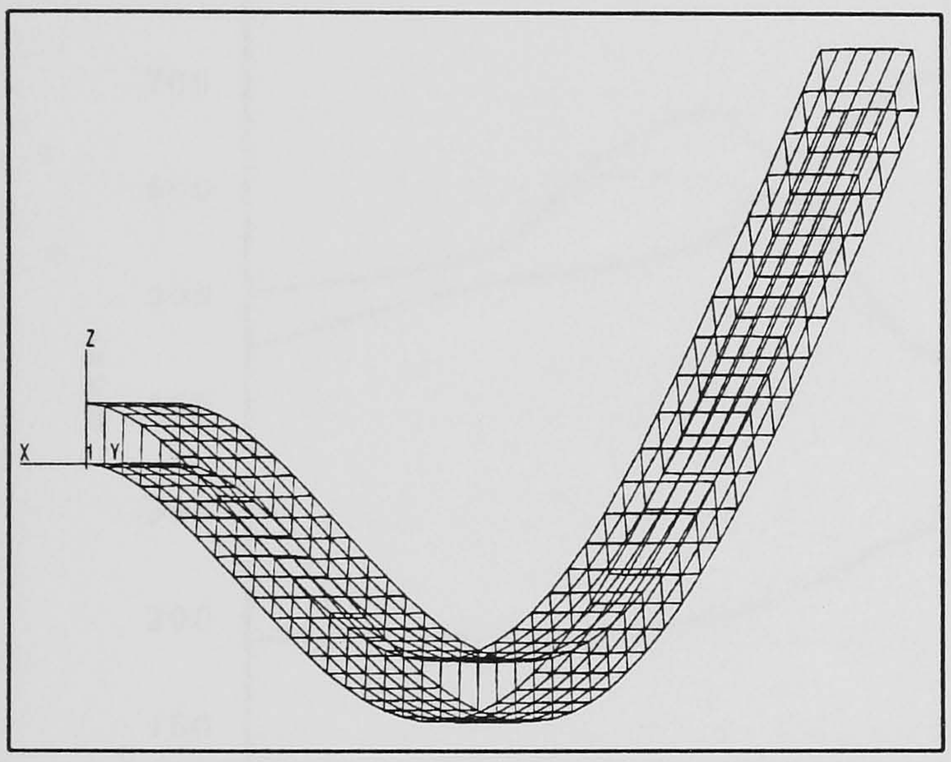

Fig. 8.24 2nd Bending mode (194.985 Hz) for the wing 1 model at θ=90 degree.

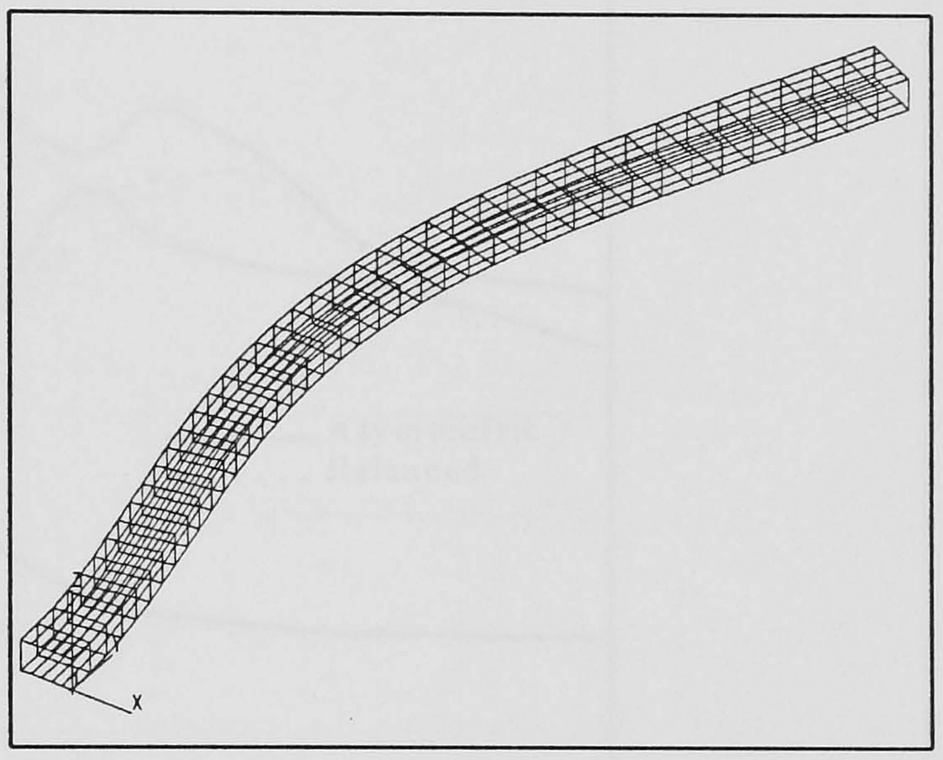

Fig. 8.25 2nd Chord wise mode (326.252 Hz) for the wing 1 model at θ=90 degree.

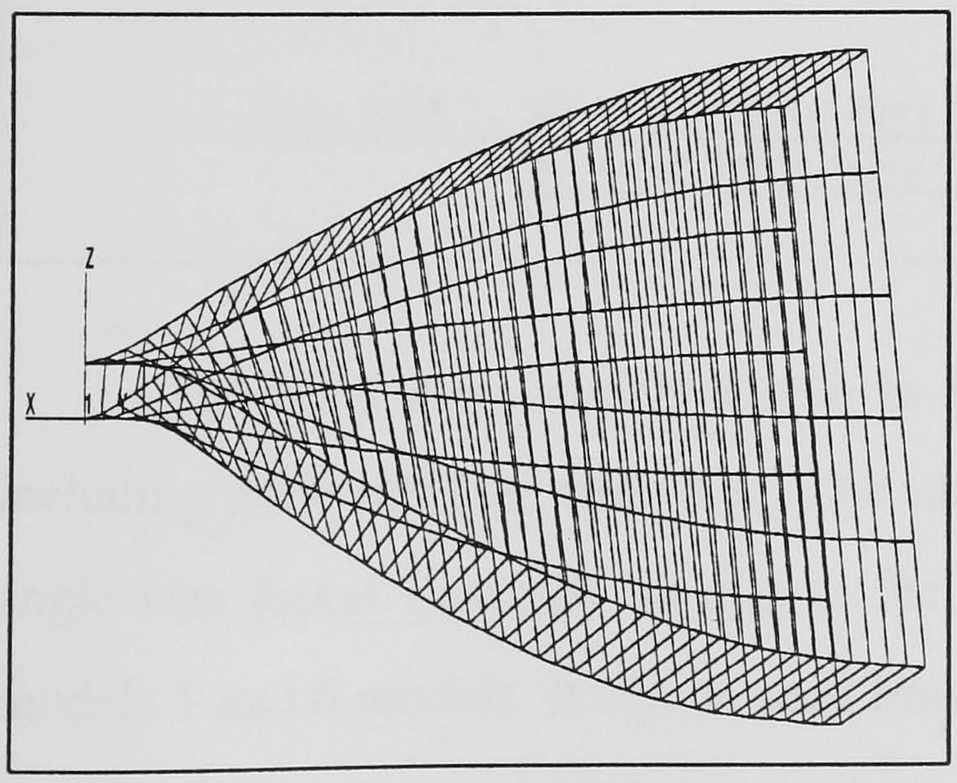

Fig. 8.26 1st Torsion mode (461.232 Hz) for the wing 1 model at θ=90 degree.

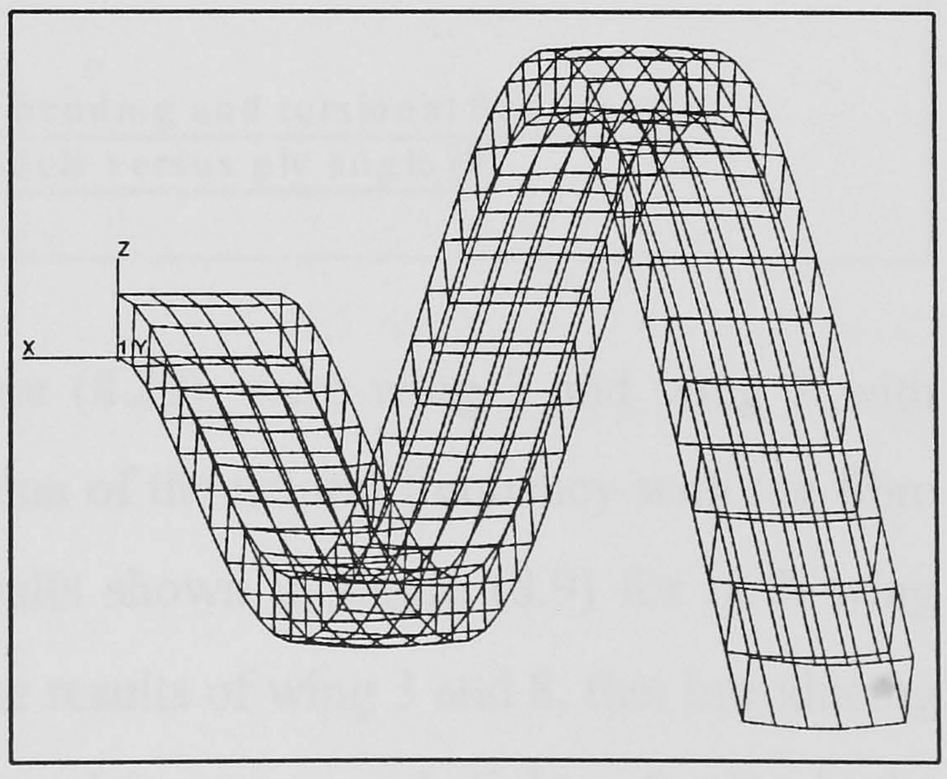

Fig. 8.27 3rd Bending mode (522.630 Hz) for the wing 1 model at θ=90 degree.

Figure (8.28), shows the variation of the first four bending and torsional frequency against the fibre angle θ of the wing models 2 and 7, which were modelled using the asymmetric unbalanced laminate configuration $[\theta_2/0]_2$ for the wing skin as shown in table (8.9). In this laminate form, all the coupling terms are present.

A similar trend of variation was observed in the wing model 2 (CAS) and wing model 7 (CUS) as compared with the wing models 1 and 6 discussed above respectively. The natural frequencies of wing 2 and wing 7 models were slightly lower than wing 1 and wing 6 models (very small).

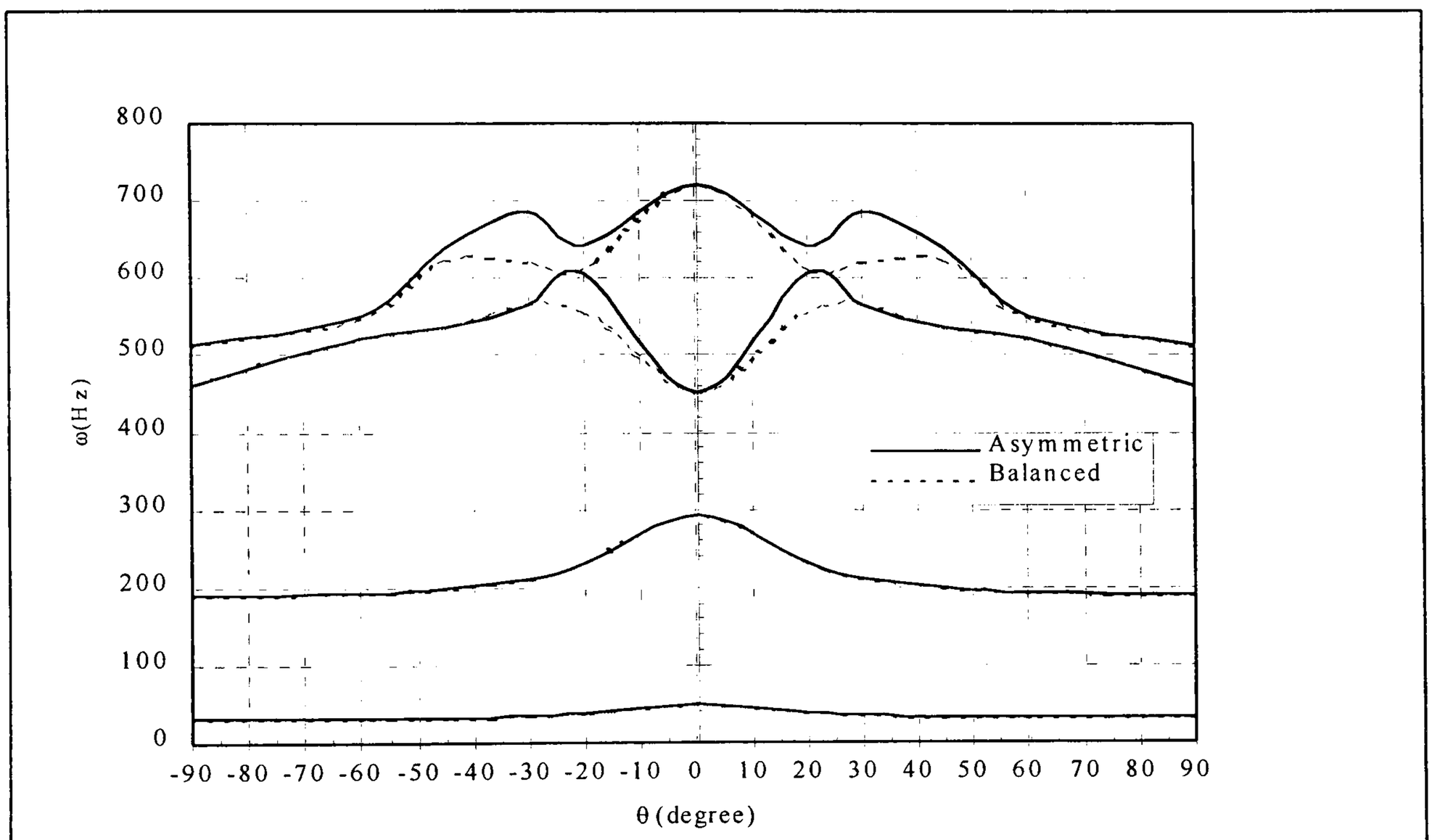

Fig. 8.28 Variation of the first four bending and torsional frequencies of wing 2 and wing 7 models versus ply angle (θ).

The next wing models shown in figure (8.29), were wing 3 and wing 8 with including three ribs (see table 8.9). The variation of the natural frequency with the fibre angle was found generally similar to the results shown in figure (8.9) for both wing models 1 and 6 models. It can be seen from the results of wing 3 and 8, that introducing the ribs to the structure, leads to a higher torsional frequency and slight reduction in the bending frequency compared with wing 1 model and wing 6 model, even though the

mass of the structure was slightly greater in the case of wing 3 and wing 8 models.

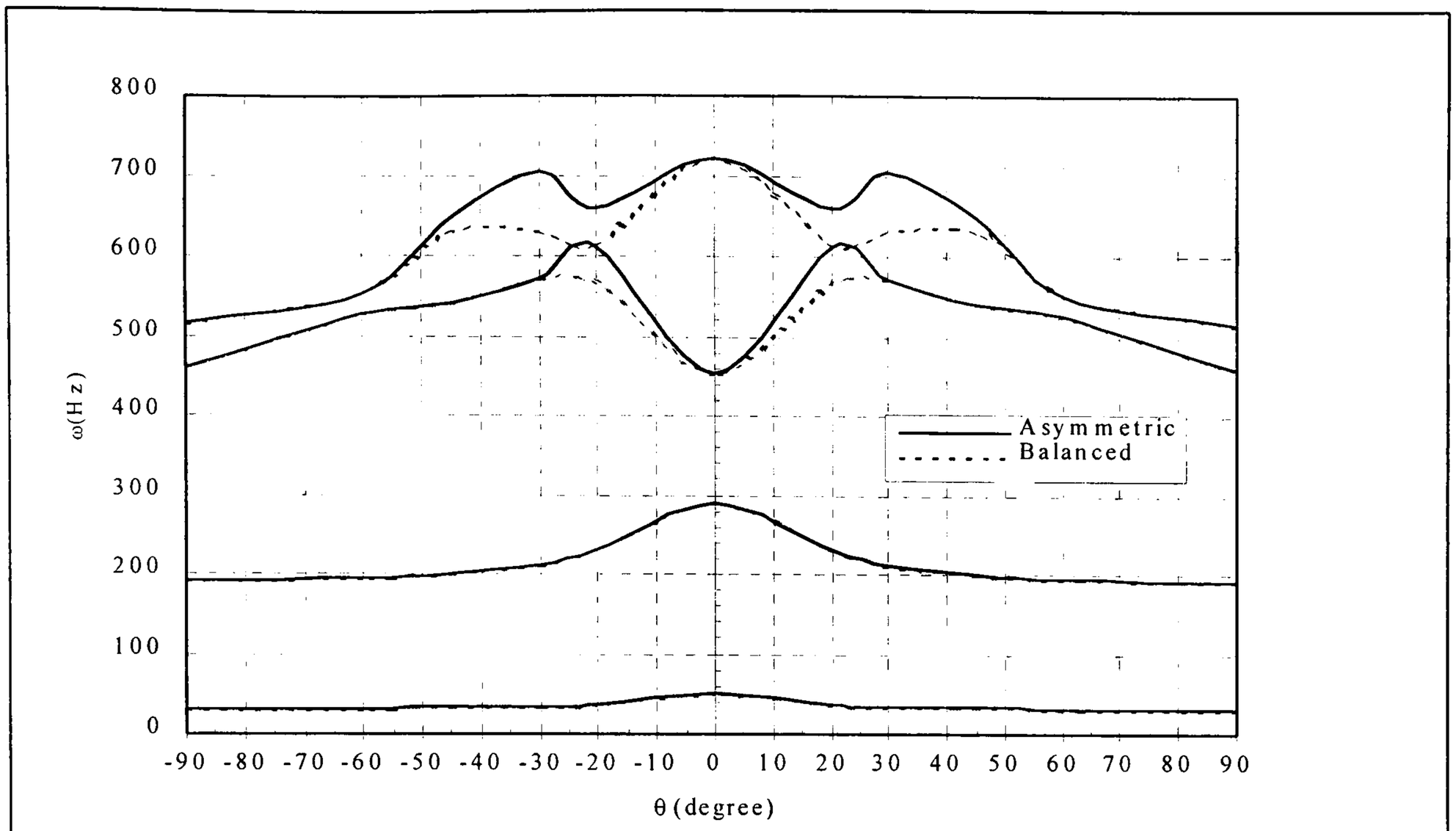

Fig. 8.29 Variation of the first four bending and torsional frequencies of wing 3 and wing 8 models versus ply angle (θ).

A similar response was observed in the wing models (4 and 9) and (5 and 10) shown in figure (8.30) and (8.31) compared with the response of the wing 1 model and wing 6 model shown in figure (8.9). In this case, stringer was located at the middle of the upper and lower skin for wing 4 (CAS) and 9 (CUS) and close to the rear spar web for wing 5 (CAS) and 10 (CUS). It was noticed that with adding stringer to the structure, the bending frequency decreases more than the torsional frequency compared with wing 1 and wing 6 models. It was found that including the structural coupling (offset between the elastic and inertia axis) as in wing 5 and wing 10 leads to a higher reduction in the torsional frequency than bending frequency compared with wing 4 and wing 9 models as shown in figures (8.30) and (8.31).

It can be seen that from figures (8.9 and 8.28-8.31) that the variation of the natural frequency and mode shapes versus the fibre orientations are symmetric about zero degree. This was observed by [8.14] for a solid plate beam and in [8.15] for thin walled structure in case of no offset between the flexural and inertia axes.

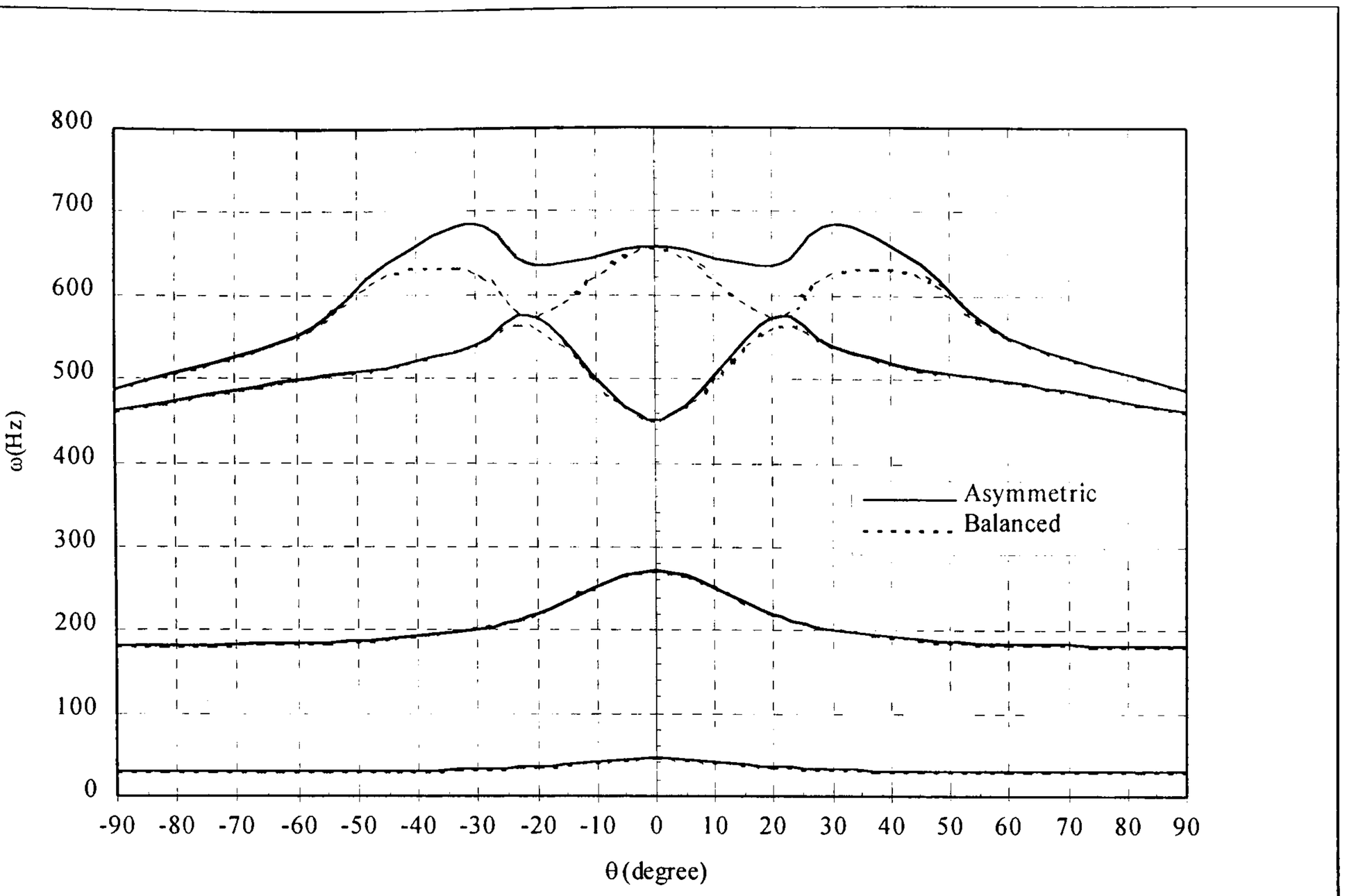

Fig. 8.30 Variation of the first four bending and torsional frequencies of wing 4 and wing 9 models versus ply angle (θ).

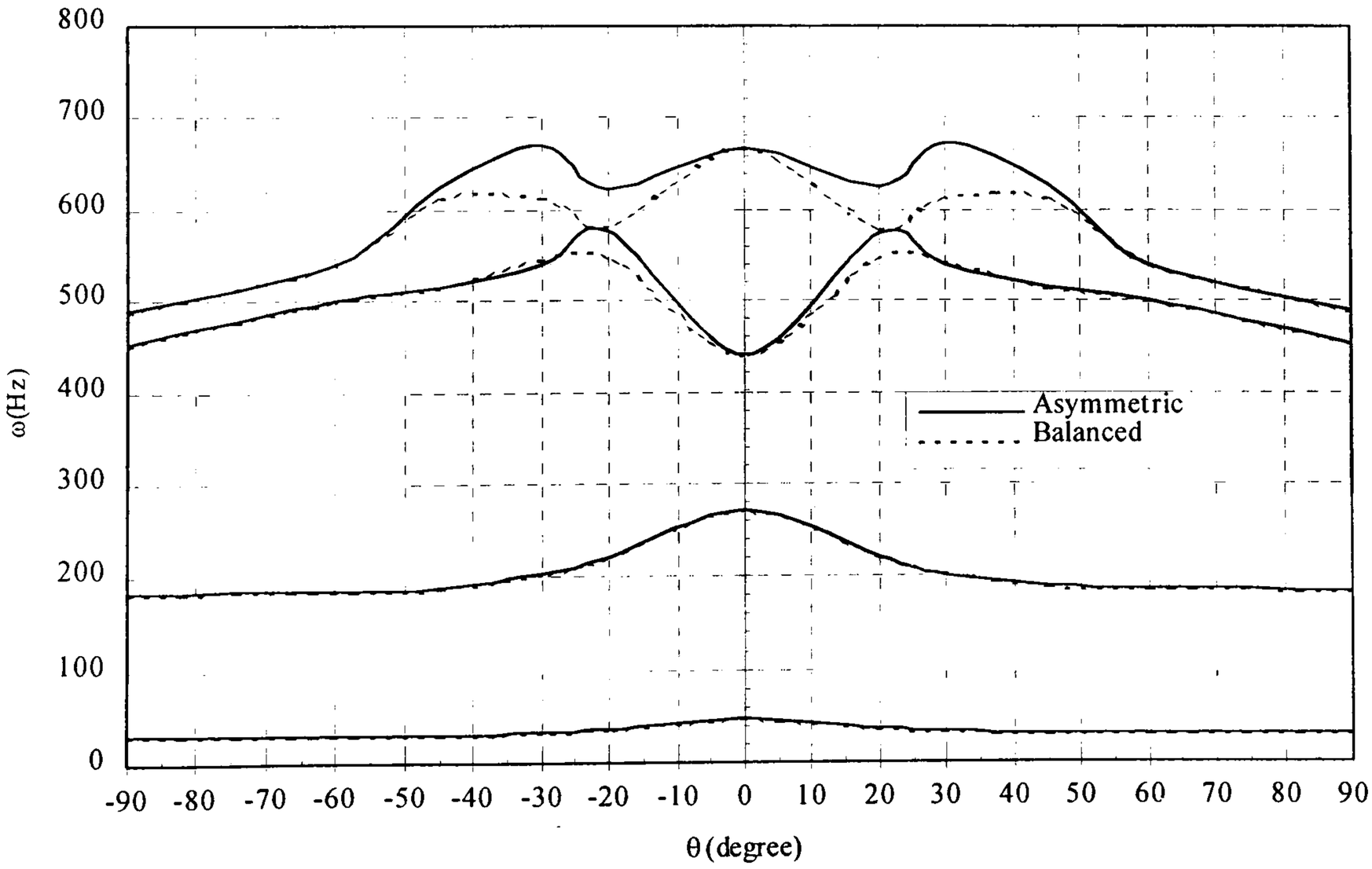

Fig. 8.31 Variation of the first four bending and torsional frequencies of wing 5 and wing 10 models versus ply angle (θ).

8.4.6 Flutter analysis:

8.4.6.1 Introduction:

In this section, the flutter analysis was carried out for all configurations of the thin-walled structures (wing models) shown in table (8.9). The flutter speed was obtained using MSC/NASTRAN as in the previous chapter. The variations of the nondimensional flutter speed against the fibre angle θ and bending frequency to torsional frequency ratio (ω_b/ω_t) (with subsequent effect of coupling (K) and wash-in and wash-out) were investigated.

8.4.6.2 Aerodynamic modelling and Flutter solutions:

Aerodynamic analysis, like structural analysis, is based upon a finite element approach. The aerodynamic models of the wing models (wing1 to wing 10) were generated using DLM and the flutter solution method was the British method (PK). A structural damping of 2% was imported for all the modes as a complex stiffness matrix. The leading edge and trailing edge of the wing models were taken as the front and rear spar location respectively. The first six natural frequencies and mode shapes of all the wing models were used in the flutter equations. The aerodynamic and flutter solution cards used in the input flutter data file was presented in section A2 of appendix A.

8.4.6.3 Results and Discussion:

A representative variation of the flight speed with the damping and frequency were taken from the output of the PK method and presented in figures (8.32-8.39) of wing 1 model for fibre angle of 0, 30, 90 and –30 degrees.

Figures (8.32-8.33) show the trend of variations of damping and frequency of the first six natural frequencies as a function of the flight speed at 0° fibre angles. It can be seen that the damping of the first mode started increasing up to 350 m/sec and then declines till intersect with the zero damping line at 510.263 m/sec. At this speed the

frequency was zero, which indicated that the static aeroelastic instability (divergence speed) has reached. The damping of the second mode was very small due to the nature of this mode (in-plane mode) and its frequency did not change with the flight speed. The damping of the third mode is increasing with the speed and there was not much changing in the frequency. The damping of the fourth mode was started as negative damping till the intersection with the zero damping line at 383.901 m/sec with frequency of 312.03 Hz as shown in figures (8.32-8.33) respectively. The variation of the fifth mode was similar to the variation of the second mode. The damping variation of the sixth mode was similar to the variation of the third mode, whereas small reduction of frequency was observed.

However, from the definition of flutter speed, it can be seen that the flutter speed was at 383.901 m/sec of the fourth mode and its corresponding frequency was at 312.03 Hz. This is called the flutter mode or the critical mode. It is the mode that goes unstable and normally, it can be seen from figure (8.33), that its frequency was very close with another mode (third mode), which indicated that these two modes are very important role in the calculation of the flutter speed.

The flutter speed at the rest of the fibre angles of all the wing models were identified after close inspection of the damping variation with the flight speed for each mode (point). It was identified as the flight speed at which the damping of the system under the action of the airforces (and the inertia, elastic, and friction forces) changes sign. At this flight speed, the total damping is zero [8.1] and [8.3].

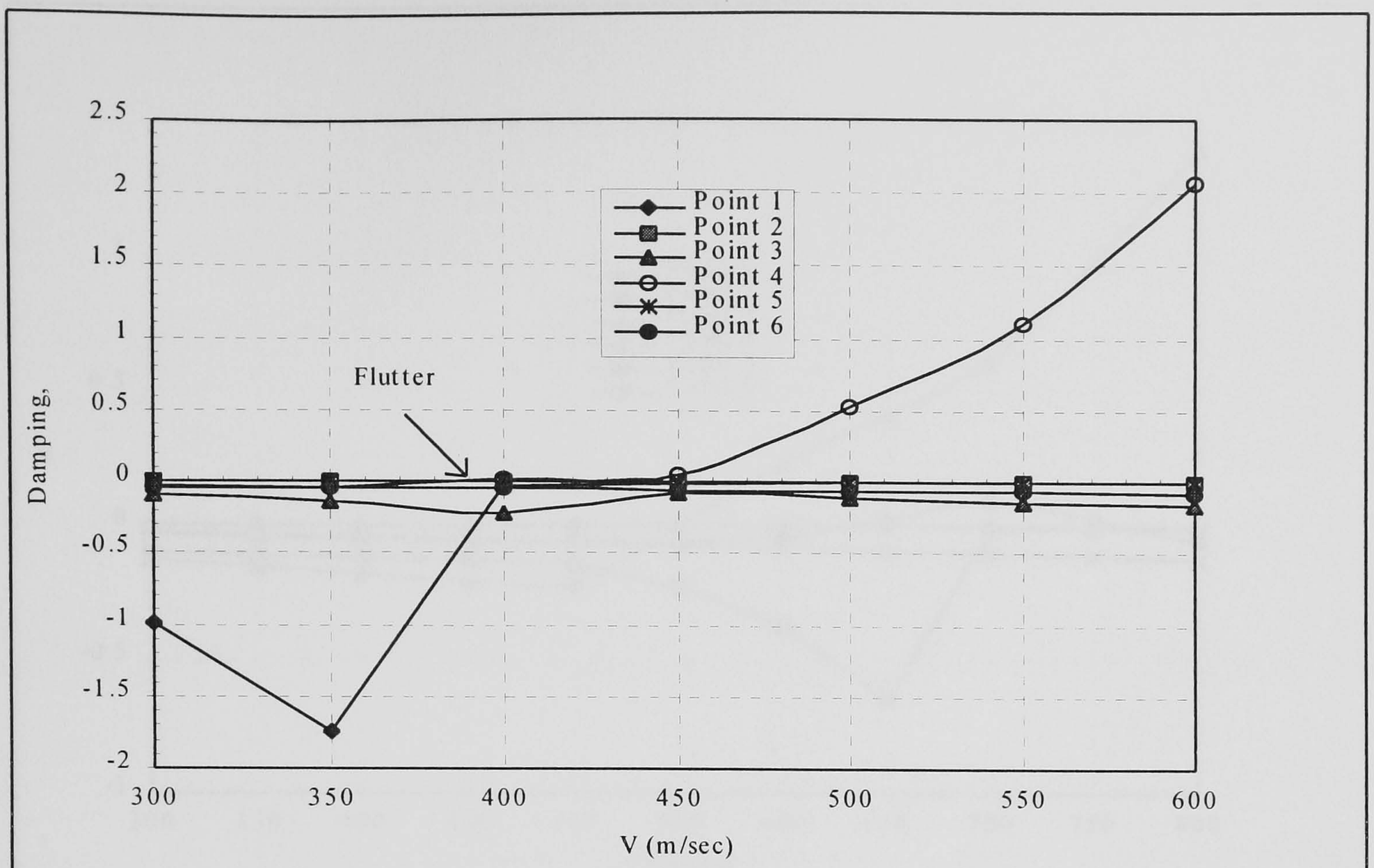

Fig. 8.32 Velocity vs Damping of the wing 1 model for the upper and lower skin at $\theta = 0$ degree.

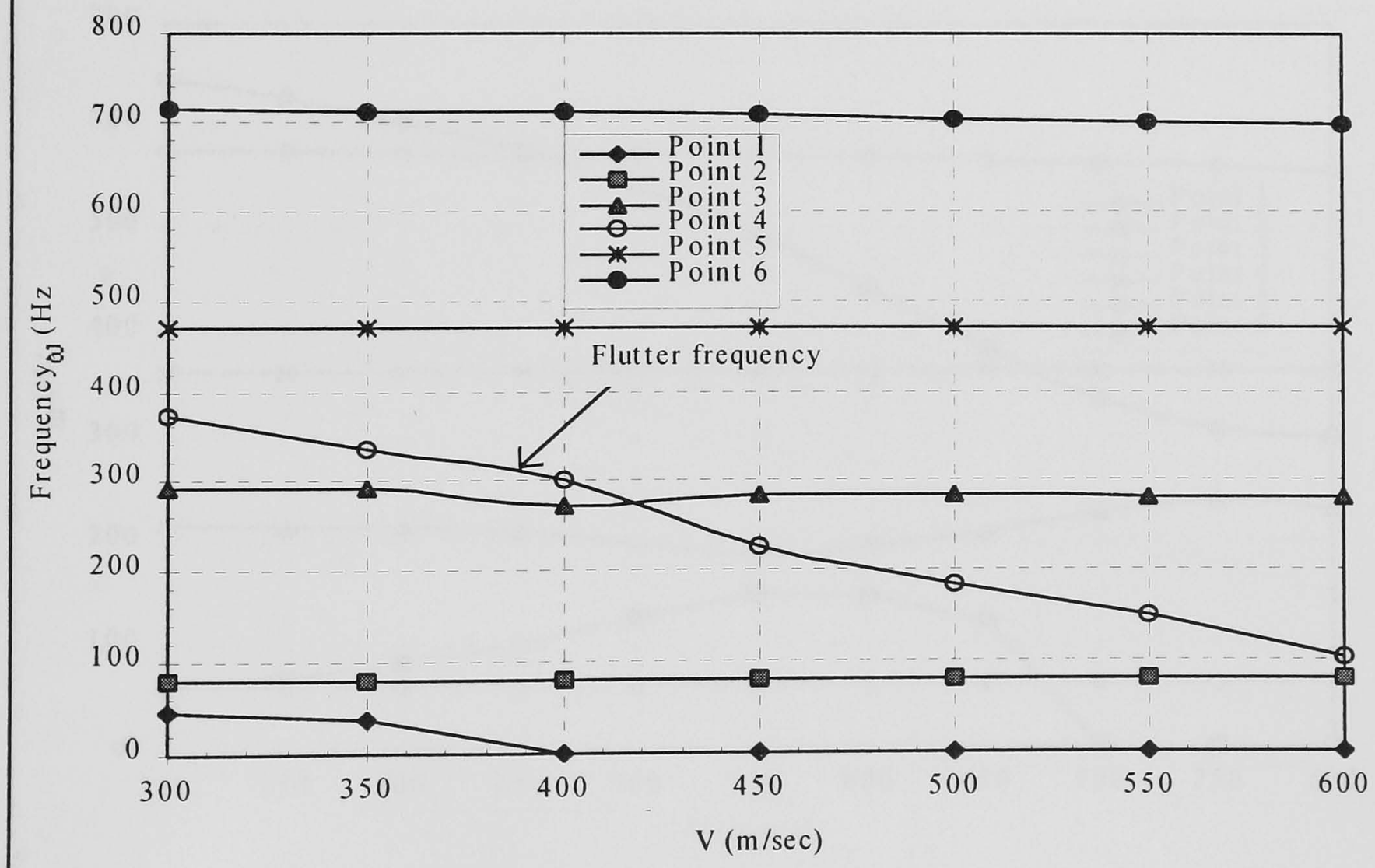

Fig. 8.33 Velocity vs Frequency of the wing 1 model for the upper and lower skin at $\theta = 0$ degree.

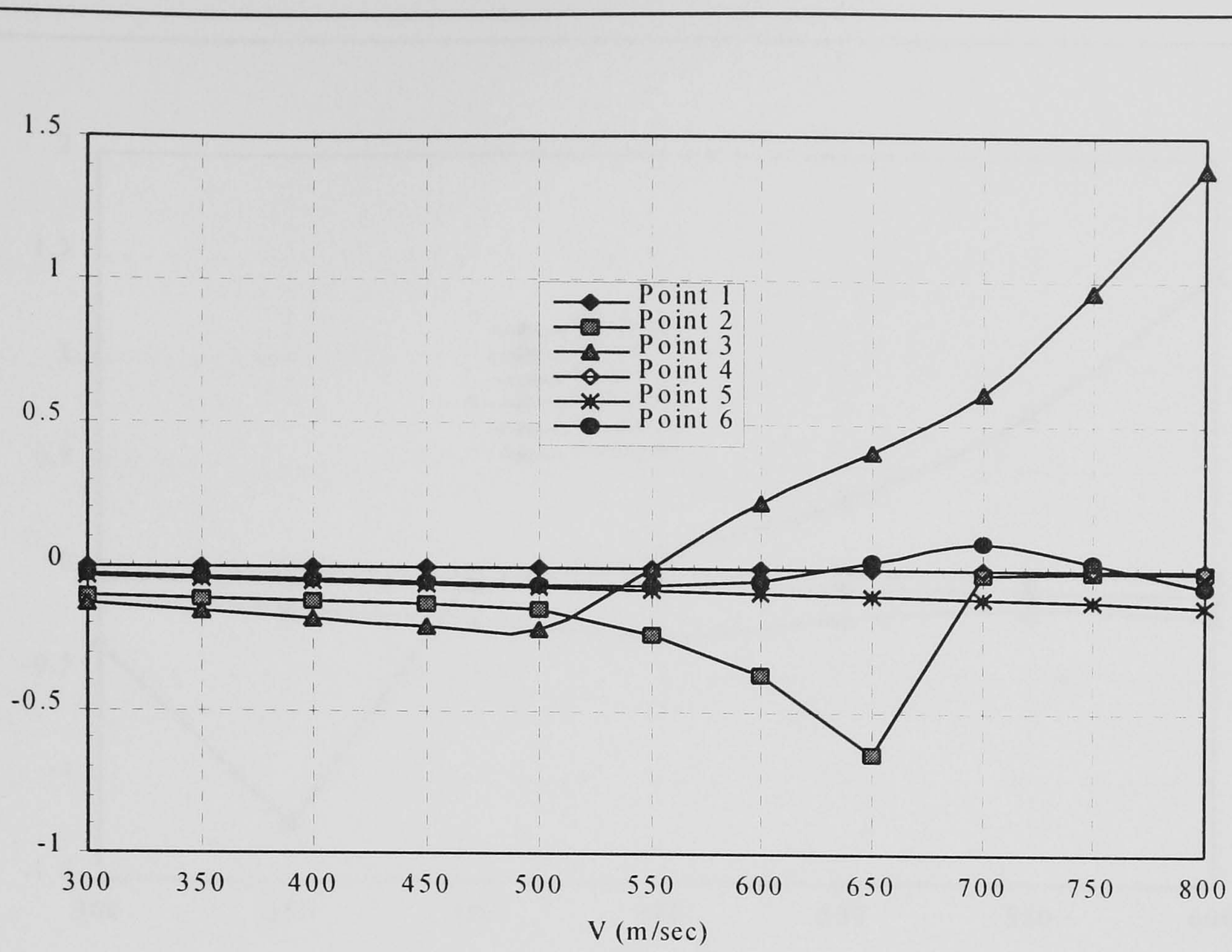

Fig. 8.34 Velocity vs Damping of the wing 1 model for the upper and lower skin at θ =30 degree.

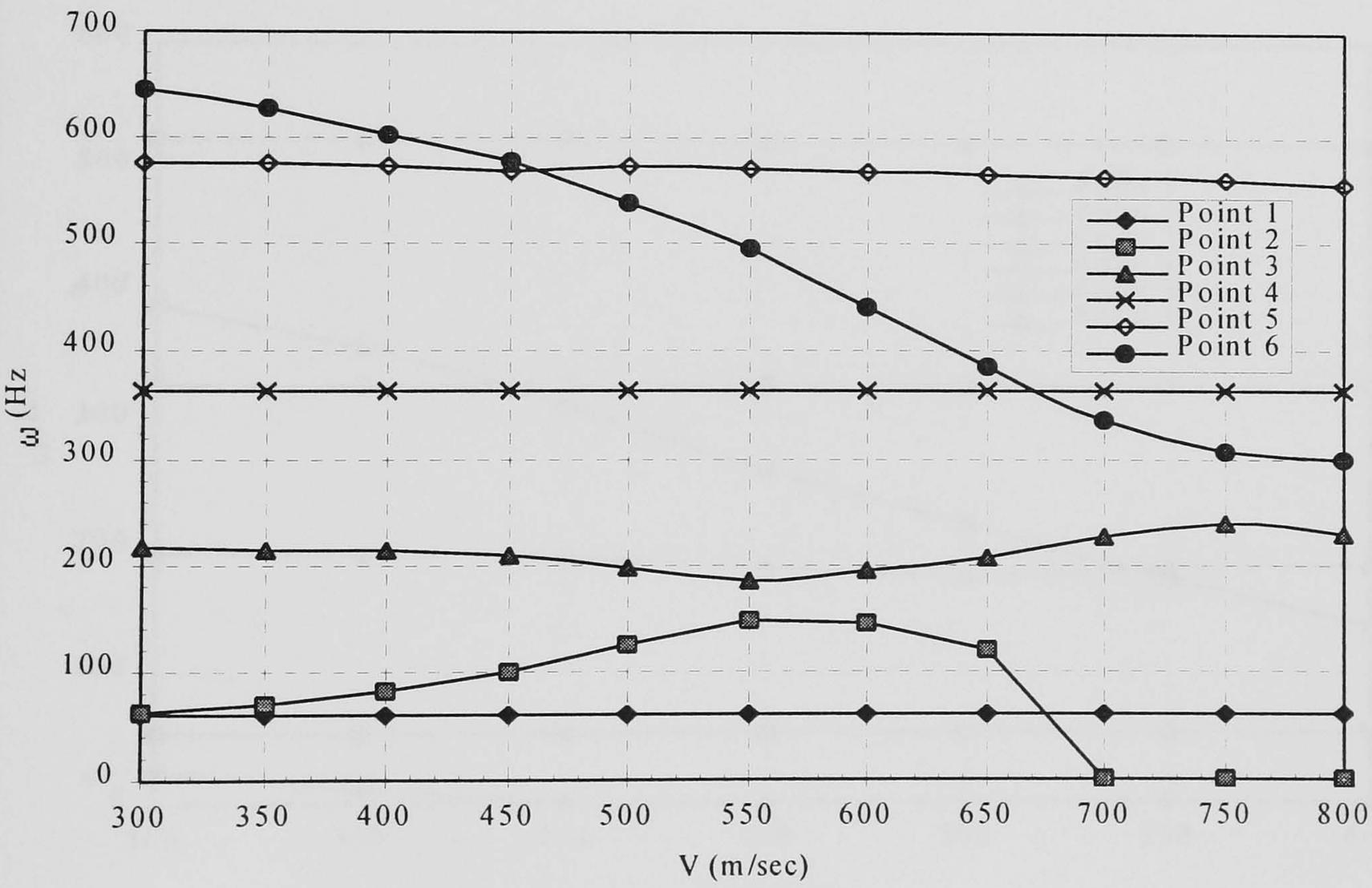

Fig. 8.35 Velocity vs Frequency of the wing 1 model for the upper and lower skin at θ = 30 degree.

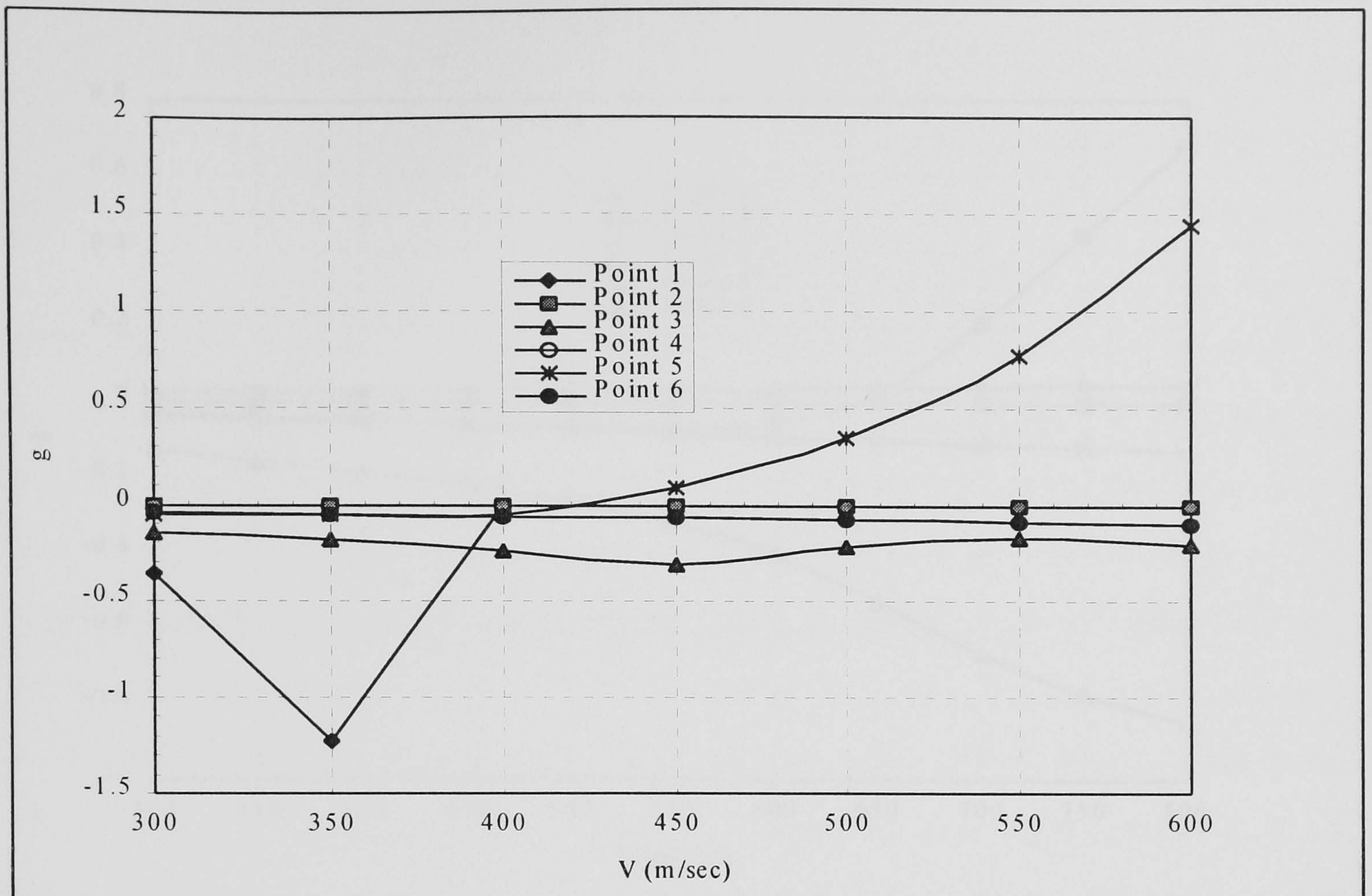

Fig. 8.36 Velocity vs Damping of the wing 1 model for the upper and lower skin at $\theta = 90$ degree.

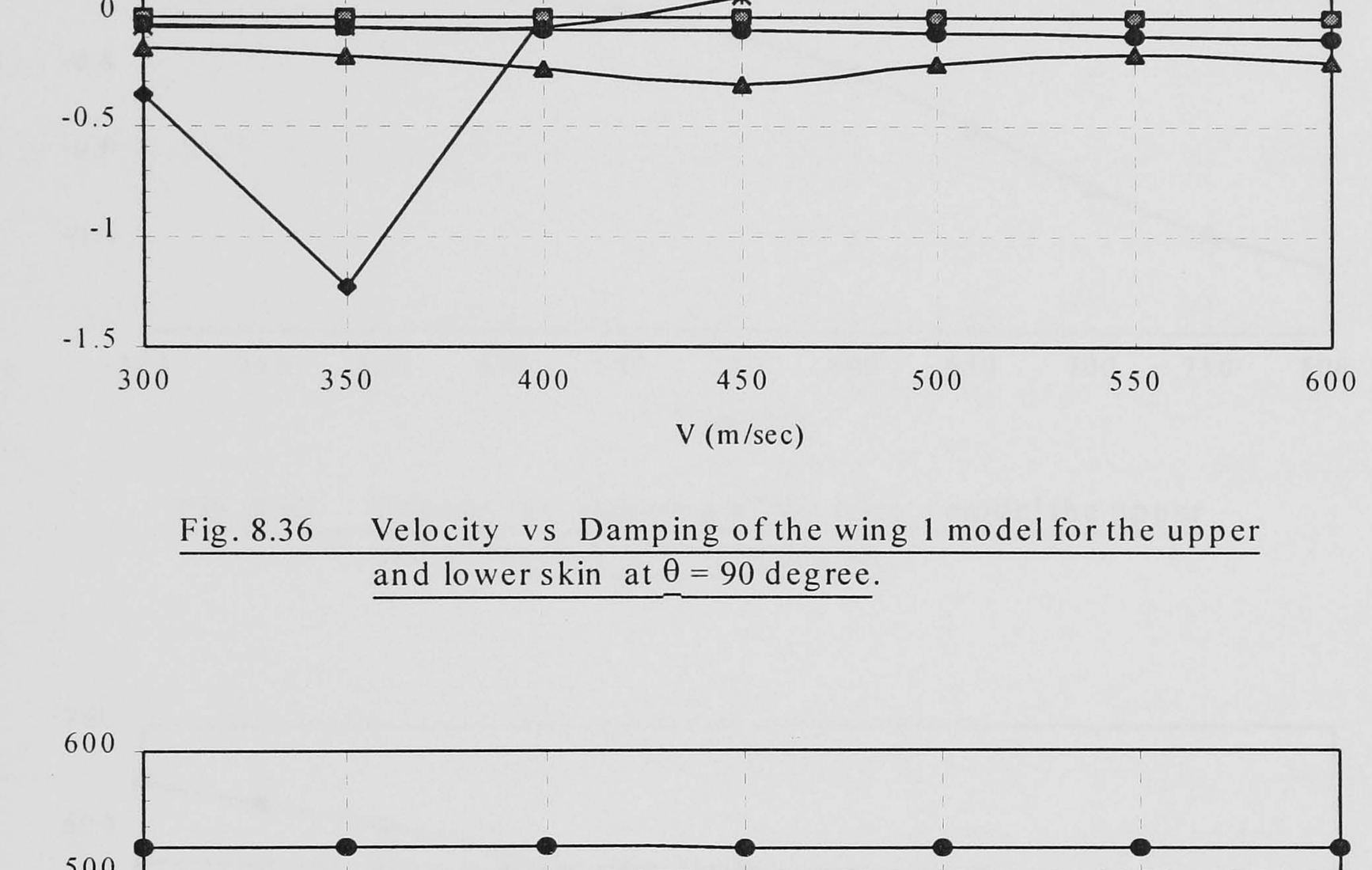

Fig. 8.37 Velocity vs Frequency of the wing 1 model for the upper and lower skin at $\theta = 90$ degree.

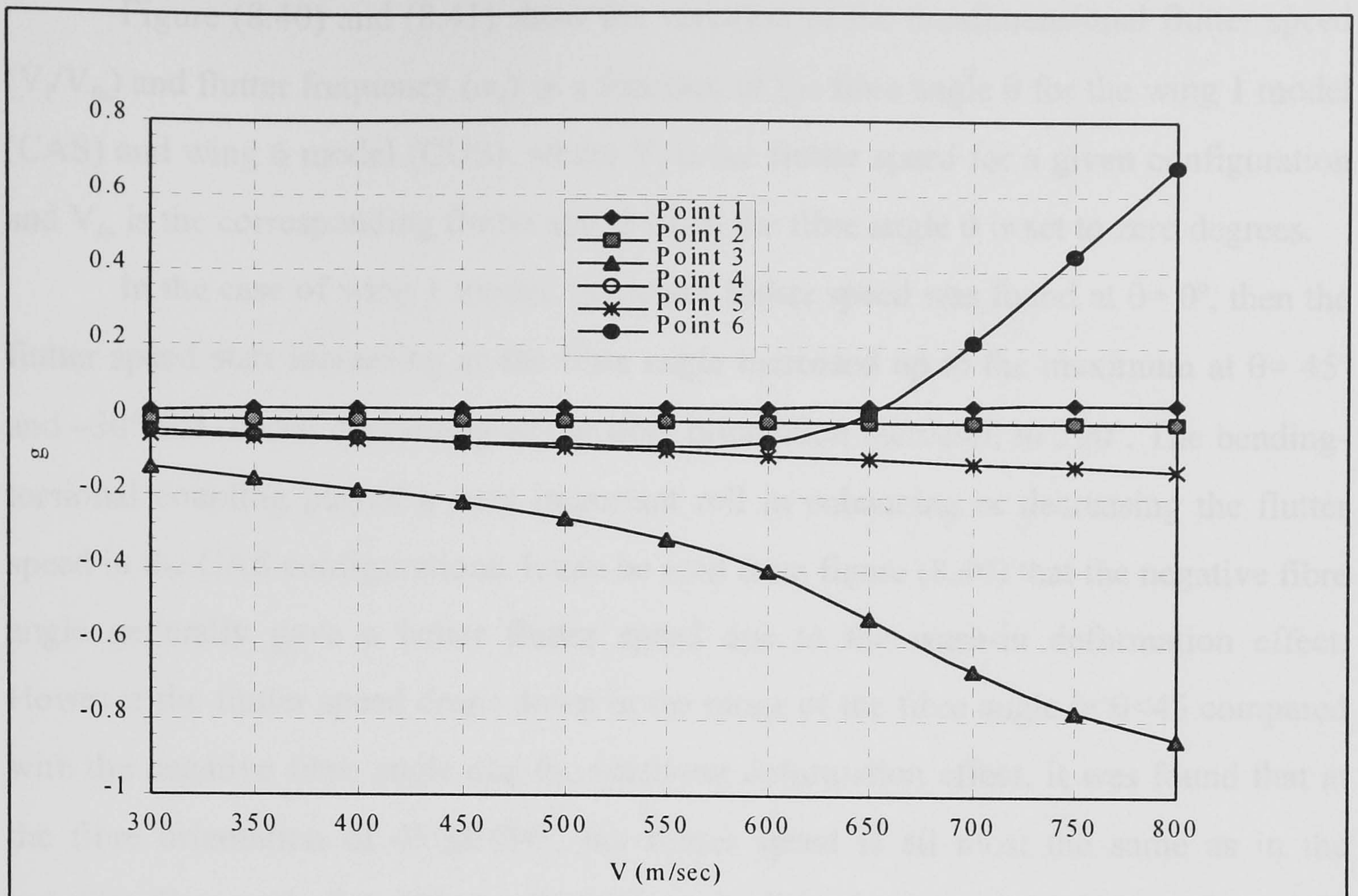

Fig. 8.38 Velocity vs Damping of the wing 1 model the upper and lower skin at θ = -30 degree.

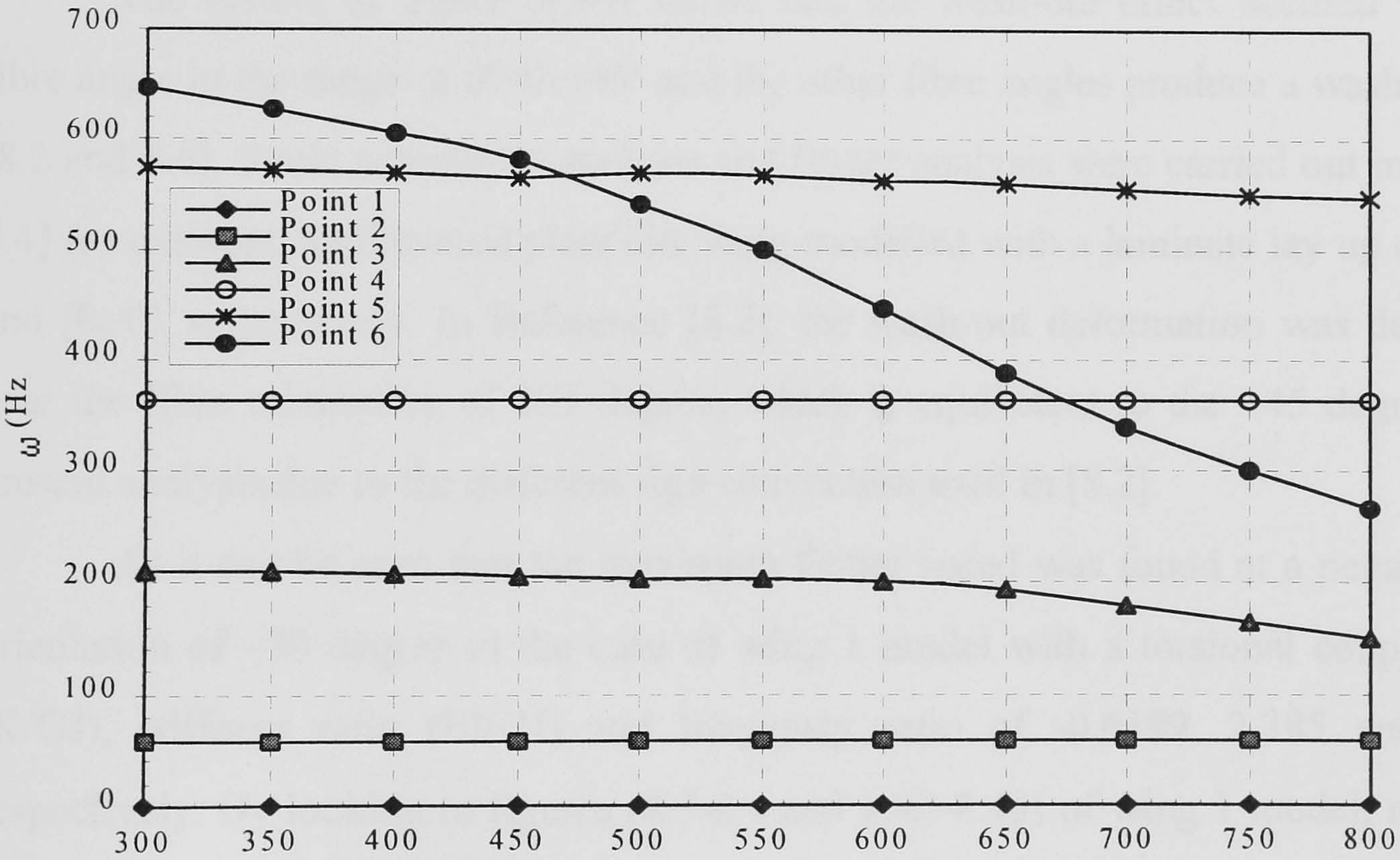

Fig. 8.39 Velocity vs Frequency of the wing 1 model for the upper and lower skin at θ = -30 degree.

Figure (8.40) and (8.41) show the variation of the nondimensional flutter speed (V_f/V_{fo}) and flutter frequency (ω_f) as a function of the fibre angle θ for the wing 1 model (CAS) and wing 6 model (CUS), where V_f is the flutter speed for a given configuration and V_{fo} is the corresponding flutter speed when the fibre angle θ is set to zero degrees.

In the case of wing 1 model, the lower flutter speed was found at $\theta = 0^\circ$, then the flutter speed start increasing as the fibre angle increased up to the maximum at $\theta = 45^\circ$ and -30° and started decreasing as the fibre orientation increased to $\pm 90^\circ$. The bending-torsional coupling played a very important roll in enhancing or decreasing the flutter speed in the CAS configurations. It can be seen from figure (8.40) that the negative fibre angle generally gave a better flutter speed due to the wash-in deformation effect. However the flutter speed drops down in the range of the fibre angle $0<\theta<45$ compared with the negative fibre angle due the wash-out deformation effect. It was found that at the fibre orientation of $45^\circ \leq \theta \leq 90^\circ$, the flutter speed is all most the same as in the negative fibre angle for $-45^\circ \leq \theta \leq -90^\circ$ because both having a wash-in deformations. The wash-in deformation usually improves the flutter speed while the wash-out effect usually enhanced the divergence speed as reported in [8.6, 8.7, 8.16, 8.17 and 8.18].

The results of figure (8.40) shows that the wash-out effect occured when the fibre angle in the range of $0^\circ<\theta<45^\circ$ and the other fibre angles produce a wash-in effect [8.2 and 8.4]. Static aeroelastic analysis and flutter analysis were carried out in [8.2 and 8.4] for unswept cantilevered plate like wing modelled with a laminate lay up of $[\theta_2/0_2]_s$ and $[\theta_2/0]_s$ respectively. In Reference [8.2], the wash-out deformation was determined near the fibre orientation of 135 degree, which is equivalent to the +45 degree in the present analysis due to the different sign convention used in [8.2].

As it can be seen that the maximum flutter speed was found at a negative fibre orientation of –30 degree in the case of wing 1 model with a torsional coupling ratio (K/GJ), stiffness ratio (EI/GJ) and frequency ratio of -0.6189, 2.385 and 0.0506 respectively. By looking to figures (8.3-8.4 and 8.42-8.43) of wing 1 model, maximum torsional rigidity (GJ), lower stiffness ratio (EI/GJ), and relatively higher negative torsional coupling stiffness (K/GJ) could lead to a higher flutter speed. This can be investigated by looking at two fibre angles -20 and -30 degrees as an example.

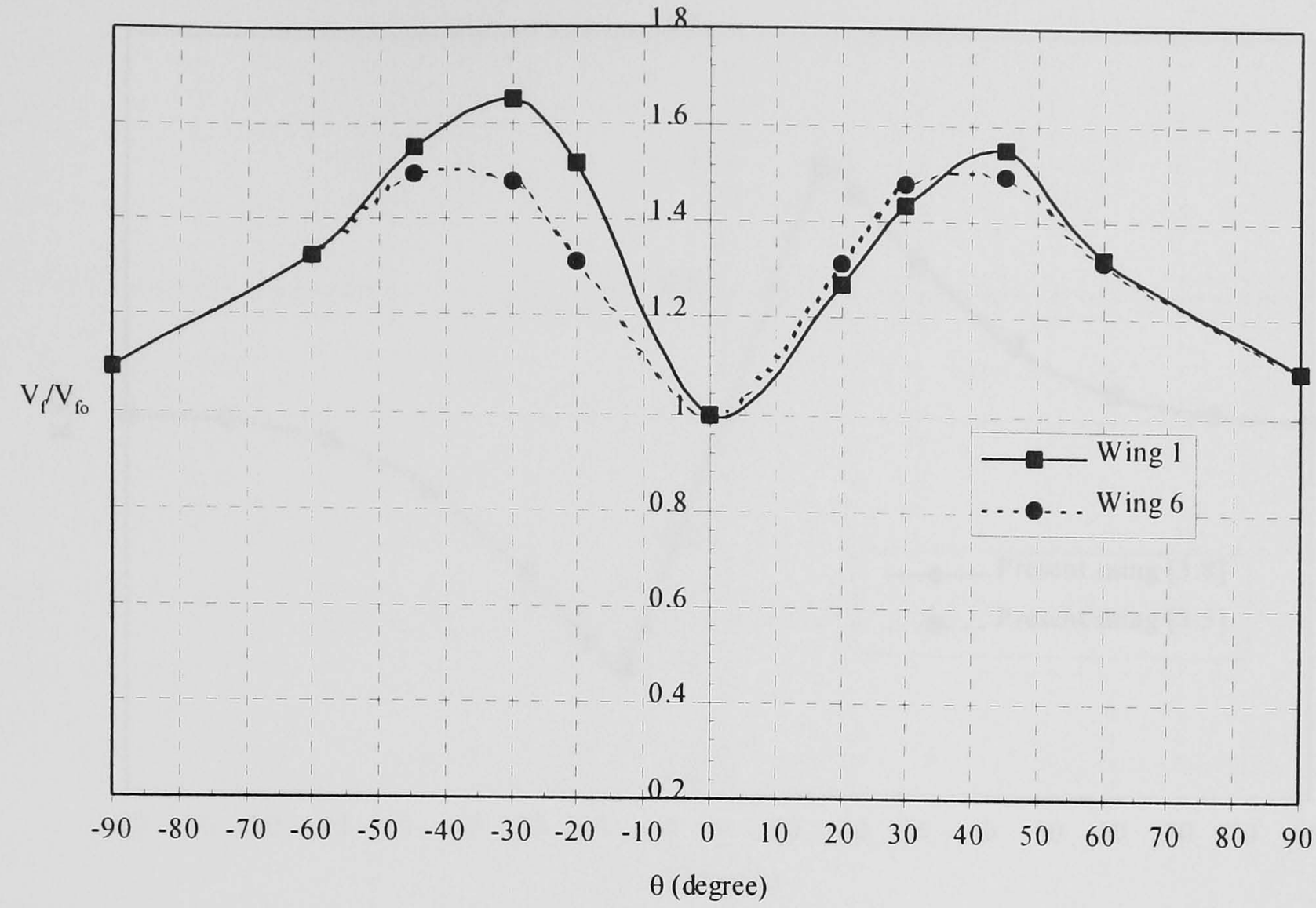

Fig. 8.40 Nondimensional flutter speed for the wing 1 and wing 6 models as a function of the ply angle θ.

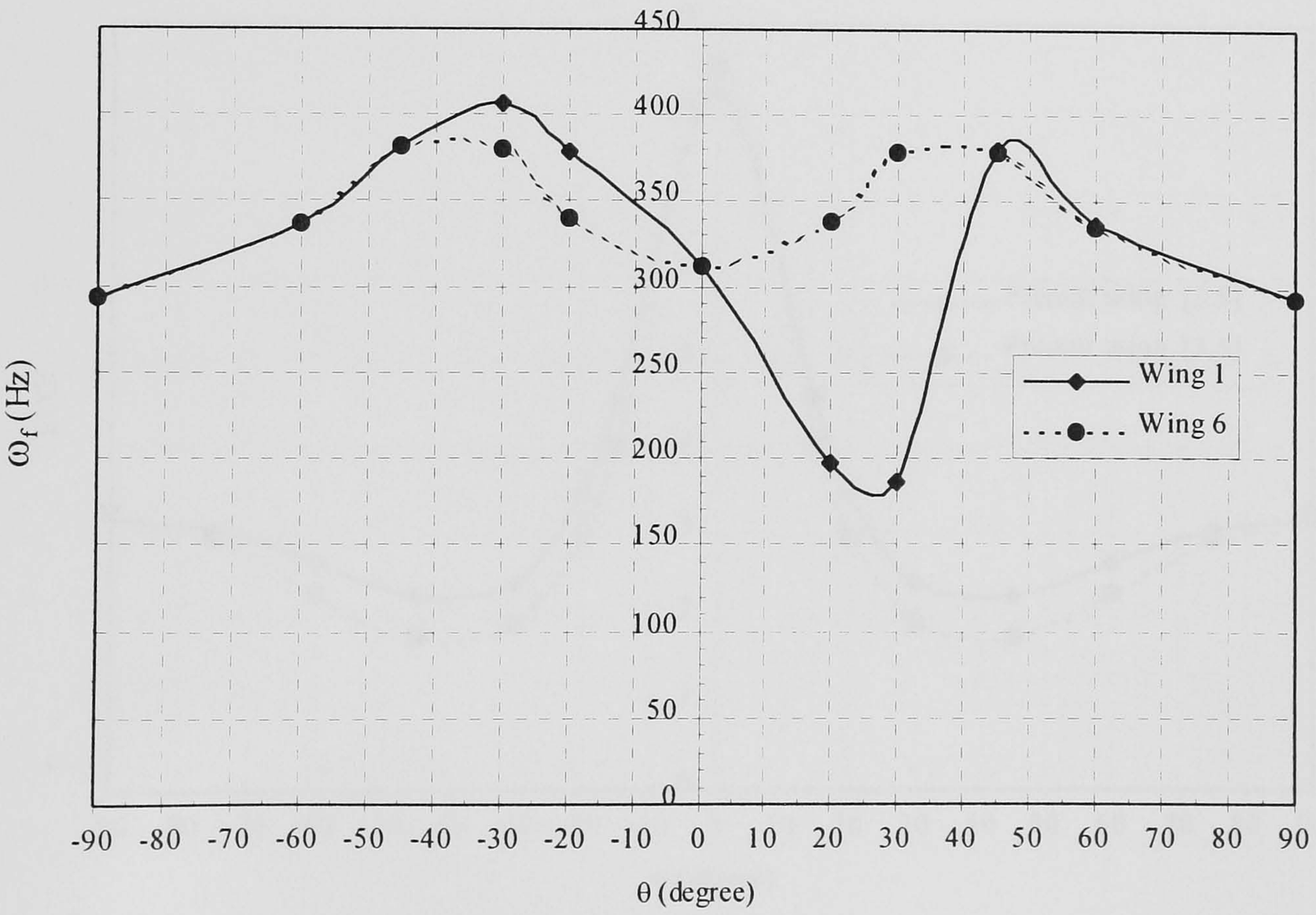

Fig.8.41 Flutter frequency vs Fibre angle θ of the wing 1 and wing 6 models.

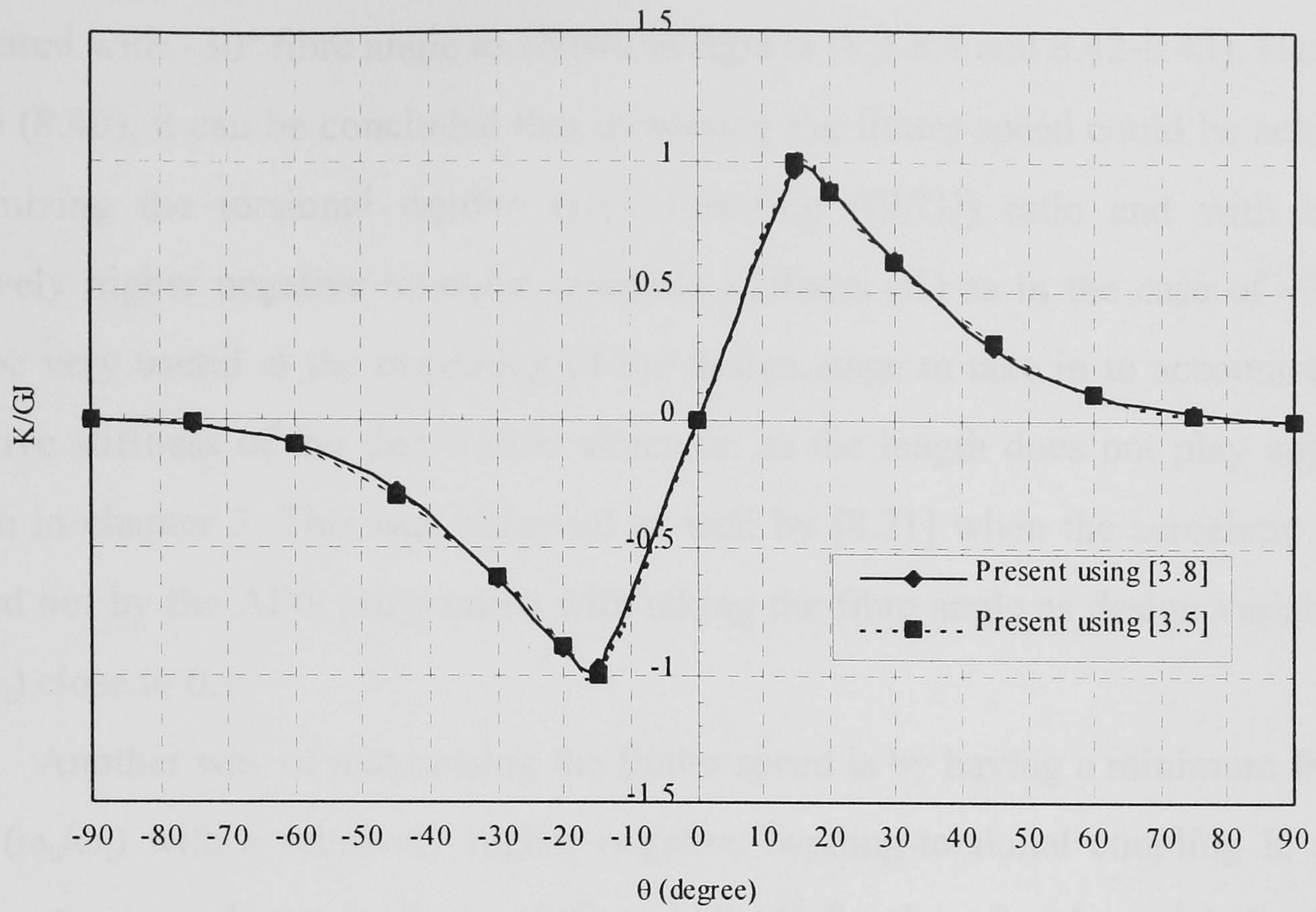

Fig. 8.42 Relationship between the parameter (K/GJ) and the fibre angle θ for the wing 1 model.

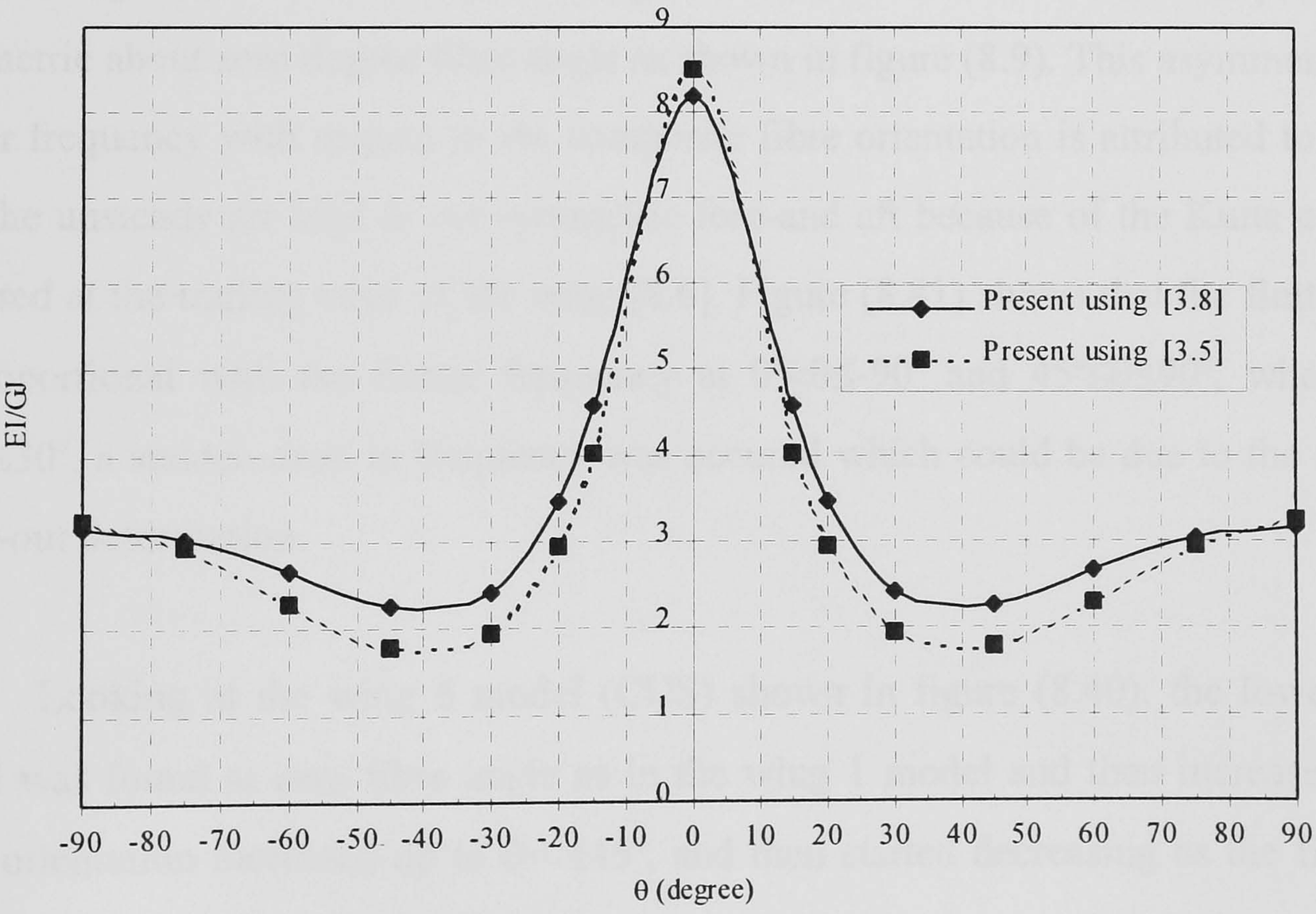

Fig. 8.43 Stiffness ratio (EI/GJ) vs the fibre angle θ for the wing 1 and wing 6 models.

The first fibre angle (-20°) with maximum negative bending-torsional stiffness (K), higher bending stiffness (EI), lower torsional stiffness (GJ) and higher (EI/GJ) ratio compared with –30° fibre angle as shown in figures (8.2-8.4 and 8.42-8.43). Hence from figure (8.40), it can be concluded that increasing the flutter speed could be achieved by maximizing the torsional rigidity (GJ), lowering (EI/GJ) ratio and with having a relatively higher negative torsional coupling stiffness (K) as in the case of –30°. This will be very useful at the beginning of the design stage to take in to account the static effective stiffness of the thin-walled structure, as the length does not play any part as shown in chapter 3. This was observed as well by [8.21] when the aeroelatic tailoring carried out by the ADS programme with taking the fibre angle as design variable when (ω_b/ω_t) close to 0.1.

Another way of maximising the flutter speed is by having a minimum frequency ratio (ω_b/ω_t) with a relatively higher negative bending-torsional coupling K (wash-in deformation) as shown in figure (8.4) and (8.44) for the wing 1 model. In this way, some parameters such as mass, inertia and length of the wing will be involved.

The asymmetry of flutter frequencies with respect to the fibre orientation θ are shown in figure (8.41) in the case of wing 1, where the structural natural frequencies are symmetric about zero degree fibre angle as shown in figure (8.9). This asymmetry in the flutter frequency with respect to the composite fibre orientation is attributed to the fact that the unsteady air load is not symmetric fore-and aft because of the Kutta condition required at the trailing edge of the wing [8.6]. Figure (8.41) shows that the flutter speed is proportional with the flutter frequency at $0°<\theta\leq-90°$ and $45°\leq\theta\leq90°$, where as at $0°<\theta\leq30°$, a sudden drop in frequency was occured which could be due to the effect of wash-out deformation.

Looking at the wing 6 model (CUS) shown in figure (8.40), the lower flutter speed was found at zero fibre angle as in the wing 1 model and then increased as the fibre orientation increased up to $\theta= \pm45°$, and then started decreasing as the fire angle increasing.

In this balanced configuration (CUS), where the bending-torsional coupling stiffness is zero (K=0) and it does not played any roll in enhancing or decreasing the

flutter speed. It can be seen from figure (8.40) that both positive and negative fibre angles gave all most the same flutter speed. Two parameters are very important to be considered in this configuration at the design stage. These are the stiffness ratio (EI/GJ) or the frequency ratios (ω_b/ω_t). Figure (8.46) of wing 6 model shows that the flutter speed is universally proportional with the frequency ratio (i.e. the lower the frequency ratio the higher the flutter speed). It can be said that designing the wing model such as wing 6 model with lower stiffness or frequency ratios lead to a maximum flutter speed (see fig. 8.45 and 8.46).

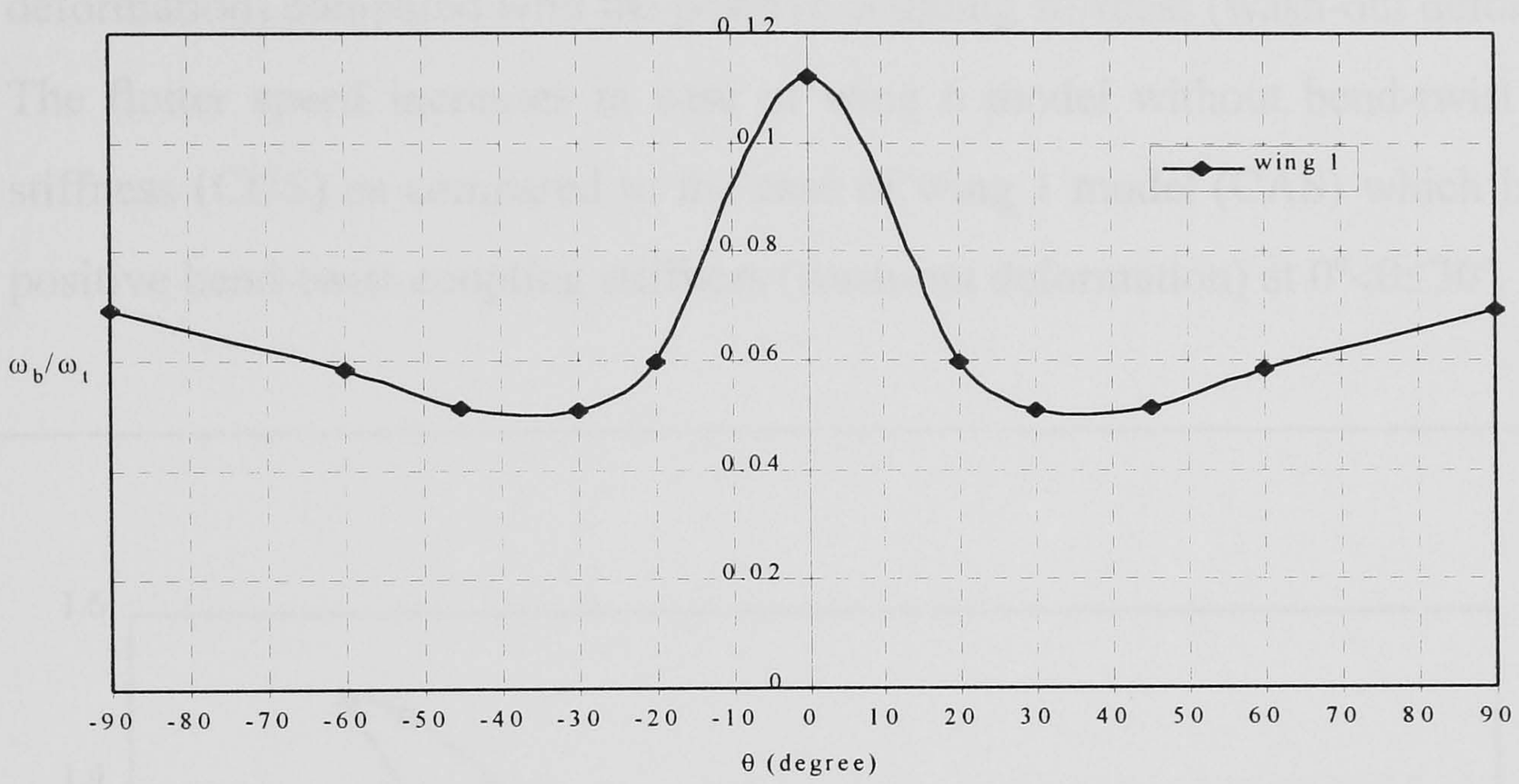

Fig. 8.44 Frequency ratio ω_b/ω_t vs the fibre angle θ of the wing 1 model.

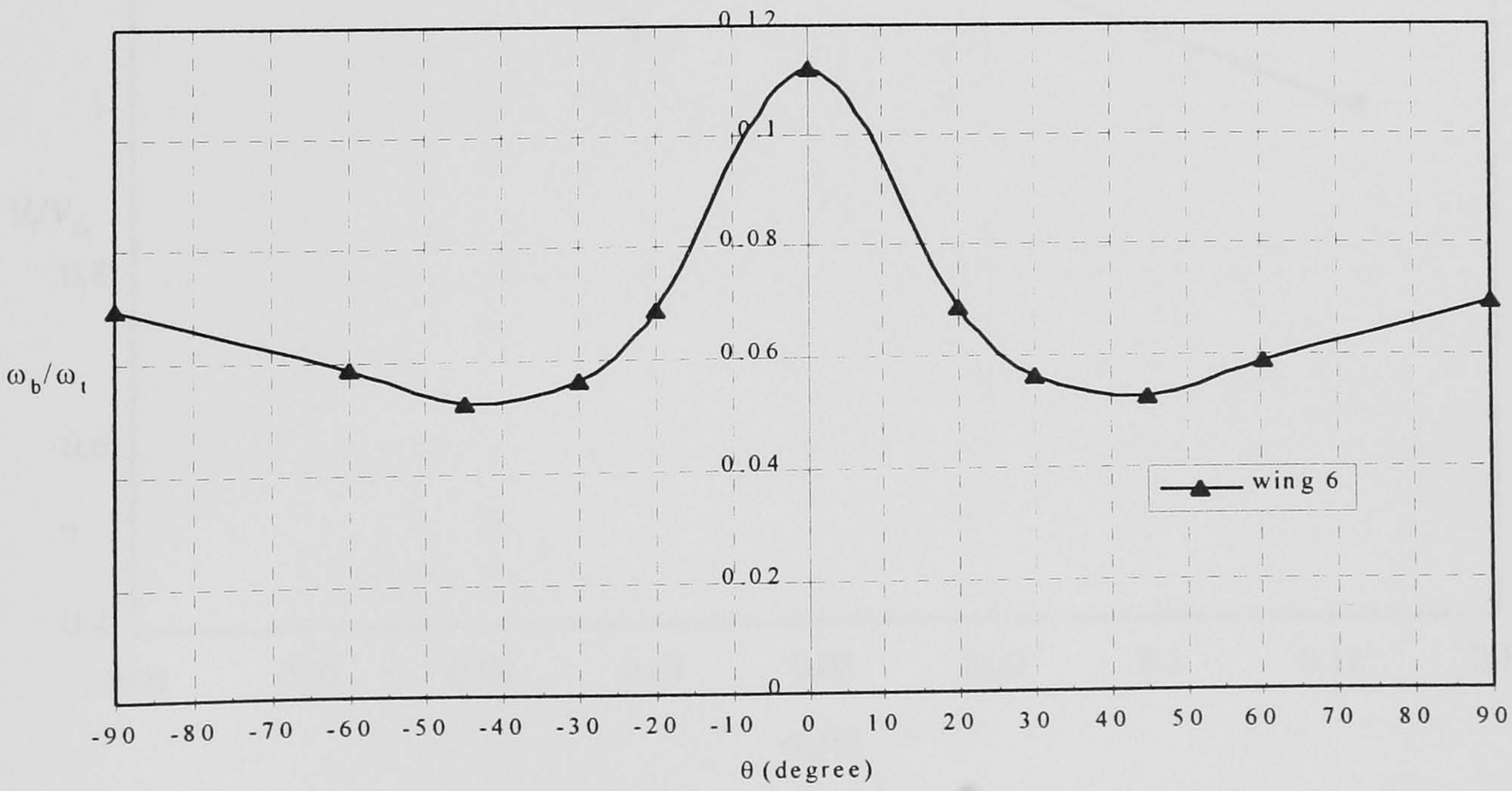

Fig. 8.45 Frequency ratio ω_b/ω_t vs the fibre angle θ of the wing 6 model.

The maximum flutter speed was observed at frequency ratio of 0.05249 and stiffness ratio of 2.238, which corresponds to the fibre angle of ±45° as shown in figure (8.43 and 8.46).

The flutter frequencies with respect to the fibre orientation θ were shown in figure (8.41), The flutter frequency was almost symmetric about zero degree fibre angles as compared with wing 1 model, which was not symmetric.

Comparing the results obtained from wing 1 and wing 6 models (see figure 8.40), the following can be concluded:

- The flutter speed increased by having a higher negative coupling stiffness (wash-in deformation) compared with the positive coupling stiffness (wash-out deformation).
- The flutter speed increases in case of wing 6 model without bend-twist coupling stiffness (CUS) as compared to the case of wing 1 model (CAS) which has higher positive bend-twist coupling stiffness (wash-out deformation) at $0° < \theta \leq 30°$.

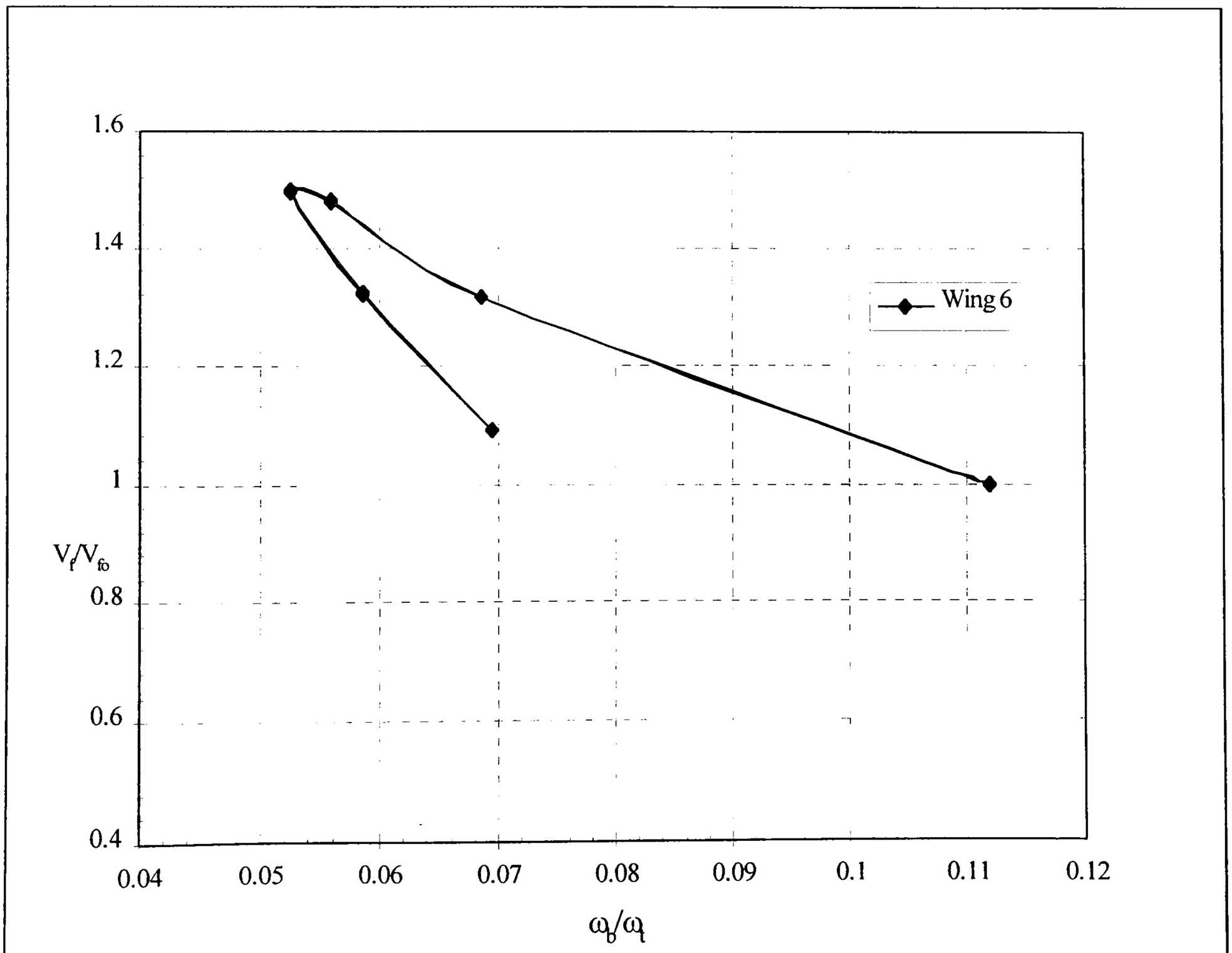

Fig. 8.46 Nondimensional flutter velocity vs Frequency ratio of the wing 6 model.

Figure (8.47) and (8.48) show the variation of the nondimensional flutter speed (V_f/V_{fo}) and flutter frequency (ω_f) as a function of the fibre angle θ for the wing 2 model (CAS) and wing 7 model (CUS). The trends of the frequency ratio against the fibre angle (see figure 8.49-8.50) and the variation of the flutter speed and frequency were very similar to the variation found in wing 1 and wing 6 models, therefore same conclusions are still valid.

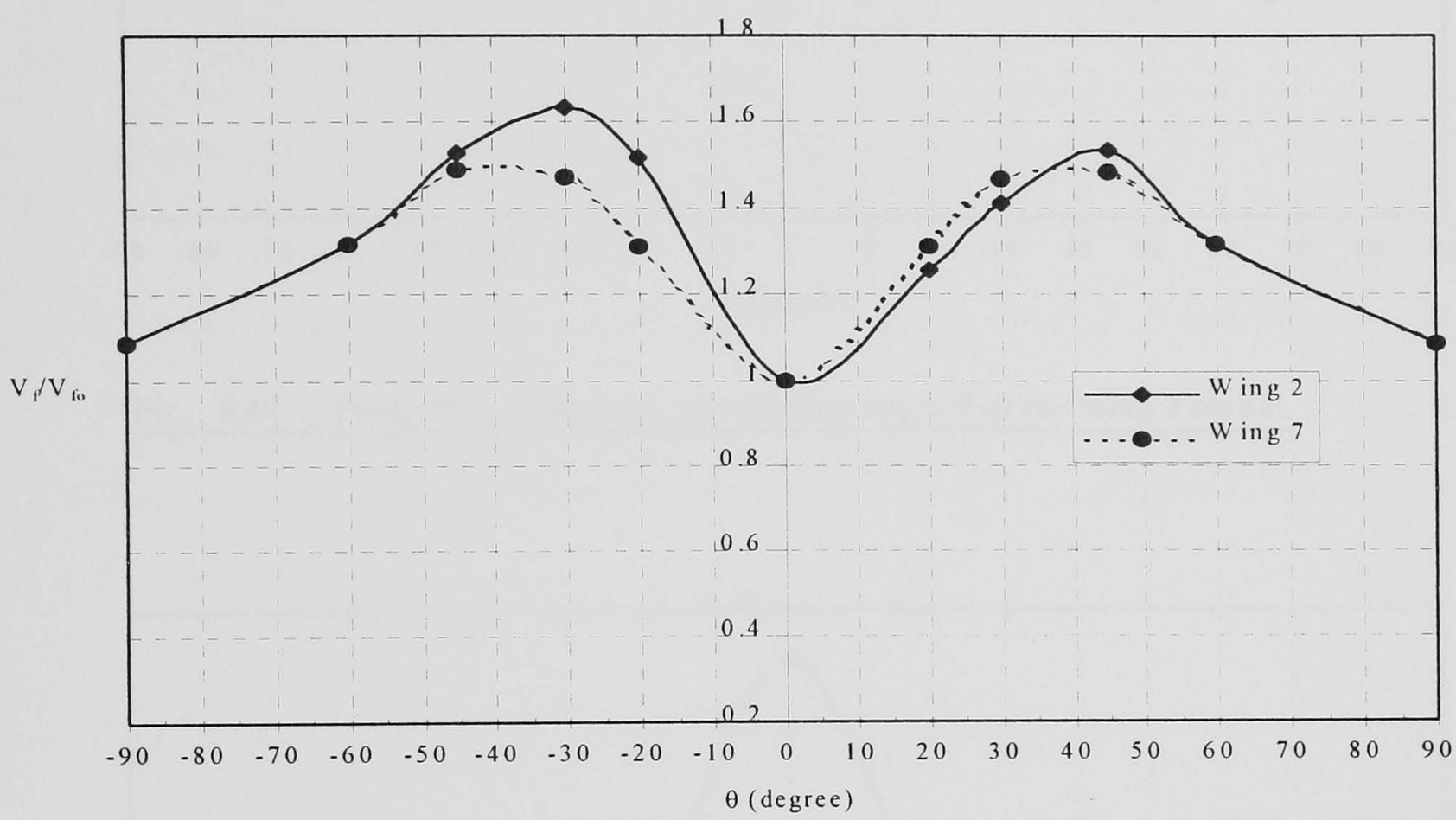

Fig. 8.47 Nondimentional flutter speed for the wing 2 and wing 7 models as a function of the ply angle θ.

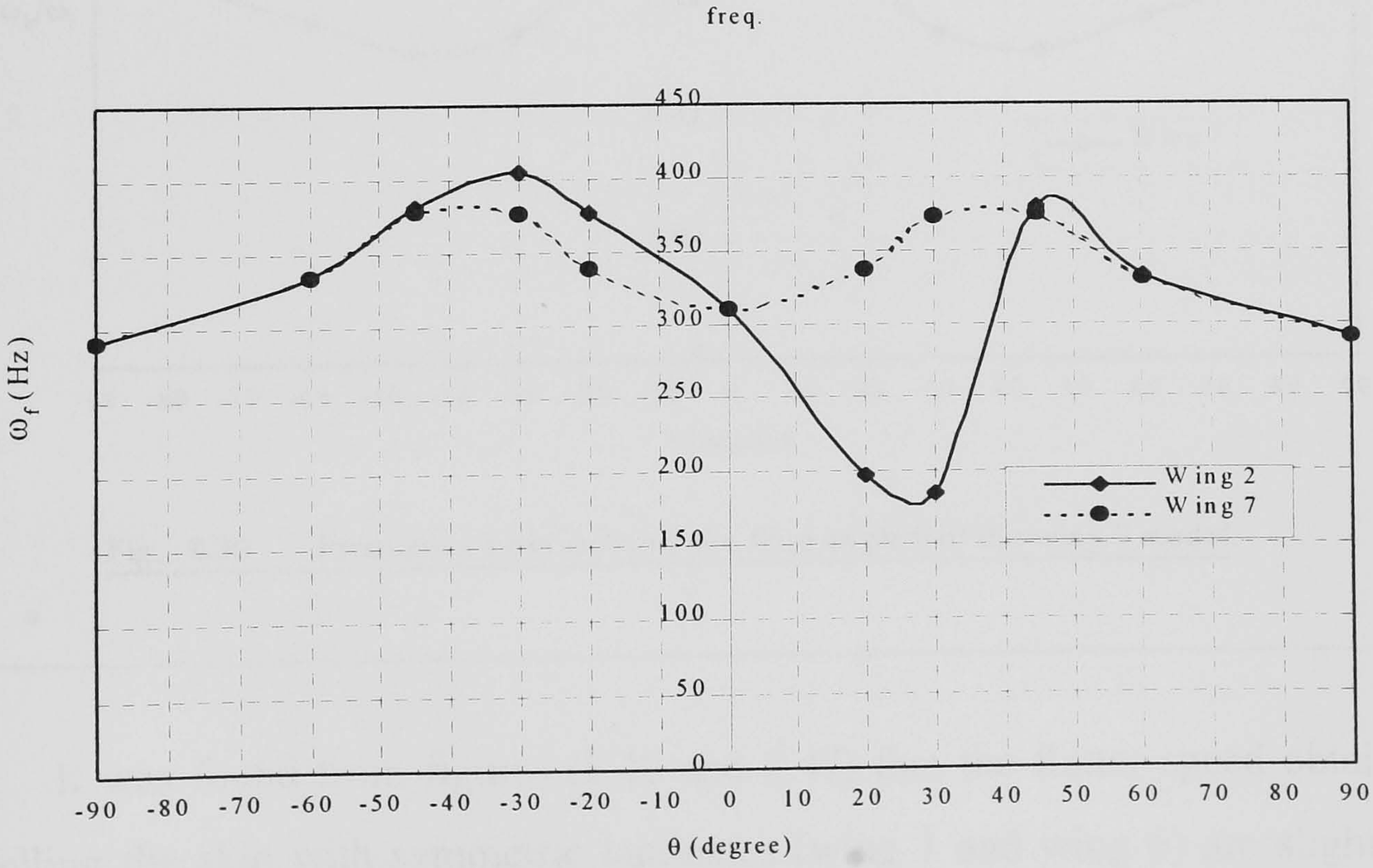

Fig. 8.48 Flutter frequency vs fibre angle θ of the wing 2 and wing 7 models.

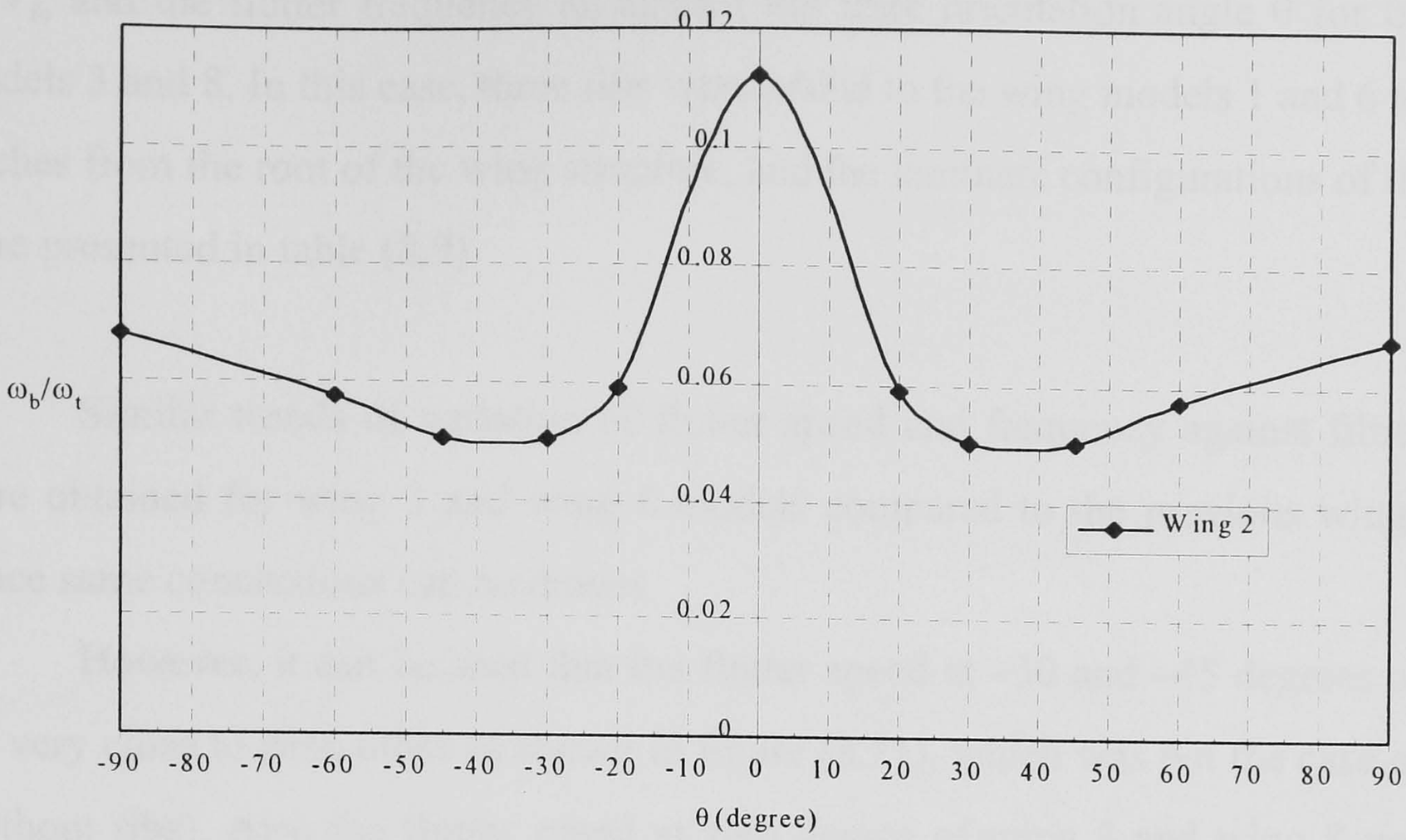

Fig. 8.49 Frequency ratio ω_b/ω_t vs the fibre angle θ of the wing 2 model.

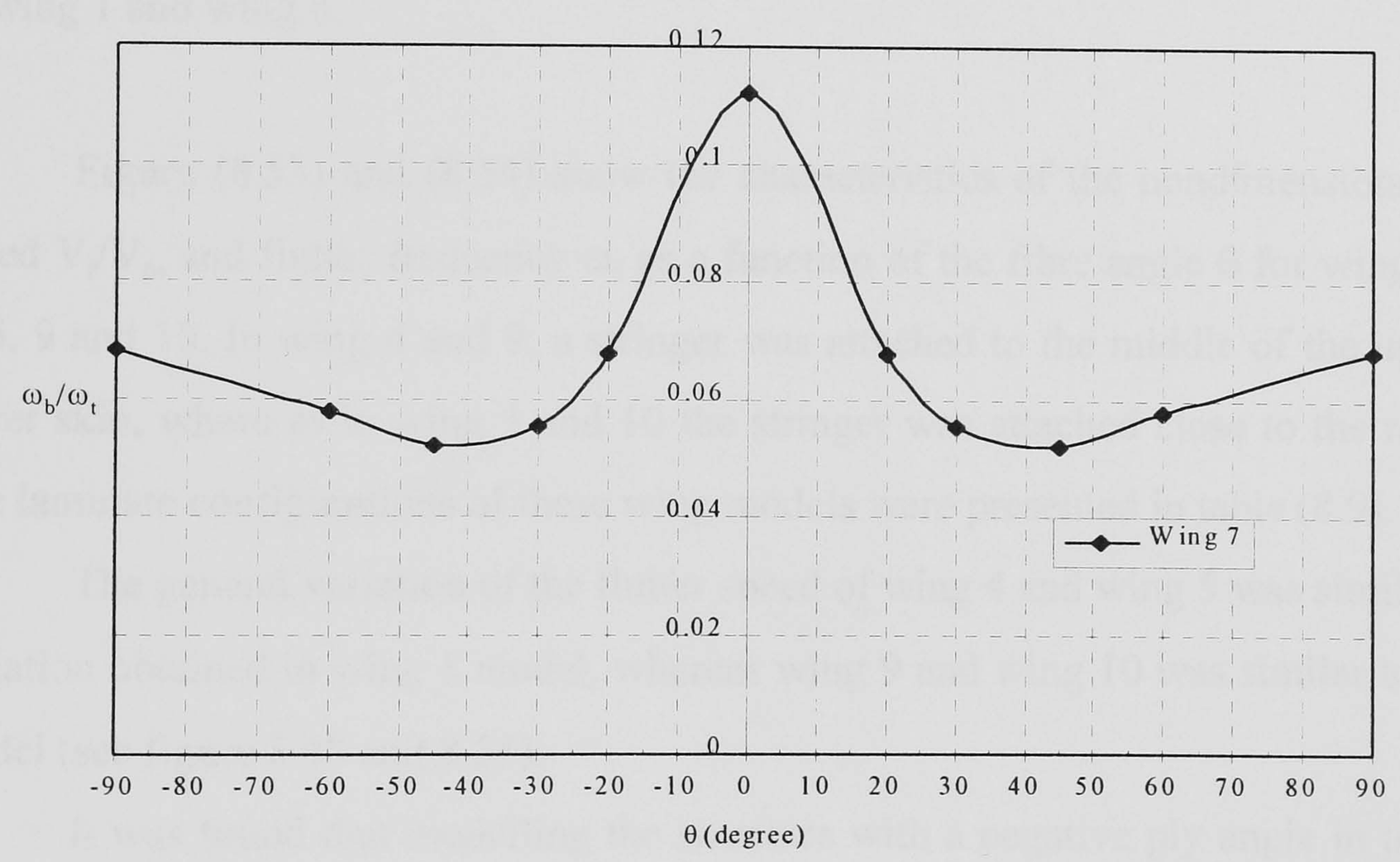

Fig. 8.50 Frequency ratio ω_b/ω_t vs the fibre angle θ of the wing 7 model.

It was found from figures (8.40 and 8.47) that the flutter speed obtained from modelling the skin with symmetric laminates (wing 1 and wing 6) are slightly higher than wing 2 and wing 7 models which were modelled with asymmetric laminates.

Figure (8.51) and (8.52) show the change of the nondimensional flutter speed V_f/V_{fo} and the flutter frequency ω_f against the fibre orientation angle θ for both wing models 3 and 8. In this case, three ribs were added to the wing models 1 and 6 at equal pitches from the root of the wing structure, and the laminate configurations of the ribs were presented in table (8.9).

Similar trends of variation of flutter speed and frequency against fibre angle θ were obtained for wing 3 and wing 8 models compared to the previous wing models, hence same conclusions can be drawn.

However, it can be seen that the flutter speed at –30 and –45 degrees of wing 8 are very close to each other as shown in figure (8.51), which was not the case of wing 6 (without ribs). Also the flutter speed at zero degree of wing 3 and wing 8 was higher than at 90 degree, which was the opposite in figure (8.40) of wing 6. It can be concluded that the flutter speed of wing 3 and wing 8 (with ribs) was higher than the flutter speed of wing 1 and wing 6.

Figure (8.53) and (8.54) show the characteristics of the nondimensional flutter speed V_f/V_{fo} and flutter frequency ω_f as a function of the fibre angle θ for wing models 4, 5, 9 and 10. In wing 4 and 9, a stringer was attached to the middle of the upper and lower skin, where as in wing 5 and 10 the stringer was attached close to the rear spar. The laminate configurations of these wing models were presented in table (8.9).

The general variation of the flutter speed of wing 4 and wing 5 was similar to the variation obtained in wing 1 model, whereas wing 9 and wing 10 was similar to wing 6 model (see figure 8.40 and 8.53).

It was found that modelling the structure with a negative ply angle in the upper skin and positive ply angle in the lower skin increases slightly the flutter speed as in the case of wing 9 and wing 10.

Comparing the results of the wing 4 and wing 5 shown in figures (8.53), it can be seen that the flutter speed was higher in the case of having a bending-torsional coupling without offset (wing 4) than in the case of having both material and structural coupling (wing 5). Similarly the results obtained for the wing 9 were higher than the

results obtained for wing 10 and wing 5 for $0^{o} \leq \theta \leq \pm 90^{o}$ and ($0^{o} \leq \theta \leq 90^{o}$ and $-40^{o} \leq \theta \leq -90^{o}$) respectively (see figure 8.53) due to the effect of the gap between the shear centre and the centre of gravity.

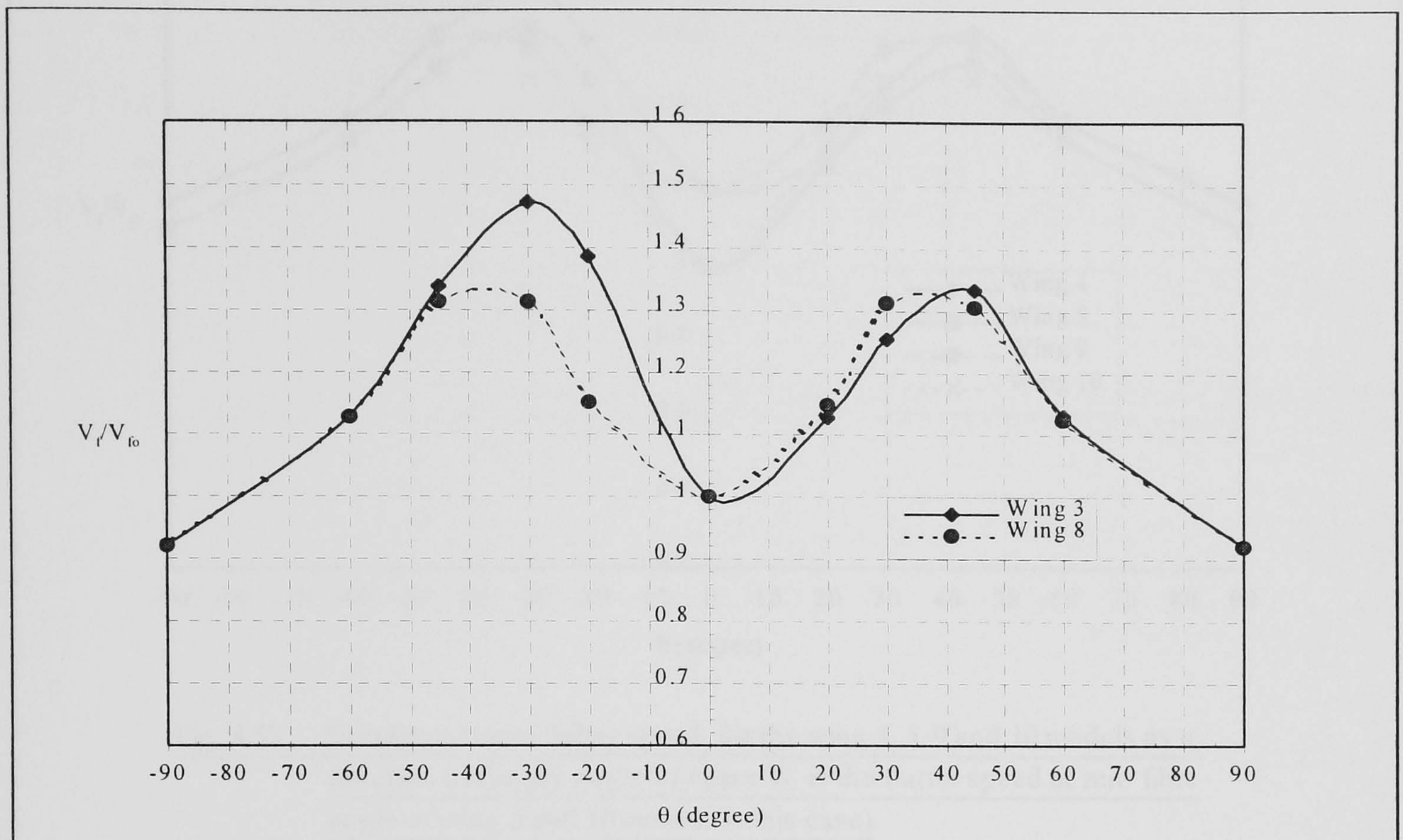

Fig. 8.51 Nondimensional Flutter speed for the wing 3 and wing 8 models as a function of the ply angle θ.

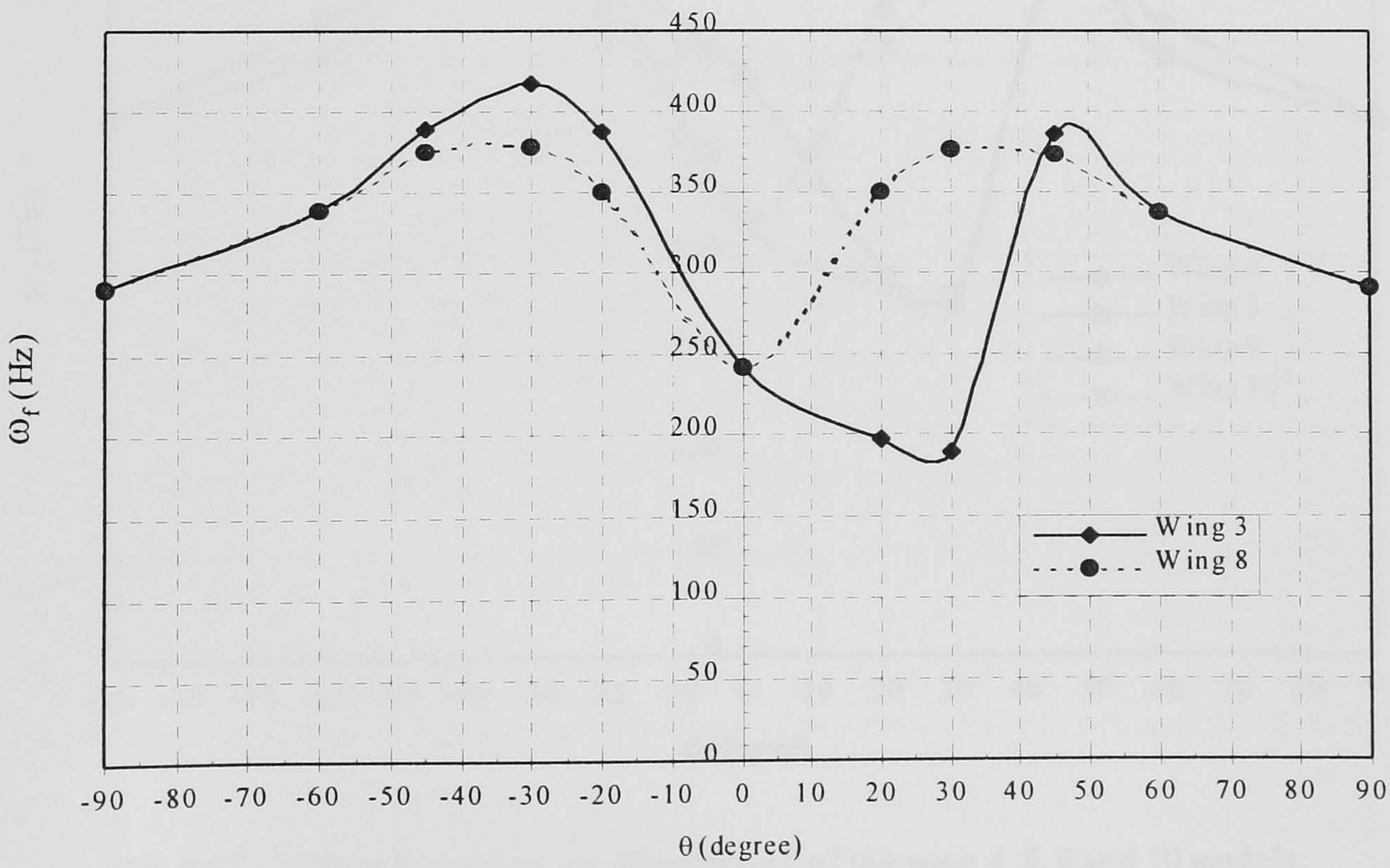

Fig. 8.52 Flutter frequency vs Fibre angle θ of the wing 3 and wing 8 models.

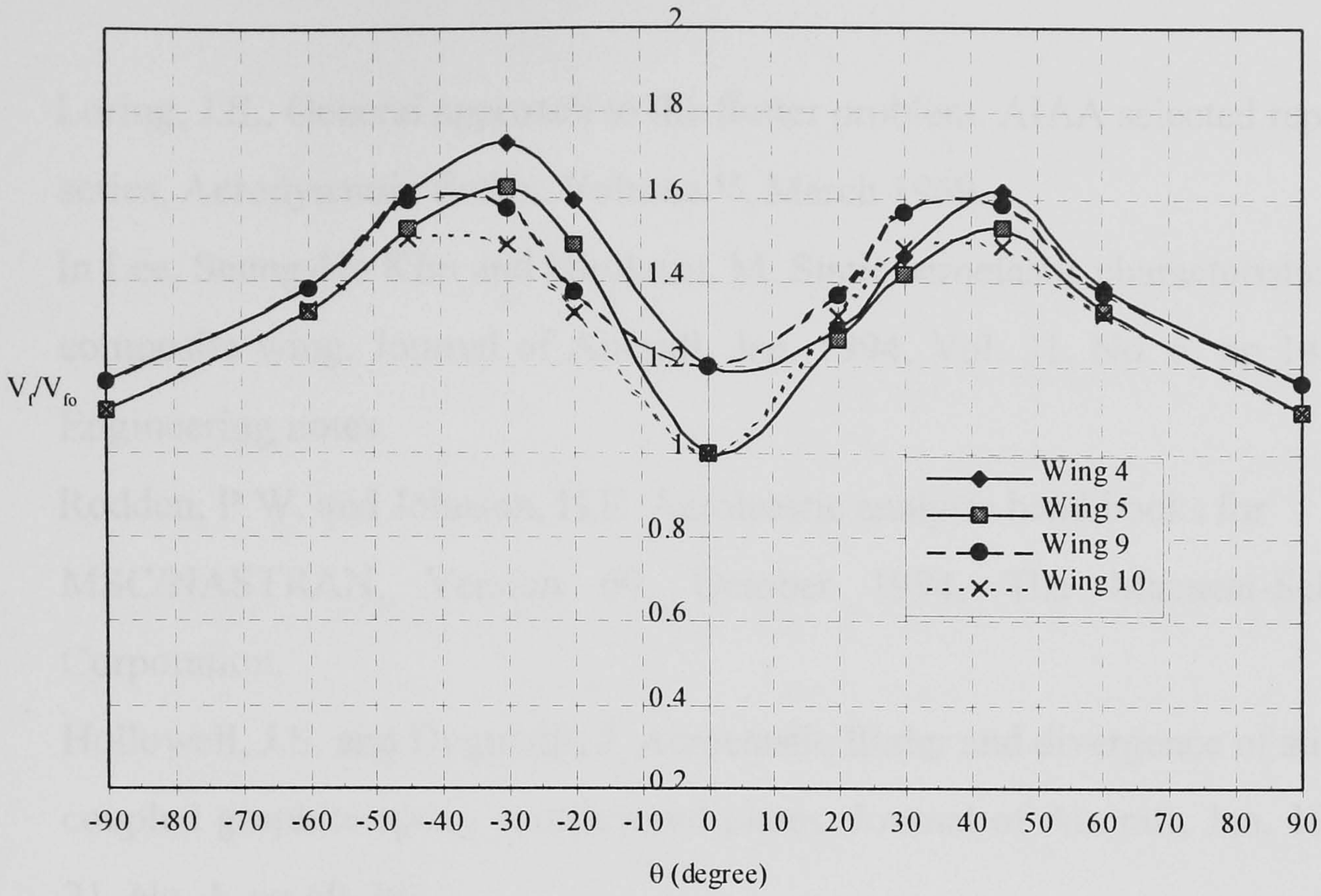

Fig. 8.53 Nondimensional flutter speed for the wing 4, 5, 9 and 10 models as a function of the ply angle θ (where V_{fo} is the flutter speed at zero fibre angle of wing 5 and 10 models in this case).

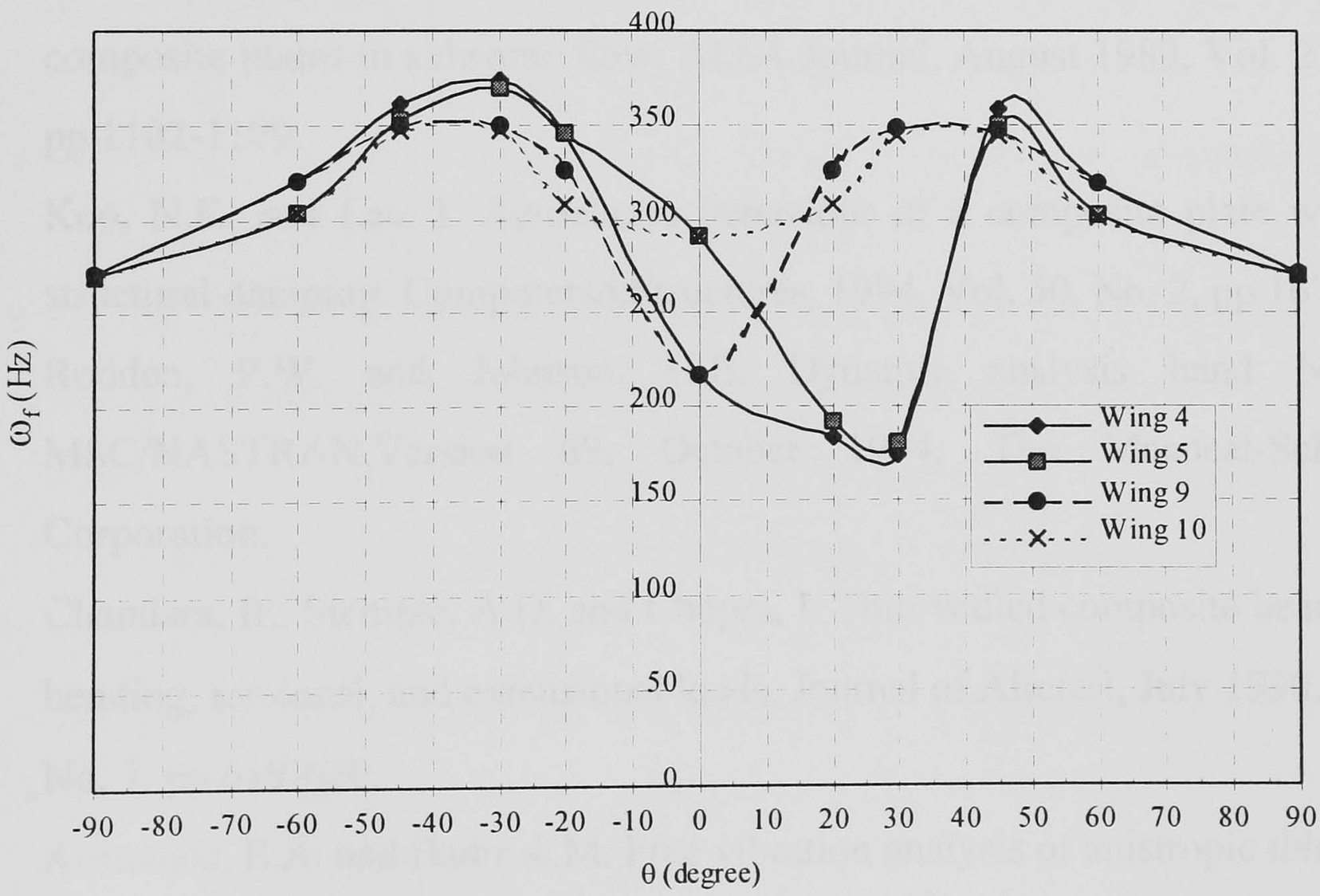

Fig. 8.54 Flutter frequency vs fibre angle θ of the wing 4, 5, 9 and 10 models.

References

8.1 Loring, J.S., General approach to the flutter problem. AIAA selected reprint series, Aerodynamic flutter, Volume V, March 1969.

8.2 In Lee, Seung-Ho Kim and Hirokazu, M. Static aeroelastic characteristics of a composite wing. Journal of Aircraft, Jan. 1994, Vol. 31, No. 6, pp 1413-1416, Engineering notes.

8.3 Rodden, P.W. and Johnson, H.E. Aeroleastic analysis hand books for MSC/NASTRAN, Version 69, October 1994, The Macneal-Schwendler Corporation.

8.4 Hollowell, J.S. and Dugundji, J. Aeroelastic flutter and divergence of stiffness coupled graphite/epoxy cantilevered plates. Journal of Aircraft, Jan. 1984, Vol. 21, No. 1, pp 69-76.

8.5 Niu, C.M. Composite airframe structures "Practical design information and data", Conmilit Press Ltd, 1992.

8.6 Kuo-Juin Lin, Pong-Jeu Lu, Jiann-Quo Tarn. Flutter analysis of cantilevered composite plates in subsonic flow. AIAA Journal, August 1989, Vol. 27, No. 8, pp 1102-1109.

8.7 Koo, N.K. and Lee, I. Aeroelastic behaviour of a composite plate wing with structural damping. Computers&Structures, 1994, Vol. 50, No. 2, pp 167-176.

8.8 Rodden, P.W. and Johnson, H.E. Dynamic analysis hand book for MSC/NASTRAN,Version 69, October 1994, The Macneal-Schwendler Corporation.

8.9 Chandara, R., Stemple, A.D. and Chopra, I. Thin-walled composite beams under bending, torsional, and extensional loads. Journal of Aircraft, July 1990, Vol. 27, No. 7, pp 619-626.

8.10 Armanios, E.A. and Badir A.M. Free vibration analysis of anistropic thin-walled closed-section beams. AIAA Journal, October 1995, Vol. 33, No. 10, pp 1905-1910.

8.11 Banerjee, J. R. Use and capability of CALFUN- A program for Calculation of Flutter speed Using Normal Modes. Porc. Int. AMSE conf. On modelling & simulation, Vol. 27-29, Athens, Greece, June 1984.

8.12 Rudisill, C. S. and Bhatia, K. G. Optimization of complex structure to satisfy requirements AIAA Journal, August 1971, Vol. 9, No. 8 pp 1487-1491.

8.13 Brooks, W. G. Design, construction and test of a post buckling carbon fibre reinforced plastic wing box. PhD Thesis, 1984/1987, Cranfield University.

8.14 Weisshaar, T. A. and Foist, L. B. Vibration tailoring of advanced lifting surfaces. Journal of Aircraft, Feb. 1985, Vol. 22, No. 2, pp 141-147.

8.15 Librescu, L., Meirovitch, L. and Song, O. Refined structural modelling for enhancing vibrational and aeroelastic characteristics of composite aircraft wings. La Recherche Aerospatiale, 1996, no. 1, pp 23-35.

8.16 Georghiades, G. A., Guo, J.S. and Banerjee, R. J. Flutter analysis of composite wings using an exact dynamic stiffness matrix method. AIAA-95-1488-cp, pp 3019-3027.

8.17 Lottati, I. Flutter and divergence aeroelastic characteristics of composite forward swept cantilevered wing. Journal of Aircraft, 1985, Vol. 22, No. 11 pp 1001-1007.

8.18 Weisshaar, T. A. and Foist, L. B. Vibration and Flutter of advanced lifting surfaces. A83-29861or A83-0961, pp 498-508.

8.19 Souahi, A. (1986). Structural optimization of aircraft lifting surfaces to satisfy flutter requirements. PhD thesis, Cranfield University.

8.20 Samuel, C., Mcintosh, JR. and Ashley, H. (1978). "On the optimization of discrete structures with aeroelastic constrains". Computers & Structures, vol. 8, pp. 411-419.

8.21 Georghiades, G. A., Guo, J.S. and Banerjee, R. J. Parametric investigation into the flutter characteristics of composite wings. AIAA-96-1351-cp, pp 300-310.

CHAPTER 9

PARAMETRIC AEROELASTIC STUDY OF THE CRANFIELD A1 COMPOSITE WING BOX

9.1 Introduction:

In this chapter, some simplifications on the original materials and laminate lay ups of the Cranfield A1 composite wing box were carried out as presented in table (9.1) and (9.2-9.5) respectively. Four A1 wing models (see table 9.2-9.5) were created from the Coarse finite element model (see figure 7.1 of chapter 7). Two types of laminate lay ups were used in the modeling of the upper and lowers skin, namely the unbalanced symmetric and asymmetric laminates. Two A1 wing models (A1 wing 1 and A1 wing 2) were modeled using symmetric laminates for the CAS and CUS configurations respectively. The other two models (A1 wing 3 and A1 wing 4) were modeled using the asymmetric laminates for the CAS and CUS configurations respectively.

The objective of this chapter is to investigate the effect of the fibre angle θ of the upper and lower skin (with subsequent effect of bending-torsional coupling stiffness) on the natural frequency and mode shapes of a practical or real composite wing box of the Cranfield A1 aerobatic aircraft.

The investigations will cover also the effects of wash-in, wash-out deformations and structural damping on the flutter speed.

9.2 Fibre orientation of the A1 composite wing box:

9.2.1 Lay-ups and configurations used in the analysis:

The structural configuration and the dimensions of the A1 composite wing box were shown in figure (5.6) of chapter 5. This section will preset some simplifications, which were made in the original material properties and the laminate lay ups of the upper and lower skin of the composite wing box; these simplifications are as follows:

- The entire structural component's of the wing box such as skins, ribs, spars and stringers were only constructed from the Uni-Directional material (UD) (CIBA-GEIGY 913-27 Carbon/Epoxy Prepreg) instead of both UD and UD woven materials.
- The upper and lower skin are made from the same laminate foam along the span of the composite wing box.

- The anti-peel layers of the top hat stringers ($0^o/90^o$) were removed.

The material stiffness and the laminate thickness of the simplified composite wing model (coarse model) are not uniform along the span. Unbalanced symmetric and asymmetric laminate foams were used in the modeling of the upper and lower skin of the wing box, and balanced unsymmetric laminate foams were used in the spar webs and stringers.

Four different stiffness A1 wing models were created from the coarse model. The description of each model is as follows:

- The first A1 wing model was the A1 wing1 model, which was modeled with having unbalanced symmetric laminates for the upper and lower skin with the same sign of fibre orientations (CAS). The remaining fibre angle of the structural component's were unchanged.
- The second A1 wing model was the A1 wing 2, which was modeled with the unbalanced symmetric laminates for the upper and lower skin. The fibre angle θ of the upper and lower skin was reversed to simulate the CUS configuration. More over, the fibre angle of other components of the wing box such as spar webs, ribs and stringer sides and caps were unchanged.
- The third A1 wing model was the A1 wing 3 model, which was modeled with unbalanced asymmetric laminates for the upper and lower skin (up to 3706 mm from the aircraft center line) and the rest with the unbalanced symmetric laminates. This A1 wing 3 model was modeled to simulate the CAS configuration. The fibre angle of the rest of the structural component's were unchanged.
- The fourth A1 wing model was the A1 wing 4, which was modeled with the same laminates as in the A1 wing 3 model, but the fibre angle θ of the upper and lower skin were reversed to simulate the CUS configuration.

The materials properties and the structural laminates of the A1 wing models (A1 wing 1-A1 wing 4) were presented in table (9.1) and (9.2-9.5) respectively.

Table (9.1) Material properties of the A1 composite wing boxes (A1 wing 1 to A1 wing 4).

Material type / Properties	XAS (UD)	R51	R71
E_{11} (N/mm^2)	130×10^3	0.07×10^3	$.092\times10^3$
E_{22} (N/mm^2)	9.0×10^3	0.07×10^3	0.092×10^3
ν_{12}	0.28	0.3	0.3
G_{12} (N/mm^2)	4.8×10^3	0.021×10^3	0.03×10^3
Density (ρ) Kg/mm^3	1.61×10^{-6}	0.05×10^{-6}	0.07×10^{-6}
0^o thermal e/c	-0.1×10^{-6}	33×10^{-6}	35×10^{-6}
90^o thermal e/c	28×10^{-6}	33×10^{-6}	35×10^{-6}

Where XAS is Ciba-Geigy 913 carbon/epoxy prepreg

R51 and R71 are Rohacell 51 and 71 polymethylacrylate foams respectively [9.5].

UD is the Uni-Directional

Table (9.2) Laminates Configuration of the A1 composite wing box (A1 wing 1)

Stations (mm) / Laminate	0- 431	431- 868	868 - 1411	1411-1981	1981 - 2556	2556 - 3131	3131 - 3706	3706 - 4281	4281-4902
Upper skin	$[\theta_4 / 0_2]_s$	$[\theta_4 / 0_2]_s$	$[\theta_4 / 0_2]_s$	$[\theta_4 / 0]_s$	$[\theta_4 /0]_s$	$[\theta_2/0]_s$	$[\theta_2/0]_s$	$[\theta_2]_s$	$[\theta_2]_s$
Top upper Stringer	$[\theta_4 / 0_2]_s$	$[\theta_4/ 0_2]_s$	$[\theta_4 / 0_2]_s$	$[\theta_4 / 0]_s$	$[\theta_4 /0]_s$	$[\theta_2/0]_s$	$[\theta_2/0]_s$	$[\theta_2]_s$	$[\theta_2]_s$
Lower skin	$[\theta_4 / 0_2]_s$	$[\theta_4 / 0_2]_s$	$[\theta_4 /0_2]_s$	$[\theta_4 / 0]_s$	$[\theta_4/0]_s$	$[\theta_2/0]_s$	$[\theta_2/0]_s$	$[\theta_2]_s$	$[\theta_2]_s$
Top lower Stringer	$[\theta_4 / 0_2]_s$	$[\theta_4 / 0_2]_s$	$[\theta_4 / 0_2]_s$	$[\theta_4 / 0]_s$	$[\theta_4/0]_s$	$[\theta_2/0]_s$	$[\theta_2/0]_s$	$[\theta_2]_s$	$[\theta_2]_s$
Top upper spar Stiffener	$[\theta_4 / 0_2]_s$	$[\theta_4 / 0_2]_s$	$[\theta_4 / 0_2]_s$	$[\theta_4 / 0]_s$	$[\theta_4 /0]_s$	$[\theta_2/0]_s$	$[\theta_2/0]_s$	$[\theta_2]_s$	$[\theta_2]_s$
Top lower spar Stiffener	$[\theta_4 / 0_2]_s$	$[\theta_4 / 0_2]_s$	$[\theta_4 / 0_2]_s$	$[\theta_4 / 0]_s$	$[\theta_4/0]_s$	$[\theta_2/0]_s$	$[\theta_2/0]_s$	$[\theta_2]_s$	$[\theta_2]_s$
Upper stringer Side walls	$[\pm45_2]$	$[\pm45_2]$	$[\pm45_2]$	$[\pm45_2]$	$[\pm45_2]$	[±45]	[±45]	[±45]	[±45]
Lower stringer Side walls	$[\pm45_2]$	$[\pm45_2]$	$[\pm45_2]$	$[\pm45_2]$	[±45]	[±45]	[±45]	[±45]	[±45]
Upper stringer Caps	$[\pm45/0_{15}/\pm45]$	$[\pm45/0_{15}/\pm45]$	$[\pm45/0_{15}/\pm45]$	$[\pm45/0_{15}/\pm45]$	$[\pm45/0_{13}/\pm45]$	$[\pm45/0_{12}]$	$[\pm45/0_{10}]$	$[\pm45/0_9]$	$[\pm45/0_8]$
Lower stringer Caps	$[\pm45/0_{13}/\pm45]$	$[\pm45/0_{13}/\pm45]$	$[\pm45/0_{12}/\pm45]$	$[\pm45/0_{12}/\pm45]$	$[\pm45/0_{12}]$	$[\pm45/0_9]$	$[\pm45/0_9]$	$[\pm45/0_7]$	$[\pm45/0_5]$
Front & rear Spar webs	$[\pm45_2/F51/\pm45_2]$	$[\pm45_2/F51/\pm45_2]$	$[\pm45_2/F51/\pm45_2]$	$[\pm45_2/F51/\pm45_2]$	$[\pm45_2/F51/\pm45_2]$	$[\pm45_2/F51/\pm45_2]$	[±45/F51/±45]	[±45/F51/±45]	[±45/F51/±45]
Front and rear Spar flanges	$[\pm45_2]$	$[\pm45_2]$	$[\pm45_2]$	$[\pm45_2]$	$[\pm45_2]$	$[\pm45_2]$	[±45]	[±45]	[±45]

Table (9.2) Laminates Configuration of the A1 composite wing box (A1 wing 1)

Stations (mm) / Laminate	431	868	1411	1981	2556	3131	3706	4281
ribs	$[\pm 45_2]_s$	$[\pm 45_2]_s$	$[\pm 45_2]_s$	0-127 mm upper and lower parts from the rear spar $[\pm 45_4/0_4/F51/\pm 45_4/0_4]$	$[\pm 45_2]_s$	$[\pm 45_2]_s$	0-127 mm upper and lower parts from the rear spar $[\pm 45_4/0_4/F51/\pm 45_4/0_4]$	$[\pm 45_2]_s$
				0-127 mm middle part from the rear spar $[\pm 45_4/F51/\pm 45_4]$			0-127 mm middle part from the rear spar $[\pm 45_4/F51/\pm 45_4]$	
				127-481 mm upper and lower parts from the rear spar $[\pm 45_s]_s/\ 0_2$			127-633 mm upper and lower parts from the rear spar $[\pm 45_2]_s/\ 0_2$	
				127-481mm middle part from the rear spar $[\pm 45_2]_s$			127-633 mm middle part from the rear spar $[\pm 45_2]_s$	
				481-812 mm upper and lower part from the rear spar $[\pm 45_2]_s/0$				
				481-812 mm middle part from the rear spar $[\pm 45_2]_s$				

- Note: All the stringer sides, stringer caps, spar webs, spar flanges and ribs were modeled with the same laminates for all the A1 wing models.

Table (9.3) Laminates Configuration of the A1 composite wing box (A1 wing 2)

Stations (mm) / Laminate	0- 431	431- 868	868 - 1411	1411-1981	1981 - 2556	2556 - 3131	3131 - 3706	3706 - 4281	4281-4902
Upper skin	$[\theta_4 / 0_2]_s$	$[\theta_4 / 0_2]_s$	$[\theta_4 / 0_2]_s$	$[\theta_4 / 0]_s$	$[\theta_4 /0]_s$	$[\theta_2/0]_s$	$[\theta_2/0]_s$	$[\theta_2]_s$	$[\theta_2]_s$
top upper stringer	$[\theta_4 / 0_2]_s$	$[\theta_4/ 0_2]_s$	$[\theta_4 / 0_2]_s$	$[\theta_4 / 0]_s$	$[\theta_4 /0]_s$	$[\theta_2/0]_s$	$[\theta_2/0]_s$	$[\theta_2]_s$	$[\theta_2]_s$
Lower skin	$[-\theta_4 / 0_2]_s$	$[-\theta_4 / 0_2]_s$	$[-\theta_4 /0_2]_s$	$[-\theta_4 / 0]_s$	$[-\theta_4/0]_s$	$[-\theta_2/0]_s$	$[-\theta_2/0]_s$	$[-\theta_2]_s$	$[-\theta_2]_s$
top lower stringer	$[-\theta_4 / 0_2]_s$	$[-\theta_4 / 0_2]_s$	$[-\theta_4 / 0_2]_s$	$[-\theta_4 / 0]_s$	$[-\theta_4/0]_s$	$[-\theta_2/0]_s$	$[-\theta_2/0]_s$	$[-\theta_2]_s$	$[-\theta_2]_s$
top upper spar stiffener	$[\theta_4 / 0_2]_s$	$[\theta_4 / 0_2]_s$	$[\theta_4 / 0_2]_s$	$[\theta_4 / 0]_s$	$[\theta_4 /0]_s$	$[\theta_2/0]_s$	$[\theta_2/0]_s$	$[\theta_2]_s$	$[\theta_2]_s$
top lower spar stiffener	$[-\theta_4 / 0_2]_s$	$[-\theta_4 / 0_2]_s$	$[-\theta_4 / 0_2]_s$	$[-\theta_4 / 0]_s$	$[-\theta_4/0]_s$	$[-\theta_2/0]_s$	$[-\theta_2/0]_s$	$[-\theta_2]_s$	$[-\theta_2]_s$
Upper stringer Side walls	$[\pm45_2]$	$[\pm45_2]$	$[\pm45_2]$	$[\pm45_2]$	$[\pm45_2]$	[±45]	[±45]	[±45]	[±45]
Lower stringer Side walls	$[\pm45_2]$	$[\pm45_2]$	$[\pm45_2]$	$[\pm45_2]$	[±45]	[±45]	[±45]	[±45]	[±45]
Upper stringer Caps	$[\pm45/0_{15}/\pm45]$	$[\pm45/0_{15}/\pm45]$	$[\pm45/0_{15}/\pm45]$	$[\pm45/0_{15}/\pm45]$	$[\pm45/0_{13}/\pm45]$	$[\pm45/0_{12}]$	$[\pm45/0_{10}]$	$[\pm45/0_9]$	$[\pm45/0_8]$
Lower stringer Caps	$[\pm45/0_{13}/\pm45]$	$[\pm45/0_{13}/\pm45]$	$[\pm45/0_{12}/\pm45]$	$[\pm45/0_{12}/\pm45]$	$[\pm45/0_{12}]$	$[\pm45/0_9]$	$[\pm45/0_9]$	$[\pm45/0_7]$	$[\pm45/0_5]$
Front & rear Spar webs	$[\pm45_2/F51/\pm45_2]$	$[\pm45_2/F51/\pm45_2]$	$[\pm45_2/F51/\pm45_2]$	$[\pm45_2/F51/\pm45_2]$	$[\pm45_2/F51/\pm45_2]$	$[\pm45_2/F51/\pm45_2]$	[±45/F51/±45]	[±45/F51/±45]	[±45/F51/±45]
Front and rear Spar flanges	$[\pm45_2]$	$[\pm45_2]$	$[\pm45_2]$	$[\pm45_2]$	$[\pm45_2]$	$[\pm45_2]$	[±45]	[±45]	[±45]

Table (9.4) Laminates Configuration of the A1 composite wing box (A1 wing 3)

Stations (mm) / Laminate	0- 431	431- 868	868 - 1411	1411-1981	1981 - 2556	2556 - 3131	3131 - 3706	3706 - 4281	4281-4902
Upper skin	$[\theta_4 / 0_2]_2$	$[\theta_4 / 0_2]_2$	$[\theta_4 / 0_2]_2$	$[\theta_4 / 0]_2$	$[\theta_4 /0]_2$	$[\theta_2/0]_2$	$[\theta_2/0]_2$	$[\theta_2]_2$	$[\theta_2]_2$
top upper stringer	$[\theta_4 / 0_2]_2$	$[\theta_4/ 0_2]_2$	$[\theta_4 / 0_2]_2$	$[\theta_4 / 0]_2$	$[\theta_4 /0]_2$	$[\theta_2/0]_2$	$[\theta_2/0]_2$	$[\theta_2]_2$	$[\theta_2]_2$
Lower skin	$[\theta_4 / 0_2]_2$	$[\theta_4 / 0_2]_2$	$[\theta_4 /0_2]_2$	$[\theta_4 / 0]_2$	$[\theta_4/0]_2$	$[\theta_2/0]_2$	$[\theta_2/0]_2$	$[\theta_2]_2$	$[\theta_2]_2$
top lower stringer	$[\theta_4 / 0_2]_2$	$[\theta_4 / 0_2]_2$	$[\theta_4 / 0_2]_2$	$[\theta_4 / 0]_2$	$[\theta_4/0]_2$	$[\theta_2/0]_2$	$[\theta_2/0]_2$	$[\theta_2]_2$	$[\theta_2]_2$
top upper spar stiffener	$[\theta_4 / 0_2]_2$	$[\theta_4 / 0_2]_2$	$[\theta_4 / 0_2]_2$	$[\theta_4 / 0]_2$	$[\theta_4 /0]_2$	$[\theta_2/0]_2$	$[\theta_2/0]_2$	$[\theta_2]_2$	$[\theta_2]_2$
top lower spar stiffener	$[\theta_4 / 0_2]_2$	$[\theta_4 / 0_2]_2$	$[\theta_4 / 0_2]_2$	$[\theta_4 / 0]_2$	$[\theta_4/0]_2$	$[\theta_2/0]_2$	$[\theta_2/0]_2$	$[\theta_2]_2$	$[\theta_2]_2$
Upper stringer Side walls	$[\pm 45_2]$	$[\pm 45_2]$	$[\pm 45_2]$	$[\pm 45_2]$	$[\pm 45_2]$	$[\pm 45]$	$[\pm 45]$	$[\pm 45]$	$[\pm 45]$
Lower stringer Side walls	$[\pm 45_2]$	$[\pm 45_2]$	$[\pm 45_2]$	$[\pm 45_2]$	$[\pm 45]$	$[\pm 45]$	$[\pm 45]$	$[\pm 45]$	$[\pm 45]$
Upper stringer Caps	$[\pm 45/0_{15}/\pm 45]$	$[\pm 45/0_{15}/\pm 45]$	$[\pm 45/0_{15}/\pm 45]$	$[\pm 45/0_{15}/\pm 45]$	$[\pm 45/0_{13}/\pm 45]$	$[\pm 45/0_{12}]$	$[\pm 45/0_{10}]$	$[\pm 45/0_9]$	$[\pm 45/0_8]$
Lower stringer Caps	$[\pm 45/0_{13}/\pm 45]$	$[\pm 45/0_{13}/\pm 45]$	$[\pm 45/0_{12}/\pm 45]$	$[\pm 45/0_{12}/\pm 45]$	$[\pm 45/0_{12}]$	$[\pm 45/0_9]$	$[\pm 45/0_9]$	$[\pm 45/0_7]$	$[\pm 45/0_5]$
Front & rear Spar webs	$[\pm 45_2/F51/\pm 45_2]$	$[\pm 45_2/F51/\pm 45_2]$	$[\pm 45_2/F51/\pm 45_2]$	$[\pm 45_2/F51/\pm 45_2]$	$[\pm 45_2/F51/\pm 45_2]$	$[\pm 45_2/F51/\pm 45_2]$	$[\pm 45/F51/\pm 45]$	$[\pm 45/F51/\pm 45]$	$[\pm 45/F51/\pm 45]$
Front and rear Spar flanges	$[\pm 45_2]$	$[\pm 45_2]$	$[\pm 45_2]$	$[\pm 45_2]$	$[\pm 45_2]$	$[\pm 45_2]$	$[\pm 45]$	$[\pm 45]$	$[\pm 45]$

Table (9.5) Laminates Configuration of the A1 composite wing box (A1 wing 4)

Stations (mm) / Laminate	0- 431	431- 868	868 - 1411	1411-1981	1981 - 2556	2556 - 3131	3131 - 3706	3706 - 4281	4281-4902
Upper skin	$[\theta_4 / 0_2]_2$	$[\theta_4 / 0_2]_2$	$[\theta_4 / 0_2]_2$	$[\theta_4 / 0]_2$	$[\theta_4 /0]_2$	$[\theta_2/0]_2$	$[\theta_2/0]_2$	$[\theta_2]_2$	$[\theta_2]_2$
top upper stringer	$[\theta_4 / 0_2]_2$	$[\theta_4/ 0_2]_2$	$[\theta_4 / 0_2]_2$	$[\theta_4 / 0]_2$	$[\theta_4 /0]_2$	$[\theta_2/0]_s$	$[\theta_2/0]_2$	$[\theta_2]_2$	$[\theta_2]_2$
Lower skin	$[-\theta_4 / 0_2]_2$	$[-\theta_4 / 0_2]_2$	$[-\theta_4 /0_2]_2$	$[-\theta_4 / 0]_2$	$[-\theta_4/0]_2$	$[-\theta_2/0]_2$	$[-\theta_2/0]_2$	$[-\theta_2]_2$	$[-\theta_2]_2$
top lower stringer	$[-\theta_4 / 0_2]_2$	$[-\theta_4 / 0_2]_2$	$[-\theta_4 / 0_2]_2$	$[-\theta_4 / 0]_2$	$[-\theta_4/0]_2$	$[-\theta_2/0]_2$	$[-\theta_2/0]_2$	$[-\theta_2]_2$	$[-\theta_2]_2$
top upper spar stiffener	$[\theta_4 / 0_2]_2$	$[\theta_4 / 0_2]_2$	$[\theta_4 / 0_2]_2$	$[\theta_4 / 0]_2$	$[\theta_4 /0]_2$	$[\theta_2/0]_2$	$[\theta_2/0]_2$	$[\theta_2]_2$	$[\theta_2]_2$
top lower spar stiffener	$[-\theta_4 / 0_2]_2$	$[-\theta_4 / 0_2]_2$	$[-\theta_4 / 0_2]_2$	$[-\theta_4 / 0]_2$	$[-\theta_4/0]_2$	$[-\theta_2/0]_2$	$[-\theta_2/0]_2$	$[-\theta_2]_2$	$[-\theta_2]_2$
Upper stringer Side walls	$[\pm45_2]$	$[\pm45_2]$	$[\pm45_2]$	$[\pm45_2]$	$[\pm45_2]$	$[\pm45]$	$[\pm45]$	$[\pm45]$	$[\pm45]$
Lower stringer Side walls	$[\pm45_2]$	$[\pm45_2]$	$[\pm45_2]$	$[\pm45_2]$	$[\pm45]$	$[\pm45]$	$[\pm45]$	$[\pm45]$	$[\pm45]$
Upper stringer Caps	$[\pm45/0_{15}/\pm45]$	$[\pm45/0_{15}/\pm45]$	$[\pm45/0_{15}/\pm45]$	$[\pm45/0_{15}/\pm45]$	$[\pm45/0_{13}/\pm45]$	$[\pm45/0_{12}]$	$[\pm45/0_{10}]$	$[\pm45/0_9]$	$[\pm45/0_8]$
Lower stringer Caps	$[\pm45/0_{13}/\pm45]$	$[\pm45/0_{13}/\pm45]$	$[\pm45/0_{12}/\pm45]$	$[\pm45/0_{12}/\pm45]$	$[\pm45/0_{12}]$	$[\pm45/0_9]$	$[\pm45/0_9]$	$[\pm45/0_7]$	$[\pm45/0_5]$
Front & rear Spar webs	$[\pm45_2/F51/\pm45_2]$	$[\pm45_2/F51/\pm45_2]$	$[\pm45_2/F51/\pm45_2]$	$[\pm45_2/F51/\pm45_2]$	$[\pm45_2/F51/\pm45_2]$	$[\pm45_2/F51/\pm45_2]$	$[\pm45/F51/\pm45]$	$[\pm45/F51/\pm45]$	$[\pm45/F51/\pm45]$
Front and rear Spar flanges	$[\pm45_2]$	$[\pm45_2]$	$[\pm45_2]$	$[\pm45_2]$	$[\pm45_2]$	$[\pm45_2]$	$[\pm45]$	$[\pm45]$	$[\pm45]$

9.3 Results:

Normal mode analysis (undamped free vibration) was carried out for all the A1 wing models using Lanczos method provided in MSC/NASTRAN. The variation of the first four bending and torsional frequencies as a function of the fibre angle of the upper and lower skin of the A1 wing models were shown in figure (9.1-9.2). However, the variation of the fibre angle of the skins were varied from -90^{o} to 90^{o} in steps of (0^{o}, 30^{o}, 45^{o}, 60^{o}, 90^{o}, -30^{o}, -45^{o}, -60^{o} and -90^{o}).

Representative eigenvectors were generated using MSC/PATRAN 6 for the A1 wing 1 model at fibre angle of (0^{o}, 30^{o}, 45^{o} and 90^{o}) as shown in figures (9.3-9.22).

9.4 Discussion of results:

The essential purpose of figure (9.1) of the A1 wing 1 and A1 wing models was to illustrate the changes of the first four bending and torsional natural frequencies as results of ply orientations, which can be discussed each in turn as follows:

Looking first at the A1 wing 1 model, the first natural frequency was the fundamental bending mode (with small amount of torsion displacement). The maximum natural frequency in this mode was found at $\theta = 0^{o}$ and then decreases as the fibre angle θ increases. This frequency mode is highly dependent on the spanwise bending stiffness (EI). It can be seen from figure (9.1) that the first bending frequency are not symmetrical about zero degree fibre angle due to the asymmetry of the airfoil section used in the A1 composite wing box which was not the case in chapter 8. The asymmetry airfoil will create an offset between the elastic axis and the inertia axis. Both axes will not be straight lines as result of the non-uniform stiffness along the span and the kink of the front spar. This asymmetric frequency was observed by [9.6] when the wing was modeled as a plate with an offset.

The second natural frequency was the second bending mode with various amount of torsion displacement as shown in the selected mode shapes (see figures 9.5, 9.10, 9.15, and 9.20). This is due to both material and structural coupling present in the model. The natural frequency of the second bending mode on the positive angle was started decreasing as the fibre angle increased from 0^{o}, where as on the negative fibre

angle, the frequency started slightly increasing as the fibre angle increases from 0^o to -30^o and then started declined.

The third natural frequency was dominated by the first torsional mode with small bending displacement in all the investigated fibre angles except at $\theta = \pm 30$ degree was with a higher bending displacement involved as shown in figure (9.11). This mode is highly dependent on the torsional stiffness (GJ). The first torsional frequency started increasing as the fibre angle increasing up to $\pm 30^o$ and then started decreasing as the fibre angle increased (see figure 9.1).

The fourth frequency was dominated by the third bending mode in the regions of 0^o and $\pm 60^o \leq \theta \leq \pm 90^o$ as shown in the selected figures (9.7 and 9.22). However, the third bending mode at $\pm 30^o$ and $\pm 45^o$ were coupled (third bending with torsion displacement) as shown in figure (9.12) and (9.17) respectively. The natural frequency of this mode started decreasing as the fibre angle increased from 0^o on the positive fibre, whereas on the negative fibre angle the frequency slightly increased as the fibre angle increases from 0^o to -30^o and then started decreasing. This could be due to the combinations of the material coupling and the structural geometric coupling.

In the previous chapter, the CUS configuration was considered as the configuration, which did not produce bending-torsional coupling stiffness due to the modeling and the symmetry of the structure. However, in the case of real aircraft wings such as the A1 Cranfield composite wing box (A1 wing 2), the bending-torsional coupling stiffness still exists due to the asymmetry of the airfoil section of the wing structure.

Looking at the A1 wing 2 model shown in figure (9.1), the first and second natural frequencies were the first and second bending modes (with very small a mount of torsion displacement) respectively. The natural frequencies are all most symmetrical about 0^o fibre angles (with very small differences) as compared with the results of the A1 wing 1 model. This could be due to the combinations of small amount of the material bending-torsional coupling stiffness and the structural geometric coupling present in the A1 wing 2 model.

The third frequency mode was similar to the mode observed in the A1 wing 1 model, while the fourth frequency was dominated by the third bending mode. The

natural frequency of the third bending mode started decreasing as the fibre angle increases from zero degree.

Comparing the results shown in figure (9.1) of the A1 wing 1 and A1 wing 2 models, the following conclusions can be observed:

- Reduced amount of bending-torsion coupling stiffness in the A1 wing 2 model compared with the A1 wing 1 model. This was due to different modeling configurations (CAS and CUS).
- Due to the combination of small bending-torsion coupling stiffness and the structural geometric coupling in the A1 wing 2 model, the variation of the frequencies shown in figure (9.1) are all most symmetric about 0^o fibre angle (very close) compared with A1 wing 1 model.
- The effect of the including a higher bending-torsional coupling stiffness ($0<\theta\leq\pm45$) as in the case of A1 wing 1 model is that the torsional frequency becomes higher as compared to the A1 wing 2 model.
- The effect of the including a higher bending-torsional coupling stiffness was found quite pronounced on the bending frequencies (see figure 9.1), which will be beneficial to the flutter speed of the A1 wing 2 model.

Looking next at the A1 wing 3 and A1 wing 4 models, which were modeled with both unbalanced asymmetric and symmetric laminates (see table 9.4-9.5). It can be seen from figure (9.2) of A1 wing 3 and A1 wing 4 models that a similar trend of behaviours were observed as in the case of the A1 wing1 and A1 wing 2 models respectively. Hence a similar conclusions are still valid.

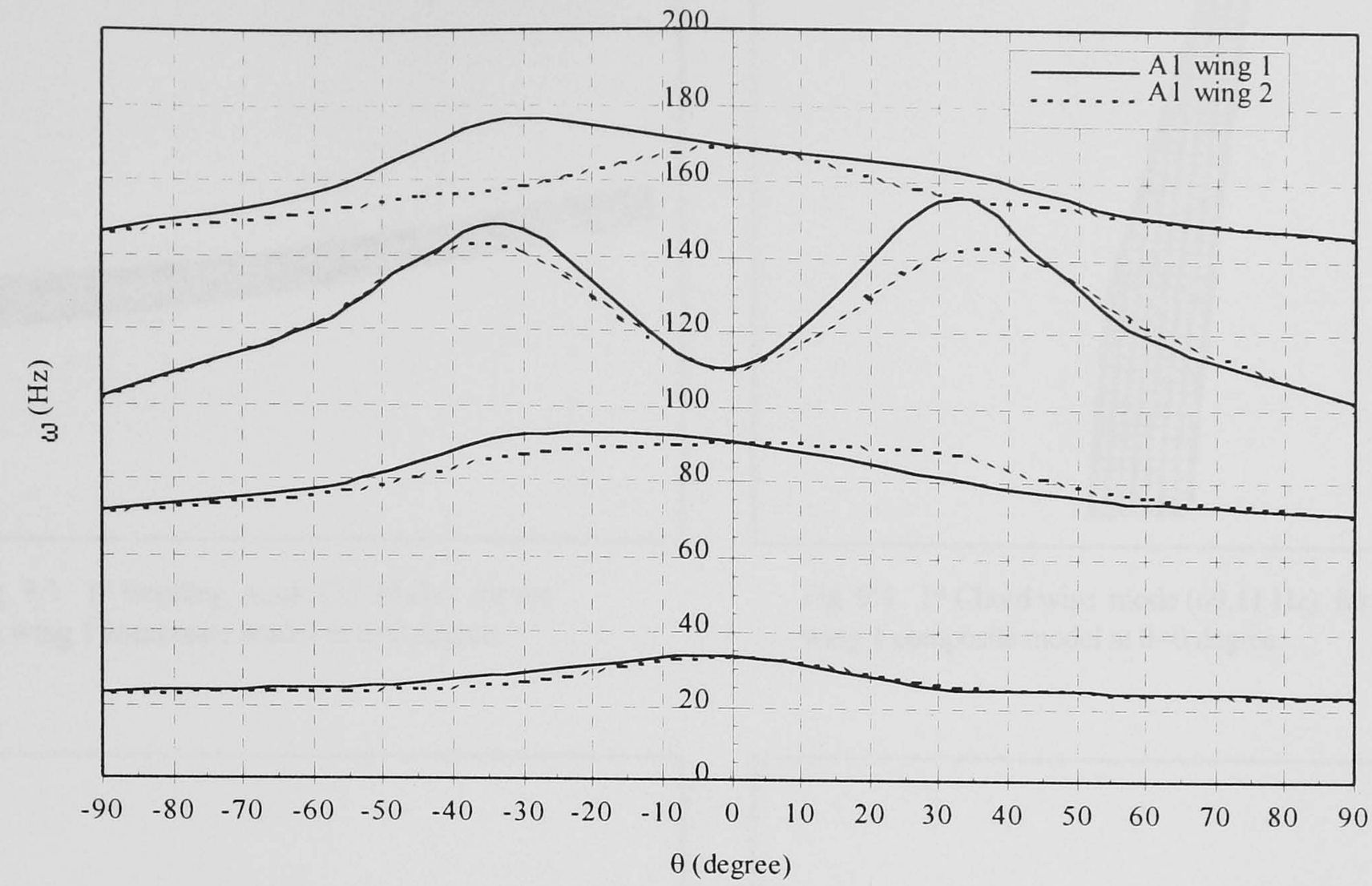

Fig. 9.1 Natural frequencies vs Fiber orientation angle (θ) of the A1 wing 1 and A1 wing 2 composite models.

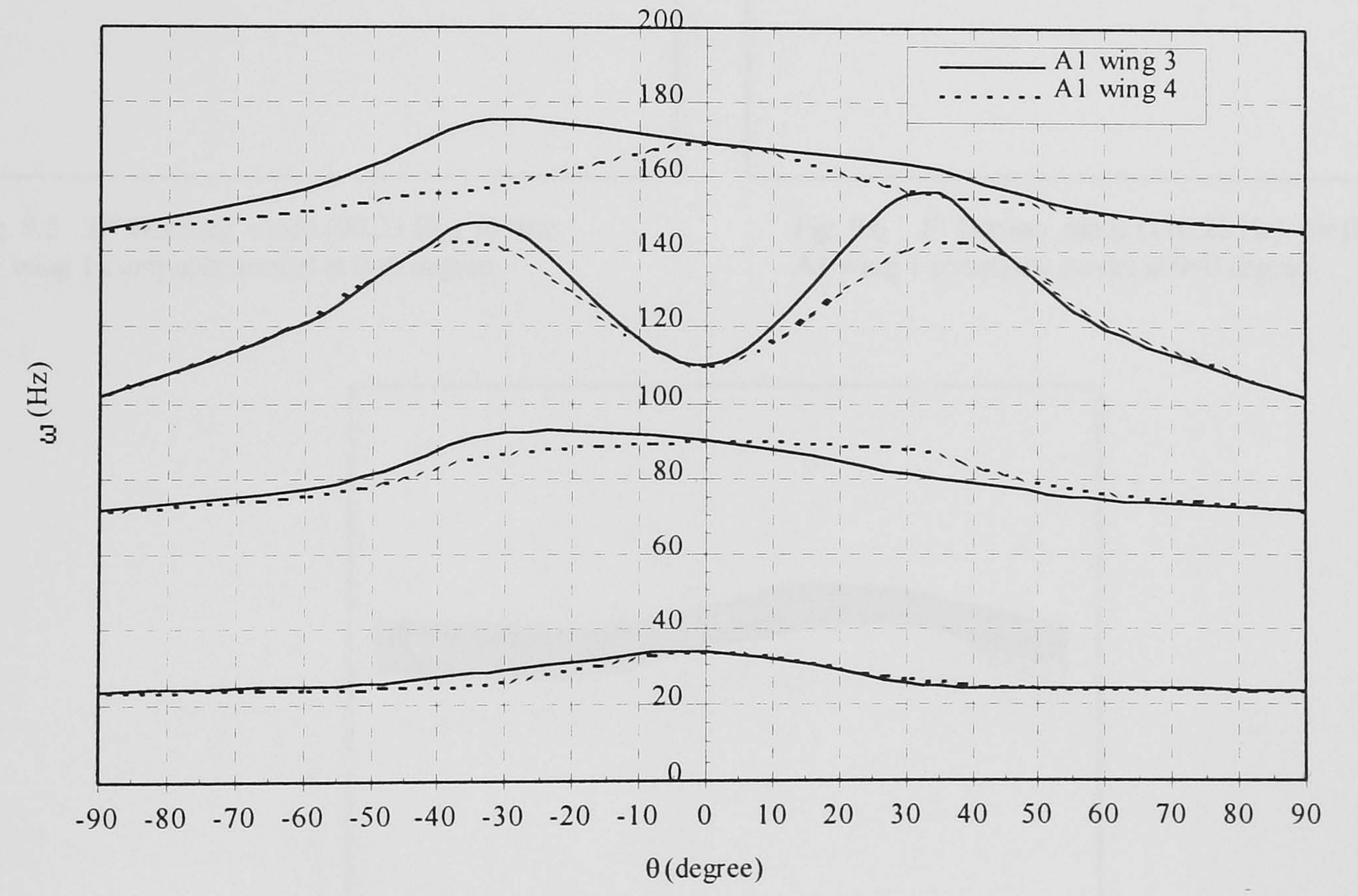

Fig. 9.2 Natural frequencies vs Fiber orientation angle (θ) of the A1 wing 3 and A1 wing 4 composite models.

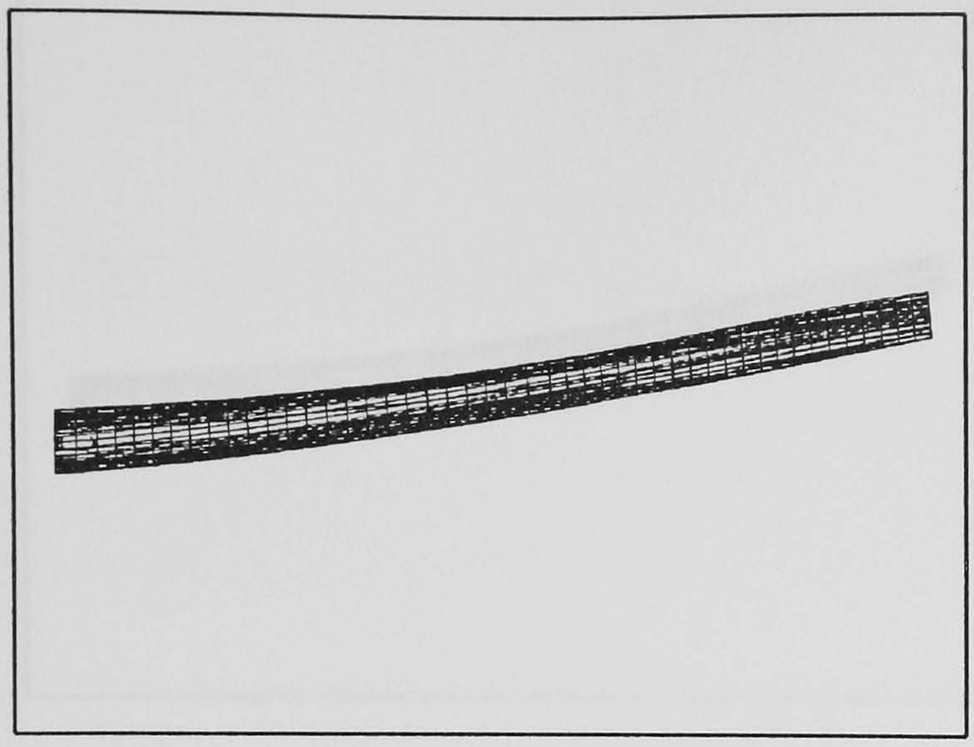

Fig. 9.3 1st Bending mode (33.39 Hz) for the A1 wing 1 composite model at θ=0 degree.

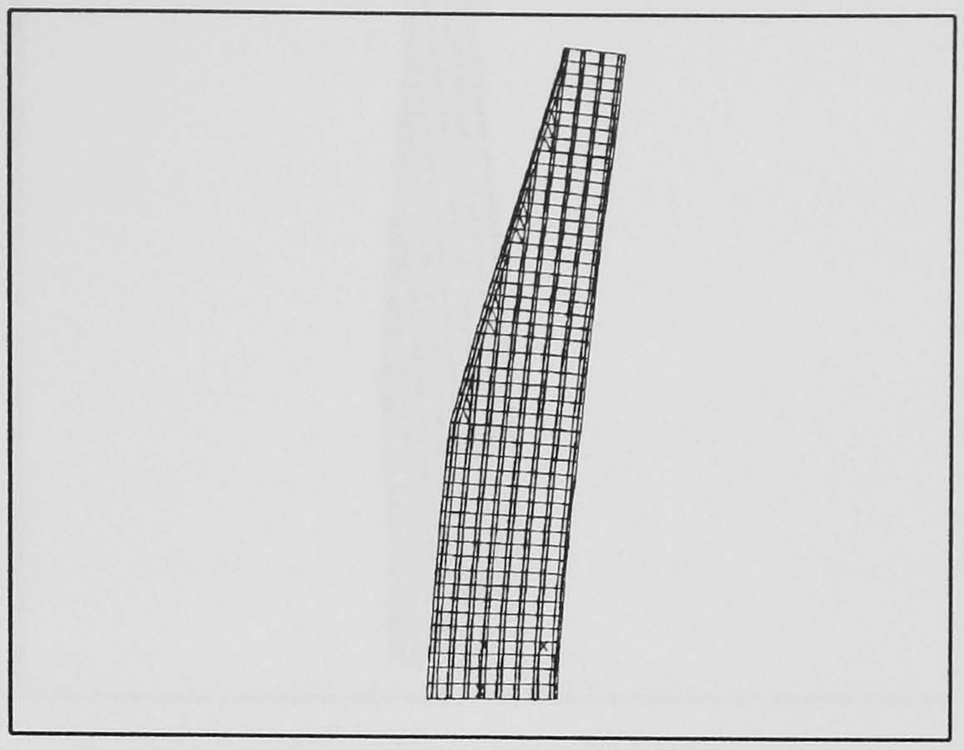

Fig. 9.4 1st Chord wise mode (69.11 Hz) for the A1 wing 1 composite model at θ=0 degree.

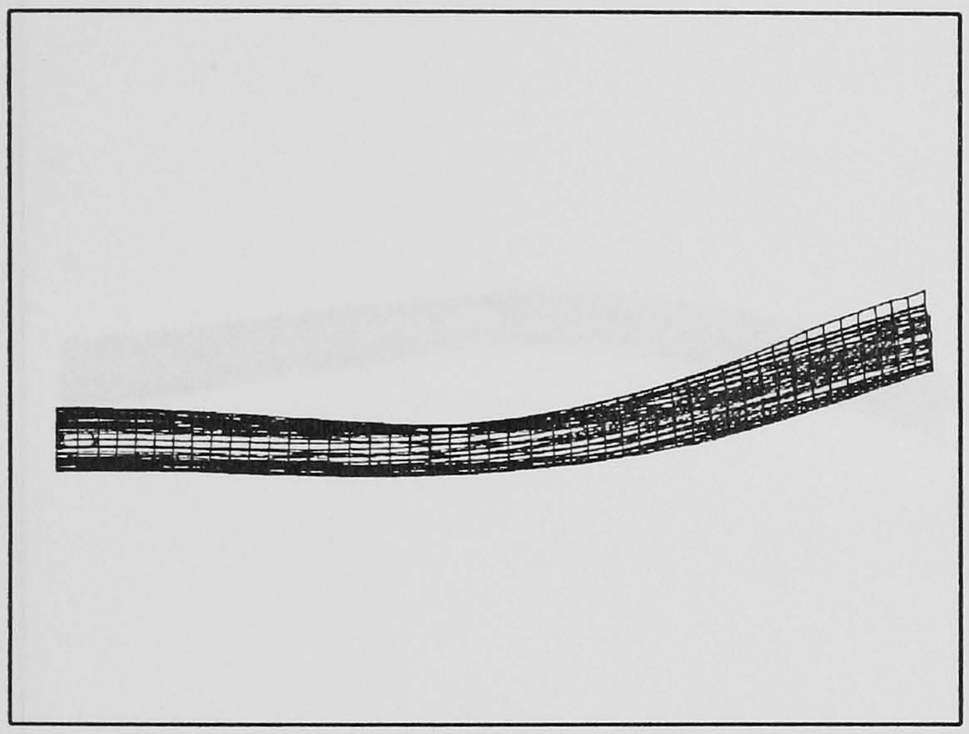

Fig. 9.5 2nd Bending mode (90.33 Hz) for the A1 wing 1 composite model at θ=0 degree.

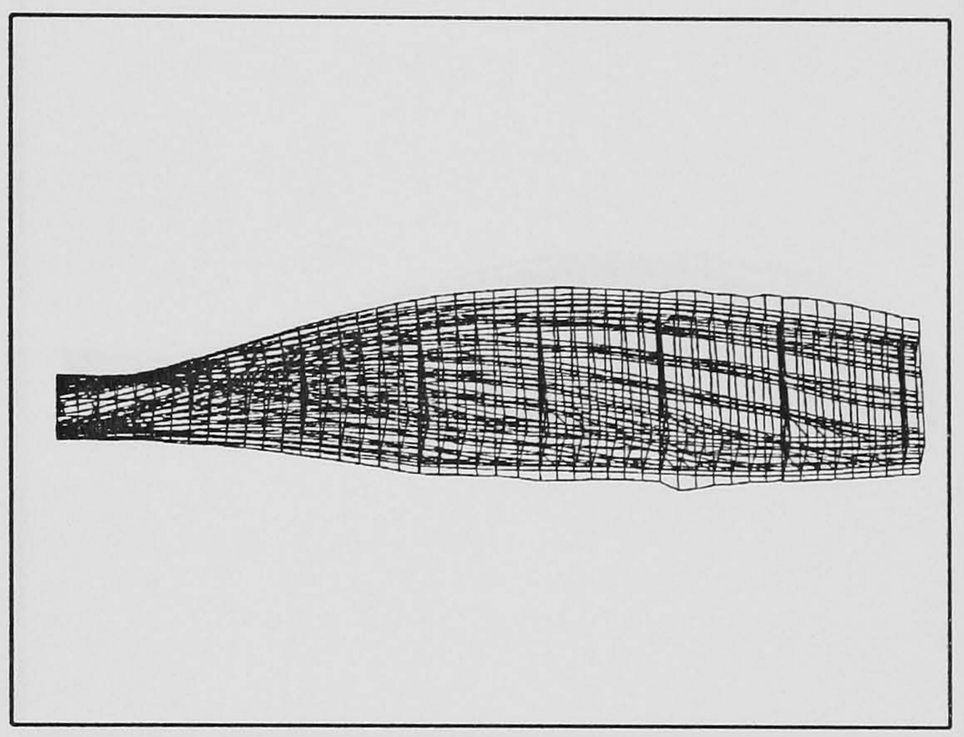

Fig. 9.6 1st Torsion mode (110.25 Hz) for the A1 wing 1 composite model at θ=0 degree.

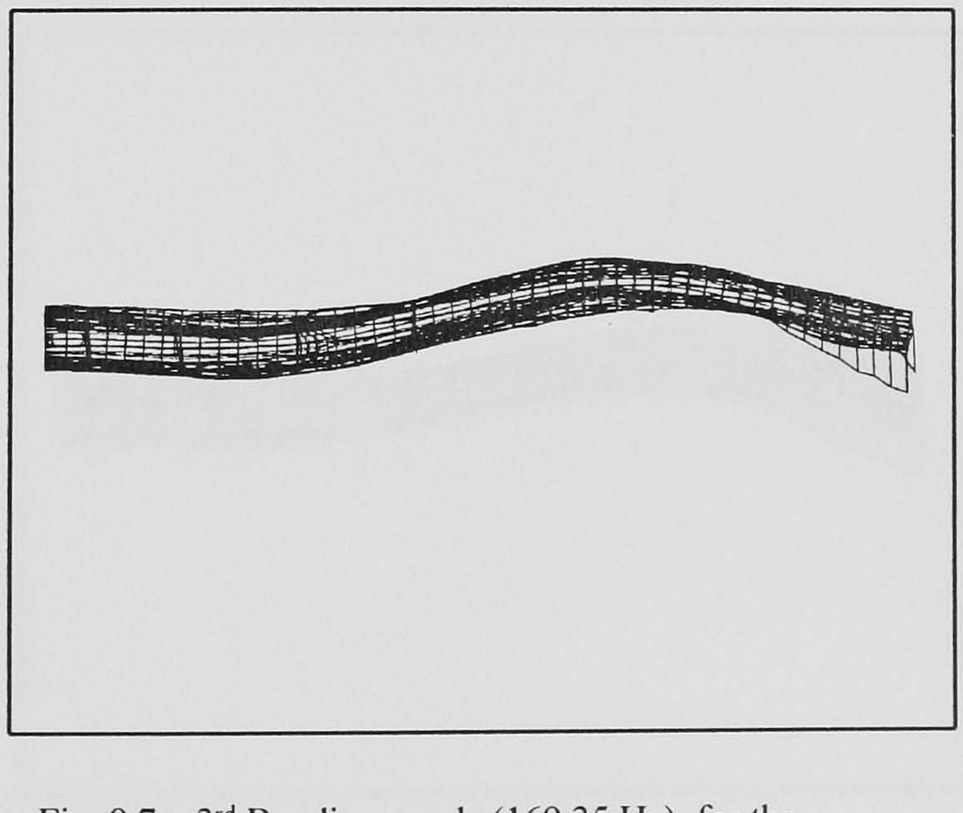

Fig. 9.7 3rd Bending mode (169.35 Hz) for the A1 wing 1 composite model at θ=0 degree.

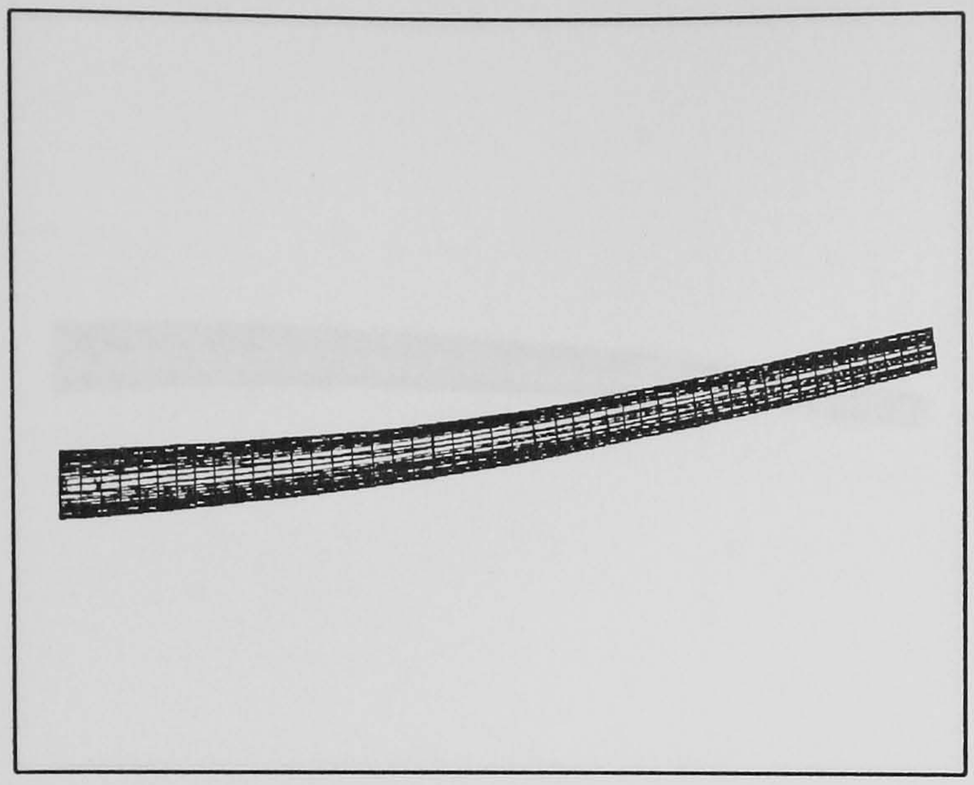

Fig. 9.8 1st Bending-Torsion mode (25.23 Hz) for the A1 wing 1 composite model at θ=30 degree.

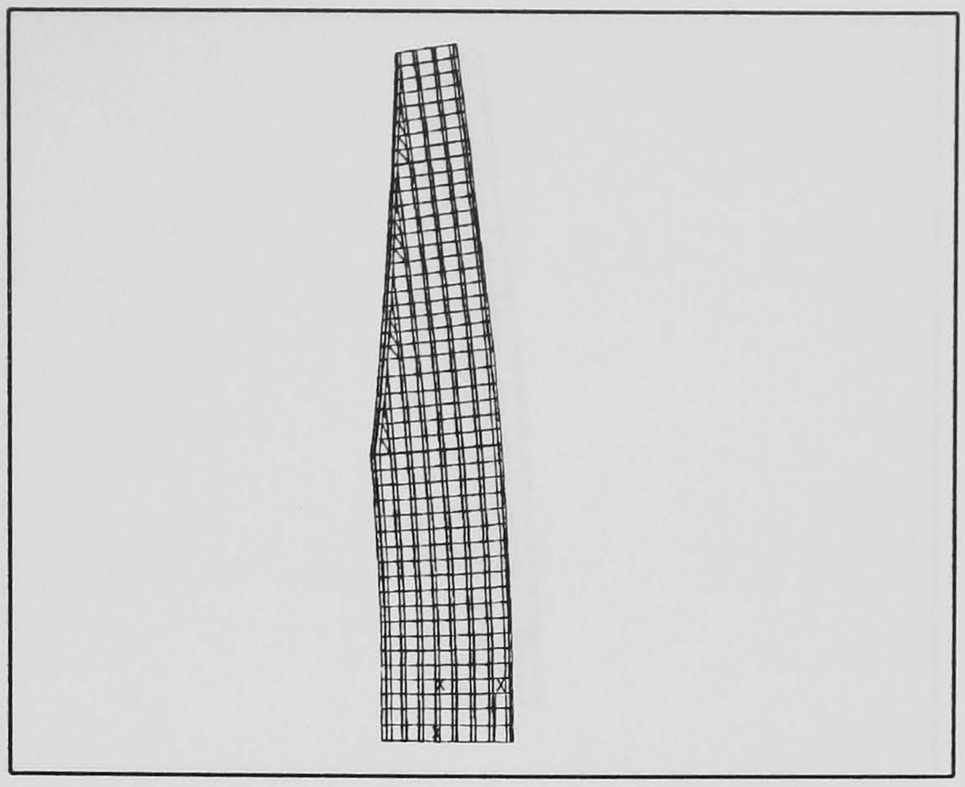

Fig. 9.9 1st Chord wise mode (65.71 Hz) for the A1 wing 1 composite model at θ=30 degree.

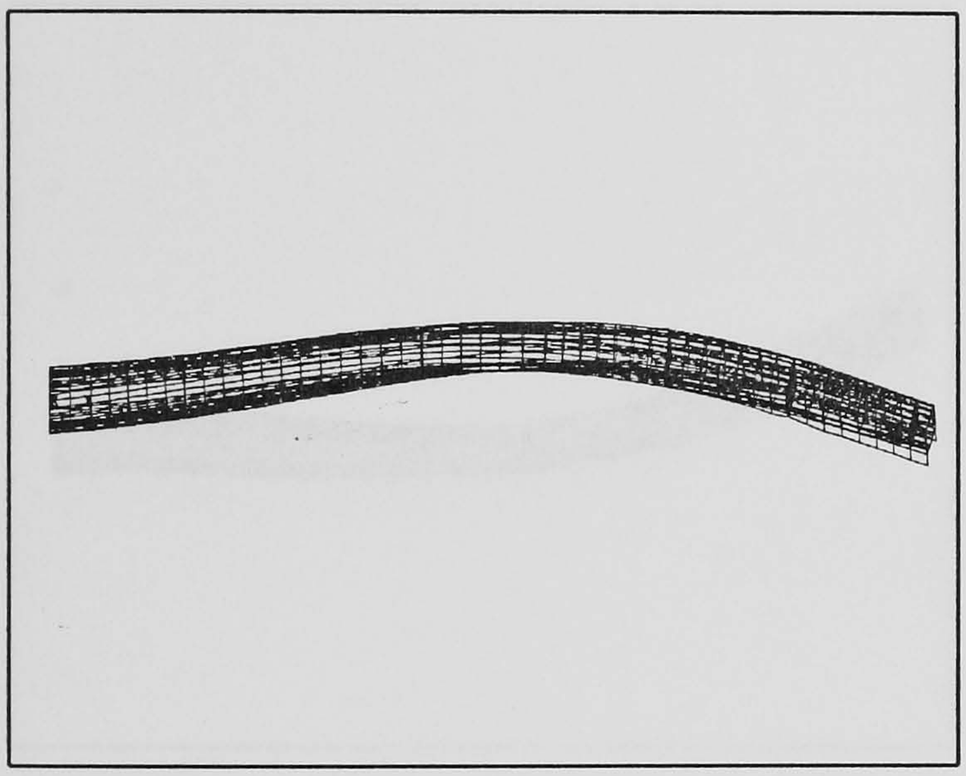

Fig. 9.10 2nd Bending-Torsion mode (81.12 Hz) for the A1 wing 1 composite model at θ=30 degree.

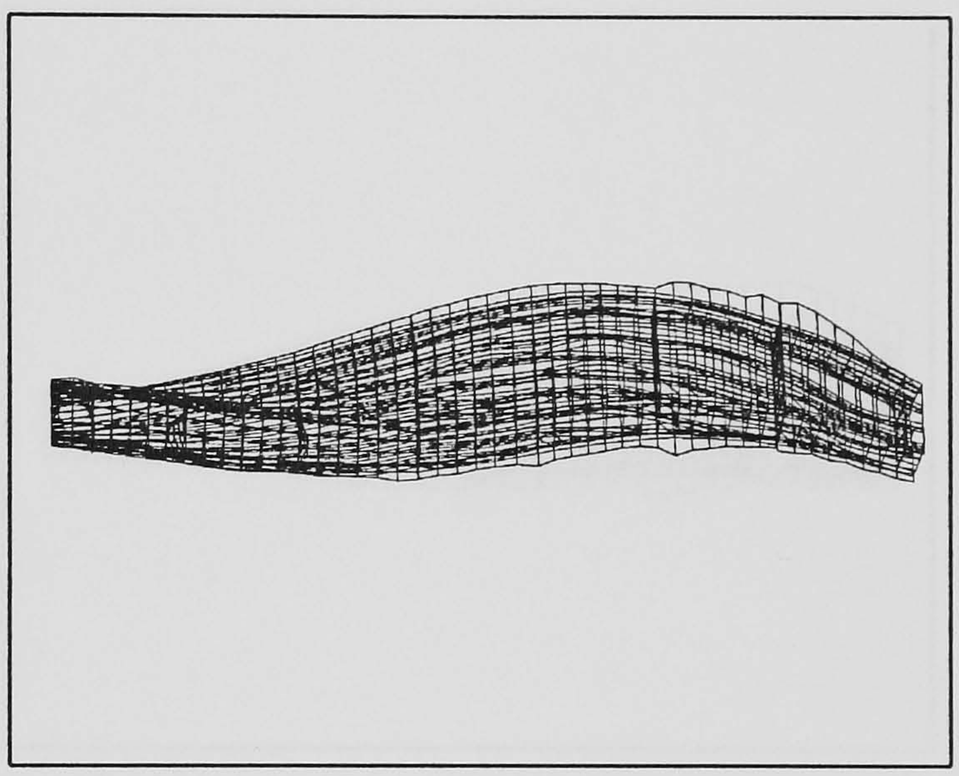

Fig. 9.11 1st Torsion-Bending mode (155.25 Hz) for the A1 wing 1 composite model at θ=30 degree.

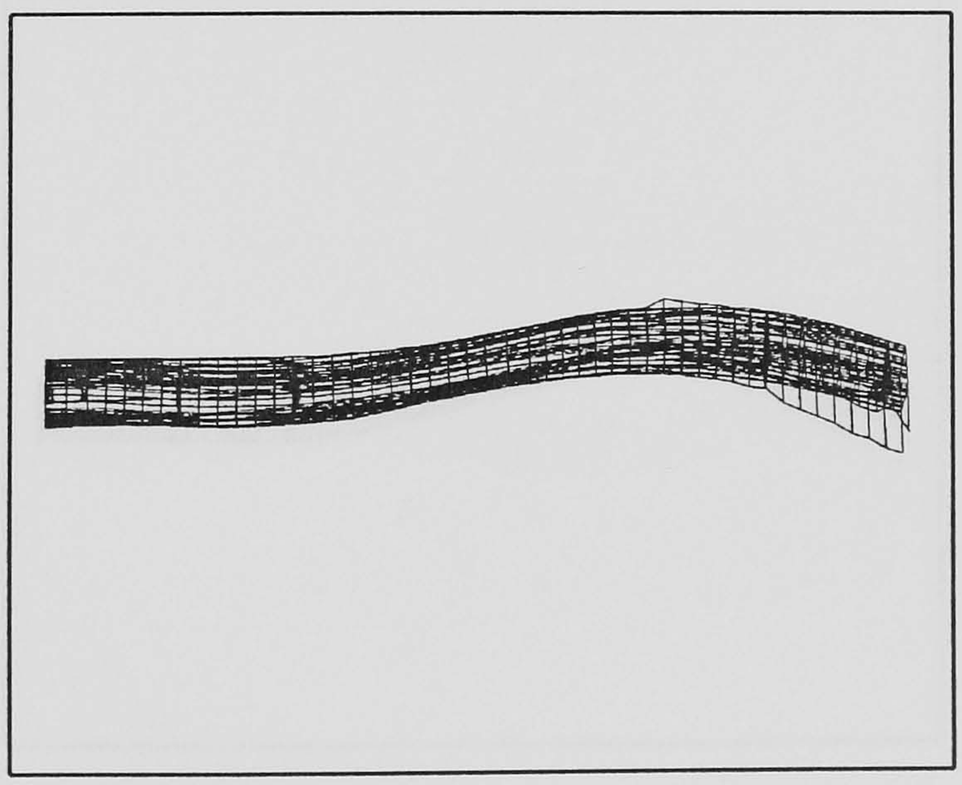

Fig. 9.12 3rd Bending-Torsion mode (163.7 Hz) for the A1 wing 1 composite model at θ=30 degree.

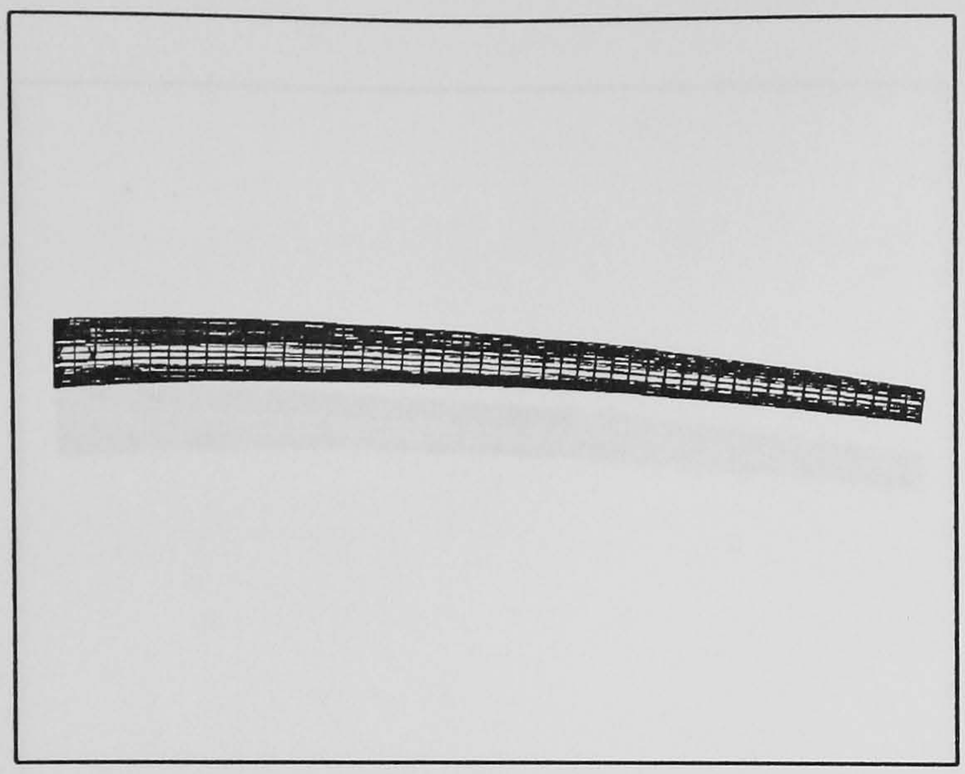

Fig. 9.13 1st Bending-Torsion mode (24.28 Hz) for the A1 wing 1 composite model at θ=45 degree.

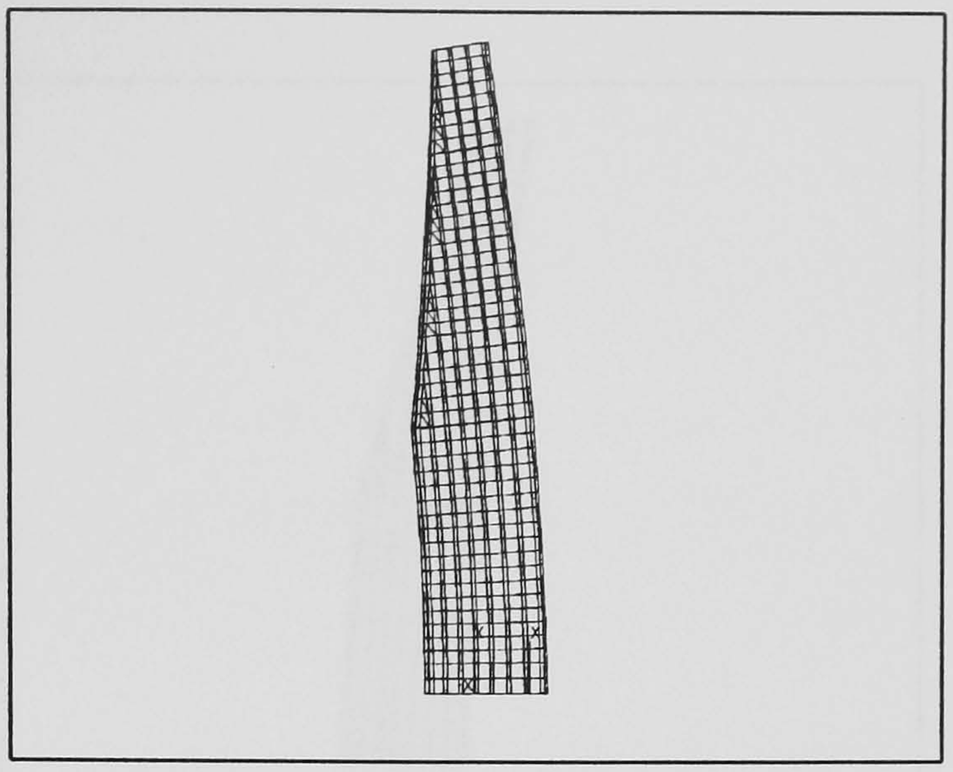

Fig. 9.14 1st Chord wise mode (62.51 Hz) for the A1 wing 1 composite model at θ=45 degree.

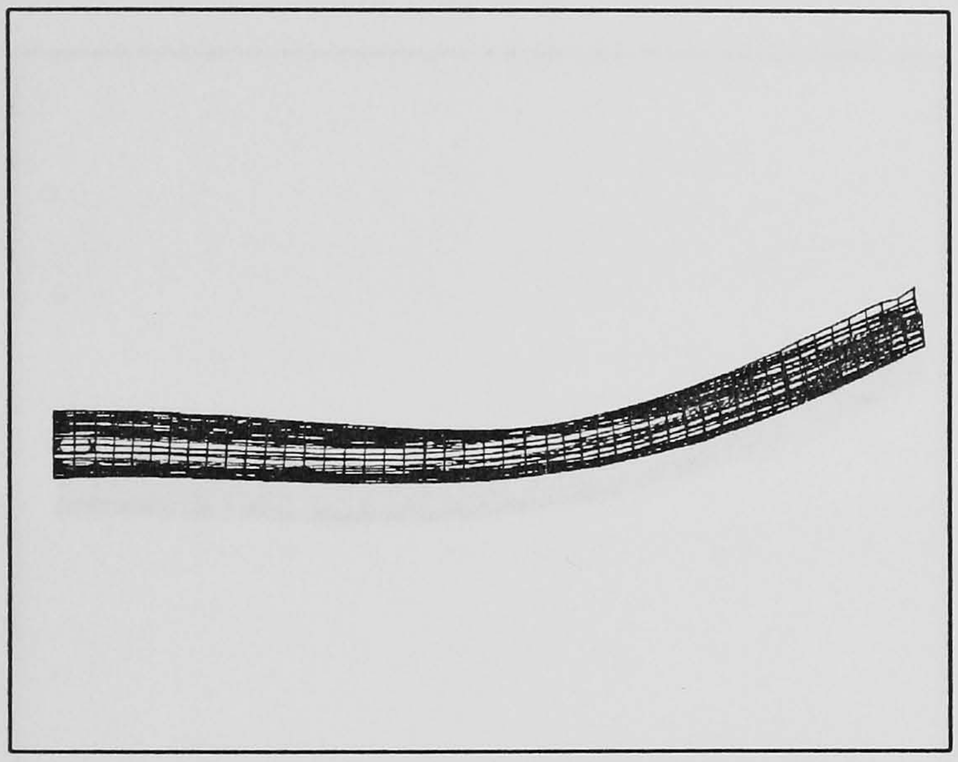

Fig. 9.15 2nd Bending-Torsion mode (77.46 Hz) for the A1 wing 1 composite model at θ=45 degree.

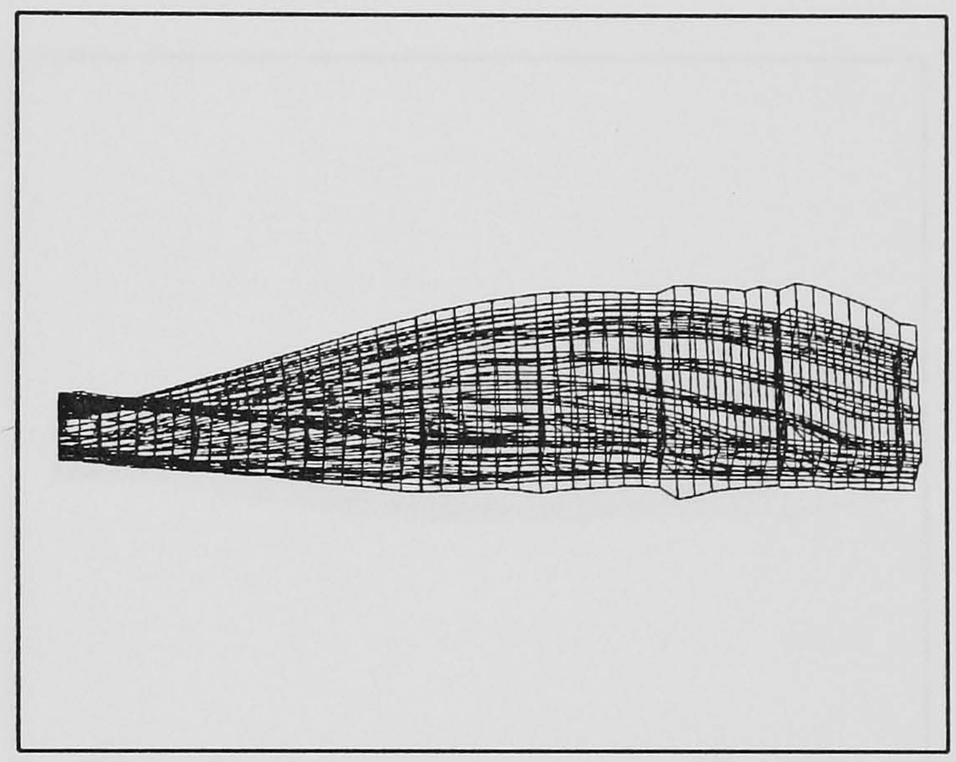

Fig. 9.16 1st Torsion-Bending mode (139.51 Hz) for the A1 wing 1 composite model at θ=45 degree.

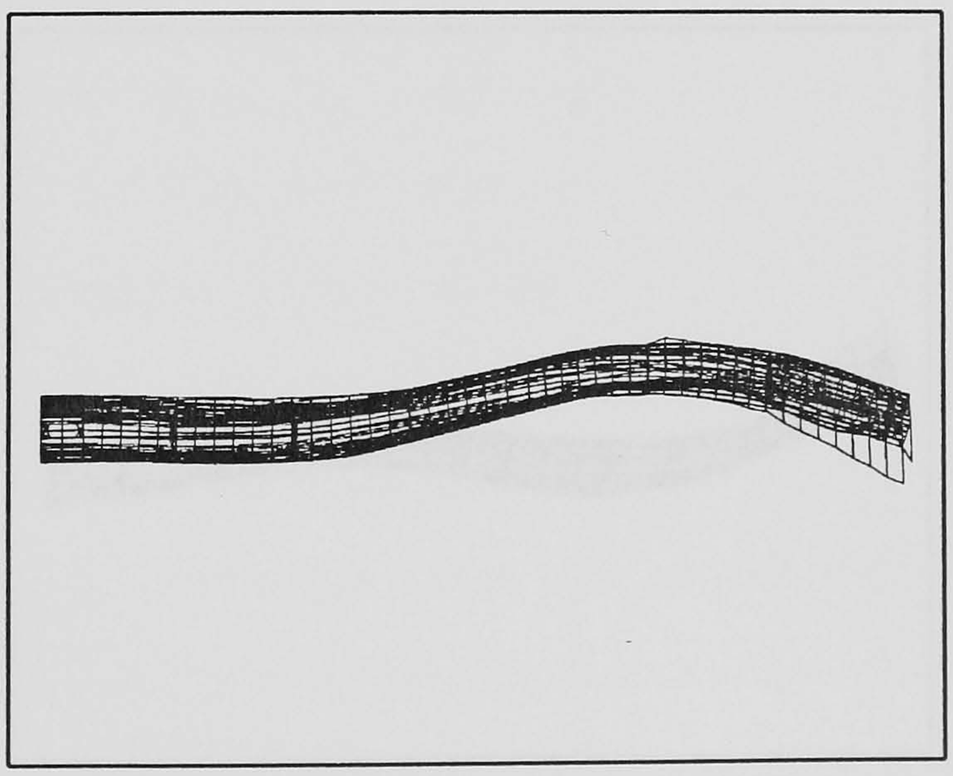

Fig. 9.17 3rd Bending-Torsion mode (157.2 Hz) for the A1 wing 1 composite model at θ=45 degree.

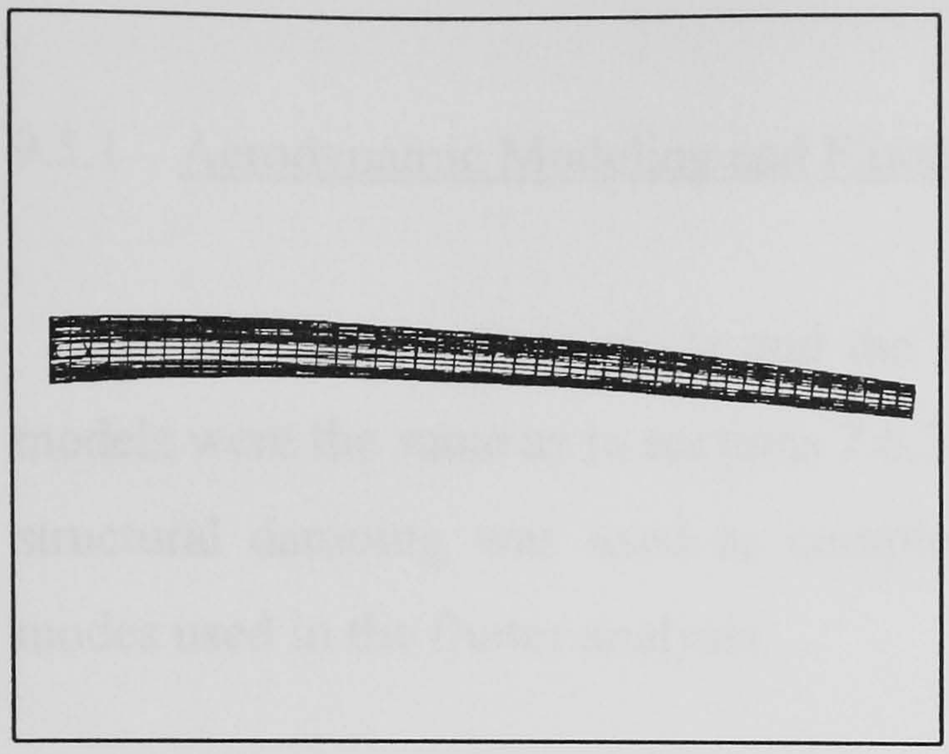

Fig. 9.18 1st Bending mode (23.39 Hz) for the A1 wing 1 composite model at θ=90 degree.

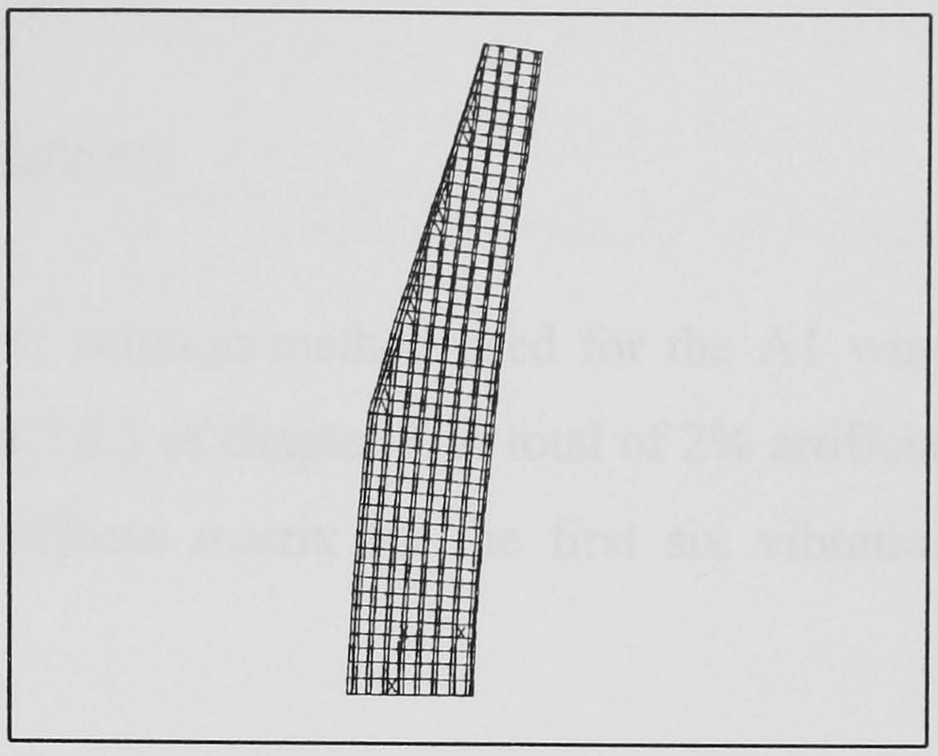

Fig. 9.19 1st Chord wise mode (56.19 Hz) for the A1 wing 1 composite model at θ=90 degree.

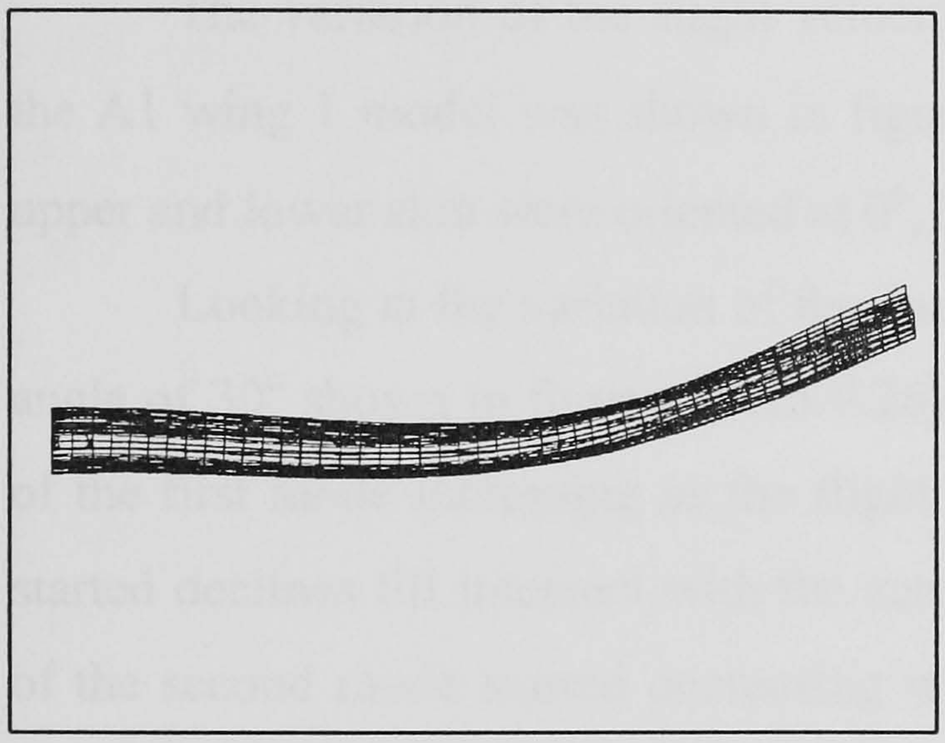

Fig. 9.20 2nd Bending mode (71.49 Hz) for the A1 wing 1 composite model at θ=90 degree.

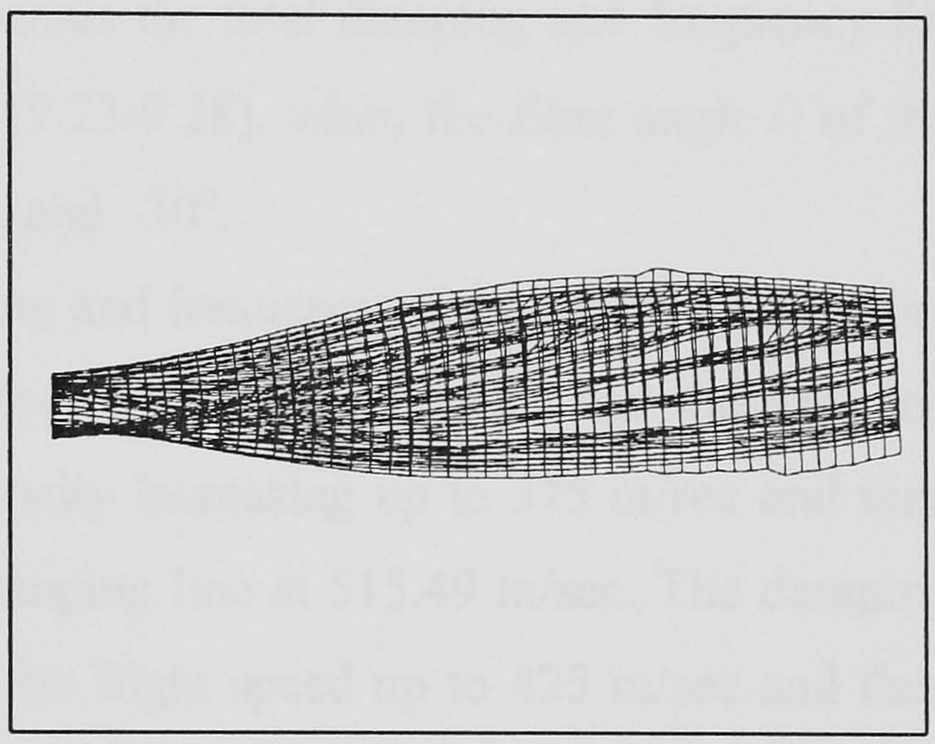

Fig. 9.21 1st Torsion mode (101.83 Hz) for the A1 wing 1 composite model at θ=90 degree.

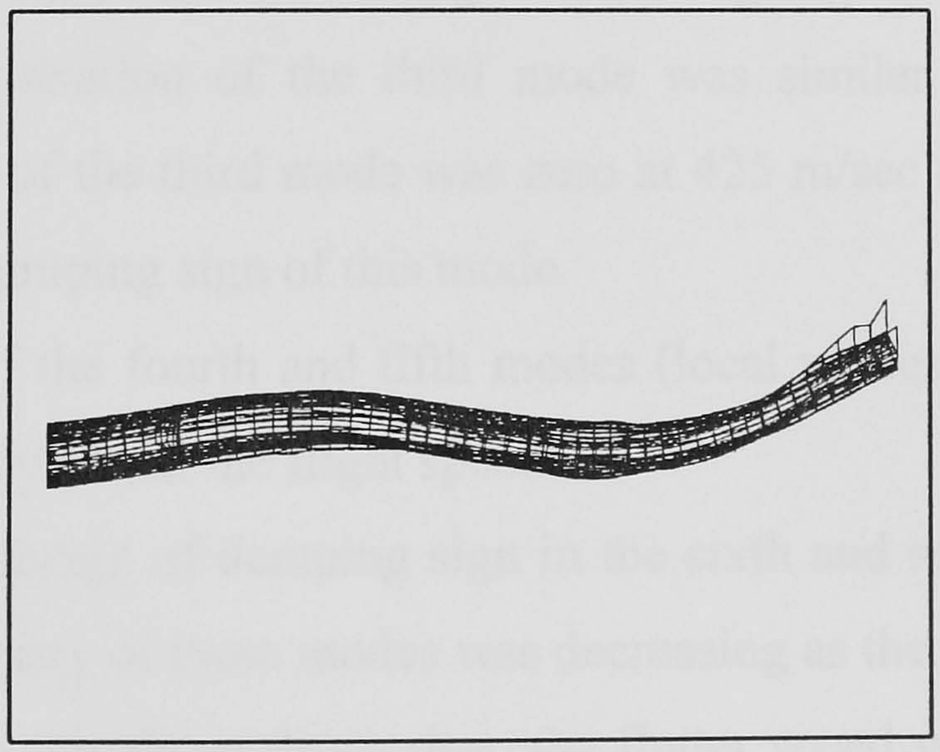

Fig. 9.22 3rd Bending mode (146.12 Hz) for the A1 wing 1 composite model at θ=90 degree.

9.5 Flutter analysis:

9.5.1 Aerodynamic Modeling and Flutter solutions:

The aerodynamic mode and the flutter solution method used for the A1 wing models were the same as in sections 7.6.2 and 7.6.3 of chapter 7. A total of 2% artificial structural damping was used as complex stiffness matrix for the first six vibration modes used in the flutter analysis.

9.5.2 Results and Discussion:

The variation of the flight velocity versus the total damping and frequency for the A1 wing 1 model was shown in figures (9.23-9.28), when the fibre angle θ of the upper and lower skin were oriented at 0^o, 30^o, and -30^o.

Looking at the variation of the damping and frequency of the A1 wing 1 at fibre angle of 30^o shown in figures (9.25-9.26) respectively. It can be seen that the damping of the first mode increasing as the flight velocity increasing up to 375 m/sec and then started declines till intersect with the zero damping line at 515.49 m/sec. The damping of the second mode started decreasing with the flight speed up to 425 m/sec and then increased with the flight speed as shown in figure (9.25). However, the frequency of this mode was almost constant up to 425 m/sec, drops at 450 m/sec due to the intersection with the first mode and then starts increasing with the flight speed.

The damping variation of the third mode was similar to the second mode, whereas the frequency of the third mode was zero at 425 m/sec and remains zero , but without changing the damping sign of this mode.

The damping of the fourth and fifth modes (local modes) was very small with the unchanged frequency for all the flight speed.

There was no change of damping sign in the sixth and seventh modes with the flight speed. The frequency of these modes was decreasing as the flight speed increases.

Therefore, from the above discussion, the flutter speed was at 515.49 m/sec of the first mode and this mode considered as flutter mode.

The flutter speed at the rest of fibre angles of all the A1 wing models were identified after close inspection of the variation of the damping with the flight speed for each point (mode), it was identified as the speed at which the total damping changes the sign. At this speed the total damping is zero [9.1] and [9.3]. Similarly, the flutter frequency is that of the critical mode at the flutter speed.

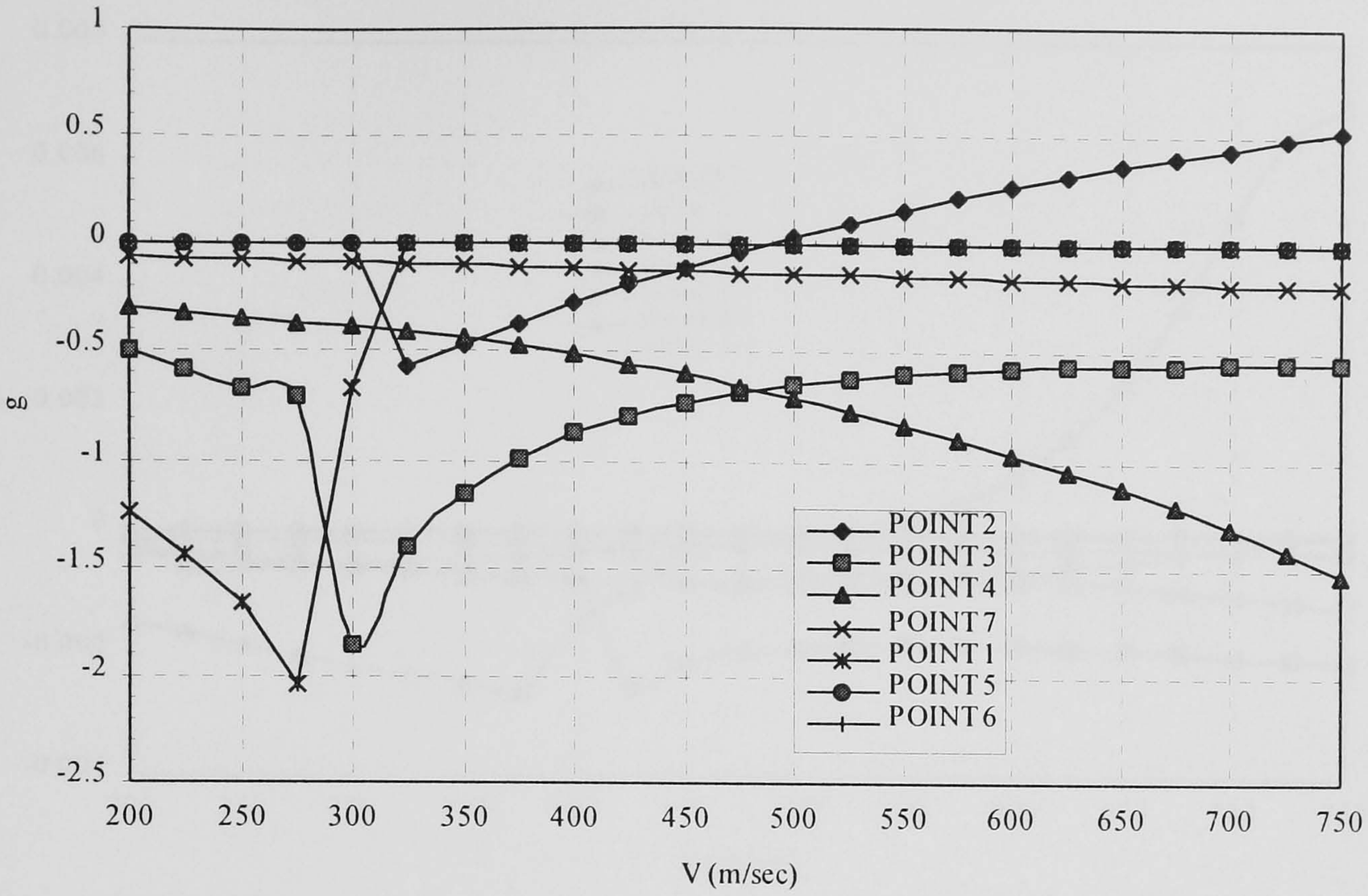

Fig. 9.23 Velocity vs Damping (g) of the A1 wing 1 composite model at $\theta = 0$ degree for the upper and lower skin.

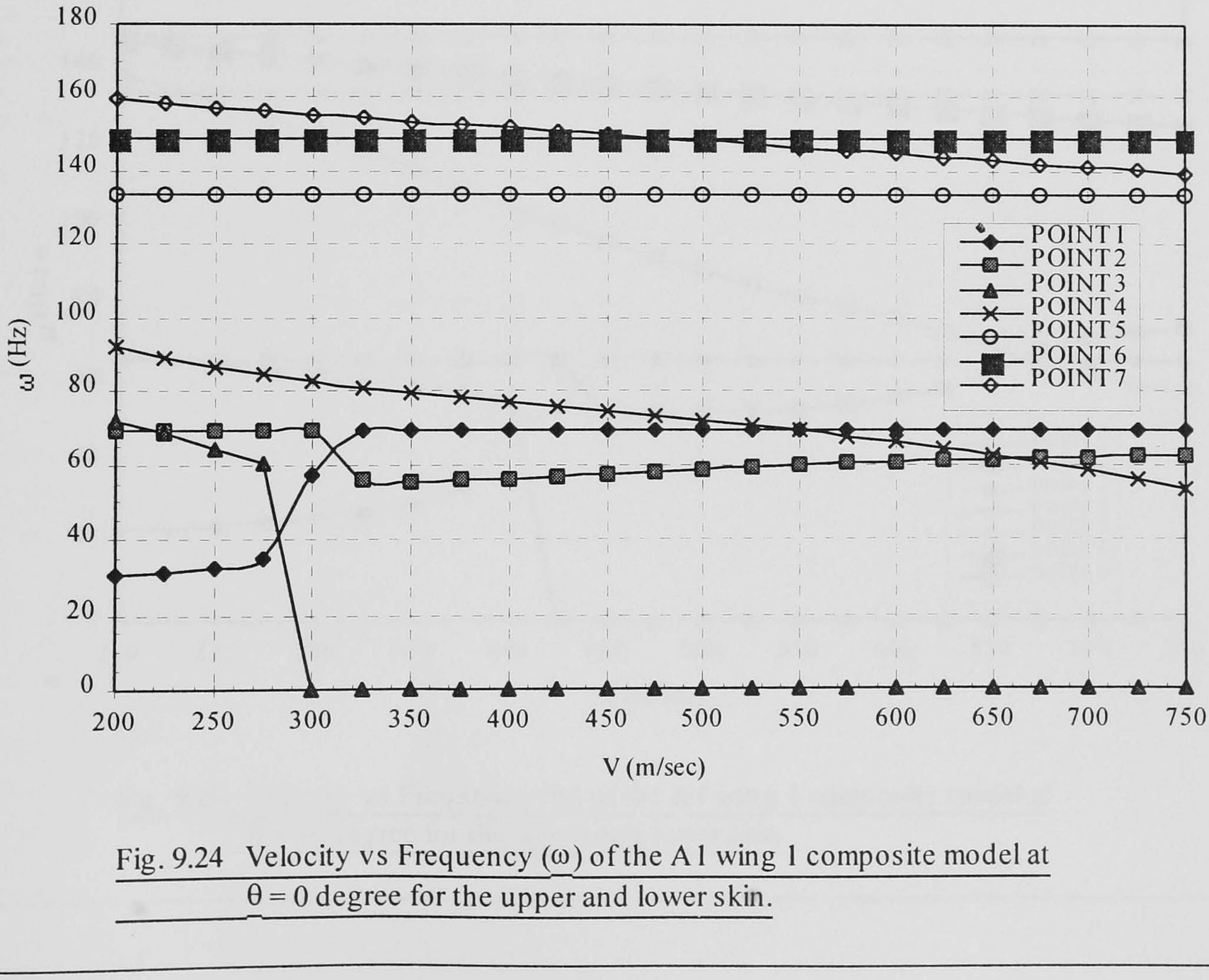

Fig. 9.24 Velocity vs Frequency (ω) of the A1 wing 1 composite model at $\theta = 0$ degree for the upper and lower skin.

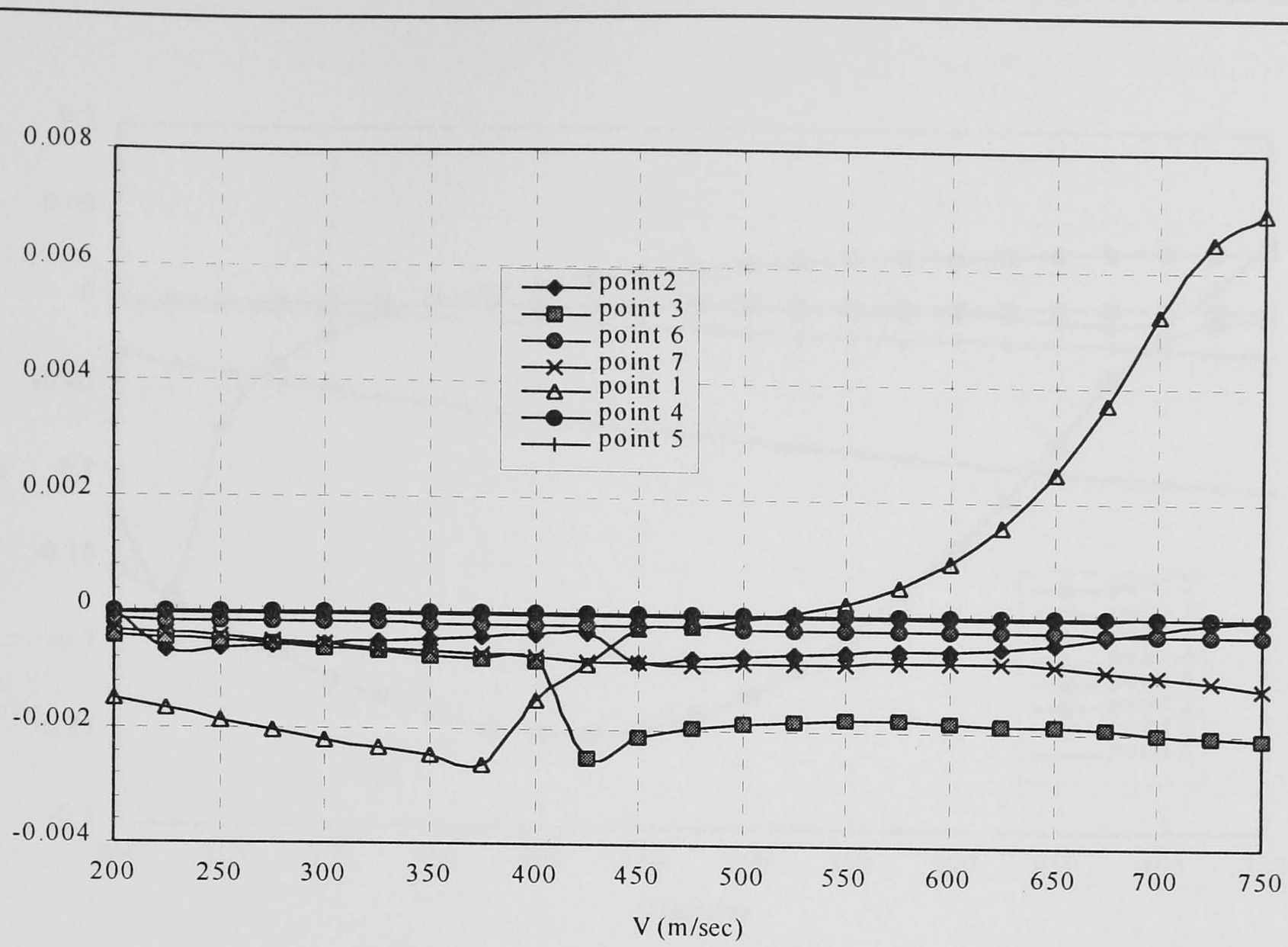

Fig. 9.25 Velocity vs Damping of the A1 wing 1 composite model at $\theta = 30$ degree for the upper and lower skin.

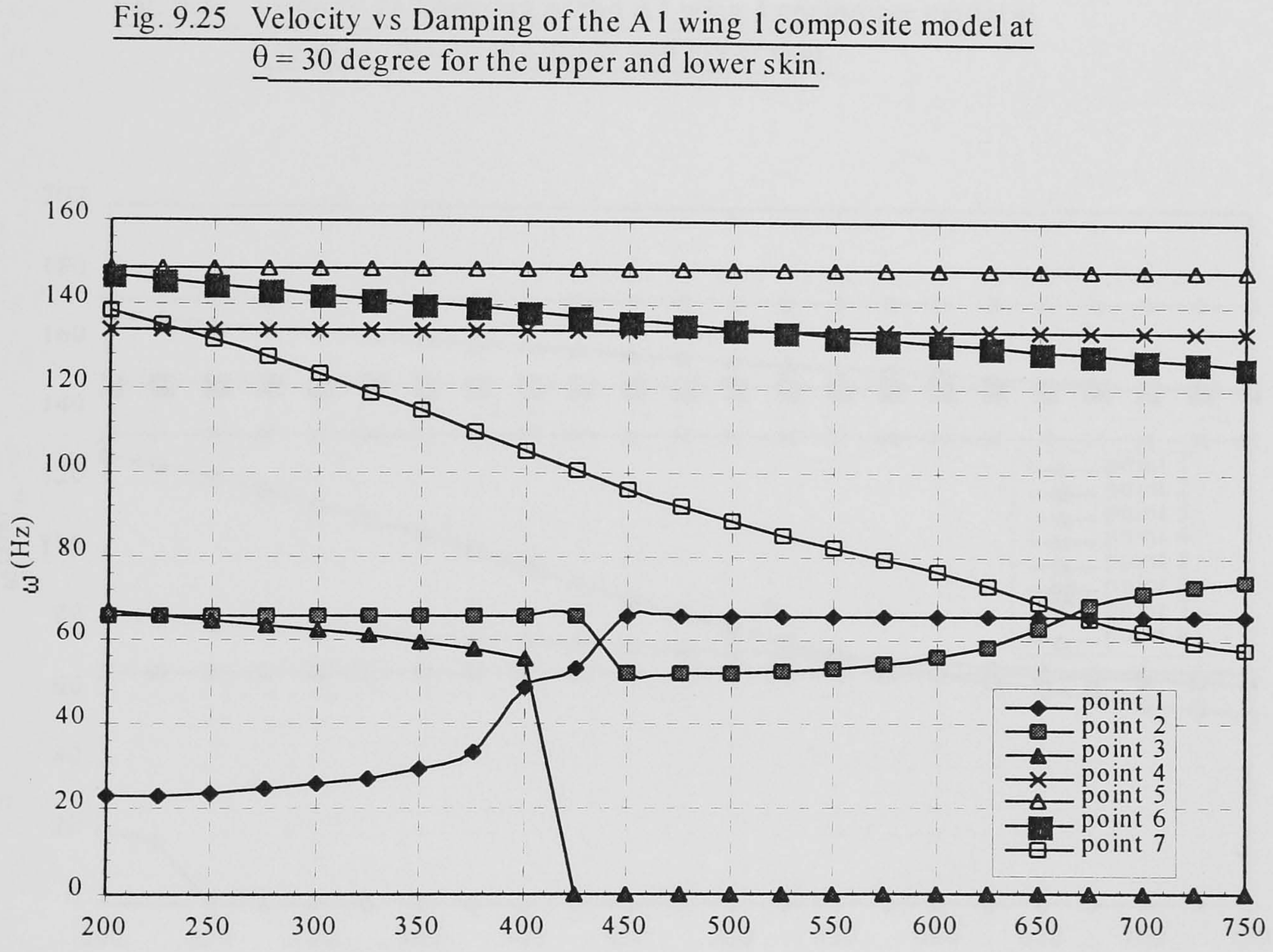

Fig. 9.26 Velocity vs Frequency (ω) of the A1 wing 1 composite model at $\theta = 30$ degree for the upper and lower skin.

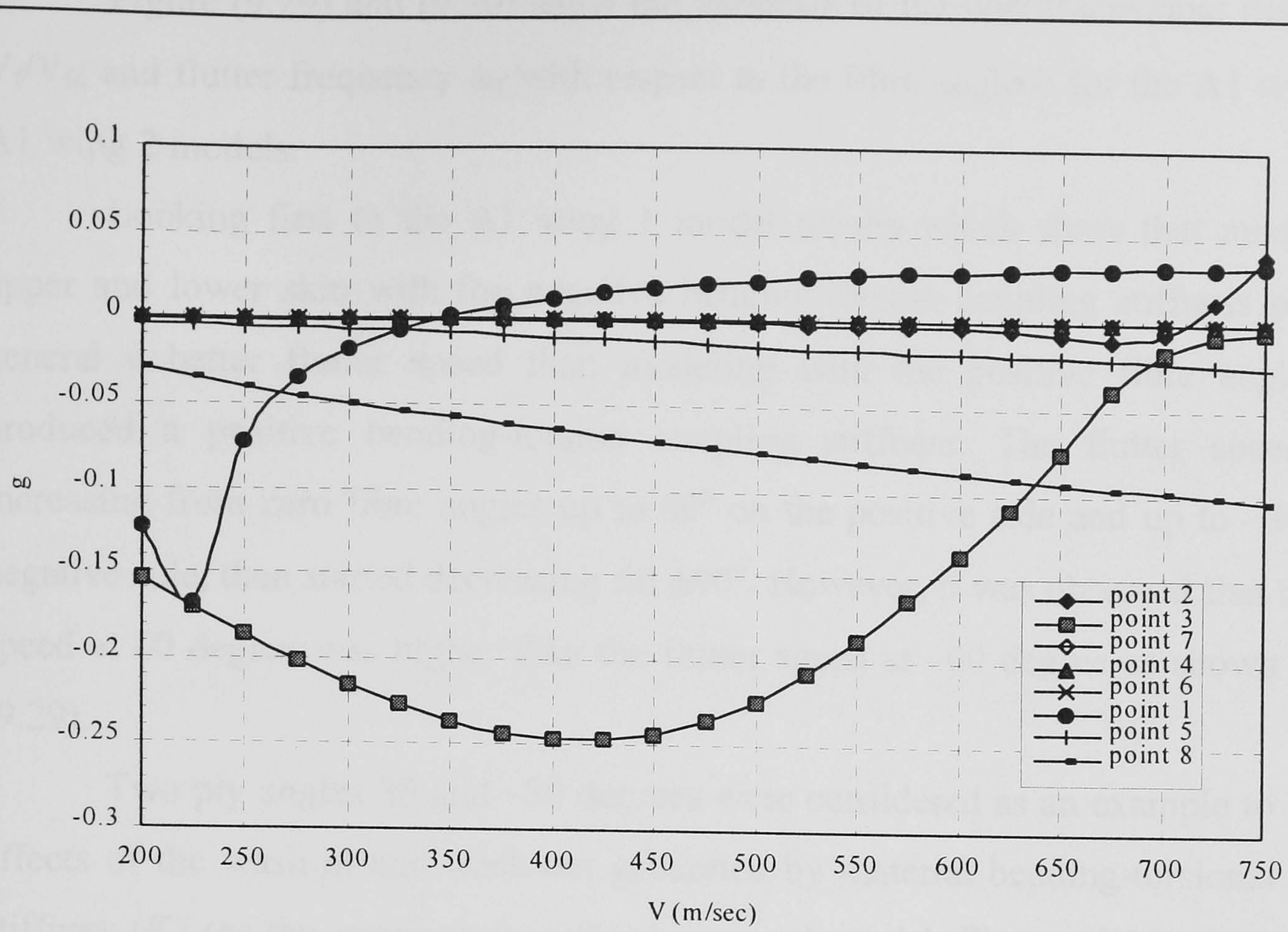

Fig. 9.27 Velocity vs Damping of the A1 wing 1 composite model at θ =-30 degree for the upper and lower skin.

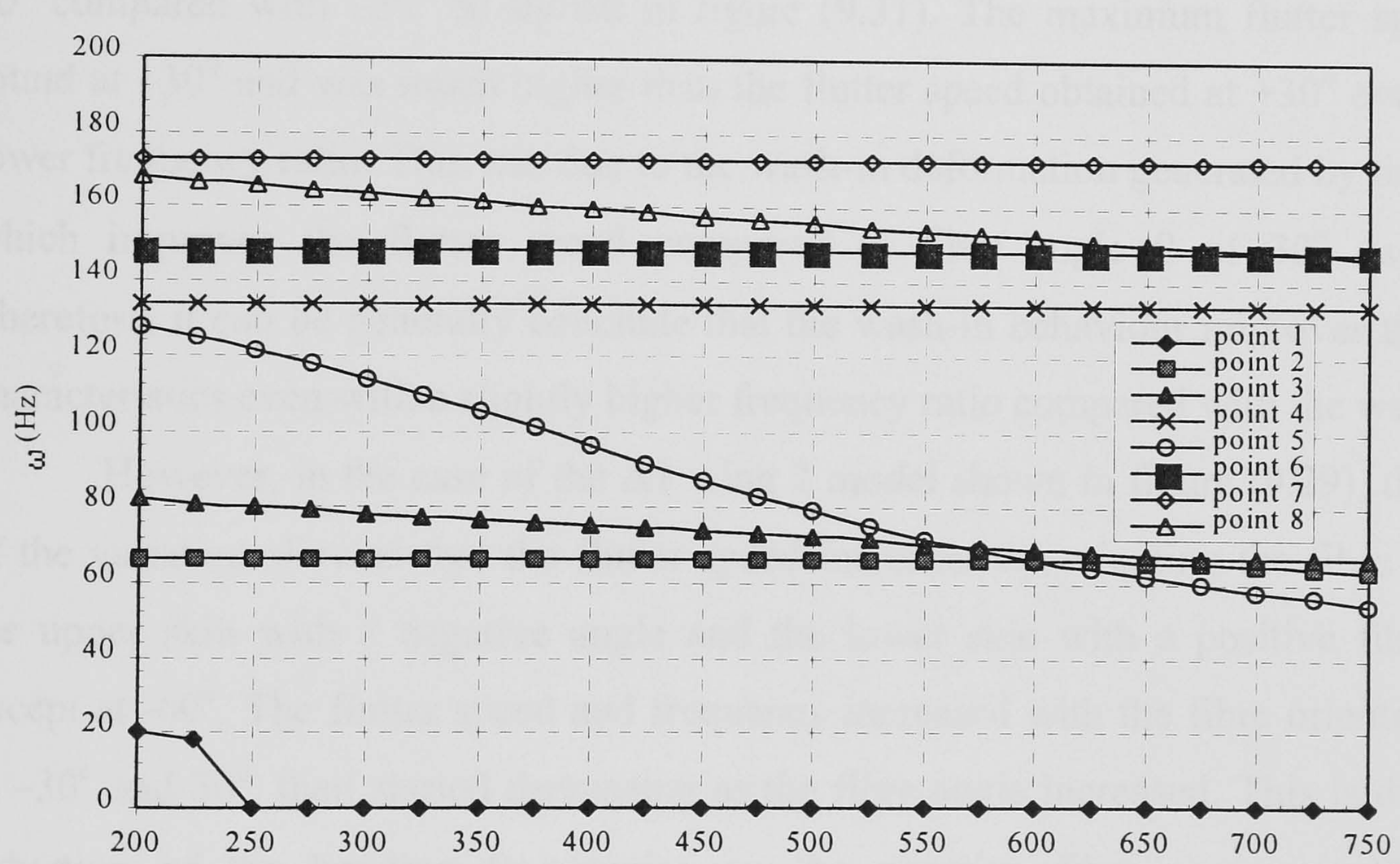

Fig. 9.28 Velocity vs Frequency of the A1 wing 1 composite model at θ =-30 degree for the upper and lower skin.

Figure (9.29) and (9.30) show the variation of the nondimensional flutter speed V_f/V_{fo} and flutter frequency ω_f with respect to the fibre angle θ for the A1 wing 1 and A1 wing 2 models.

Looking first to the A1 wing 1 model results which show that modeling the upper and lower skin with the negative bending-torsion coupling stiffness provide in general a better flutter speed than modeling with the positive fibre angle, which produced a positive bending-torsion coupling stiffness. The flutter speed started increasing from zero fibre angles up to 60^o on the positive side and up to -30^o on the negative side, then started decreasing till $\pm 90^o$. However, it was observed that the flutter speed at 60 degree was higher than the flutter speed at –60 degree as shown in figure (9.29).

Two ply angles 30 and –30 degrees were considered as an example to show the effects of the wash-in and wash-out generated by material bending-torsional coupling stiffness (K) (as the maximum) in the A1 wing 1 model. Figure (9.31) shows that the variation of the frequency ratio as a function of the fibre angle of the upper and lower skin of the A1 wing 1 model. The lower frequency ratio ω_b/ω_t was found at ply angle of 30^o compared with -30^o as shown in figure (9.31). The maximum flutter speed was found at -30^o and was much higher than the flutter speed obtained at $+30^o$ even with a lower frequency ratio. This was due to the wash-in deformation generated by the model, which improves the flutter speed compared to fibre angle θ of 30^o (wash-out). Therefore, it can be generally conclude that the wash-in behaviour improves the flutter characteristics even with a slightly higher frequency ratio compared with the wash-out.

However, in the case of the A1 wing 2 model shown in figure (9.29), the trends of the variation showed that the flutter speed increased by orienting the fibre angle of the upper skin with a negative angle and the lower skin with a positive fibre angle except at -60^o. The flutter speed and frequency increased with the fibre orientations up to -30^o and 30^o, then started decreasing as the fibre angle increased. This is due to the reduction of the bending frequencies on the negative fibre angles at $0^o<\theta<-90^o$ compared with the positive fibre angles (see figure 9.1) and to the small reduction of the torsional frequencies at $0^o<\theta<-45^o$ compared with positive fibre angle. The variation of the frequency ratio was presented in figure (9.32), which showed that the lower frequency ratio was at -45^o.

Considering two ply angles 30^o and -30^o as an example to show the effect of the wash-in and wash-out generated by the material bending-torsion coupling stiffness (K) on the flutter speed which did not exist in the case of wing 6 model of chapter 8. The maximum flutter speed was found at $\theta = -30^o$ due to the higher coupling stiffness in the model, which produced a wash-in deformation compared with 30^o even though the lower frequency ratio $\omega_b/\omega t$ was found at ply angle of -45^o compared with -30^o (see figure 9.32). This shows the importance of including a higher negative bending-torsional coupling stiffness in this model.

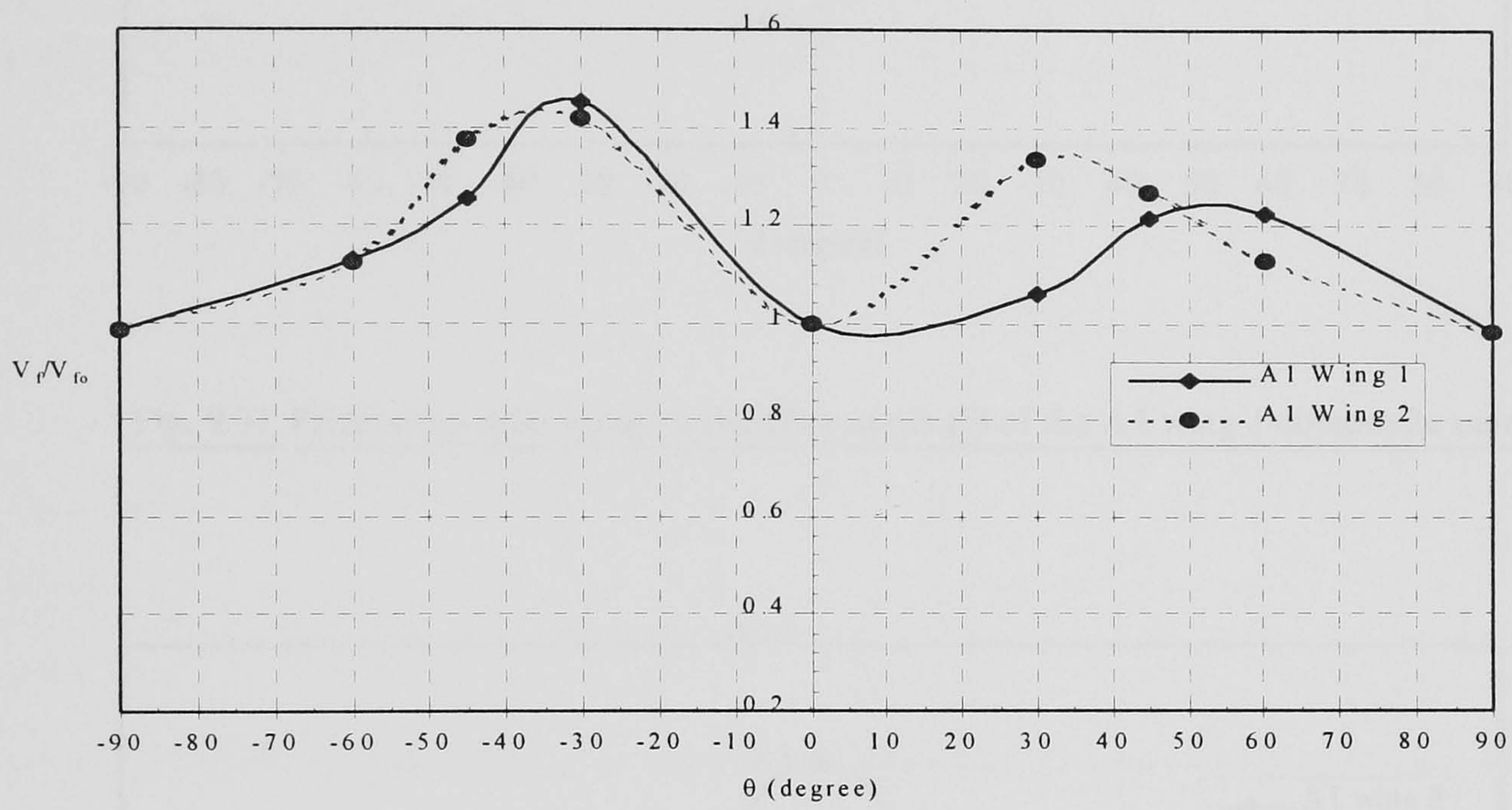

Fig. 9.29 Nondimensional flutter speed for the A1 wing 1 and A1 wing 2 composite models as a function of the ply angle θ

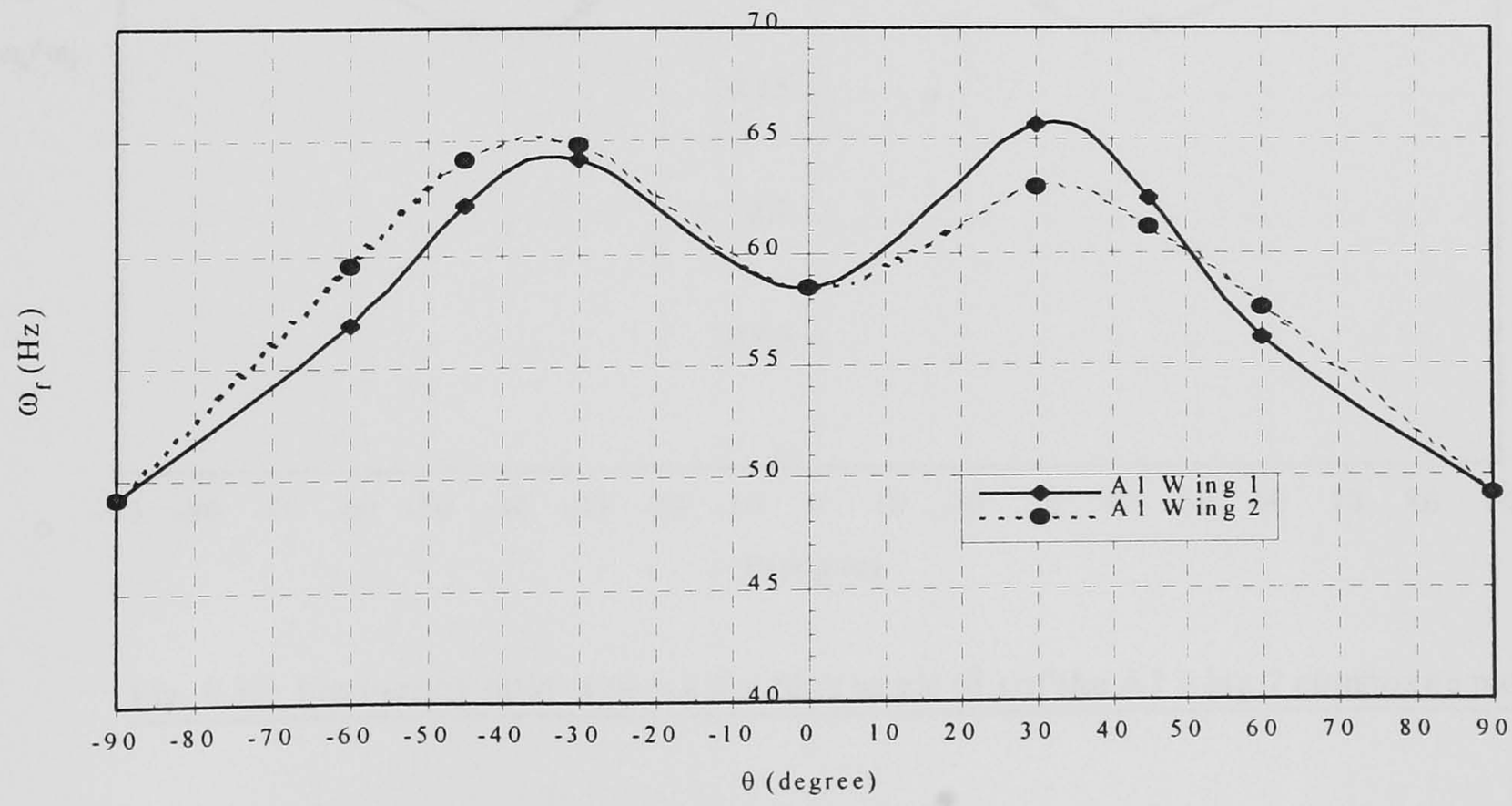

Fig. 9.30 Variation of the flutter frequency with the fiber angle (θ) of the A1 wing 1 and A1 wing 2 composite models.

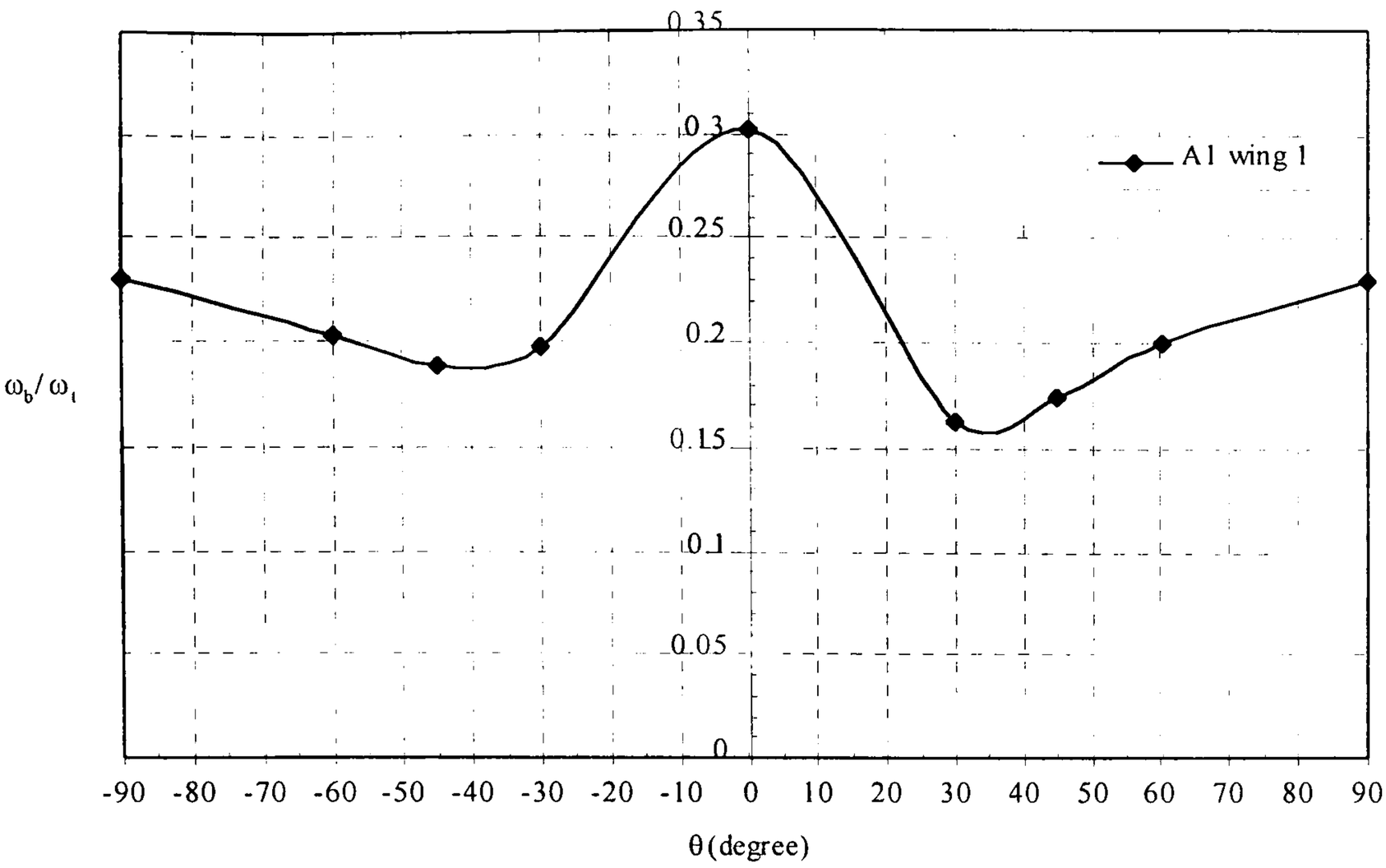

Fig. 9.31 Frequency ratio ω_b/ω_t vs the fibre angle (θ) of the A1 wing 1 composite model.

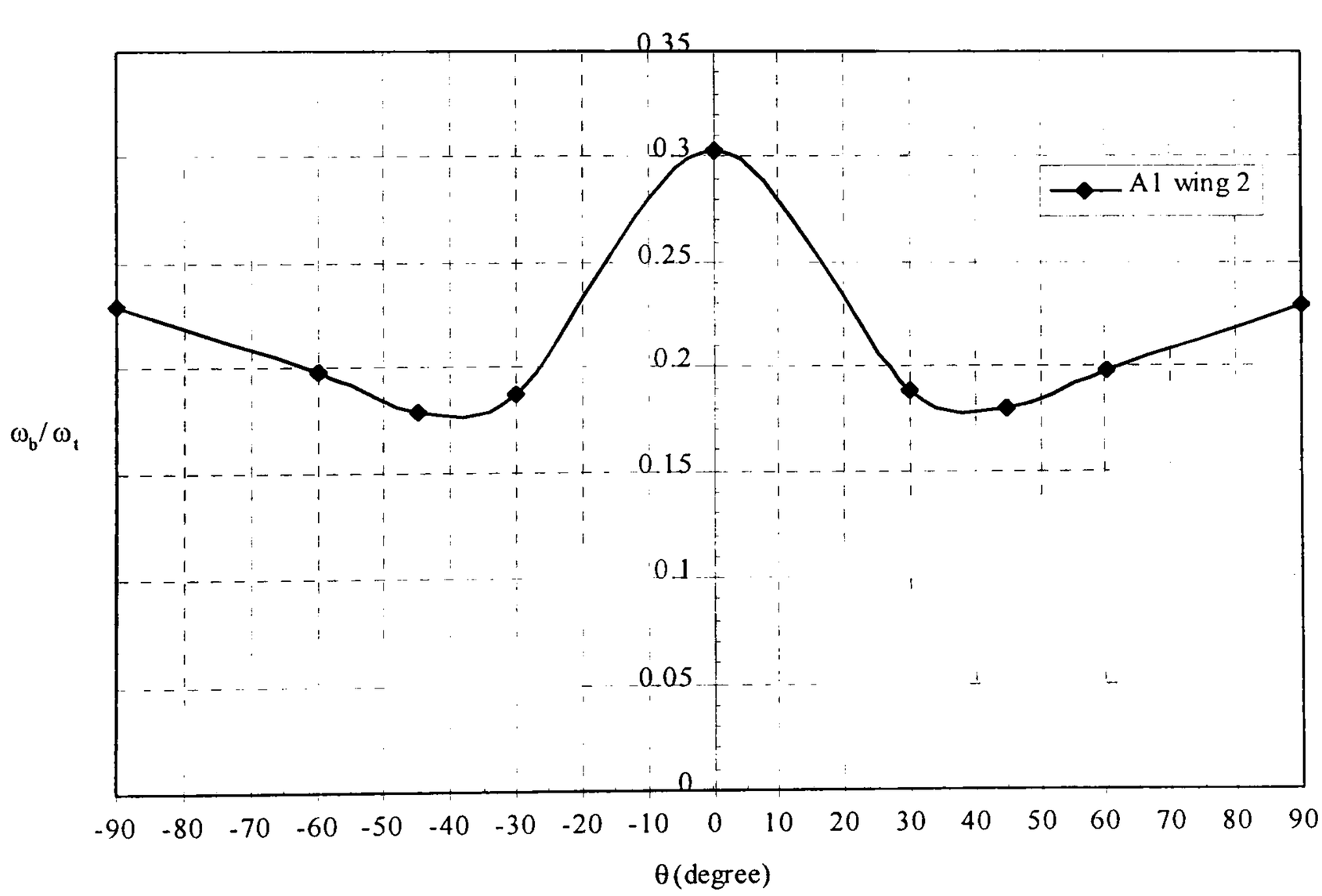

Fig. 9.32 Frequency ratio ω_b/ω_t vs the fibre angle (θ) of the A1 wing 2 composite model.

Comparing the results of the A1 wing 1 and A1 wing 2 models (see figure 9.29), the following conclusions can be drawn:

- Modeling the structure with small material coupling (K) provides a higher flutter speed than modeling it with a higher positive coupling stiffness as observed at 30^{o} and 45^{o}.
- The combination of lower frequency ratio $\omega_b/\omega t$, lower material coupling stiffness (K) and geometrical structural coupling are very important as at -45^{o} of A1 wing 2 model compared with the A1 wing 1 model.
- Negative material coupling (K) generally increase the flutter speed of the A1 wing1 (CAS) and A1 wing 2 (CUS) compared with the Positive material coupling (K). However, the results of figure (9.29) showed that positive material coupling (K) with a higher frequency ratio and structural geometrical coupling provides a higher flutter speed at 60^{o}fibre angle compared with -60^{o} fibre angle in the case of A1 wing 1 model (CAS). This means that the combinations of the positive material coupling (wash-out) with a higher frequency ratio and structural geometrical coupling could be used to increase the flutter speed as at 60^{o}, which was not observed in the open literature. Thus, the common philosophy [9.2, 9.4, 9.7, 9.8 and 9.9] that the wash-in deformation is always improves the flutter speed, whereas wash-out deformation is decreasing the flutter speed, is not always true.

The results presented in figures (9.33-9.36) of the A1 wing 3 and A1 wing 4 models shows a similar behaviour to that of A1 wing 1 and A1 wing 2 models and hence a similar remarks were valid.

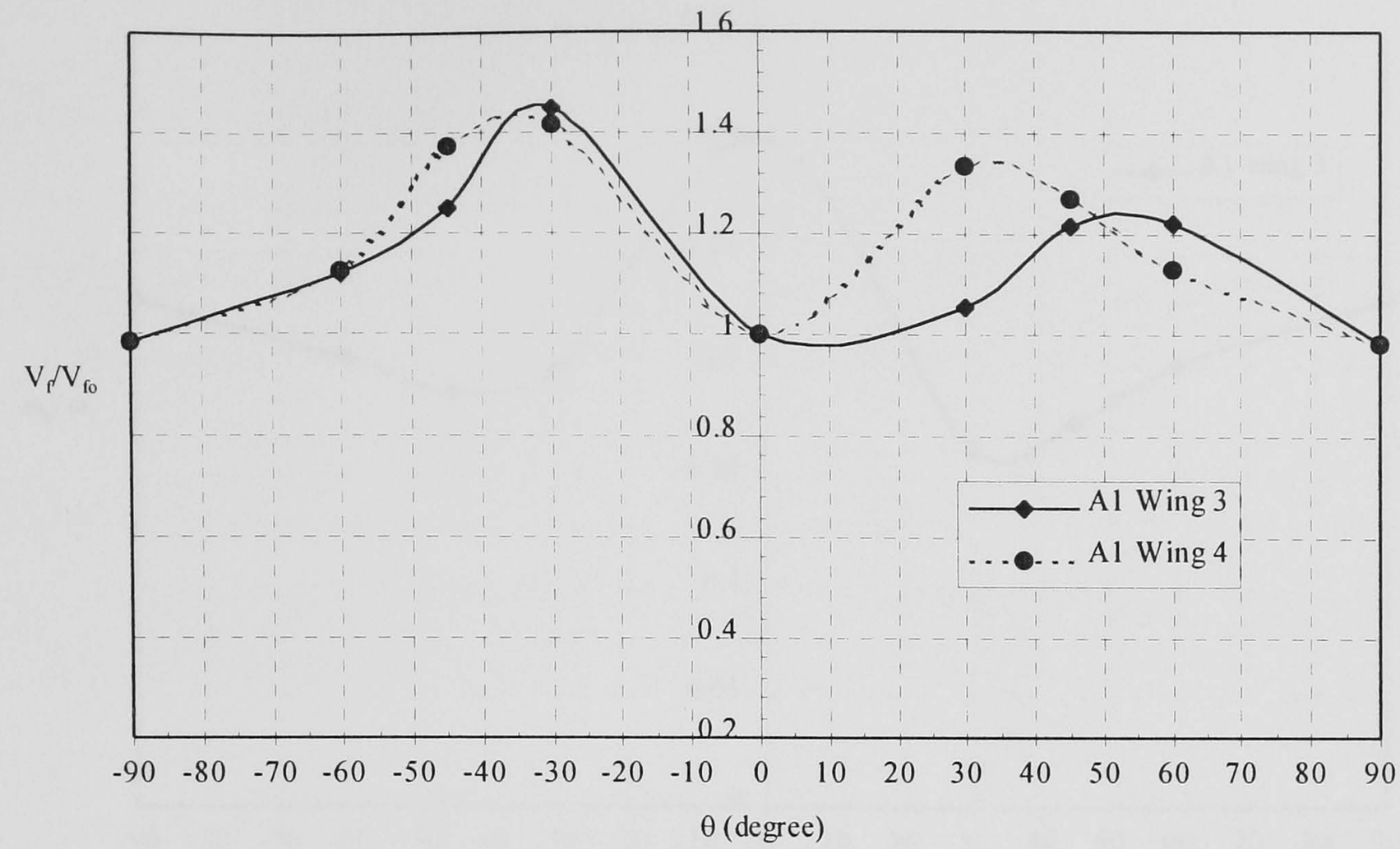

Fig. 9.33 Nondimensional flutter speed for the A1 wing 3 and A1 wing 4 composite models as a function of the ply angle (θ).

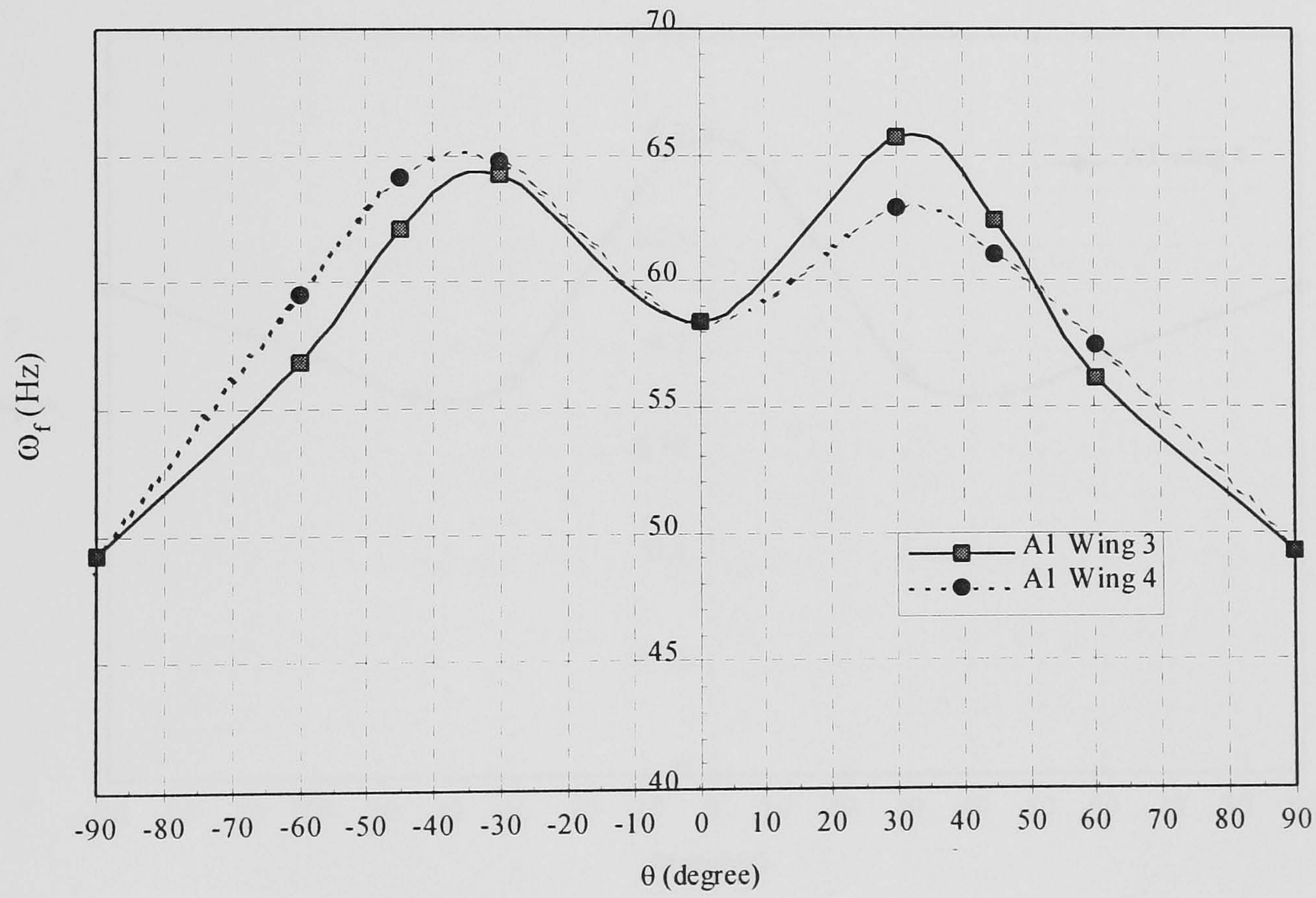

Fig. 9.34 Variation of the flutter frequency of the A1 wing 3 and A1 wing 4 composite models against ply angle (θ).

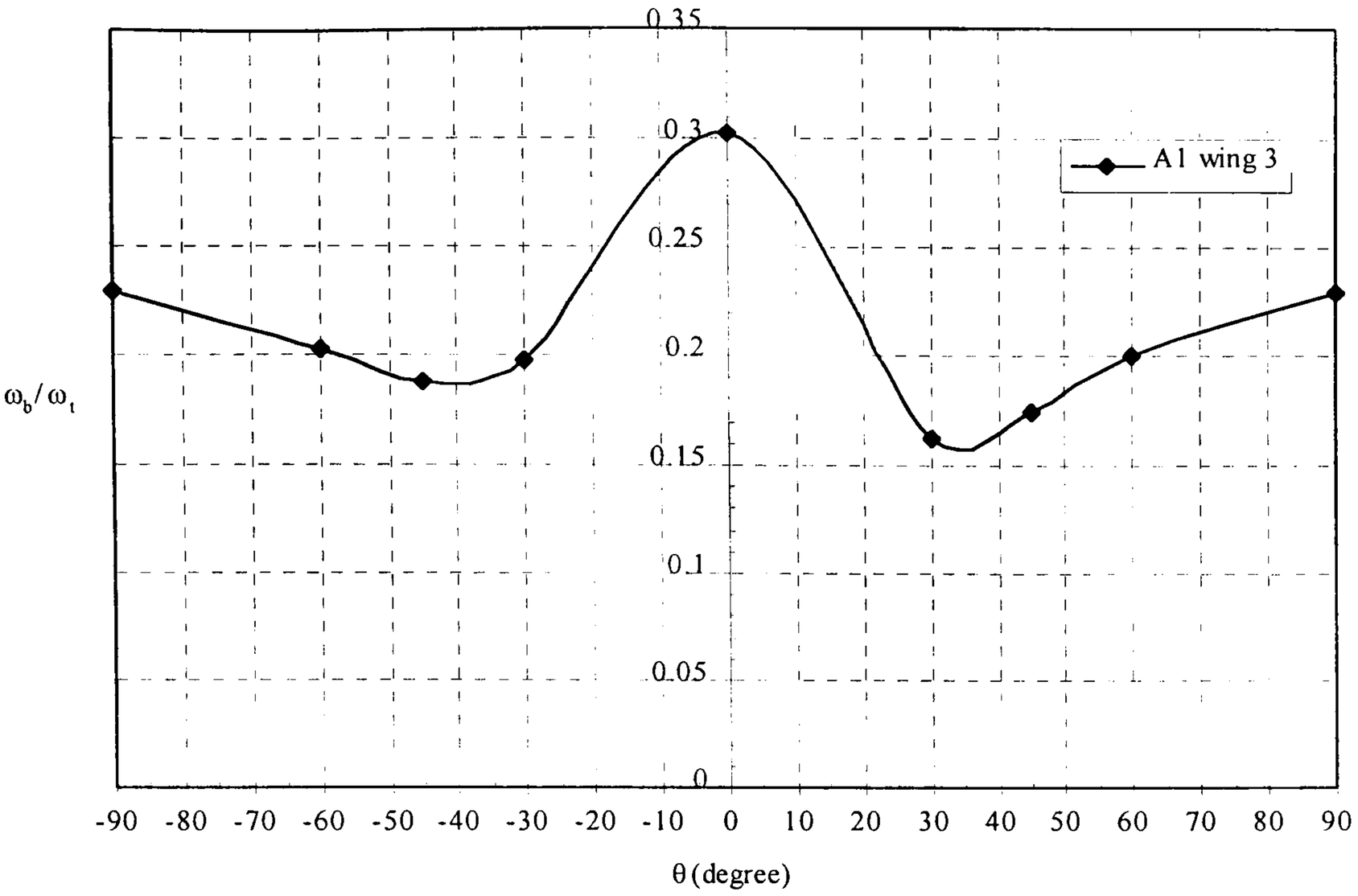

Fig. 9.35 Frequency ratio ω_b/ω_t vs the fibre angle (θ) of the A1 wing 3 composite model.

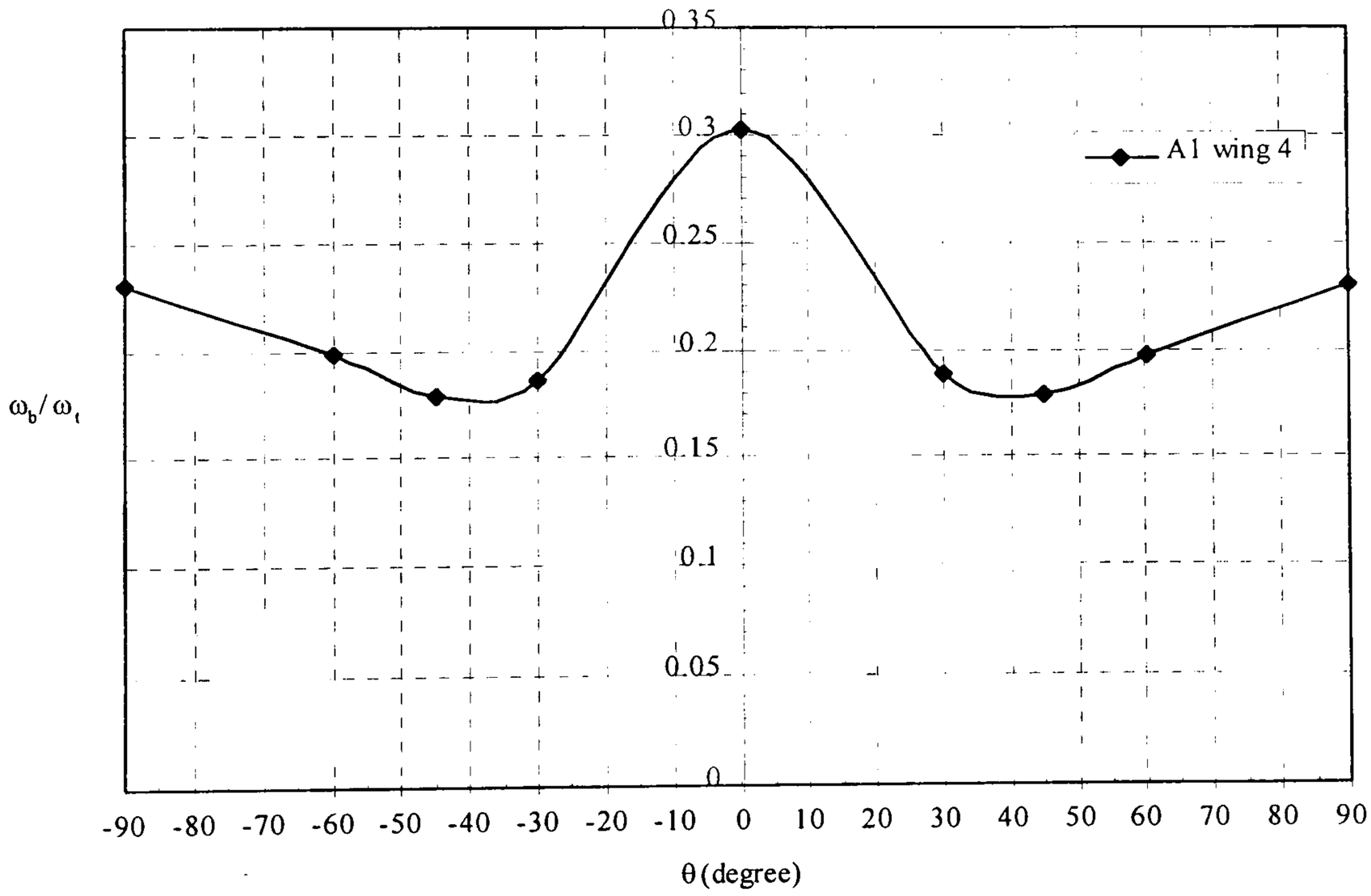

Fig. 9.36 Frequency ratio ω_b/ω_t vs the fibre angle (θ) of the A1 wing 4 composite model.

9.6 Effect of Structural Damping (g):

Damping in flutter calculations is developed from two main sources. The two main sources of damping are:

- Aerodynamic damping caused by the flapping of the structure through the air.
- Structural damping arising from hysteresis in the material and from frictions at joints and connections between the different aircraft components.

While natural damping inherent in material is relatively small, the energy dissipation in a structure due to the joint interface slips can give rise to relatively significant damping. Analyzing the damping of a structural assembly is not an easy task. It is important to consider not only the material composing of the structure but also the way the structure is constructed. Riveted and bolted structures possess more damping than one using largely integrally machined components. Moreover, with increasing age, the loosening of bolts and joints may well change the damping propriety of the structure.

Because of these difficulties, structural damping values are often based on the results of a dynamic test. Most structures have a typical range of critical damping [g/2] values of 1 to 5% [9.10], where (g) is the structural damping coefficient.

In this section, the effect of the structural damping on the flutter speed was studied on the A1 wing 1 configuration shown in table (9.2) with the fibre orientation θ of 45^{o}. The structural damping (g) was used as complex stiffness through the use of three PARAM, KDAMP, TABDMP1 cards in the bulk data entry with specifying the SDAMPING in the case control section [9.3].

The damping values are linear between the frequency and damping pairs and are extrapolated outside the tabulated frequency range. The analysis was done for different values of structural damping, at 10000 ft (3.048 km) and 55000 ft (16.765 km) at Mach number of 0.4. The range of structural damping was varied from 0 to 0.6 in steps of 0.005.

It was found from the output of the analyzed cases that there is no change in the flutter speed with the structural damping for the clean real composite wing box (A1 wing1 configuration) at $\theta = 45$ degree. From the analysis it can be concluded that the structural damping can be neglected in the analysis for structures like the A1 wing1

configuration (clean structure with out fuel tanks and engines as an example) as mentioned in [9.3] and [9.11].

References

9.1 Loring, J.S., General approach to the flutter problem. AIAA selected reprint series, Aerodynamic flutter, Volume V, March 1969.

9.2 In Lee, Seung-Ho Kim and Hirokazu, M. Static aeroelastic characteristics of a composite wing. Journal of Aircraft, Jan. 1994, Vol. 31, No. 6, pp 1413-1416, Engineering notes.

9.3 Rodden, P.W. and Johnson, H.E. Aeroleastic analysis hand books for MSC/NASTRAN, Version 69, October 1994, The Macneal-Schwendler Corporation.

9.4 Hollowell, J.S. and Dugundji, J. Aeroelastic flutter and divergence of stiffness coupled graphite/epoxy cantilevered plates. Journal of Aircraft, Jan. 1984, Vol. 21, No. 1, pp 69-76.

9.5 Brooks, W. G. Design, construction and test of a post buckling carbon fibre reinforced plastic wing box. PhD Thesis, 1984/1987, Cranfield University.

9.6 Weisshaar, T. A. and Foist, L. B. Vibration tailoring of advanced lifting surfaces. Journal of Aircraft, Feb. 1985, Vol. 22, No. 2, pp 141-147.

9.7 Georghiades, G. A., Guo, J.S. and Banerjee, R. J. Flutter analysis of composite wings using an exact dynamic stiffness matrix method. AIAA-95-1488-cp, pp 3019-3027.

9.8 Weisshaar, T. A. and Foist, L. B. Vibration and Flutter of advanced lifting surfaces. A83-29861or A83-0961, pp 498-508.

9.9 Georghiades, G. A., Guo, J.S. and Banerjee, R. J. Parametric investigation into the flutter characteristics of composite wings. AIAA-96-1351-cp, pp 300-310.

9.10 Rodden, P.W. and Johnson, H.E. Dynamic analysis hand book for MSC/NASTRAN,Version 69, October 1994, The Macneal-Schwendler Corporation.

9.11 .Broadbent, E.G. and Williams, M. The effect of structural damping on binary flutter. Aeronautical Research Council, R.&M. No. 3169, 1960.

CHAPTER 10

CONCLUSIONS AND RECOMMENDATION FOR FUTURE WORK

10 Conclusions and Recommendation for future work

10.1 Conclusions:

The literature review has shown that, most of the previous research activity on composite wing structures for performing dynamic aeroelastic analysis (flutter) was carried out on a less practical wing structure. These were usually modeled as beam (flat plate) or a closed thin-walled structure with the symmetrical section and un-practical laminate and with uniform stiffness along its length. However, it is clear from these studies that the unique features of laminated composite materials make them prime candidates for aeroelastic tailoring applications by fibre orientations. However, despite the extensive but basic research that has been carried out, the effect of fibre orientations (with subsequent effect on bending-torsional coupling stiffness, wash-in and wash-out) and structural damping on the flutter speed were investigated for box beams with the inclusion of additional structural components. Specifically, a practical composite wing box structure such as the Cranfield A1 aerobatic aircraft is subject of investigation. This is the intent of this research investigation, which has not well documented, in the open literature.

The wing models, which were analysed in this work, are presented as follows:

- Metal and composite wing box of the Cranfield A1 aerobatic aircraft with the original material properties.
- Ten analytical wing models were created from four thin-walled structures as shown in chapter 1 and in table (8.6), which were simulated Circumferentially Asymmetric Stiffness (CAS) and Circumferentially Uniform Stiffness (CUS).
- Another four analytical wing models were created from the Cranfield A1 composite wing box (simplified material properties) simulating both CAS and CUS configurations as presented in table (9.2-9.5)

The objectives of the research were outlined in chapter 1, which have been fulfilled.

All the wing models have been analyzed using MSC/NASTRAN and the primary research outcome of each section is summarized in the following three sections:

1. Experimental free vibration and flutter analysis of the real Cranfield A1 metal and composite wing box (with original properties):

In this section, both analytical and experimental vibration and flutter analysis were carried out on the composite wing box, while only analytical analysis was carried out on the metal wing box. The following points were concluded during the analysis:

- Natural frequencies, mode shapes, and flutter speed of the analytical lumped beam model of the metal wing box were very close to the detailed metal model. Hence the simplified model was considered to be very useful to the structural designer at the early stage of the design.
- The structural behaviour (mode shapes) of the metal wing box are similar compared to the composite wing box, except in the sequence of the third mode. In the metal wing model the third and fourth modes were the first torsion and third bending mode respectively, whereas in the composite wing model the third and fourth modes were third bending mode and coupled mode respectively.
- Close proximity of results are obtained between the mode shapes from experimental and analytical investigations of the composite wing box, despite large frequency variation, which was then investigated by conducting a static test. It was found from the static test that several factors caused variations. In brief these differences may be attributed to the age of the wing box, previous history of post buckling, the deterioration of structural integrity with the age, effect of delamination of the composite plies, modeling differences between the actual structure and the analytical model and a combination of some or all of the above.
- The flutter speed of the metal wing box was slightly higher than the composite wing box by about 10%, but the composite wing box was lighter than the metal wing box by 25% (with some differences in structural dimensions, see figures 5.6 and 6.2).

2. Analytical free vibration and flutter analysis of thin-walled structures:

Ten analytical wing models were analyzed simulating CAS and CUS configurations as presented in table (8.6). The following comments conclude the investigations:

- The effect of including bending-torsional coupling stiffness as in the case of CAS wing models was that the torsional frequency becomes higher as compared to the CUS wing models, when the bending-torsional was not included.
- The effect of bending-torsional coupling on the bending frequency was almost negligible. However, the effect of material coupling on the mode shapes were pronounced in the case of CAS wing models especially at the area of higher coupling stiffness.
- The inclusion of bending-torsional coupling may be used to prevent modal interchange as at $\pm 20^{o}$ fibre angle in this case.
- Incorporation of three ribs to the first thin-walled structure, as in wing 3 and wing 8 models increases the torsional frequency with slight reduction in the bending frequency compared with wing 1 and wing 6 models respectively, even though it has slightly greater mass.
- By adding a hat section stringer at the middle of the skins to the first thin-walled structure (wing 4 and wing 9 models), the bending frequency decreases more than the torsional frequency compared with wing 1 and wing 6 models respectively.
- The provision of structural geometric coupling as in wing 5 and wing 10 models led to a higher reduction in the torsional frequency than the bending frequency, compared with the wing 4 and wing 9 models respectively.
- The negative bend-twist coupling stiffness (wash-in) generally increases the flutter speed compared with the positive bend-twist coupling stiffness. However, the results in these wing models (CAS) showed that the flutter speed at $45^{o} \leq \theta \leq 90^{o}$ and $-45^{o} \leq \theta \leq -90^{o}$ were almost the same.
- The maximum flutter speed of the wing models (CAS) was found at a lower stiffness ratio or lower frequency ratio and relatively higher negative bend-twist coupling (wash-in) compared to the slightly higher stiffness or frequency ratios and a maximum bend-twist coupling as in the case of wing 1 model.
- In the case of CUS wing models, the flutter speed increases with lower stiffness or frequency ratios, as in the case of wing 6 model.
- The flutter speed increases in the CUS wing models as compared to the CAS wing models which have higher positive bend-twist coupling at $0^{o} < \theta \leq 30^{o}$.

- The flutter speed increases with the flutter frequency for all the wing models with the exception of a sudden drop of flutter frequency in the area, where a higher wash-out deformation occurred for all the wing models (CAS) at $0^o<\theta\leq30^o$.
- The flutter speed of wing 3 (CAS) and wing 8 (CUS) models (with ribs) were higher compared to the rest of the corresponding wing models.
- The flutter speed in the case of CUS wing models was almost symmetric about the 0^o fibre angle.
- The flutter speed obtained without structural geometric coupling as in wing 4 and wing 9 models was higher than wing 5 and wing 10 models respectively with structural geometric coupling.
- The flutter speed obtained from wing 9 model was higher than wing 5 model at $0^o\leq\theta\leq90^o$ and $-40^o\leq\theta\leq-90^o$.

3. <u>Analytical free vibration and flutter analysis of the Cranfield A1 composite wing box (with the simplified materials and laminate lay ups):</u>

Some simplifications were carried out on the original material properties and laminate lay ups of the upper and lower skin. Four analytical A1 wing models were created to simulate CAS and CUS configurations as presented in table (9.2-9.5). Some useful comments were concluded during the investigations, which are listed as follows:

- Small amount of bend-twist coupling stiffness exists in the CUS A1 wing models compared with the CAS A1 wing models due to the asymmetry of the airfoil section.
- The variation of the natural frequencies in the CUS A1 wing models were almost symmetric about 0^o fibre angle compared to the CAS A1 wing models.
- The effect of including higher bending-torsional coupling ($0^o<\theta\leq\pm45^o$) in the CAS A1 wing models was pronounced on the torsional, bending frequencies and mode shapes compared with the CUS A1 wing models.
- Combinations of lower frequency ratio, lower bending-torsional coupling stiffness and structural geometric coupling as in CUS A1 wing models led to a higher flutter speed compared with the CAS A1 wing models at -45^o fibre angle.

- The flutter speed of CUS A1 wing models was higher than of the CAS A1 wing models at 30^{o} and 45^{o} fibre angle.
- Negative material coupling stiffness of the A1 wing models generally increases the flutter speed compared with the positive material coupling stiffness.
- The results also showed for the A1 wing models (CAS), that at 60^{o} fibre angle of the upper and lower skin, the flutter speed was higher than -60^{o} fibre angle. Hence having the combination of positive material coupling stiffness, higher frequency ratio, and structural geometric coupling could be used to increase the flutter speed.
- The analysis showed that the structural damping had no effect on the flutter speed of the Cranfield A1 aerobatic composite clean wing box.

There are other important aeroelastic instabilities, which were not covered in this work such as divergence, which is a static aeroelastic problem. It is the speed at which the total damping is zero at zero frequency. Usually the wash-in deformation is beneficial to the flutter speed and vise versa for the divergence speed. Therefore, in practice all of the aeroelastic instability needs to be investigated to ensure that the aeroelastic instability is out of the operating flight envelope of the aircraft.

Manufacturing considerations are very important in the design and prototype construction of any aircraft in terms of cost and reliability. However since this work did not deal with the manufacturing process, hence same is not being discussed here.

10.2 Recommendation for future work:

As with any study, a great number of new studies suggest themselves. The investigation discussed in this thesis has given birth to some interesting areas for further research, which should include the following:

- Development of a methodology concept automatic for aeroelastic (flutter) optimization. The methodology should take into account all primary design parameters, which are relevant for the calculation of the flutter speed.

- Aeroelastic tailoring could be done on the thin-walled and on the Cranfield A1 composite wing box, which has rapidly attracted the attention of many researchers in the field, by applying optimization techniques. Aeroelastic tailoring is considered to be a particular application of the general field of structural optimization under aeroelastic constrains.
- Further basic understanding could be generated by:

1. Investigations of the effect of sweep angle for different aspect ratio of a thin-walled structure with having both uniform and non uniform stiffness along the span of the wing on the dynamic and aeroelastic (flutter speed) characteristics.
2. The analysis could be done for different practical laminate lay ups using balanced and unbalanced configurations using symmetric, unsymmetric, and asymmetric stacking sequence with having both uniform and non uniform stiffness along the span of the wing.
3. The sensitivity of the fibre angle of other structural components than the upper and lower skin such as spar webs on the dynamic (eigenvalues and eigenvectors) and flutter speed of the composite wing structure.

- The possibility of performing a wind tunel test on both thin-walled wing and the Cranfield A1 composite wing box, to compare and validate the obtained theoretical results.
- Making the thin-walled structure and the A1 aerobatic composite wing more practical by attaching the wing box to a lumped mass representing the aircraft engine or landing gear could be added to the model. The variation of the lumped mass in both chordwise and spanwise locations and its subsequence effects on the eigenvalues and eigenvectors and on the flutter speed.
- The analytical and experimental investigation using a cantilevered wing should be extended to the whole aircraft configuration. A comparison between the cantilever flutter speed with that of the whole aircraft is important since the rigid-body modes can play an important role on the flutter of composite wings. It would also be interesting to show how the fibre of the tail can be oriented in order to assist in increasing the flutter speed of the whole aircraft and also to eliminate wing-tail interference flutter.

APPENDIX A

A1 Flutter input data file of the Cranfield A1 simplified metal wing box:

The input data file presented below is for the simplified model of the metal wing box structure of the Cranfield A1 aerobatic aircraft for performing the flutter analysis (Sol. 145). This input data file was created by the preprocessor MSC/XL and analyzed by MSC/NASTRAN.

```
ID    MSC-XL, MSC-NASTRAN
SOL 145
TIME 600000
CEND
$ Direct Text Input for Global Case Control Data
TITLE = SIMPLIFIED METAL WING BOX STRUCTURE
  ECHO = BOTH
  SPC = 1
  SDAMP = 2000
  METHOD = 70
  FMETHOD = 30
$
OUTPUT(XYOUT)
  CSCALE 2.0
  PLOTTER NASTRAN
  CURVELINESYMBOL =6
  YTTITLE = DAMPING G
  YBTITLE = FREQUENCY F HZ
  XTITLE = VELOCITY V (M/S)
  XTGRID LINES = YES
  XBGRID LINES = YES
  YTGRID LINES = YES
  YBGRID LINES = YES
  UPPER TICS = -1
  TRIGHT TICS = -1
  BRIGHT TICS = -1
  XYPLOT VG / 1(G,F) 2(G,F) 3(G,F) 4(G,F)
$
BEGIN BULK
PARAM    POST    -1
PARAM    PATVER  3.
PARAM   COUPMASS 0
PARAM   AUTOSPC YES
PARAM        WTMASS     0.001
PARAM        GRDPNT     1
PARAM,NOCOMPS,-1
$ THIS SECTION CONTAINS BULK DATA FOR THE SIMPLIFIED CRANFIELD-
$ A1 METAL WING BOX.
$
$                              * WING BOX GRID *
```

```
$
$       The grid card defines the location of a structural grid point. Listed are its
$       coordinate system ID, its location, the ID of the coordinate system in which its
$       displacements are defined, its permanent single-point constraints and its
$       associated super element ID.
$
GRID    1       -638.15     0.0     0.0
GRID    2       -637.63     55.     0.0
GRID    3       -637.11     110.    0.0
GRID    5       -636.36     190.    0.0
GRID    6       -635.61     270.    0.0
GRID    8       -634.855    350.5   0.0
GRID    9       -634.1      431.    0.0
GRID    11      -628.525    545.7   0.0
GRID    12      -622.95     660.4   0.0
GRID    14      -615.544    812.8   0.0
GRID    15      -608.138    965.2   0.0
GRID    17      -600.119    1130.2  0.0
GRID    18      -592.1      1295.2  0.0
GRID    20      -587.065    1339.7  0.0
GRID    21      -582.03     1384.2  0.0
GRID    23      -568.375    1504.9  0.0
GRID    24      -554.72     1625.6  0.0
GRID    26      -534.61     1803.4  0.0
GRID    27      -514.5      1981.2  0.0
GRID    29      -496.025    2159.   0.0
GRID    30      -477.55     2336.8  0.0
GRID    32      -457.755    2527.3  0.0
GRID    33      -437.96     2717.8  0.0
GRID    35      -416.845    2921.   0.0
GRID    36      -395.73     3124.2  0.0
GRID    38      -371.06     3340.1  0.0
GRID    39      -346.39     3556.   0.0
GRID    41      -321.72     3771.9  0.0
GRID    42      -297.05     3987.8  0.0
GRID    44      -268.09     4216.4  0.0
GRID    45      -239.13     4445.   0.0
GRID    47      -210.175    4673.6  0.0
GRID    48      -181.22     4902.2  0.0
$
$       The CBEAM card defines a beam element. Listed are its property card ID, the
$       two grid points jointed by the beam and components of a vector from the first
$       point. This vector defines the direction of the structural deflection of the point
$       and its positive sense, pin flags for beam ends, components of offset vectors in
$       the displacement coordinate system and scalar or grid point identification
$       numbers for the ends.
$
CBEAM   1       50      1       2       0.0     1.      1.
```

```
CBEAM  2       50      2       3       0.0     1.      1.
CBEAM  3       51      3       5       0.0     1.      1.
CBEAM  4       51      5       6       0.0     1.      1.
CBEAM  5       52      6       8       0.0     1.      1.
CBEAM  6       52      8       9       0.0     1.      1.
CBEAM  7       53      9       11      0.0     1.      1.
CBEAM  8       53      11      12      0.0     1.      1.
CBEAM  9       54      12      14      0.0     1.      1.
CBEAM  10      54      14      15      0.0     1.      1.
CBEAM  11      55      15      17      0.0     1.      1.
CBEAM  12      55      17      18      0.0     1.      1.
CBEAM  13      56      18      20      0.0     1.      1.
CBEAM  14      56      20      21      0.0     1.      1.
CBEAM  15      57      21      23      0.0     1.      1.
CBEAM  16      57      23      24      0.0     1.      1.
CBEAM  17      58      24      26      0.0     1.      1.
CBEAM  18      58      26      27      0.0     1.      1.
CBEAM  19      59      27      29      0.0     1.      1.
CBEAM  20      59      29      30      0.0     1.      1.
CBEAM  21      60      30      32      0.0     1.      1.
CBEAM  22      60      32      33      0.0     1.      1.
CBEAM  23      61      33      35      0.0     1.      1.
CBEAM  24      61      35      36      0.0     1.      1.
CBEAM  25      62      36      38      0.0     1.      1.
CBEAM  26      62      38      39      0.0     1.      1.
CBEAM  27      63      39      41      0.0     1.      1.
CBEAM  28      63      41      42      0.0     1.      1.
CBEAM  29      64      42      44      0.0     1.      1.
CBEAM  30      64      44      45      0.0     1.      1.
CBEAM  31      65      45      47      0.0     1.      1.
CBEAM  32      65      47      48      0.0     1.      1.
$
$       The CONM2 card defines a concentrated mass at grid point. Listed are its ID,
$       grid location, coordinate system to locate the center of gravity, the mass value
$       and the location of the center of gravity relative to the grid location, mass
$       moment of inertia measured at the grid location.
$
CONM2  50      3       0       1.-9    54.22                   +
+                118447.
CONM2  51      6       0       1.-9    52.722                  +
+                172398.
CONM2  52      9       0       1.-9    51.2                    +
+                172317.
CONM2  53      12      0       1.-9    40.061                  +
+                244306.
CONM2  54      15      0       1.-9    60.328                  +
+                289235.
CONM2  55      18      0       1.-9    56.42                   +
```

```
+               268123.1
CONM2  56   21     0      1.-9    48.6                  +
+               71522.91
CONM2  57   24     0      1.-9    92.835                 +
+               178167.
CONM2  58   27     0      1.-9    52.62                  +
+               220968.
CONM2  59   30     0      1.-9    47.15                  +
+               169226.
CONM2  60   33     0      1.-9    85.471                 +
+               131850.
CONM2  61   36     0      1.-9    84.57                  +
+               84011.
CONM2  62   39     0      1.-9    84.07                  +
+               57876.1
CONM2  63   42     0      1.-9    48.78                  +
+               44344.
CONM2  64   45     0      1.-9    52.314                 +
+               24352.
CONM2  65   48     0      1.-9    34.665                 +
+               12499.
$ THIS SECTION CONTAINS THE LOADS, CONSTRAINTS, AND CONTROL
$ BULK DATA ENTRIES
$       The SPC1 card defines a set of single point constraints and enforced
$       displacements. It listed the ID, grid point number, constrained degree of
$       freedoms and value of an enforced displacement.
SPC    1      1      123456  0.0
$
$ THIS SECTION CONTAINS THE PROPERTY AND MATERIAL BULK DATA
$ ENTRIES
$       The PBEAM card defines the properties of a beam element (CBEAM card).
$
PBEAM  50     60     3052.   4.795+7 2.48+8        6.2+7   .015073 +
+                                      +
+      YESA   1.                              +
+      1.     1.                               +
+
PBEAM  51     60     3052.   4.73+7  2.47+8        6.1+7   .015812 +
+                                      +
+      YESA   1.                              +
+      1.     1.                               +
+
PBEAM  52     60     3052.   4.58+7  2.47+8        5.9+7   .01578  +
+                                      +
+      YESA   1.                              +
+      1.     1.                               +
+
PBEAM  53     60     3052.   4.40+7  2.47+8        5.83+7  .014787 +
```

```
+                                                +
+     YESA   1.                                    +
+     1.     1.                                     +
+
PBEAM  54     60     2862.  3.80+7  2.34+8          5.6+7   .0132   +
+                                                +
+     YESA   1.                                    +
+     1.     1.                                     +
+
PBEAM  55     60     2513.  3.04+7  2.04+8          5.32+7  .01207  +
+                                                +
+     YESA   1.                                    +
+     1.     1.                                     +
+
PBEAM  56     60     2345.  2.66+7  1.88+8          4.97+7  .015712 +
+                                                +
+     YESA   1.                                    +
+     1.     1.                                     +
+
PBEAM  57     60     2125.  2.24+7  1.66+8          4.83+7  .0119   +
+                                                +
+     YESA   1.                                    +
+     1.     1.                                     +
+
PBEAM  58     60     1886.  1.737+7 1.42+8          4.51+7  .010414 +
+                                                +
+     YESA   1.                                    +
+     1.     1.                                     +
+
PBEAM  59     60     1738.  1.43+7  1.215+8         4.02+7  .0089   +
+                                                +
+     YESA   1.                                    +
+     1.     1.                                     +
+
PBEAM  60     60     1451.  1.034+7 8.533+7         2.86+7  .00783  +
+                                                +
+     YESA   1.                                    +
+     1.     1.                                     +
+
PBEAM  61     60     1288.  7477000.5.67+7         2.+7    .00643  +
+                                                +
+     YESA   1.                                    +
+     1.     1.                                     +
+
PBEAM  62     60     1059.  5388000.3.59+7         1.518+7 .0054   +
+                                                +
+     YESA   1.                                    +
+     1.     1.                                     +
```

```
+
PBEAM  63     60     952.   3840000.2.45+7        1.+7    .004704 +
+                                          +
+      YESA   1.                                    +
+      1.     1.                                     +
+
PBEAM  64     60     840.   2620000.1.77+7        5929000..003615 +
+                                          +
+      YESA   1.                                    +
+      1.     1.                                     +
+
PBEAM  65     60     671.   1580500.9500000.      3602000..0030603+
+                                          +
+      YESA   1.                                    +
+      1.     1.                                     +
+
$
$       The MAT1 card defines the material properties. Listed are its ID, its elastic
$       modulus, Poisson's ratio, mass density, temperature expansion coefficient,
$       reference temperature and a structural damping coefficient.
MAT1    60     72400. 27000. .33
$
$       The ASET1 card defines the degree of freedoms that the user desired to be in the
$       analysis set. It lists the degree of freedom and the grid ID numbers.
ASET1   35     2      3      5      6      8      9      11
        12     14     15     17     18     20     21     23
        24     26     27     29     30     32     33     35
        36     38     39     41     42     44     45     47
        48
$
$       The parameter KDAMP determines the manner of including structural damping
$       in the equation of motion. If set to –1, modal structural damping is included as
$       the imaginary part of a complex stiffness matrix.
$
PARAM   KDAMP  -1
$       The TABDMP1 card and table define modal damping as a tabular function of
$       frequency. The damping values are linear between the frequency and damping
$       pairs and are extrapolated outside the tabulated frequency range.
TABDMP1 2000
      0.0    0.01   130.   0.01   ENDT
$                                  ***AERODYNAMIC DATA***
$                                   **ELEMENT GEOMETRY**
$       The AERO card gives the basic aerodynamic parameters for unsteady
$       aerodynamics. It specifies the AERO coordinate system, the velocity, the
$       reference chord and fluid density, plus the symmetry keys for the AERO
$       coordinate x-z and x-y planes respectively.
AERO    0              1207.0 1.22e-12 1
$       The CAERO1 card is used for Doublet-Lattice aerodynamic method. Listed are
```

```
$       its element ID, PAERO card ID, the coordinate system for locating the inboard
$       and outboard leading edge points, aerodynamic meshing (panels), ID for its
$       associated interference group. The continuation card defines points of the
$       inboard and outboard of the leading edge, root and tip chord.
CAERO1  300     600     0       10      4                               1
            -1578.7 0.0     0.0     2075.7  -420.50 5029.2  0.0     917.50
$
$       The PAERO1 card is required even though it is non-functional (because there
$       are no associated bodies in this case.
PAERO1  600
$
$       The SPLINE2 card specifies a beam spline for interpolation over the region of
$       CAERO1 card, SETG refers to a SET1 card where the structural grid points are
$       defined, smoothing constants for linear attachment and torsional flexibility,
$       rectangular coordinate system that defines the y-axis of the spline and rotational
$       attachment flexibility's.
SPLINE2 400     300     300     339     450     0.      1.      0
        0.0
$
$       The SET1 card defines the sets of structural grid points to be used by the beam
$       spline for interpolation.
SET1    450     1       3       6       9       12      15      18
        21      24      27      30      33      36      39      42
        45      48
$       All the combinations of Mach number and reduced frequency listed on the
$       MKAERO1 card and its continuation card will be used to generate generalized
$       AERO force matrices.
MKAERO1  0.4
        0.001   0.1     0.2     0.3     0.4     0.5     0.7     0.8
$
$       The EIGRL card specifies the method of extracting the eigen-solutions of the
$       wing structure using the Lanczos method. Ten modes are desired, normalized to
$       the unit value of the generalized mass.
EIGRL   70                      10      1
$       The PARAM, OPPHIPA, 1 provides the vibration modes for the modal plot
$       requests.
PARAM   OPPHIPA 1
$
$       The PARAM, LMODES, N card specifies that N modes are to be used in the
$       flutter analysis.
PARAM   LMODES  4
$
$       The flutter card defines the method of solution, identifies the FLFACT cards that
$       follow, specifies the interpolation method, the number of roots desired in the
$       output and the criterion for convergence.
FLUTTER 30      pk      10      20      25      L       4
$
$       FLFACT cards are used to specify density ratios, Mach number's and reduced
```

```
$       frequencies/velocities for flutter analysis.
$
FLFACT  10     0.7386
$
FLFACT  20     0.40
$
FLFACT  25     2.0e5  3.0e5  4.0e5  5.0e5  5.5e5  5.75e5  6.0e5
               6.5e5  7.0e5  7.5e5
$
$       The PARAM, VREF, C card specifies a conversion factor to be used to convert
$       the dimensions of the output velocities by dividing by C (1000 in this case).
PARAM   VREF    1000.0
ENDDATA
```

A2 Flutter input data file of the composite wing 1 model:

This is the flutter input data file of the wing1 model (see chapter 8). In this case the fibre angle of the upper and lower skin of the structure was oriented only at 30 degree to simulate (CAS) configuration. The structural was modeled using the preprocessor MSC/PATRAN 6.0 and analyzed by MSC/NASTRAN.

```
$ NASTRAN input file created by the MSC MSC/NASTRAN input file
$ translator ( MSC/PATRAN Version 6.0 ) on May       26, 1998 at
$ 19:06:24.
ASSIGN OUTPUT2 = 'thin33e5b30f.op2', UNIT = 12
$ Direct Text Input for File Management Section
$ Flutter Analysis (solution number 145)
SOL 145
TIME 600000000
CEND
$ Direct Text Input for Global Case Control Data
TITLE = COMPOSITE WING BOX (WING1/CASE1)
MAXLINES = 999999999
  ECHO = BOTH
  SPC = 2
  SDAMP = 2000
  METHOD = 40
  FMETHOD = 30
  VECTOR(PLOT)=ALL
$
OUTPUT(PLOT)
  CSCALE 2.0
  PLOTTER NASTRAN
  SET 1 = QUAD4
```

```
   PTITLE = STRUCTURAL ELEMENTS
   FIND SCALE, ORIGIN 1, SET 1
   PLOT MODAL 0 ORIGIN 1, SET 1
$
OUTPUT(XYOUT)
   CSCALE 2.0
   PLOTTER NASTRAN
   CURVELINESYMBOL =6
   YTTITLE = DAMPING G
   YBTITLE = FREQUENCY F HZ
   XTITLE = VELOCITY V (M/S)
   XTGRID LINES = YES
   XBGRID LINES = YES
   YTGRID LINES = YES
   YBGRID LINES = YES
   UPPER TICS = -1
   TRIGHT TICS = -1
   BRIGHT TICS = -1
   XYPLOT VG / 1(G,F) 2(G,F) 3(G,F) 4(G,F) 5(G,F) 6(G,F)
$ Direct Text Input for this Subcase
BEGIN BULK
PARAM    POST    -1
PARAM    PATVER  3.
PARAM   COUPMASS 0
PARAM    K6ROT   1.
PARAM    WTMASS  .001
PARAM,NOCOMPS,-1
$ Direct Text Input for Bulk Data
$ Elements and Element Properties for region : p1
$ Composite Property Record created from P3/PATRAN composite material
$ record : upper skin (us)
$ Composite Material Description :
$       The PCOMP card defines the properties of an n-ply composite material
$       laminate. Listed are its property ID of PCOMP of the upper skin, offset, material
$       ID, ply thickness and orientation angle of the longitudinal direction of each ply
$       with the material axis of the element.
PCOMP   1                               0.      0.          +     A
+     A 1      .17     30.     YES     1      .17     30.     YES   +     B
+     B 1      .17     0.      YES     1      .17     0.      YES   +     C
+     C 1      .17     30.     YES     1      .17     30.     YES
$       The CQUAD4 card defines an isoparametric membrane-bending or plane strain
$       quadrilateral plate element of the upper skin. Listed are its element ID, property
$       identification of PCOMP, grid points and material coordinate system
$       identification number.
CQUAD4  1       1       1       2       43      42      0
CQUAD4  2       1       2       3       44      43      0
CQUAD4  3       1       3       4       45      44      0
```

```
CQUAD4  4      1      4      5      46     45     0
$TO
CQUAD4  198    1      202    203    244    243    0
CQUAD4  199    1      203    204    245    244    0
CQUAD4  200    1      204    205    246    245    0
$ Elements and Element Properties for region : p2
$ Composite Property Record created from P3/PATRAN composite material
$ record : lower skin (ls)
$ Composite Material Description :
$       The PCOMP card defines the properties of an n-ply composite material
$       laminate of the lower skin. Listed are its property ID of PCOMP, offset, material
$       ID, ply thickness and orientation angle of the longitudinal direction of each ply
$       with the material axis of the element.
PCOMP   2                              0.     0.          +     D
+     D 1      .17    30.    YES    1      .17    30.    YES   +     E
+     E 1      .17    0.     YES    1      .17    0.     YES   +     F
+     F 1      .17    30.    YES    1      .17    30.    YES
$       The CQUAD4 card defines an isoparametric membrane-bending or plane strain
$       quadrilateral plate element of the lower skin. Listed are its element ID, property
$       identification of PCOMP of the lower skin, grid points and material coordinate
$       system identification number.
CQUAD4  201    2      247    248    289    288    0
CQUAD4  202    2      248    249    290    289    0
CQUAD4  203    2      249    250    291    290    0
CQUAD4  204    2      250    251    292    291    0
$TO
CQUAD4  398    2      448    449    490    489    0
CQUAD4  399    2      449    450    491    490    0
CQUAD4  400    2      450    451    492    491    0
$ Elements and Element Properties for region : p3
$ Composite Property Record created from P3/PATRAN composite material
$ record : front spar (fs)
$ Composite Material Description :
$       The PCOMP card defines the properties of an n-ply composite material
$       laminate of front spar. Listed are its property ID of PCOMP of the front
$       spar, offset, material ID, ply thickness and orientation angle of the longitudinal
$       direction of each ply with the material axis of the element.
PCOMP   3                              0.     0.          +     G
+     G 1      .17    45.    YES    1      .17    -45.   YES   +     H
+     H 1      .17    45.    YES    1      .17    -45.   YES
$       The CQUAD4 card defines an isoparametric membrane-bending or plane strain
$       quadrilateral plate element of the front spar. Listed are its element ID, property
$       identification of PCOMP of the front spar, grid points and material coordinate
$       system identification number.
CQUAD4  401    3      452    453    207    206    0
CQUAD4  402    3      453    454    208    207    0
CQUAD4  403    3      454    455    209    208    0
```

```
CQUAD4  404    3      455    456    210    209    0
$TO
CQUAD4  438    3      489    490    244    243    0
CQUAD4  439    3      490    491    245    244    0
CQUAD4  440    3      491    492    246    245    0
$ Elements and Element Properties for region : p4
$ Composite Property Record created from P3/PATRAN composite material
$ record : rear spar (rs)
$ Composite Material Description :
$       The PCOMP card defines the properties of an n-ply composite material
$       laminate of rear spar. Listed are its property ID of PCOMP of the rear
$       spar, offset, material ID, ply thickness and orientation angle of the longitudinal
$       direction of each ply with the material axis of the element.
PCOMP   4                              0.     0.          +     I
+     I 1      .17    -45.    YES     1      .17    45.    YES   +     J
+     J 1      .17    -45.    YES     1      .17    45.    YES
$       The CQUAD4 card defines an isoparametric membrane-bending or plane strain
$       quadrilateral plate element of the rear spar. Listed are its element ID, property
$       identification of PCOMP of the rear spar, grid points and material coordinate
$       system identification number.
$
CQUAD4  441    4      247    248    2      1      0
CQUAD4  442    4      248    249    3      2      0
CQUAD4  443    4      249    250    4      3      0
CQUAD4  444    4      250    251    5      4      0
$TO
CQUAD4  478    4      284    285    39     38     0
CQUAD4  479    4      285    286    40     39     0
CQUAD4  480    4      286    287    41     40     0
$ Referenced Material Records
$ Material Record : mid10
$ Description of Material : Date: 25-Mar-98         Time: 11:39:24
$       The MAT8 card defines the material properties for an orthotropic material for
$       shell elements. Listed are its material ID on the PCOMP card, modulus of
$       elasticity in longitudinal direction (1), modulus of elasticity in lateral direction
$       (2), poisson's ratio, in-plane shear modulus, transverse shear modulus in 1-Z
$       plane, transverse shear modulus in 2-Z plane, mass density, thermal expansion
$       coefficient in 1-direction, thermal expansion coefficient in 2-direction, structural
$       damping coefficient, reference temperature.
MAT8    1      130000. 9000.  .28    4800.                1.61-6 +     K
+     K-1.-7   2.8-5
$ Nodes of the Entire Model
$       The grid card defines the location of a structural grid point. Listed are its
$       coordinate system ID, its location, the ID of the coordinate system in which its
$       displacements are defined, its permanent single-point constraints and its
$       associated super element ID.
GRID    1      1      0.     0.          13.    1
GRID    2      1      0.     19.0500     13.    1
```

```
GRID    3       1       0.      38.1000 13.     1
GRID    4       1       0.      57.1500 13.     1
$TO
GRID    488     1       -35.    685.799 0.      1
GRID    489     1       -35.    704.849 0.      1
GRID    490     1       -35.    723.899 0.      1
GRID    491     1       -35.    742.949 0.      1
GRID    492     1       -35.    762.    0.      1
$ Loads for Load Case : Default
$       The SPCADD card defines a single point constraint set as a union of single
$       point constraint sets defined on SPC or SPC1 entries. Listed are its
$       identification number and identification of single point constraint sets
$       defined via SPC or SPC1 entries.
SPCADD  2       1
$ Displacement Constraints of Load Set : b
$       The SPC1 card defines a set of single point constraints and enforced
$       displacements. It listed the ID, grid point number, constrained degree of
$       freedoms and value of an enforced displacement.
SPC1    1       123456  1       42      83      124     165     206     +       L
+       L 247   288     329     370     411     452
$ Referenced Coordinate Frames
$       This CORD2R card defines the aerodynamic coordinate system flagged by the
$       AERO card. Listed are the origin, a point along the Z-axis and a point in the X-Z
$       plane. All the coordinate points are based on the basic coordinate system (0) in
$       this case.
CORD2R  1               0.      0.      0.      0.      1.      0.      +       M
+       M 0.    0.      1.
$
PARAM   KDAMP   -1
$
TABDMP1 2000
        0.0     0.02    750.0   0.02    ENDT
$
$                                       AERODYNAMIC DATA
$
AERO    1               35.     1.22e-12 1
$
CAERO1  800     600     1       20      4                       1
            -35.    0.0     13.0 35.    -35.    762.    13.0    35.
$
PAERO1  600
$
$       The SPLINE1 card specifies a surface spline for interpolating out of plane
$       motion displacement from the structural grid points on the SETG card to the
$       sub-region defined by aerodynamic boxes 800 through 879 of the region on the
$       CAERO1 card. It is also specifies the linear attachment flexibility through DZ in
$       the SPLINE1 card, which is zero in this case (i.e. no smoothing of the spline is
$       imposed).
```

```
SPLINE1 950     800     800     879     450     .0
SET1    450     1       3       5       7       9       11      13
        15      17      19      21      23      25      27      29
        31      33      35      37      39      41      42      44
        46      48      50      52      54      56      58      60
        62      64      66      68      70      72      74      76
        78      80      82      83      85      87      89      91
        93      95      97      99      101     103     105     107
        109     111     113     115     117     119     121     123
        124     126     128     130     132     134     136     138
        140     142     144     146     148     150     152     154
        156     158     160     162     164     165     167     169
        171     173     175     177     179     181     183     185
        187     189     191     193     195     197     199     201
        203     205     206     208     210     212     214     216
        218     220     222     224     226     228     230     232
        234     236     238     240     242     244     246
MKAERO1 0.4
      0.001   0.1     0.2     0.3     0.4     0.5     0.7     0.8
$
$       The EIGRL card specifies the method of extracting the eigen-solutions of the
$       wing structure using the Lanczos method. Six modes are desired, normalized to
$       the unit value of the generalized mass.
EIGRL   40                      6       1
$
PARAM   OPPHIPA 1
$                               FLUTTER   ANALYSIS
$
$       The PARAM, LMODES, N card specifies that N modes are to be used in the
$       flutter analysis. In this case the first six vibration modes are used in flutter
$       analysis.
PARAM   LMODES  6
$
FLUTTER 30      PK      10      20      25      L       6
$
FLFACT  10      0.7386
$
FLFACT  20      0.4
$
FLFACT  25      3.0e5   3.5e5   4.0e5   4.5e5   5.0e5   5.5e5   6.0e5
                6.5e5   7.0e5   7.5e5   8.0e5   8.5e5
$
PARAM   VREF    1000.0
ENDDATA 77141a67
```